Understanding and simulating vibrations of plain bridge cables under varying meteorological conditions

Wind tunnel experimental work and analytical modelling

Matteoni, Giulia; Georgakis, Christos T.; Ricciardelli, Francesco; Arentoft, Mogens; Koss, Holger; Svensson, Eilif

Publication date:
2014

Document Version
Peer reviewed version

Citation (APA):
Matteoni, G., Georgakis, C. T., Ricciardelli, F., Arentoft, M., Koss, H., & Svensson, E. (2014). Understanding and simulating vibrations of plain bridge cables under varying meteorological conditions: Wind tunnel experimental work and analytical modelling. DTU Tryk.

Understanding and simulating vibrations of plain bridge cables under varying meteorological conditions

- Wind tunnel experimental work and analytical modelling

G. Matteoni

Ph.D. Thesis

Department of Civil Engineering
Technical University of Denmark

2013

Supervisors:

Associate Professor C.T. Georgakis, DTU Byg
Associate Professor H.H. Koss, DTU Byg
Associate Professor F. Ricciardelli, University of Reggio Calabria
Mogens Arentoft, IPU
Eilif Svensson, ES-Consult A/S

Assesment Committee:

Professor Jasna B. Jakobsen, University of Stavanger
Doctor John Macdonald, University of Bristol
Associate Professor Gregor Fischer, DTU Byg

Understanding and simulating vibrations of plain bridge cables
under varying meteorological conditions
-Wind tunnel experimental work and analytical modelling

Printed by DTU-Tryk
Department of Civil Engineering
Technical University of Denmark
ISBN: 1234567891234
ISSN: 1234-5678

a Tommaso, con affetto

Preface

This thesis is submitted in partial fulfilment of the requirements for the Danish Ph.D. degree. The work has been carried out at the Department of Civil Engineering at the Technical University of Denmark in collaboration with IPU and took place in the period between May 2010 to July 2013, with Associate Professor Christos T. Georgakis as main supervisor and Associate Professor Holger Koss, Associate Professor Francesco Ricciardelli, Mogens Arentoft and Eiliff Svensson as co-supervisors.

This thesis is based upon published and under-review articles in ISI journals. The first chapter gives a literature review on bridge cable vibration phenomena under varying meteorological conditions, while each of the subsequent four chapters are made up by separate and unedited reproduction of above mentioned journal papers. Lastly, the combined work is discussed and conclusions are made in respect to the initially introduced problems, together with other outcomes of the work.

Kongens Lyngby, the 31st July 2013

G. Matteoni

Preface to published version

The thesis was defended at a public defence on the ... . The official assessment committee consisted of Associate Professor Gregor Fischer (chairman), Technical University of Denmark, Doctor John Macdonald, University of Bristol, and Professor Jasna B. Jakobsen, University of Stavanger.

Kongens Lyngby, the 31st July 2013

G. Matteoni

Acknowledgements

My first debt of gratitude goes to my supervisor, Associate Professor Christos T. Georgakis, who has patiently provided the vision, encouragement and advise necessary to complete the project, while leaving at the same time great freedom to pursue independent work.

Special thanks go to all my co-supervisors, Associate Professor Holger Koss, Associate Professor Francesco Ricciardelli, Mogens Arentoft and Eilif Svensson, for their support, guidance and helpful suggestions.

I acknowledge the financial support from Femern Belt A/S, funding the construction of a state of the art wind tunnel testing facility, which made all this possible.

I'd like to express my gratitude to the technicians at DTU-BYG, in particular Keld Plougmann, Robert Svan and Erik Bjørn Kristiansen, for their patience and precious work.

A special thank goes to the PhD student Cristoforo Demartino, who collaborated to the analytical model.

Thanks to all other fellow students and PhDs for direct help or inspiration, in particular Nina Gall Jørgensen, Joan Hee Roldsgaard, Mia Schou Møller Lund, Anna Emilie Thybo, Annett Anders, Ieva Paegle, Antonio Acampora, Jan Winkler, Kenneth Kleissl, Emanuele Mattiello, Mads Beedholm Eriksen, Rocco Custer, Shouyung Zhan.

Thanks to my family, who always encouraged me during this very long stay in Denmark, to my friends, and to Rocco for his loving support.

Abstract

The dissertation investigates the phenomenon of wind induced vibration of bridge cables under varying meteorological conditions. A twin research approach is adopted, where wind tunnel investigation of full-scale bridge cable section models is paralleled with theoretical modelling.

A literature review on bridge cable vibration mechanisms under the three surface states possibly achieved by cables, i.e. dry, wet and iced, was first undertaken. The study helped to systematize the understanding of the excitation phenomena occurring in the different climatic conditions, based on results of full-scale monitoring, wind tunnel testing and theoretical modelling.

An extensive wind tunnel test campaign was then undertaken in order to further understand the onset conditions and characteristics of instability in the different climatic conditions described in the literature. Tests were separated into two different categories, i.e. static and passive-dynamic.

Static wind tunnel tests were performed in dry surface conditions, for varying Reynolds number, turbulence intensity, cable-wind angle, and angle-of-attack. It was understood that dry instability is very sensitive to microscopic imperfections of the cable surface, such as deviations from the nominal shape of the external HDPE tubing or alterations of its inherent surface roughness. It was in fact observed that in the critical Reynolds number range, while the drag coefficient is consistent with changes in the angle-of-attack, the lift coefficient exhibits marked variations. This variation is sufficient to generate negative quasi-steady aerodynamic damping, and thus to potentialy lead to galloping instability.

Passive dynamic wind tunnel tests were subsequently undertaken for a cable section model of the same type as the one tested in static conditions. Tests were undertaken at a critical cable-wind angle for the occurrence of dry inclined galloping, for varying Reynolds numbers and angles-of-attack. As confirmation of the findings from the static tests, it was observed that the dynamic response of the cable section, i.e. in terms of peak-to-peak amplitudes and aerodynamic damping, changes consistently with Reynolds number, for the tested wind angles-of-attack. In fact, for selected angles-of-

attack, the response was stable thoughout the whole tested range of Reynolds number, while for other angles, negative aerodynamic damping, accompanied by large amplitude peak to peak amplitudes, occurred. This latter behaviour was likely to be associated to dry inclined galloping.

Passive dynamic wind tunnel tests were finally undertaken in presence of rain, using the same cable model as adopted in the dry state. The tests served to improve the current understanding of the phenomenon of rain-wind induced vibration. Test results showed that when the a critical surface tension is achieved for the cable sheating, an oscillating lower and upper water rivulet form on its surface. The angular oscillation of the rivulets contribute to amplify the vertical vibration of the cable, which becomes large in amplitude and is accompanied by negative aerodynamic damping. On the other hand, when the surface tension of the cable is too low a steady upper and lower non-coherent water rivulets form. These are not sufficient for the excitation to get started, independently of the cable mass. The cable model was in fact manifestly stable and exhibited positive aerodynamic damping throughout the whole range of tested Reynolds number, being accompanied by limited peak-to-peak amplitude.

A generalized quasi-steady 3 DOF analytical model for the prediction of the aerodynamic instability of a slender prism with generic cross section, i.e. either bluff or streamlined, immersed in unsteady wind flow, and characterized by a general spatial orientation with respect to the wind direction, was finally developed. The model accounted for variation of the force coefficients, i.e. drag, lift, and moment, with Reynolds number based on the relative flow velocity, with relative angle-of-attack, and relative cable-wind angle. The aerodynamic forces acting on the structure were linearized about zero structural velocities, structural rotation and about the steady component of the total wind velocity. Based on the analytical solution of the eigenvalue problem, by applying the Routh-Hurwitz criterion, an expression of the minimum structural damping and structural stiffness required to prevent aerodynamic instabilities of galloping- and static divergence-type respectively are given.

Resumé

Denne afhandling undersøger fænomenet vind-inducerede vibrationer af brokabler under forskellige meteorologiske forhold. Forskningsmetoden, der er anvendt, paralleliserer vindtunneltests udført på sektioner af fuldskala brokabler med teoretisk modellering.

Det indledende litteraturstudium, der omhandlede vibrationsmekanismer for brokabler under tre mulige overfladetilstande, tør, våd og iset, hjalp med at systematisere forståelsen for de fænomener, der igang-sætter kabelvibrationer under forskellige klimatiske forhold. Studiet var baseret på resultater fra fuldskala overvågning, vindtunneltests og teoretisk modellering.

Et omfattende program for vindtunneltests blev igangsat for at opnå en dybere forståelse for begyndel-sesbetingelserne og kendetegnene ved instabilitet for de forskellige klimatiske forhold beskrevet i litteraturen.

Først blev statiske vindtunneltests udført på sektioner af fuldskala brokabler orienteret vinkelret og skråt i forhold til vindretningen under tørre forhold. Forsøgene blev udført for varierende Reynolds tal, angrebsvinkler samt turbulensintensiteter. De enkelte parametres betydning blev detaljeret evalueret. Det fremgik af forsøgene, at instabilitet af tørre kabler er yderst følsom over for mikroskopiske imperfektioner såsom afvigelser i den nominelle diameter af det ydre HDPE rør og forandringer i rørets naturlige overfladeruhed. Mens drag koefficienterne er konstante med ændringer i angrebsvinklen, udviser lift koefficienterne en markant variation. Denne variation er tilstrækkelig til at danne negativ kvasi-permanent aerodynamisk dæmpning og dermed teoretisk set potentielt tilstrækkelig til at medføre galloping instabilitet. Passive dynamiske vindtunneltests blev efterfølgende foretaget på samme kabeltype som den, der var anvendt under de statiske forsøg. Forsøge blev udført for en kritisk kabel-vindvinkel med hensyn til dry inclined galloping. Denne kabel-vindvinkel var ligeledes blevet testet under statiske forhold.

De dynamiske forsøg blev udført for varierende Reynolds tal og angrebsvinkler. Det blev observeret, at kabelsektionens dynamiske respons med hensyn til *peak-to-peak* amplituder og aerodynamisk dæmpning ændres konsistent med Reynolds tallet for de undersøgte angrebsvinkler, hvilket bekræf-

ter resultaterne fra de statiske tests. Responset var stabilt gennem hele det testede interval af Reynolds tal for visse angrebsvinkler, hvorimod negativ aerodynamisk dæmpning ledsaget af store *peak-to-peak* amplituder forekom for andre angrebsvinkler. Sidstnævnte observation kan sandsynligvis associeres med dry inclined galloping. Endvidere blev der udført passive dynamiske vindtunneltests under regnpåvirkning ved at anvende den samme kabelmodel, som var anvendt i tør tilstand. Disse forsøg tjente det formål at få en forståelse for to parametres betydning − kablets overfladespænding og masse − hvis indflydelse i tidligere forsøg ikke var blevet undersøgt detaljeret. Forsøgresultaterne viste, at når overfladespændingen af kablet er for lav, vil der dannes en jævn øvre og nedre usammenhængende formation af løbende regnvand. Disse er, uafhængigt af kablets masse, ikke tilstrækkelige til at initiere instabilitet. Kablet var helt tydeligt stabilt og oplevede positiv aerodynamisk dæmpning gennem hele det testede interval af Reynolds tal. Dette var desuden ledsaget af begrænset *peak-to-peak* amplitude. Når det rette niveau i overfladespænding derimod opnås, vil der forekomme en øvre og nedre oscillerende formation af løbende regn, hvilket udløser vibrationer med stor amplitude. Disse vibrationer er ledsaget af negativ aerodynamisk dæmpning i et begrænset interval af Reynolds tal.

Endelig er en generel kvasi-permanent analytisk model med tre frihedsgrader blevet udviklet. Modellen er i stand til at forudsige aerodynamisk instabilitet af et legeme med generelt tværsnit, dvs. enten *bluff* eller strømlinet, nedsænket i ikke-stationær vindstrømning og karakteriseret ved en generel rumlig orientering med hensyn til vindretningen. Modellen tager hensyn til variation i kraftkoefficienterne, dvs. drag, lift og moment, med et Reynolds tal baseret på den relative vindhastighed, med relative angrebsvinkler og relative kabel-vindvinkler. De aerodynamiske kræfter, der virker på konstruktionen, er lineariseret omkring nul strukturel hastighed, nul strukturel rotation og omkring den steady komponent af den totale vindhastighed. Ved anvendelse af Routh-Hurwitz kriteriet er en analytisk løsning på egenværdiproblemet givet, hvorved der er fundet et udtryk for den mindste strukturelle dæmpning og strukturelle stivhed påkrævet for at forhindre aerodynamisk galloping instabilitet og static divergence instabilitet.

Contents

Chapter 1

Introduction

The development of cable-stayed bridges as a structural choice for medium to long span bridges has been remarkable through the closing decades of the last century. Stay cables play an essential role in the dynamic behaviour of cable-stayed bridges, and, being characterised by low mechanical damping, they are extremely vulnearable to wind excitation, (Fujino et al., 2012).

In the past years, numerous efforts have been made in order to understand the mechanisms of various types of wind-induced cable vibration phenomena and to find solutions for alleviating vibration problems. Some of the identified mechanisms, particularly when related to inclined bridge cables, such as rain-wind induced vibration, ice-induced vibrations, vortex-induced vibration at high reduced velocity and dry inclined galloping, generate serious preoccupation for the bridge designers. In fact, the associated vibration amplitudes are much larger than for classical vibration mechanisms, for example vortex-induced vibration or buffeting. Moreover, the excitation mechanisms of inclined cables still remain partially not understood, so that the amount of mechanical damping/stiffness necessary to couteract the vibration is still under discussion.

Rain-wind induced vibration represents the most frequently observed vibration mechanism on bridges. It was first recognised in 1988 at the Meiko-Nishi Bridge in Japan, during its period of construction. Here, the cables experienced large amplitude vibrations under the combination of certain wind conditions, i.e. in terms of velocity and direction, only when it was raining, (Hikami and Shairaishi, 1988). Fig. 1.1 shows the first prototype observation of rain water rivulet on the surface of a bridge cable, at the Meiko-Nishi Bridge, (Hikami and Shairaishi, 1988). After its first report, it became clear that some other cable vibration episodes observed earlier for other bridges, could have been classified in the same category as rain-wind induced vibration.

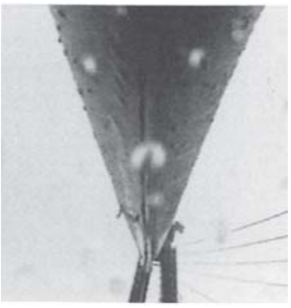

***Figure 1.1**: Prototype observation of rain water rivulet along the lower surface of the cable at the Meiko-Nishi Bridge in Japan, (Hikami and Shairaishi, 1988).*

The excitation mechanisms of rain-wind induced vibration has been made clearer in recent years, and some effective control methods have been successfully applied in practice.

Vortex-induced vibration at high reduced velocity and dry inclined galloping are on the other hand less understood and would require more intensive research attention. The dry inclined galloping, in particular, causes a very strong concern since it has been suggested that it can result in undesiderably large amplitude motion. For example vibrations amplitudes of 1.5 m have been reported for the inclined cables of a cable-stayed a bridge in Japan, in dry conditions, under the occurrence of a typhoon, at wind velocity of 18 m/s. The mechanism of excitation of such vibration episode has been interpreted as dry inclined galloping, (Matsumoto et al., 2010). Nevertheless, bridge failures due to dry cable vibration have been reported to occur for much lower wind velocities. For example, on February 2012, a vibration accident occurred at the Martin Olav Sabo Pedestrian Bridge in Minnesota, where the diaphragm plate holiding the cables to the main pylon fractured, see Fig. 1.2. The fracture was attributed to vibration of the cables occurring at low wind velocity, i.e. in the range of 2-5 m/s.

Numerous accidents have been reported for bridges worldwide in presence of ice accretions on the cable surface. Such accretions can provoke the phenomenon of ice shedding, which consists in the falling of large pieces of ice/snow from the cable surface to the bridge deck, thus threatening the safety of passengers. Moreover an aerodynamic modification of cable's surface usually occurs due to the ice formation which can lead to dynamic instabilities of galloping-type. Fig. 1.3 shows a view of the Toledo Skyway Bridge cables in Ohio, which in 2011 experienced the formation of thick and heavy ice accretions, leading to the bridge closure for several hours.

Episodes of inclined cable vibrations in the different meteorological con-

(a) (b)

Figure 1.2: *Episode of wind-induced bridge cable failure at the Sabo Pedestrian Bridge in Minnesota (Picture from **http://failures.wikispaces.com/Cable+Bridge+Failures+Overview**).*

ditions have motivated extensive research, which have been developing by following three main approaches, i.e. wind tunnel testing of small or full-scale bridge cable sections in static/dynamic conditions, full-scale monitoring on bridges, and theoretical modelling.

1.1 The research problem and the methodology

The main objective of the present research is the understanding and simulation of bridge cable vibration phenomena under the most prevalent meteorological conditions in Scandinavia, i.e. dry, wet and iced. In order to achieve this objective, a twin research method is adopted, where theoretical investigation of wind-induced bridge cable vibration phenomena is paralleled with novel climatic wind tunnel tests at the DTU/Force Climatic Wind Tunnel in Lyngby.

The work was divided in the following parts:

- The first part consisted in a literature review on the wind-induced vibration phenomena of inclned bridge cables. Vibration mechanisms occurring under each possible surface state achieved by bridge cable, i.e. dry, wet or iced, were examined based on field monitoring data, static and dynamic wind tunnel tests, and theoretical modelling. The purpouse of this was to explore the existing research within the field and to provide a database of knowledge and experience from which the current research could draw from. Gaps in the existing research were identified, so to plan the experimental work and theoretical analyses to

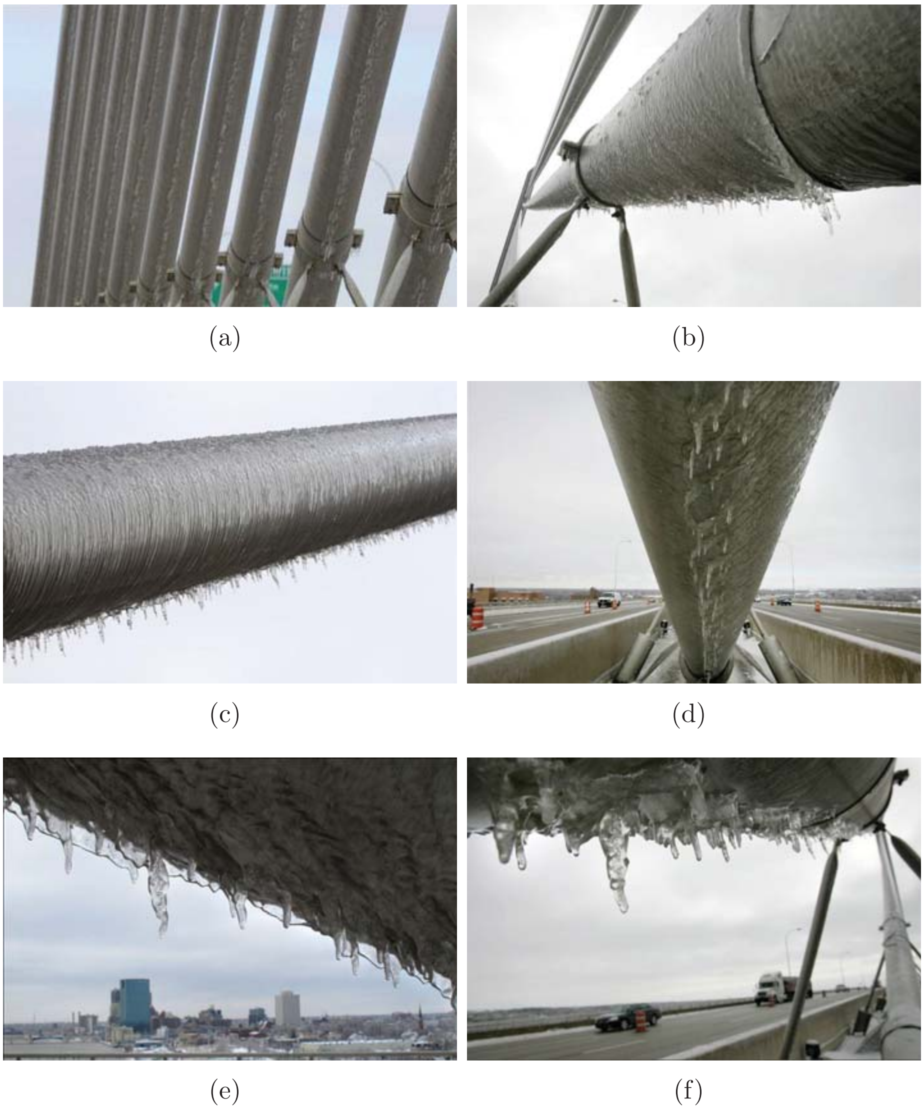
(a) (b)

(c) (d)

(e) (f)

Figure 1.3: *Ice formations on the cable sections at Toledo Skyway Bridge, in Ohio (Picture from* ***http://www.toledoblade.com/gallery/Ice-closes-Skyway****).*

be undertaken for this disseration.

- In the second part of the work an extensive wind tunnel test campaign was performed. Tests were separated into two different categories, i.e. static and passive-dynamic. Static wind tunnel tests were performed in dry surface conditions, while passive-dynamic tests were undertaken in both dry and wet state. For each category effects of Reynolds number, turbulence intensity, cable-wind angle, angle-of-attack were investigated. The overall study helped to significantly enhance the current undertanding of dry and wet cable instability.

- In the thrid part a generalized analytical model for the prediction of aerodynamic instability of inclined bridge cables was developed. In particular, the model applies for prisms with generic cross-section, i.e. either bluff, for example ice-accreted bridge or dry cables charactericted by minor impefections of their inherent surface, or streamlined bodies, such as bridge decks.

1.2 Thesis outline

The thesis is divided into seven chapters which are following the chronological research pattern.

Chapter II, Background review gives a literature review on the wind induced vibration phenomena of bridge cables, under varying meteorogical conditions, i.e. dry, wet and iced.

Chapter III, Static wind tunnel tests presents results of static wind tunnel tests undertaken on perpendicular, inclined and yawed bridge cables in dry conditions.

Chapter IV, Passive-dynamic wind tunnel tests in dry state shows results of passive-dynamic wind tunnel tests undertaken on inclined and yawed bridge cables in dry conditions.

Chapter V, Passive-dynamic wind tunnel tests in wet state shows results of passive-dynamic wind tunnel tests undertaken on inclined and yawed bridge cables in wet conditions.

Chapter VI, Analytical model describes the development of the analytical model and its practical application for a set of wind tunnel data obtained from the literature for an iced bridge cable.

Chapter VII, Conclusion presents the overall conclusions of the dissertation.

Bibliography

Fujino, Y., Kimura, K., Tanaka, H., 2012. Wind Resistant Design of Bridges in Japan. Springer.

Hikami, Y., Shiraishi, N., 1988. Rain-wind induced vibrations of cables stayed bridges. J. Wind Eng. Ind. Aerodyn. 29, 409-418.

Matsumoto, M., Yagi, T., Hatsuda, H., Shima, T., Tanaka, M., Naito, H., 2010. Dry galloping characteristics and its mechanism of inclined/yawed cables. J. Wind Eng. Ind. Aerodyn. 98, 317-327.

Chapter 2

Background review

A literature review on bridge cable vibration phenomena is given in this chapter. Focus is on the vibration mechanisms which are observed in the three surface states possibly achieved by inclined bridge cables: i.e. rainy (rain-wind induced vibration), dry (dry inclined galloping and and vortex induced vibration at high reduced wind velocity) and iced (galloping).

Abstract

Stay cables are very flexible structural members of cable-stayed bridges, characterised by low damping ratios. The most important loading acting on stay cables is the wind, which comprises a mean component, plus nil-mean fluctuating components induced by the turbulence. The cables are often exposed to wind with skew angles, leading to flow patterns with strong three-dimensional characteristics. Thus, they experience, besides conventional wind-induced excitation phenomena, such as Kármán-vortex excitation, possible wind-induced excitation phenomena specifically related to their inclined nature, for example dry inclined galloping, vortex shedding at high reduced velocity and rain-wind induced vibrations. Unstable motions of bridge cables represent not only a concern for the bridge users, but also raise safety issues such as fatigue at the cable anchorage points. Therefore it is quite relevant they are taken into account in the bridge design.

Aerodynamics of inclined cables has attracted increasing research attention since the 1980s, following field reports of large amplitude vibration on several cable-stayed bridges. A literature review on the different excitation mechanisms of inclined cables under varying meteorological conditions, i.e. in the dry, rainy and iced state, is here given. An attempt is made to systematize the understanding of the most recent phenomena of cable vibration, based

on results from full scale monitoring of cable vibrations on bridges, as well as wind tunnel testing of cable sectional models, and to present methodologies for their prediction, based on theoretical analyses. Lacks in the current understanding of the vibration phenomena are identified which motivate future research.

2.1 Introduction

Stay cables of cable stayed bridges are very flexible structural elements generally characterized by low levels of structural damping, therefore they are prone to vibrations, (Caetano, 2007). As cable-stayed bridges are being constructed with longer and longer spans, the wind loading becomes larger and it is comparable to the load acting on the deck, (Miyata et al., 1994b). Experience of cable vibrations is probably in every country where cable stayed bridges have been constructed, (Matsumoto et al., 2006). Vibrations of inclined cables are of concern because they can induce undue stresses and fatigue in the cables themselves and in the connections to the bridge deck, thus threatening safety and serviceability of the bridge.

Research attention on bridge cable vibration phenomena has been attracted following a field report of violent cable vibrations at the Meiko-Nishi Bridge in Japan, (Hikami and Shairaishi, 1988). Vibrations were experienced during its period of construction and occurred under the combined action of wind and rain. Following this episode and similar on existing bridges, cable vibrations have been investigated by following three complementary approaches, i.e. full scale monitoring of bridges, static and dynamic wind tunnel testing of scaled or full-scale cable sections, and theoretical modelling. Research has been undertaken in all climatic conditions possibly experienced by bridge cables, i.e. the dry, rainy and iced state. It has been understood that, depending on the surface state of the cable (dry, wet or iced), on its geometrical (surface roughness) and structural properties (mass, damping, stiffness), as well as on the wind velocity, direction, and wind turbulence, the features of the instability change considerably.

The rain-wind vibration (RWIV) induced instability is a limited amplitude-type vibration, occurring over a restricted range of wind velocities, corresponding to the transition between the subcritical and the critical Reynolds number range. It is provoked by the circumferential oscillation of the upper and lower water rivulets, which form on the cable surface when the right level of wettablility is achieved. This oscillation appears as a periodic change of the cable cross-section, seen from the flow, thus making the cable section unstable.

In the dry state, two types of instability can occur. The first one is known as vortex shedding at high reduced wind speed and is characterised by limited amplitude-type vibrations, occurring for a restricted interval of wind velocities in the critical Reynolds number range. The second one, known as dry inclined galloping, is characterised by the occurrence of vibrations growing without bound, once the wind velocity exceeds the critical one. This latter still belongs to the critical Reynolds number range. Recent studies have demonstrated that the non uniform distribution of surface roughness/shape of real bridge cables can introduce a dependency of the lift coefficient with angle of attack, (Matteoni and Georgakis, 2012), (Benedir et al., 2013). This is due to anticipation/delay of the critical Reynolds number. The observed dependency might be responsible for the occurrence of dry inclined galloping excitation. Additional excitation factor for dry inclined cables, besides the critical Reynolds number, is the axial flow forming in their wake. In particular, for the case of vortex shedding at high reduced wind speed, the conventional Kármán vortex shedding interacts with the axial vortex shedding. As the frequency of the latter is one third of the former, the cylinder's response is amplified when the axial vortexes shed once every three Kármán vortices from either side of the cable's model, (Matsumoto et al., 1999). In the case of dry inclined galloping, the axial flow interrupts the fluid interaction between the cable's separated shear layers and generates an unsteady inner circulatory flow at either the lower leeward or upper leeward side of the cable circular surface. This determines a region of significantly lower surface pressure which results in higher oscillatory aerodynamic forces and consequently to violent vibrations, (Matsumoto et al., 1990). Due to the lack of field monitoring data for violent cable vibrations in dry conditions, it has been stated that this type of instability is not fully verified, and can only be reproduced in wind tunnels. On the other hand, not all vibration episodes, recorded on bridges during rainy events, are likely to be induced by the angular oscillation of the water rivulets. In fact, the rivulets do not form on the cable surface when the right level of surface wettability is not achieved. In this condition, cable vibration identified as rain-wind induced, might be provoked by other excitation factors, and resemble dry inclined instability, (Matteoni and Georgakis, 2013b).

Instability of bridge cables in the iced state has been observed on bridges but no field monitoring data based has beed collected so far. Few experimental studies exist on the static determination of the aerodynamic coefficients of bridge cable sections covered by ice accretion, in the horizontal, (Koss and Matteoni, 2011), (Koss and Lund, 2013), vertical, (Demartino et al., 2013), and inclined/yawed, (Demartino et al., 2013), configuration with respect to the wind velocity. The mechanism of vibration of iced bridge cable sections has never been investigated by performing passive-dynamic wind tunnel tests. Thus, the characteristics of this instability are still uncertain.

In the present study, bridge cable vibration mechanisms occurring under varying meteorological conditions are examined. In particular, wind loads on inclined stays cables are first presented and the origins of various aeroelastic instabilities are explained from a theoretical point of view (2.2). A review on bridge cable instability, based on field monitoring data, static and dynamic wind tunnel tests, for each possible surface state potentially achieved by the cable, i.e. dry (2.4), wet (2.3) or iced (2.5), is presented.

2.2 Bridge cable aerodynamics

Bridge cables are generally modeled as line-like bodies, with linear-elastic structural behaviour, so that any non-linear part of the relationship between load and structural displacement may be disregarded.

Considering time intervals falling into the spectral gap (T = 10 minutes - 1 hour), (Van der Hoven, 1957), the wind field acting on the cable is usually schematized as the sum of three fluctuating orthogonal components, i.e. an along-wind horizontal component, $U + \tilde{u}(t)$, where U is the free-stream or mean wind velocity, an across-wind horizontal component, $\tilde{v}(t)$, and a vertical component, $\tilde{w}(t)$. The nil-mean turbulence components, $\tilde{u}(t)$, $\tilde{v}(t)$, $\tilde{w}(t)$, are induced by the friction between the terrain and the flow. The velocity components acting on the cable are illustrated in Fig. 2.2.

If the air flow is met by an obstacle represented by a solid line-like body, such as a bridge cable, the flow-structure interaction will give raise to forces acting on the body. Unless the body is extremely streamlined and the speed of the flow is very low and smooth, these forces will fluctuate. In fact, the oncoming flow in which the body is submerged contains turbulence, i.e. it is itself fluctuating in time and space. Moreover, additional flow turbulence and vortices are created on the surface of the body, due to friction. For example, if the body has sharp edges, the flow will separate on these edges and fluctuate, causing the vortices to be shed in the wake. Finally, as bridge cables are flexible, the fluctuating forces may cause the body to oscillate, and the alternating flow and the oscillating body may interact and generate additional forces.

Thus, the nature of wind forces may stem from pressure fluctuations (turbulence) in the oncoming flow, vortices shed on the surface and into the wake of the body, and from the interaction between the flow and the oscillating body itself. The first of these effects is known as *buffeting*, the second is known as *vortex shedding*, while the third one is usually named *motion-induced forces*, (Strømmen, 2010). Note that if the section of the body is not streamlined, the buffeting forces include, besides the force components induced by the undisturbed turbulence of the oncoming wind, additional force components associated with flow fluctuations which are body-initiated, i.e. due to the signature turbulence, (Davenport, 1962).

In structural engineering the wind-induced fluctuating forces and corresponding response quantities are usually assumed stationary, and thus, response calculations may be split into a time invariant and a fluctuating part (static and dynamic response), i.e.

$$r_{max} = \bar{r} + k_p \sigma_r \tag{2.1}$$

where r_{max} is the maximum structural response, $\bar{r}$ is the mean value of the response, k_p is the peak factor which depends on the type of process, σ_r is the standard deviation of the fluctuating part of the response. Fig. 2.1 shows the static and dynamic response variation of a slender structure with mean wind velocity.

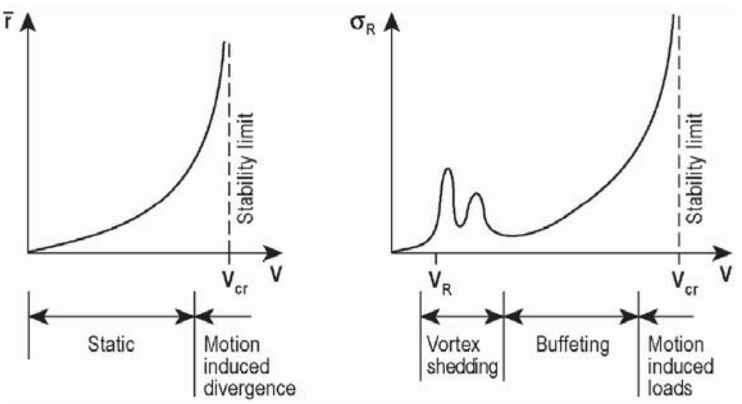

Figure 2.1*: Static (left) and dynamic (right) response variation with mean wind velocity, (Strømmen, 2010).*

The static part of the response ($\bar{r}$) is proportional to the mean velocity pressure, i.e. to the mean wind velocity squared, until motion induced forces may reduce the total stiffness of the combined structure and flow system, after which the static response may approach an instability limit (torsional divergence). The dynamic part of the response (σ_r) may conveniently be separated into three mean wind velocity regions, i.e. vortex shedding, buffeting and motion-induced, respectively. Vortex shedding effects will usually occur at fairly low mean wind velocities, buffeting will usually be the dominant effect in an intermediate velocity region, while at high wind velocities motion-induced load effects, i.e. galloping and flutter, may entirely govern the response. In the vicinity of a certain limiting (critical) mean wind velocity the response curve may increase rapidly, i.e. the structure shows signs of unstable behaviour in the sense that a small increase of the mean wind velocity implies a large increase of the static or dynamic response, indicating an upper stability limit, identified as critical wind velocity.

2.2.1 The quasi-steady assumption

When modelling the interaction between a bridge cable and the air flow, the validity of the *quasi-steady* assumption is normally assumed. A parameter which is generally used to assess the applicability of the quasi-steady assumption is the reduced wind velocity, U_r, defined as

$$U_r = \frac{U}{fD} \tag{2.2}$$

where U is the free-stream wind velocity, f is the frequency of cable oscillation and D is the cable's diameter.

- Large values of U_r imply that the cable moves slowly in the air, so that it can be considered fixed at any time from the flow point of view, i.e. the air flow can be considered as steady. Thus when the cable motion parameters change, the flow reaches instantaneously the time domain equilibrium. Under these conditions, the wind-cable interaction is considered weak, i.e. the forces acting on the cable depend only on the instantaneous cable configuration, while the time history of the cable motion do not play a role. In particular, the aerodynamic forces are evaluated based on the instantaneous flow velocity and on the static force coefficients of the cable section, these latter determined by performing for example wind tunnel tests.

- For low values of U_r, corresponding to high frequency motions, unsteady aerodynamic phenomena occur. This because a change in the structural configuration occurs fastly than a change in the wind configuration. In this case, the self-excited forces depend on the history of motion. This corresponds, in a frequency domain representation of the self-excited forces, to introducing a set of filters between the components of motion of the section and the corresponding forces; such filters are called aerodynamic or flutter derivatives and are determined experimentally by wind tunnel tests or numerically by Computational Fluid Dynamics, (Tubino, 2005).

An additional simplifying assumption which is normally made is that the cable is *slender* with respect to its longitudinal axis. Such hypothesis holds if the characteristic size of the section is small when compared to the length scale of the turbulence, i.e. the size of the eddies composing the turbulent flow, (Davenport, 1962). If the body is small compared to this scale, then the turbulent eddies can be considered as perfectly correlated around the cable. In this condition, the turbulent flow around the cable's body can be regarded as uniform and the forces acting on the section can be defined as function of the turbulence components in a point representative of the section. If this hypothesis holds, the buffeting forces (due to the undisturbed turbulence) can be evaluated by defining an instantaneous velocity corresponding to the resultant of the mean wind velocity and of the turbulence components. As the standard diameter of a structural cable can reach up to one fifth of a meter, it is reasonable to assume this hypothesis to hold. On the other hand, this assumption is not valid for bridge decks, whose cross-sections are normally very elongated and the shape is not always streamlined, (Tubino, 2005).

The wind loading and force components acting on the cable are treated in paragraph 2.2.2 by assuming the quasi-steady and slenderness hypotheses to hold.

2.2.2 Wind loading and force components

A stay cable can be modeled as a non-circular cylinder of infinite length, immersed in a 2-D flow, see Fig. 2.2, where (X, Y, Z) is a global reference system, with Y parallel to the free-stream velocity U, and Z being vertical. In Fig. 2.2, $\tilde{\mathbf{U}}(t)$ is the vector obtained by the summation of the nil-mean fluctuating wind velocity components $\tilde{u}(t)$, $\tilde{v}(t)$ and $\tilde{w}(t)$, while $\mathbf{U}(t)$ is the total wind velocity vector, given by the summation of $\tilde{\mathbf{U}}(t)$ and U. The projection of the total wind velocity, $\mathbf{U}(t)$, in the cable's cross-sectional plane and along the cable axis are the normal wind velocity, $\mathbf{U}_N(t)$ and $\mathbf{U}_A(t)$. (x', y', z) is a local reference system, with (x', y') belonging to the body's cross-sectional plane, and x' parallel to the normal wind velocity $\mathbf{U}_N(t)$; z is parallel to the body's longitudinal axis. $C_{x'}$, $C_{y'}$, $C_{Mz'}$ are the along-wind, across-wind and moment force coefficients.

In the ideal state of absence of structural motion and laminar wind flow, the wind velocity acting on an inclined cable is time invariant, i.e.

$$U_N = U \sin \Phi \tag{2.3}$$

$$U_A = U \cos \Phi \tag{2.4}$$

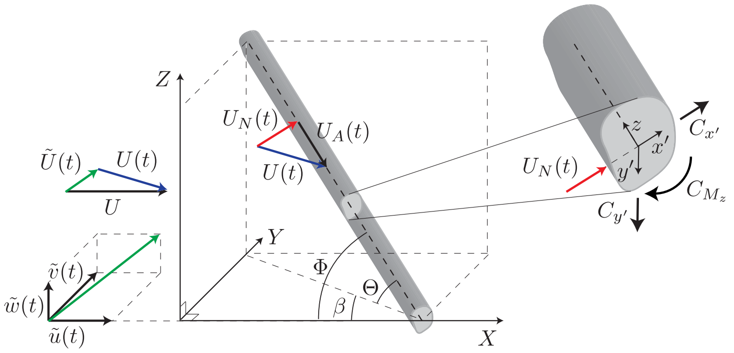

***Figure 2.2**: 3D geometry of and inclined stay cable and wind velocity components.*

The cable-wind angle, Φ, i.e. the angle between the cable axis and the free-stream velocity U is

$$\Phi = \arccos(\cos\Theta\cos\beta) \tag{2.5}$$

where Θ is the vertical inclination, and β is the horizontal yaw.

In the most generic case of an inclined cable exposed to turbulent flow, vibrating along two perpendicular directions belonging to the cable's cross-sectional plane and rotating about the longitudinal axis, the normal and axial component of the wind velocity, given by eqs. 2.3 and 2.4, are time dependent. In particular, the axial component is only affected by the fluctuating wind velocity components (induced by the turbulence), while the normal component of the wind velocity is additionally affected by the components of structural motion. Thus a relative normal wind velocity, $U_{NR}(t)$, accounting for the modification of the normal wind velocity, U_N, by the fluctuating wind velocity components (turbulence-induced) and the structural velocity components, is usually defined. The cable-wind angle Φ is as well affected by the fluctuating wind velocity components and components of structural motion, so that a relative cable-wind angle $\Phi_R(t)$ is defined.

Analytical treatment of the problem of an inclined cable vibrating along three degrees of freedom in turbulent flow is presented in Chapter 6.

The total aerodynamic loading acting on the cables is thus made of the summation of static and dynamic force components. In eq. 2.6 the total aerodynamic loading acting on the moving cable immersed in turbulent flow is reported. This comprises four force components, i.e.

$$\begin{pmatrix} F_{DR}(t) \\ F_{LR}(t) \\ M_R(t) \end{pmatrix} = \mathbf{F}_0 + \mathbf{F}_s(t) + \mathbf{F}_t(t) + \mathbf{F}_a(t) = \\ = \begin{pmatrix} F_{D0} \\ F_{L0} \\ M_0 \end{pmatrix} + \begin{pmatrix} F_{Ds}(t) \\ F_{Ls}(t) \\ M_s(t) \end{pmatrix} + \begin{pmatrix} F_{Dt}(t) \\ F_{Lt}(t) \\ M_t(t) \end{pmatrix} + \begin{pmatrix} F_{Da}(t) \\ F_{La}(t) \\ M_{ta}(t) \end{pmatrix} \tag{2.6}$$

where $F_{DR}(t)$ is the drag force parallel to the relative normal wind velocity, $U_{NR}(t)$, $F_{LR}(t)$ is the lift force, acting in the direction perpendicular to $U_{NR}(t)$, and $M_R(t)$ is the torque.

Steady wind load

The first component of eq. 2.6, $\mathbf{F}_0$, is the static wind load, i.e. due to the mean values of the wind forces

$$\mathbf{F}_0 = \begin{pmatrix} F_{D0} \\ F_{L0} \\ M_0 \end{pmatrix} = \frac{1}{2}\rho D U_N^2 \begin{pmatrix} C_{D0} \\ C_{L0} \\ DC_{M0} \end{pmatrix} \tag{2.7}$$

In the past years, i.e. up to the 1940's, the forces expressed by eq. 2.7 were used as design wind load. In fact, dynamic effects were not so evident in old structures and, to some extent, because the contribution of the dynamic action of wind to structural failures was not always recognized. Interest in dynamic effects started in the 1940's with the collapse of the suspension bridge over the Tacoma Narrows due to oscillations set up by the wind. Additionally, oscillations of overhead transmission lines were noted and discussed starting from the 1930's, (Scruton, 1963).

At the present time, it seems that all major bridges and structures are designed with the aid of the guidance provided by a wind tunnel investigation of its aerodynamic properties. Thus effects of the dynamic wind loading component are accounted for in the design.

Vortex shedding forces

The second component of eq. 2.6, $\mathbf{F}_s(t)$, is given by the (nil mean) fluctuating components of the wind loads associated with vortex shedding, i.e.

$$\mathbf{F}_s(t) = \begin{pmatrix} F_{Ds}(t) \\ F_{Ls}(t) \\ M_s(t) \end{pmatrix} \tag{2.8}$$

Forces in equation 2.8 are responsible for an aeroelastic instability known as *lock-in* or *synchronization* and are normally approximated as sinusoidal functions, (Solari, 1983). In fact, at low wind speed, and in smooth flow conditions, when the flow detaches from the cable section, it generates a turbulent wake, characterised by alternate shedding of vortexes at the top and bottom surface of the cable. These vortexes give rise to fluctuating loading components which are narrow banded and centered at a shedding frequency, f_s. The shedding frequency f_s is given by

$$f_s = St\frac{\bar{U}}{D} \tag{2.9}$$

where $\bar{U}$ is the mean wind speed, D is the cable's diameter. St represents the cable's Strouhal number, which amounts to 0.19-0.20 for a circular cross section at Reynolds number of 10^5 or less. Assuming that the free-stream velocity U is slowly increasing (from zero), then f_s will increase accordingly, and resonance will first occur when f_s becomes equal to the lowest cable's eigen-frequency. Further increase of U will cause resonance to occur when f_s is equal to the next eigen-frequency, and so on. Theoretically, resonance will occur when f_s is equal to any eigen-frequency f_i, (Strømmen, 2010).

When vortex resonance occurs, increased oscillation leads the cylinder to interact strongly with the flow and to control the vortex shedding mechanism for a certain range of wind velocities, i.e. an increase of the flow velocity by a few percent does not change the shedding frequency f_s which coincides with the cable's eigen-frequency. However, these effects are self-destructive in the sense that they diminish when fluctuating structural displacements become large. Thus, vortex shedding induced vibrations are self-limiting. Fig. 2.3 shows the qualitative trend of vortex shedding frequency with wind velocity during lock-in, (Strømmen, 2010).

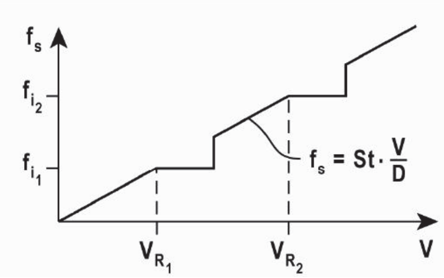

Figure 2.3: *Qualitative trend of vortex shedding frequency with wind velocity during lock-in, (Strømmen, 2010).*

For a typical bridge cable characterised by a diameter of 160 mm and a

Strouhal number of 0.19, the mean wind velocity range of 5-25 m/s corresponds to a vortex shedding frequency range of 10-50 Hz. Since the cable's fundamental frequency is often in the range of 0.2-2 Hz, resonance occurs only with much higher harmonic modes, with vibration frequencies of 10-50 Hz, where the mechanical damping is likely to be quite high. The maximum peak-to-peak vibration amplitude induced by vortex shedding usually doesn't exceed one cable diameter. The wind turbulence generally tends to reduce the response amplitude, even down to a half compared to the exposure to smooth air flow, (Ehsan et al., 1990). The mechanism of vortex-induced vibration can cause serious vibration problems for other engineering structures than bridge cables, such as towers, chimneys, bridge decks. Fig. 2.4 shows the von Kármán-vortex street obtained by performing a flow-visualization on a full-scale (160 mm in diameter) plain surfaced HDPE pipe, oriented perpendicular to the wind flow. The test was undertaken at the DTU/Force climatic wind tunnel in Lyngby.

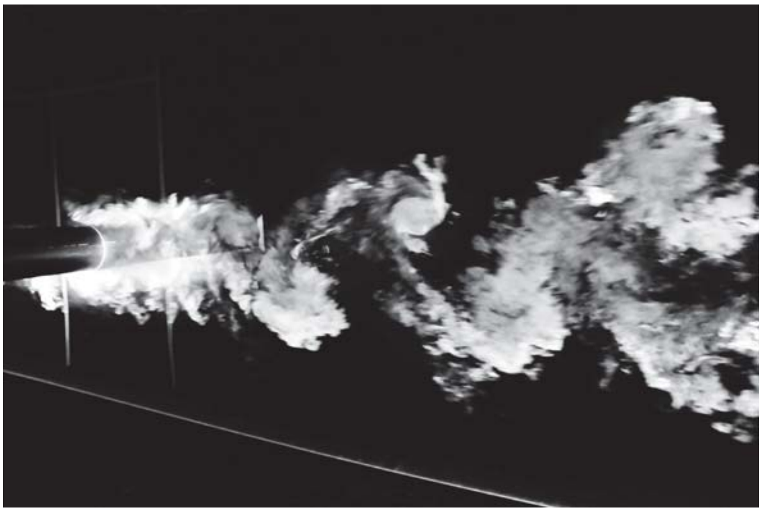

Figure 2.4: *Flow visualization of the von Kármán-vortex street performed on a full-scale plain surfaced HDPE pipe, oriented perpendicular to the wind flow.*

Buffeting forces

The third component of eq. 2.6, $\mathbf{F}_t(t)$, is given by the (nil mean) forces induced by the fluctuating wind velocity ($\tilde{u}(t)$, $\tilde{v}(t)$,$\tilde{w}(t)$), i.e.

$$\mathbf{F}_t(t) = \begin{pmatrix} F_{Dt}(t) \\ F_{Lt}(t) \\ M_t(t) \end{pmatrix} = \begin{pmatrix} F_{D\tilde{u}(t)} + F_{D\tilde{v}(t)} + F_{D\tilde{w}(t)} \\ F_{L\tilde{u}(t)} + F_{L\tilde{v}(t)} + F_{L\tilde{w}(t)} \\ M_{\tilde{u}(t)} + M_{\tilde{v}(t)} + M_{\tilde{w}(t)} \end{pmatrix} \tag{2.10}$$

A complete mathematical description of the forces in eq. 2.10, known as buffeting forces, is given by Solari (1983). Buffeting vibrations do nevertheless not represent a very serious concern for structural cables, except for powerline transmission lines. In fact, the high tension of bridge stay cables generally helps to limit the amplitude of buffeting vibrations.

Motion dependent forces

The fourth component of eq. 2.6, $\mathbf{F}_a(t)$, is given by the structural motion-dependent forces.

If the quasi-static hypothesis holds, the linearized expression of the motion-dependent forces under this assumption is

$$\mathbf{F}_a(t) = \begin{pmatrix} F_{Da}(t) \\ F_{La}(t) \\ M_{ta}(t) \end{pmatrix} = \mathbf{C}_a\dot{\mathbf{q}}(t) + \mathbf{K}_a\mathbf{q}(t) \tag{2.11}$$

where $\mathbf{C}_a$ is the aerodynamic damping matrix and $\mathbf{K}_a$ is the aerodynamic stiffness matrix; $\dot{\mathbf{q}}(t)$, $\mathbf{q}(t)$, represent the velocity and displacement vectors of the cable model, with components along the relative drag, lift and moment directions, respectively. The matrices $\mathbf{C}_a$ and $\mathbf{K}_a$ can generate either a stable or unstable response for the cable or lead to a critical point of bifurcation. Eq. 2.11 can as well be transformed in the frequency domain, i.e.

$$\mathbf{F}_a(\omega) = \begin{pmatrix} F_{Da}(\omega) \\ F_{La}(\omega) \\ M_{ta}(\omega) \end{pmatrix} = \mathbf{C}_a\dot{\mathbf{Q}}(\omega) + \mathbf{K}_a\mathbf{Q}(\omega) \tag{2.12}$$

where ω is the circular frequency, $\mathbf{F}_a(\omega)$, $\dot{\mathbf{Q}}(\omega)$, $\mathbf{Q}(\omega)$ represent the generalized Fourier transforms of $\mathbf{F}_a(t)$, $\dot{\mathbf{q}}(t)$, $\mathbf{q}(t)$.

If the quasi-steady hypothesis doesn't apply, the linearized equation of the motion-induced forces in the frequency domain is

$$\mathbf{F}_a(k) = \begin{pmatrix} \tilde{F}_{Da}(k) \\ \tilde{F}_{La}(k) \\ \tilde{M}_{ta}(k) \end{pmatrix} = \tilde{\mathbf{C}}_a(k)\dot{\mathbf{Q}}(k) + \tilde{\mathbf{K}}_a(k)\mathbf{Q}(k) \tag{2.13}$$

where $\tilde{\mathbf{C}}_a(k)$, $\tilde{\mathbf{K}}_a(k)$ are the aerodynamic damping and stiffness matrices, expressed as function of the flutter derivatives. These latter depend on the reduced frequency, $k = \omega D/U$.

Dynamic instabilities associated with negative terms in the aerodynamic damping matrix are called *galloping* and *flutter*. Only in the first case the quasi-steady assumption is taken to apply.

Bridge cables experience different forms of galloping, the most known, is the single degree-of-freedom (1 DOF) Den Hartog galloping, which occurs for sections oriented perpendicular to the flow and covered by ice accretion, and is characterised by the occurrence of large amplitude vibrations in the across-flow direction, at one of the lowest transversal modal frequencies of the cable (typically lower than 1 Hz). Vibration amplitudes can be large enough to cause serious operational problems. As the section vibrates crosswise in steady wind velocity U, the relative wind velocity changes, thereby changing the angle-of-attack. If a change in the angle-of-attack induces an increase in the lift force in the same direction of cable motion, instability occurs. This is due to continuous feeding of energy from the surrounding air flow to the cable system. As the drag force might also slightly depend on the angle-of-attack, the path of the cable motion tends to follow an elliptical trajectory, (Fujino et al., 2012). For inclined bridge cables other forms of galloping can occur. For example, dry inclined galloping, which occurs in dry surface conditions, thus for nominally circular sections, in the critical Reynolds number range. This is considered a 2 DOF-type instability, i.e. characterised by vibration components in the across- and along-flow direction, leading to elliptical trajectories. Rain-wind induced instability has also been interpreted as a form of 2 DOF galloping, i.e. due to the circumferential oscillation of the water rivulet along the cable surface, whose fundamental frequency couples to the frequency of flexural oscillation of the cable. Vibrations of inclined cables, covered by ice accretion, should similarily be explained as a form of galloping. Nevertheless, as dynamic wind tunnel test or field monitoring data are not available at the moment, the characteristics of this instability, are presently unknown. As the amplitude of galloping vibrations are in general *large*, the cable's behaviour becomes strongly non linear.

Flutter, as galloping, is again defined as a form of instability associated with negative aerodynamic damping, where continuously growing structural deflections develop, leading ultimately to failure. Flutter exists as a 1 DOF or 2 DOF instability, i.e. in the first case involving the pitching motion, i.e. torsional flutter, in the second case the coupling between pitching and heaving motions. This form is not of interest for bridge cables, but it's typical of sharp edged sections, such as airfoils or bridge decks.

Static instability associated with negative terms of the aerodynamic stiffness matrix are called *diverge*. Torsional divergence is an instance of a static structural instability. It occurs when the moment induced by the wind on the stucture induces a twist which provokes an increase in the angle-of-attack. This results in higher torsional moment as the wind velocity increases. If the structures doesn't have sufficient torsional stiffness to counteract the increasing moment, it becomes unstable and will be twisted to failure. This form of instability is not of interest for bluff bodies, such as nominally circular bridge cables, but is more typical of strealined bodies, such as bridge decks. Moreover, in most cases the critical divergence velocities are extremely high, well beyond the range which is normally considered in the design.

The study of the interaction between the force components , i.e. inertial, structural and aerodynamic, acting on the cable (or, more generically, on a structure) forms the basis of aeroelasticity. This is clearly illustrated in the *Collar's aeroelastic triangle*, (Collar, 1978), see Fig. 2.5.

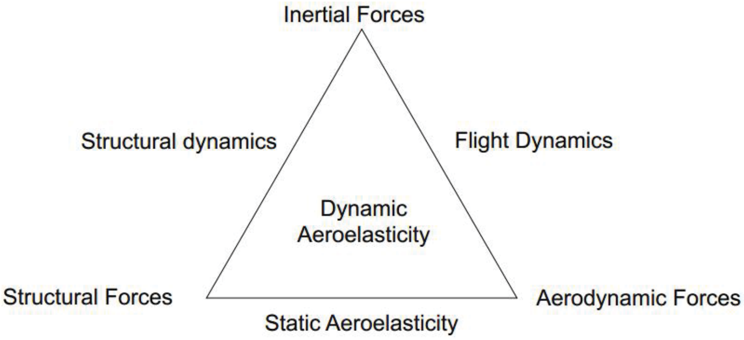

Figure 2.5: *Collar's aeroelastic triangle, (Collar, 1978).*

The interaction between the above mentioned force components can cause undesiderable instability phenomena, belonging to the following categories:

- static aeroelastic, i.e. divergence;
- dynamic aeroelastic, i.e. flutter;
- non linear aeroelastic, i.e. limit cycle oscillation;
- unsteady aerodynamic, i.e. vortex shedding, buffeting, galloping;

2.2.3 Equations of motion

The motion of the cable is normally described by a linearised system of equations of motion, i.e.

$$\mathbf{M}\ddot{\mathbf{q}}(t) + \mathbf{C}\dot{\mathbf{q}}(t) + \mathbf{K}\mathbf{q}(t) = \mathbf{F}_0 + \mathbf{F}_s(t) + \mathbf{F}_t(t) \tag{2.14}$$

where $\mathbf{M}$ represents the mass matrix, while $\mathbf{C}$ and $\mathbf{K}$ represent the effective damping and stiffness matrices respectively, given by the summation of the structural and aerodynamic components, i.e.

$$\mathbf{C} = \mathbf{C}_s - \mathbf{C}_a \tag{2.15}$$

$$\mathbf{K} = \mathbf{K}_s - \mathbf{K}_a \tag{2.16}$$

Equation 2.14 applies to the complex case of a bridge cable vibrating along 3 DOFs in unsteady flow.

2.2.4 Theoretical modelling

Several analytical models have been developed in the last years to predict the conditions of aerodynamic instability of bridge cables. The assumptions of such models depend primarily on the climatic conditions the cable is subjected to. In the dry state the cable is in fact characterised by a constant cross-sectional shape with time. In the iced and wet state the shape of the cable is time dependent. Most analytical models neglect the time variations of the cable's shape in icy conditions. This because the time scale of the cross section's variation is much slower than other aerodynamic phenomena which might be responsible for the instantaneous instability. On the other hand in rainy conditions, the time fluctuations of the cross-sectional shape are much faster and they are accounted for in the mathematical modelling of the associated excitation.

One ot the most popular solutions developed to date for the interpretation galloping instabilities of dry inclined/yawed cylinders with arbitrary cross-section, either dry or covered by ice accretions, in smooth flow conditions was developed by Macdonald and Larose (2006), and Macdonald and Larose (2008a). In the first case the cable model was modelled as a spring, mass damper system which was allowed to vibrate along one degree-of-freedom (i.e. in the across-flow direction); the second case In the 1 DOF model a general expression for the quasi-steady non-dimensional aerodynamic damping for small amplitudes of vibration in any plane, is derived. The expression covers the special cases of conventional quasi-steady aerodynamic damping, Den Hartog galloping and the drag crisis, as well as dry inclined cable galloping. The nondimensional aerodynamic damping parameter is a function of the drag C_D and lift C_L force coefficients and of their derivative with respect to Reynolds number, Re, with the the angle between the wind velocity and the cable axis, Φ, and with the orientation of the vibration plane, α, i.e.

$$\begin{aligned}\zeta_a = \frac{\mu Re}{4m\omega_n}\cos\alpha[\cos\alpha(C_D(2\sin\Phi + \frac{\tan^2\alpha}{\sin\Phi}) + \frac{\partial C_D}{\partial Re}Re\sin\Phi - \frac{\partial C_D}{\partial\alpha}\frac{\tan\alpha}{\sin\Phi}) \\ - \sin\alpha(C_L(2\sin\Phi - \frac{1}{\sin\Phi}) + \frac{\partial C_L}{\partial Re}Re\sin\Phi - \frac{\partial C_L}{\partial\alpha}\frac{\tan\alpha}{\sin\Phi})]\end{aligned} \tag{2.17}$$

In the 2 DOF model the 2x2 aerodynamic damping matrix is derived, and a closed form analytical solution of the eigenvalue problem is proposed for the tuned case.

The 2 DOF model developed by Macdonald and Larose (2008a) has been extended to 3 DOF by Gjelstrup and Georgakis (2011). This latter model follows the same approach as adopted by Macdonald and Larose (2006) and Macdonald and Larose (2008a) in the modelling of the force coefficients, i.e. as functions of the cable-wind angle, angle-of-attack, and Reynolds number. Moreover, similarily as in Macdonald and Larose (2006) and Macdonald and Larose (2008a), the same forces are linearized about zero structural velocity, leading to the elimination of all aerodynamic stiffness terms. Such simplification is valid only for compact sections, with very low damping. This assumption is overcome in the analysis performed in Chapter 6, where the forces are linearized about zero structural velocity and rotation. In this way, a criterion is developed which is capable of predicting instabilities induced by negative aerodynamic damping, typical of bluff bodies, or aerodynamic stiffness, mostly occurring for streamlined bodies.

In presence of rain several analytical models have been developed where the cable-rivulet system has been typically modeled using a two-dimensional, multiple mass, multiple degree-of-freedom, spring mass damper system, and the aerodynamic forces were approximated by use of the quasi-steady theory. The accounted degrees-of-freedom are the across-flow vibration component of the cable and the angular oscillation of the rivulet, (Gu and Wang, 2008), (Peil and Dreyer, 2007), (Yamaguchi et al., 1988). Numerical models developed by Robertson and Taylor (2007) investigated the effect of both static and circumferentially oscillating rivulets. In presence of static rivulets, the cable's response is reminiscent of galloping, while in presence of oscillating rivulet the cable's response is significantly modified and more complex.

In the following, instabilities of bridge cables occurring under the three surface states, i.e. rain, wet, and iced, are reviewed, based on experiemental data, i.e. either from wind tunnel tests or field monitoring. Analytical solution of the instability, in the exclusive dry and iced surface state, is given in Chapter 6.

2.3 Rain-wind induced vibration

The excitation mechanism of RWIV was first observed in the 1980s. It was recognized to occur over a restricted range of wind velocities, under moderate rain conditions, for cables descending in the wind direction. The response was normally observed to occur in the cable-pylon plane with a larger amplitude and lower frequency than vortex induced vibration. The instability was mostly observed for plain surfaced cables, coated with polyethylene (PE), i.e. not provided of passive aerodynamic surface modifications, where the water rivulet could easily form, under the achievement of the right level of surface wettability. Due to such characteristics RWIV can be identifies as a distinct aeroelastic phenomenon, which distinguished characteristcs from other aeroelastic instabilities such as galloping or the aforementioned vortex-induced instability.

Rain-wind induced vibration has been verified in full scale, (Langsoe and Larsen, 1987), (Ohshima and Nanjo, 1987), (Yoshimura et al., 1988), (Hikami and Shairaishi, 1988), (Peersoon and Noorlander, 1999), (Ni et al., 2007), (Zuo and Jones, 2010), (Acampora and Georgakis, 2011), and in wind tunnel experiments, (Hikami and Shairaishi, 1988), (Flamand, 1995), (Larose and Smitt, 1999), (Cosentino et al., 2003), (Gu et al., 2005), (Matteoni and Georgakis, 2013b).

2.3.1 Field Measurements

Rain-wind induced vibrations were first observed in the late 1970s at Brotonne Bridge in France (Wianecki, 1979), and for powerline conductors, (Hardy and Bourdon, 1979). These reports roughly described the prototype behaviour of cables in windy and rainy conditions, without giving any explanation on the associated instability. A comprehensive investigation of the rain-wind induced vibration instability was later undertaken by Hikami and Shairaishi (1988). The study was motivated by the observation of large amplitude vibrations at the Meiko-Nishi cable-stayed bridge in Japan, under the combined action of wind and rain, during its period of construction. This new type of aerodynamic instability became then a great concern to the bridge engineers in various countries because of its large amplitudes and relatively low wind velocity. The characteristics identified by Hikami and Shairaishi (1988) were in fact soon recognized in many subsequent vibration occurrences of cable stayed bridges. Between 1988 and 1989 a committee organized by the Japanese Institute of Construction Engineering undertook a series of eye observations and field measurements on five cable-stayed bridges in Japan, in order to clarify some fundamental characteristics of rain- wind induced vibration, (Matsumoto et al., 1992). Fig. 2.6 shows an example of violent oscillation of the stay cables induced by wind and rain, at two of the monitored cable-stayed bridges in Japan, (Matsumoto et al., 2006).

Other early episodes of RWIVs were reported for the Ajigawa River Bridge in Japan (Ohshima and Nanjo, 1987), the Faroe Bridge in Denmark, (Langsoe and Larsen, 1987), and the Erasmus Bridge in the Netherlands, (Peersoon

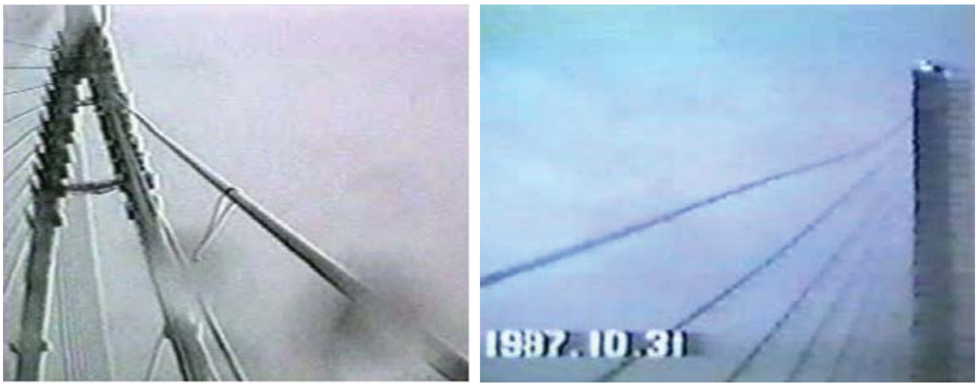

(a) (b)

Figure 2.6: *Violent cable vibration observed under the occurrence of wind and rain at (a) the Tenpozan Bridge and (b) at the Aratsu Bridge in Japan, (Matsumoto et al., 2006).*

and Noorlander, 1999). From recent research on bridge field monitoring, RWIVs were observed at the Dongting Lake Bridge, China (Ni et al., 2007), at the Fred Hartman Bridge and Veteran Memorial Bridge in the United States (Zuo et al., 2008) and at the Øresund between Denmark and Sweden, (Acampora and Georgakis, 2011). Similar conclusions on the nature of the instability as in the early studies were drawn.

In Table 2.1 a compilation of cable-stayed bridges where the rain-wind induced vibration have been observed in the last thirty years is given. Features of the RWIVs based on full-scale monitoring will be based on the observations undertaken on these bridges.

Bridge	Location	Reference
Faroe	Denmark	(Langsoe and Larsen, 1987)
Ajigawa	Japan	(Ohshima and Nanjo, 1987)
Aratsu	Japan	(Yoshimura et al., 1988)
Meiko-Nishi	Japan	(Hikami and Shairaishi, 1988)
Erasmus	The Netherlands	(Peersoon and Noorlander, 1999)
Dongting Lake	China	(Ni et al., 2007)
Fred Hartman	Texas	(Zuo and Jones, 2010)
Veterans' Memorial	Texas	(Zuo and Jones, 2010)
Øresund	Denmark/Sweden	(Acampora and Georgakis, 2011)

Table 2.1: *Compilation of cable-stayed bridges where the rain-wind induced vibration have been observed in the last thirty years.*

Geometrical characteristics of the cables undergoing rain-wind induced instability, i.e. in terms of diameter (D), total length (L), and inclination (Θ) are given in Table 2.2. Inertial and dynamic properties, in terms of mass per unit length, m, frequency, f, and structural damping, ζ_s, of the cables are given in Table 2.3. Wind velocity range and peak to peak amplitude are reported in Table 2.4.

D [m]	L [m]	$\Theta[^\circ]$	Reference
0.14	300	45	(Hikami and Shairaishi, 1988)
0.20	-	-	(Peersoon and Noorlander, 1999)
0.099-0.159	28-201	35.2	(Ni et al., 2007)
0.087-0.194	87.3-197.9	21.1-48.9	(Zuo and Jones, 2010)
0.25	192-262	30	(Acampora and Georgakis, 2011)

***Table 2.2**: Critical geometrical characteristics of the cables undergoing rain-wind induced vibration, according to field monitoring observations.*

m [kg/m]	f [Hz]	ζ_s [%]	Reference
51	1-3	0.1-0.2	(Hikami and Shairaishi, 1988)
-	1-3	0.11-0.45	(Peersoon and Noorlander, 1999)
51.8	1.07	-	(Ni et al., 2007)
48-76	1.26-0.57	-	(Zuo and Jones, 2010)
-	0.47-0.65	0.93-1.04	(Acampora and Georgakis, 2011)

***Table 2.3**: Critical inertial and dynamic properties of the cables undergoing rain-wind induced vibration, according to field monitoring observations.*

U [m/s]	A[m]	Reference
5-17	0.55	(Hikami and Shairaishi, 1988)
-	0.4-0.6	(Peersoon and Noorlander, 1999)
6-14	0.70	(Ni et al., 2007)
5-15	-	(Zuo and Jones, 2010)
11-12	0.15	(Acampora and Georgakis, 2011)

***Table 2.4**: Critical wind velocity and peak to peak amplitude for cables undergoing rain-wind induced vibration, according to field monitoring observations.*

When comparing several full-scale monitoring studies, there is a general agreement on the RWIV to occur for cables declining in the wind direction, where the rivulet can easily form. On the other hand a large scatter exists in the range of reported angles between the wind direction and the cable axis, so as to make it difficult to identify a critical range.

Vibration trajectories have almost always been observed as elliptical, with major components in the across-flow direction.

In almost all observations vibrations occur under light to medium rain conditions. Vibration doesn't occur under heavy rainfalls.

For almost all observations, the RWIV excitation occurs for smooth PE (polyethilene) lapped cables not provided of aerodynamic surface modifications, (Hikami and Shairaishi, 1988), (Matsumoto et al., 1992), (Peersoon and Noorlander, 1999), (Ni et al., 2007),(Zuo and Jones, 2010). Fig. 2.7(a) shows two examples of bridges characterised by cables coated with smooth PE pipes, i.e. the Fred Hartman in Texas, and the Erasmus Bridge in the Netherlands, where RWIVs have been observed in the past.

(a) (b)

Figure 2.7: *Cable surface at the Fred Hartman Bridge in Texas (a) and at the Erasmus Bridge in the Netherlands (b) (Pictures from* ***http://www.ourbaytown.com/*** *and* ***http://www.traveladventures.org/continents/europe/erasmus-bridge02.html****).*

Flamand (1995) designed a cable coating provided of 1.5 mm high helical fillet for the cables at the Normandie Bridge in France. The solution, which implied a minimal increase in the drag coefficient, reduced significantly the RWIV, as it interrupted the formation of the water rivulet along its length. The solution became popular on several new cable-stayed bridges in the U.S.A. Nevertheless rain-wind induced vibrations seem to take place for cables provided of helical fillet, (Acampora and Georgakis, 2011).

Monitoring campaigns of rain-wind induced vibrations were also performed for full-scale cable models installed in open-air. For example, Matsumoto et al. (2003) observed RWIVs for a 30 m long aluminium cable model wrapped by a polyethylene case, with a diameter of 0.11 m, and installed in the Shionomisaki field observatory, which is located on a flat hill, see Fig. 2.8(a). The cable, whose natural frequency was 1.37 Hz, was rigidly fixed at each end to a supporting structure. Static tests were performed by Clobes et al. (2010) on a full-scale cable section model with a diameter of 0.11 m. Each end was rigidly fixed and provided of end plates. An artificial rivulet was fixed to the cable surface. Aerodynamic drag and lift coefficients were measured for the cable model. Clobes et al. (2010) planned to use the same setup for performing aeroelastic tests. In particular, the fixed attachments will be replaced by springs in order to enable vibrations perpendicular to the longitudinal axis of the cylinder. A sprinkling system will be installed in order to produce artificial rain.

(a) (b) (c)

Figure 2.8: *Test setup of full-scale cable model (a), in Japan, (Matsumoto et al., 2003) , and in Germany (b), (c), (Clobes et al., 2010).*

2.3.2 Dynamic wind tunnel tests

Dynamic wind tunnel tests are normally performed in order to complement results from full-scale monitoring of bridge cables, and thus clarify their mechanisms of vibration. Normally, the wind tunnel cable models are designed so as to reproduce prototypes from the bridges. In particular, their spacial orientation in the test chamber, together with the support conditions, are normally chosen so as to reproduce critical conditions where large amplitude vibrations have been observed on bridges. Dynamic wind tunnel investigations have also been performed by following a parametric approach, i.e. by assuming that the conditions of instability are not know a priori, several combinations of the test parameters are attempted, so as to find the most adverse conditions for the instability. In the dynamic tests the cable model is supported by a system of springs generally arranged so to allow its vibration in the in-plane direction. Additionally, the out-of-plane and axial motions might also be allowed. Fig. 2.9 shows a conceptual sketch of a 2 DOF dynamic rig for testing of structural bridge cables.

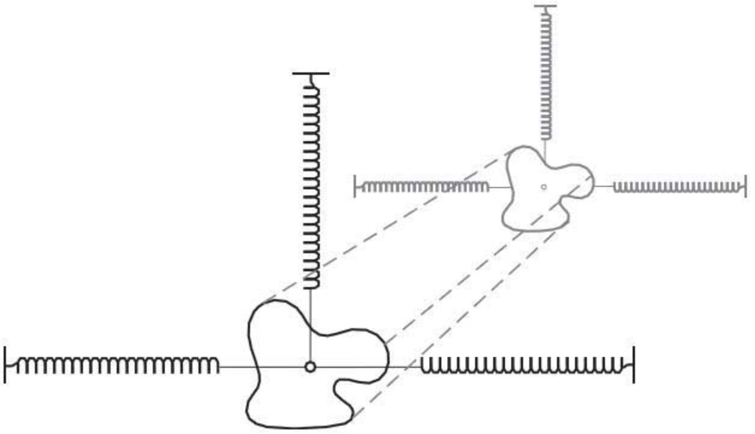

Figure 2.9: *Conceptual sketch of a 2 DOF dynamic rig for testing of structural bridge cables.*

The rain rivulets, which are considered responsible for the instability, have been simulated by following three separate approaches. Each of them implied different interpretations of the excitation mechanism. The first approach consists in spraying water onto the vibrating cable model using a shower system (Hikami and Shairaishi, 1988), (Flamand, 1995), (Flamand et al., 2001), (Cosentino et al., 2003), (Larose and Smitt, 1999), (Zhan et al., 2008), (Xu et al., 2009), (Gu et al., 2005), (Matsumoto et al., 1995), (Verwiebe and Ruscheweyh, 1998). In this way, the exciting mechanism of RWIV is generally explained in terms of periodic change of the cable cross-section, seen from the flow, due to the circumferential oscillation of the water rivulets. This generates pressure fluctuations about the cable surface, which gives rise to positive aerodynamic work and thus to the excitation, (Cosentino et al., 2003). The second approach consists in fixing stationary artificial rivulets on the surface of the cable model (Bosdogianni and Olivari, 1996), (Liu et al., 2012). The water rivulets change the cable cross section into a non-symmetrical one, making it prone to classical galloping instability. The third approach consists in simulating a rotational motion of the cable model with fixed artificial rivulet, (Matsumoto et al., 2005).

For the tests where a spray system was adopted to release a water flow on the cable model, it was important, for the rivulets to form, that the cable possessed the right level of surface wettability. Several methods were adopted at this purpose. Flamand (1995) coated the cable models with sooth, resulting from fuel oil combustion. Larose and Smitt (1999) painted the cables models with a solution of 5 % weight Gohsenol dissolved in ethanol. Similar solution was adopted by Matteoni and Georgakis (2013b), who dissolved the same percentage of Gohsenol in water. Fig. 2.10 show a view of the upper water rivulet formed on an untreated and Gohsenol treated cable mode, (Matteoni and Georgakis, 2013b). In the first case the surface wettability of the cable model was too low, so that the rivulets formed but didn't oscillate. No excitation was observed, i.e. the cable vibration was of limited amplitude, and the aerodynamic damping positive for all tested velocities up to the critical Reynolds number range. In the second case the rivulet formed and oscillated circumferentially, so that the cable vibration grew exponentially and negative aerodynamic damping was achieved for a limited range of wind velocities in the subcritical Re range.

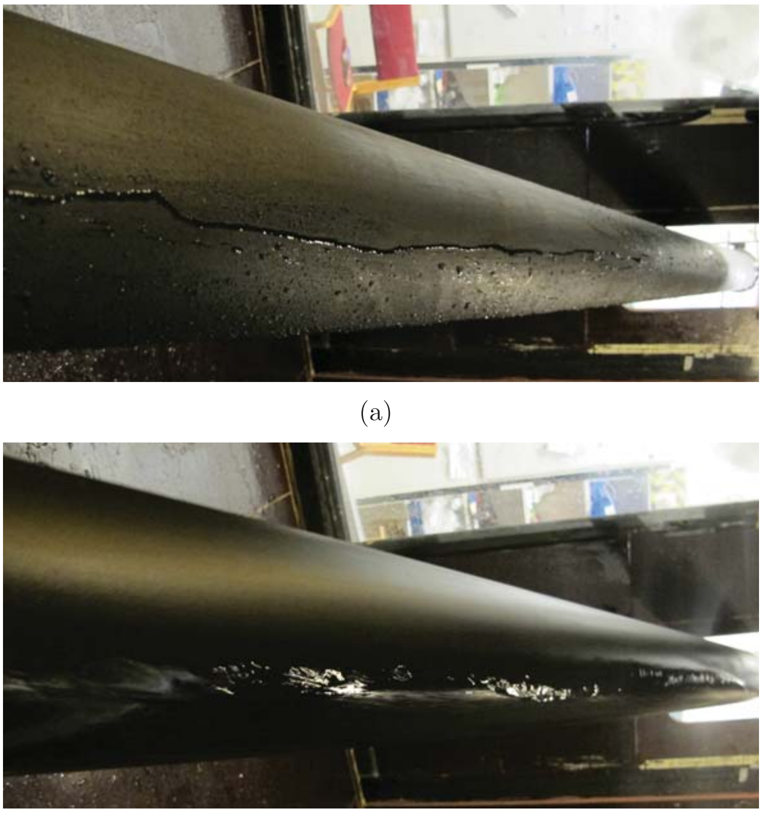

(a)

(b)

Figure 2.10: *View of the upper rivulet for an untreated cable section (a) and treated with a solution of Gohsenol dissolved in water (b), (Matteoni and Georgakis, 2013b)*

Here below are reported results from several wind tunnel test campaigns, with focus on the critical conditions where the RWIV instability has been observed. In Table 2.5 are reported the critical angles for the cable, in terms of inclination Θ, yaw β, cable-wind angle, Φ. In Table 2.6 are reported the critical geometrical properties of the cable, in terms of diameter D and length L. Note that in all experiments where RWIVs has been observed the cable models were covered by smooth PE tubing, i.e. not provided of surface modifications. In Table 2.7 are reported the critical inertial properties, i.e. in terms of mass per unit length, m, and dynamic properties, i.e. in terms of structural frequency, f, and structural damping ζ_s. Support conditions of the cable models, i.e. terms of number of degrees-of-freedom of the dynamic rig, are also included in Table 2.7. In Table 2.8 are reported the critical wind velocity range, U, and the maximum peak to peak amplitude, A.

Θ [°]	β [°]	Φ [°]	Reference
45	45	60	(Hikami and Shairaishi, 1988)
25	60	63.05	(Flamand, 1995)
30	60	64.34	(Larose and Smitt, 1999)
25	60-70	63.05-71.94	(Cosentino et al., 2003)
30	60-65	64.34-68.53	(Gu et al., 2005)
25	60	63.05	(Matteoni and Georgakis, 2013b)

Table 2.5: *Critical geometrical attitude for RWIV for the cable models tested dynamically in wind tunnels.*

D [m]	L [m]	Reference
0.14	0.6	(Hikami and Shairaishi, 1988)
0.16	7	(Flamand, 1995)
0.25	6	(Larose and Smitt, 1999)
0.16	-	(Cosentino et al., 2003)
0.12	2.5	(Gu et al., 2005)
0.16	3.35	(Matteoni and Georgakis, 2013b)

Table 2.6: *Critical geometrical characteristics for RWIV for the cable models tested dynamically in wind tunnels.*

2.3.3 Static wind tunnel tests

Static tests have been performed in order to clarify the excitation mechanism of RWIV. Mainly, two aspects were investigated, i.e. the trajectory of the water rivulets along the cable axis and the aerodynamic force coefficients.

m [kg/m]	f [Hz]	ζ_s [%]	DOF	Reference
-	2	-	-	(Hikami and Shairaishi, 1988)
16	1	0.095	2	(Flamand, 1995)
14	-	0.025	1	(Larose and Smitt, 1999)
-	1.08	0.08-0.25	2	(Cosentino et al., 2003)
6	1	0.14	1	(Gu et al., 2005)
18.07	1.1	0.1	1	(Matteoni and Georgakis, 2013b)

Table 2.7*: Critical inertial and dynamic properties for RWIV for the cable models tested dynamically in wind tunnels.*

U [m/s]	A [m]	Reference
9-13	0.11	(Hikami and Shairaishi, 1988)
6-13	0.32	(Flamand, 1995)
9-12	0.25	(Larose and Smitt, 1999)
5-17	0.14	(Cosentino et al., 2003)
7-10	0.31	(Gu et al., 2005)
8-16	>0.4	(Matteoni and Georgakis, 2013b)

Table 2.8*: Critical velocity range and maximum observed peak to peak amplitude for RWIV for cable models tested dynamically in wind tunnels.*

Limited experience exists on the measurement of the aerodynamic loading in static conditions for inclined cables in presence of rain. Several difficulties are in fact associated with this operation, depending on the aerodynamic loading measurement system. For example, if load cells fixed to ends of an inclined cable are used, separation of the aerodynamic from the inertial loading contribution (due to the rivulets) is not directly possible. If pressure taps are used to measure the loading along the local circumference of the cable, water filling of the same taps might prevent success of the reading.

? measured the mean drag coefficient, C_D, and the fluctuating drag and lift coefficients, C'_D, C'_L, for a inclined 22.5 mm diameter cylinder. Water was released from the top of the cable by use of a funnel connected to a tank. It was observed that the presence of water rivulets significantly affects the characteristics of the flow around the cable in comparison to the dry state. Five regimes were identified, see Fig. 2.11, each associated with a specific range of Reynolds number, where the rivulet assumed a different angular position on the cable model.

For $Re \leq 1500$, case (a) in Fig. 2.11, one single water rivulet occurred along the leading stagnation line. For $1500 \leq Re \leq 2500$, case (b) in Fig. 2.11, both one and two rivulets were occurring and switched from one to another intermittently. The influence of the rivulet on the fluid forces, when

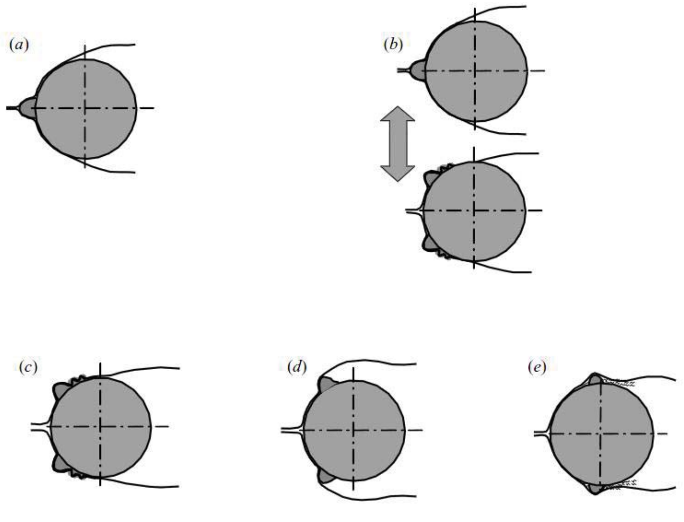

***Figure 2.11**: Position of flow separation as function of rivulet position, (Alam and Zhou, 2007).*

located at the stagnation line or close by, is very small, (Nebres and Batill, 1993). For $2500 \leq Re \leq 5300$, case (c) in Fig. 2.11, the rivulets occurred between the leading stagnation and the flow separation lines. In this range, the fluid forces on the cylinder were slightly higher than those of the dry cylinder. The boundary layers remained attached behind the rivulets. The reattachment caused some ripples of water behind the rivulet. Water rivulets occured at an angular distance $\theta_R = 28 - 60^\circ$ from the leading stagnation line. An increase was observed in C_D, C'_D, C'_L, compared with a dry cylinder which is associated with the increased effective height of the cylinders in presence of rivulets. For $5300 \leq Re \leq 8400$, case (d) in Fig. 2.11, the two rivulets move further downstream, i.e. $60^\circ \leq \theta_R <\leq 78^\circ$. An earlier separation of the boundary layer was observed in comparison with the case in absence of rivulets. This leaded to an increase in the force coefficients, which all show a pronounce peak at Re = 6800. In particular, the fluctuating drag and lift C'_D, C'_L become 4.25 and 5.75 higher than their counterparts in the absence of water rivulets. For $Re \geq 8400$, case (e) in Fig.2.11, the rivulets shifted further downstream and appeared straight again along the cylinder. The rivulets occurring probably behind the flow separation lines, acted as a stabilizer of the shear layers. This resulted in postponed flow separation and hence in smaller fluctuating fluid forces. The fluid structure in this range may resemble that of a circular cylinder at the early stage of the critical Reynolds number, as described for example by Schewe (1983). Fig. 2.12 shows the time averaged drag, and fluctuating drag and lift coefficients for the tested range of Reynolds numbers, in dry conditions and in presence of water rivulets, obtained by Alam and Zhou (2007).

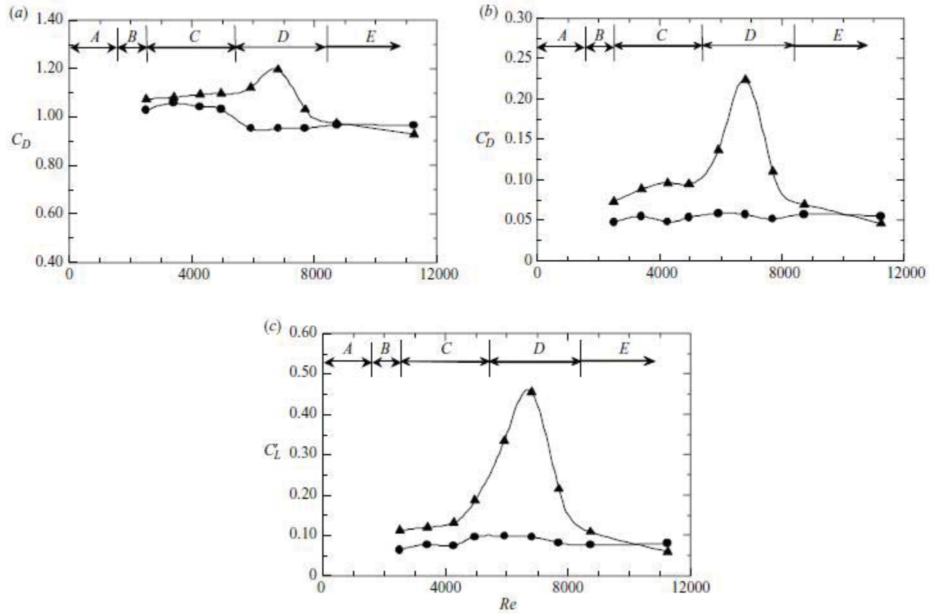

***Figure 2.12**: Average drag coefficient (a), and fluctuating drag (b) and lift (c) coefficients for an inclined cylinder,* $\Theta = 80°$, *in dry conditions and in presence of water rivulets, (Alam and Zhou, 2007).*

Fig. 2.13 shows a photograph of the tested cylinder, at two different vertical inclinations, i.e. 55° and 80°, with water running at increasing Reynolds number. Rivulets appear to be almost straight along the cylinder axis for relative low and high Reynolds numbers, but become sinusoidal, oscillating circumferentially at intermediate Reynolds number (Re = 6800 for at 80°, and Re = 9600 at 55° inclination). The axial wavelength of the rivulet is estimated equal to approximately 5 diameters at 80°, and 3.5 diameters at 55°. The width of the rivulet is estimated to be approximately constant along the cylinder axis for low wind velocities but varies when the rivulet oscillates. In particular, the thickness and width of the rivulet were estimated equal to respectively 2.8 and 3.3 mm at Re = 6800 and 80° inclination, and 3 and 3.1 mm at Re = 9600 and 55° inclination.

Additional tests on the rivulet trajectories along inclined cylinders were performed by Wang et al. (2005). Tests were performed on a rigid polyethylene-lapped acryl glass tube with lenght of 0.6 m and diameter of 19 mm, with a vertical inclination and yawing to the wind flow of 45°. Water was released on the cylinder in a similar way as by Alam and Zhou (2007). Fig. 2.14 shows

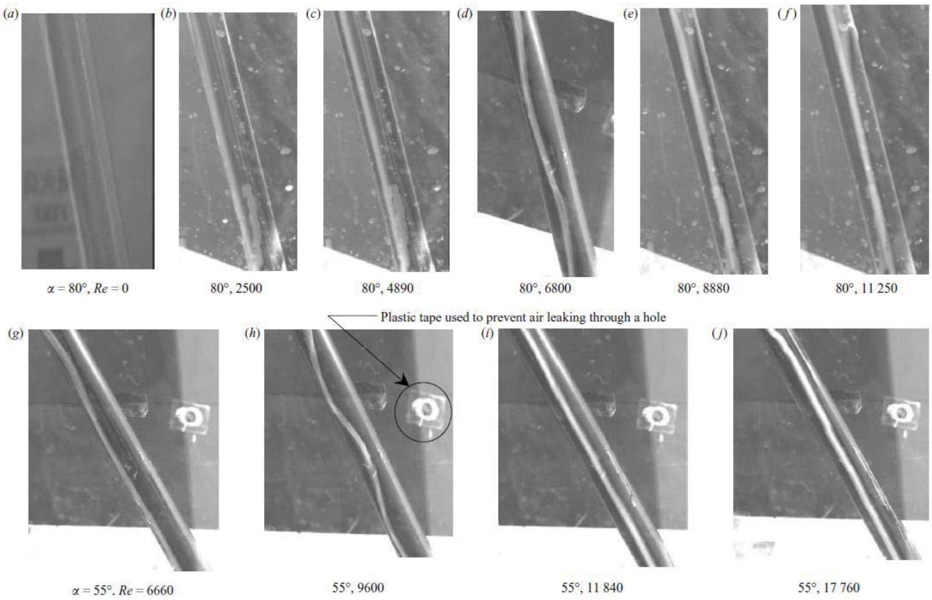

Figure 2.13: *Photographs of running water rivulets for an inclined cylinder,* $\Theta = 80°$, $55°$, *for increasing Reynolds numbers in presence of water rivulets, (Alam and Zhou, 2007).*

typical patter of the rivulet trajectory along the cylinder axis for a wind velocity of 9 m/s and a water flow rate of 8 liters per hour. Two rivulets are formed over the cable surface. The leeward, i.e. upper rivulet, oscillates circumferentially by following a pseudo-sinusoidal wave along the cylinder axis, and is characterised by an axial wavelength of approximately 2 cylinder diameters. The pseudo-sinusoidal wave described by the leeward rivulet is due to the interaction with the vortex shedding mechanism occurring along the cylinder axis. The windward, i.e. lower rivulet, runs approximately in straight line. This because, this latter rivulet, facing downwards, is affected by the gravity force, which overwhelms the 3D effects of the vortex rolls shed from the cylinder. It was observed that an increase in the yawing angle provokes a magnification of the circumferential oscillation of the water rivulet. On the contrary, by decreasing the yawing angle until reaching approximately a zero value, the pattern of the upper rivulet becomes identical to the pattern of the lower rivulet. It was then concluded that the rivulet geometry and position are affected by the orientation of the cylinder, its inherent surface roughness and the rate of the water flow.

Results presented by Alam and Zhou (2007) and Wang et al. (2005) are nevertheless of unclear applicability for the case of a real inclined bridge cable. This is most importantly due to the fact that for the tested case the

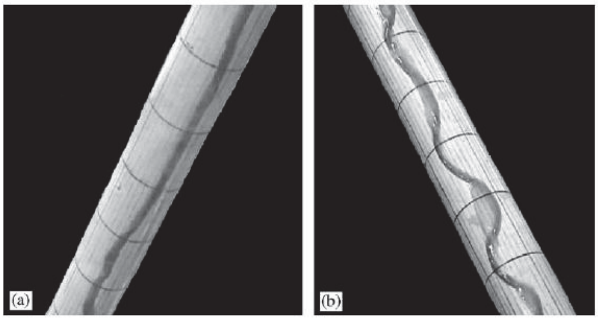

***Figure 2.14**: Photographs of running water rivulets for an inclined/yawed cylinder, $\Theta = 45°$, $\beta = 45°$, in presence of water rivulets, (Wang et al., 2005).*

ratio between the rivulet height and the cylinder diameter is much larger than for real bridge cables, thus probably affecting the aerodynamic properties of the coupled cylinder-rivulet system.

2.4 Dry state

Two types of excitation have been observed under the conditions of no precipitation on inclined bridge cables. Under a combination of parameters, such as cable attitude to the flow, wind velocity, stay cables may either undergo divergent motion (dry galloping) or limited amplitude motion under a limited interval of wind speed (vortex induced vibration at high reduced wind speed).

Dry inclined galloping has never been fully verified in full-scale. On the other hand it was reproduced in experimental studies, (Saito et al., 1994), (Honda et al., 1995), (Miyata et al., 1994b), (Cheng et al., 2003), (Cheng et al., 2008a), (Cheng et al., 2008b), (Jacobsen et al., 2012), (Matteoni and Georgakis, 2013b).

Vortex induced vibration at high reduced velocity was as well reproduced in experimental studies (Cheng et al., 2003), (Cheng et al., 2008a), (Cheng et al., 2008b), (Diana et al., 2008).

2.4.1 Field observations

Excitation of dry inclined cable has never been fully verified on full-scale, and only a limited number of reports, based on visual observations, exist. Thus a clear systematization of the excitation mechanism, based on field monitoring data, does not yet exist.

Most recently, an inclined PE-lapped cable with 187 m length of cable-stayed bridge in Japan showed violent vibration during passing of a Typhoon. The vibration, whose amplitude was estimated equal to around 1.5 m, damaged not only a part of the edge faring but also the cable surface. The estimated wind velocity was approximately 18 m/s and the wind blew with some yawing angle to the bridge axis. Eye witnesses reported that the rain had already stopped when the violent cable vibration started. No data were collected on the bridge site at the moment of violent vibration. The nature of the excitation mechanism is therefore unclear. Matsumoto et al. (2010) classified this phenomenon as a dry-galloping, generated by the axial flow in the wake and sequential 3D Kármán vortex shedding along the cable axis. In Fig. 2.15 the position of the cable before and after the vibration accident is shown. Other examples of bridges where dry inclined vibrations have been reported in the past are the Iroise Bridge in France, (Boujard, 2007), the Fred Hartman and the Veterans' Memorial Bridge in Texas, (Zuo and Jones, 2010), and the Øresund Bridge, between Denmark and Sweden, (Svensson et al., 2004). At the Iroise Bridge high amplitudes vibrations (in the order of 1 to 2 cable diameters) were experienced in absence of rain on cables characterised by low frequencies. The range of velocities associated with these vibrations was much superior to the interval where rain-wind induced vibrations usually occur, i.e. at the transition between the subcritical and critical regime. Thus, a dry galloping excitation mechanism was suggested. On the contrary at the Fred Hartman Bridge and at the Veterans' Memorial Bridge, vibrations of dry inclined cables were observed to occur under similar wind speed interval (i.e. in the subcritical Reynolds number range) and wind direction as RWIVs, thus leading to assume a similarity between the two vibration mechanisms. Due to the close connection in the features of observed rain-wind induced and dry vibrations, Zuo and Jones (2010) hypothesized that the so called rain-wind induced vibration may be due to an instability mechanism that inherently exists for inclined and/or yawed cables regardless the presence of

***Figure 2.15**: Violent cable vibration observed at a certain proto-type cable-stayed bridge in Japan, (Matsumoto et al., 2010).*

rainfall. The role of rainfall is thus to promote the inherent instability of dry inclined cables exposed to wind loading. Zuo and Jones (2010) claimed also that some of the characteristics shared by large amplitude vibrations with and without rainfall are also similar to the corresponding characteristics of Karman-vortex induced vibrations. At the Øresund Bridge large amplitude vibrations were observed in absence of rain and ice during the life time of the bridge by Svensson et al. (2004). Macdonald and Larose (2006) stated that during these episodes the stay cables might have experience dry inclined galloping excitation as the measured wind speed, i.e. in the range of 12 to 21 m/s, likely corresponds to the critical Reynolds number, for the given cables diameter, i.e. 250 mm, turbulence intensity of the wind at the cable location and surface roughness of the cables.

2.4.2 Dynamic wind tunnel tests

Dry inclined galloping excitation has been observed in wind tunnel tests conducted in Japan, (Matsumoto et al., 1990), (Saito et al., 1994), (Honda et al., 1995), (Miyata et al., 1994b), in Canada (Cheng et al., 2003), (Cheng et al., 2008a), (Cheng et al., 2008b), (Jacobsen et al., 2012), and in Denmark, (Matteoni and Georgakis, 2013a).

In the experimental investigations, undertaken by Matsumoto et al. (1990), bridge cables were modelled by means of cylinders with scaled diameter and weight with respect to real prototypes. It was observed that both horizontal and inclined cylinders can be prone to dry instability, depending on the yaw angle. Existence of a secondary axial flow, located in the near wake of the cylinder's axis, was documented, which has the role of interrupting the regular Kármán vortex shedding. In fact, as an *air curtain* or *base bleed*, or similarly a splitter plate submerged in the wake, the secondary axial flow prevents the fluid interaction between the two separated shear layers, thus generating an unsteady inner circulatory flow at the leeward surface of the cylinder. The inner circulatory flow generates a region of significantly lower pressure, this latter being responsible of activating the excitation, (Matsumoto et al., 1990). Fig. 2.16 shows the flow pattern around a yawed circular cable, obtained by means of a liquid paraffin method and around a horizontal cylinder with splitter plate submerged in the wake. A similarity was assumed by Matsumoto et al. (1990) between the axial flow excitation excitation and the galloping of rectangular cylinders described by Bearman and Trueman (1972).

In Fig. 2.17 possible unsteady flow patterns around a circular cylinder moving with velocity $\dot{y}$ in the downwards direction, in different spacial orientations are illustrated. In absence of yaw/inclination (a) regular Kármán

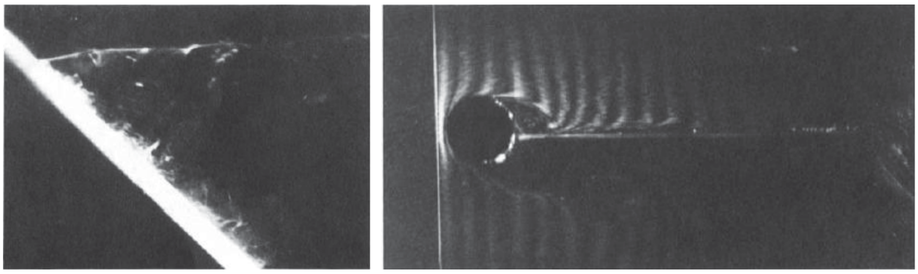

(a) (b)

***Figure 2.16**: Secondary axial flow on the leeward surface of yawed circular cylinder, (a); inner circulatory flow of a circular cylinder with splitter plate in the leeward side, (b), (Matsumoto et al., 1990).*

vortex shedding occurs in the wake. When the cylinder is yawed (b), or inclined/yawed (c), (d) to the flow, the secondary axial flow develops in the leeward side, thus generating the unsteady inner circulatory flow.

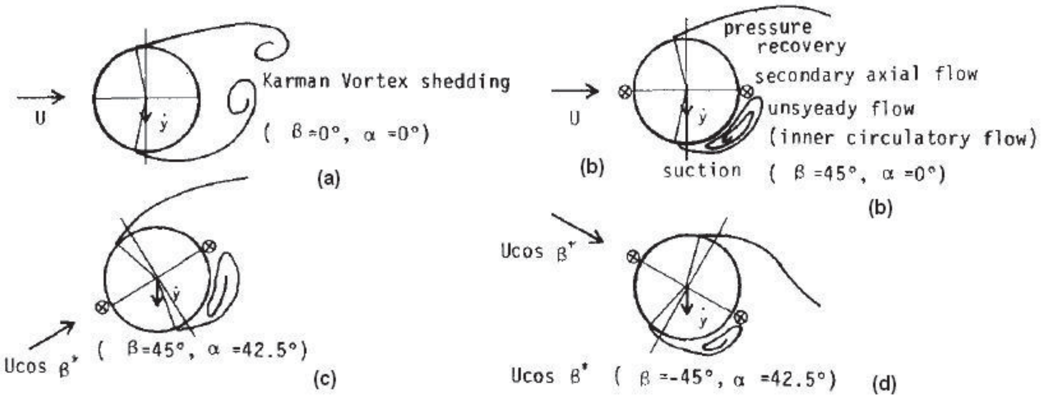

***Figure 2.17**: Unsteady flow pattern around a circular cylinder in different spacial orientations, (Matsumoto et al., 1990).*

Matsumoto et al. (1990) thus concluded that in order to prevent the excitation, the secondary axial flow need to be suppressed.

Later on, during the period of construction of the Higashi-Kobe cable-stayed bridge in Japan, seen the concern for potential heavy vibrations of the cables when excited by wind or by wind and rain, Saito et al. (1994) performed a series of wind tunnel vibration tests on a life-size cable model, identical in weight as the real cables at the mentioned bridge. It was in fact suspected that previous observations of dry inclined cable vibration could be attributed to the lower mass of the models in comparison to real cables. Several cable-wind angles for the cable model were tested, i.e. $\Phi = 30°$, 45°, 60°. A stability criterion was established as outcome of the experimental campaign, giving the reduced wind velocity U_r associated to the onset of divergent motion, i.e.

$$(U_r)_{cr} = 14\sqrt{S_c} \tag{2.18}$$

The criterion showed how the wind velocity at which the inclined cable vibration takes place does not vary appreciably over a large range of Scrouton numbers (50 and under), thus implying that dry inclined cable vibration appears to be difficult to restrain once it has taken place even if the cable structural damping is increased to some extent, for example by means of a damper. Soon later, Honda et al. (1995) established a similar instability criterion, based on wind tunnel tests undertaken on a full scale section model oriented at a cable-wind angle of 45°. Experimental results derived by Saito et al. (1994) and Honda et al. (1995) thus show how the dry instability develops for wind velocities in the subcritical Reynolds number range. On the other hand, (Miyata et al., 1994b) observed divergent motion to occur for a cable model oriented at the same cable-wind angle (45°), but for larger wind velocity, i.e. presumably corresponding to the transition between subcritical and critical Reynolds number range.

The instability criteria for galloping of dry inclined cables reported by japanese researchers caused serious concern in the design of cable stayed bridges as they implied that dry inclined cables can be excited at relatively low wind speed, even if their inherent damping is very high. On the other hand, reality is that many existing stay cables seem to survive without suffering this instability, (Cheng et al., 2008a). In order to first confirm the divergent type of instability for inclined cables and to subsequently verify the stability criterion established by japanese researchers, an experimental campaign was conducted at NRCC Ottawa in Canada. Results are reported by Cheng et al. (2003), Cheng et al. (2008a), Cheng et al. (2008b). In the experimental campaign divergent-type motion was observed for a polyethilene coated section model, inclined and yawed to the mean wind direction, oriented at a cable-wind angle of 60°. The cable surface condition was classified as *smooth* and the inherent structural damping ratio was 0.001, so as to lead to a Scrouton number, i.e. $S_c = m\delta/(\rho D^2)$, equal to 11. Divergent motion was achieved when the wind velocity reached a value of 32 m/s, i.e. corresponding to the critical range. At this velocity, the amplitude of motion increased dramatically within a short period of time, leading to a maximum recorded peak-to-peak amplitude of approximately 1D, where D is the cable diameter. Model's trajectories were elliptical and showed how the motion developed predominantly along the in-plane direction. It was finally observed that the generation of the excitation was difficult to reproduce due to strong sensitivity to the test conditions.

In Fig. 2.18, the wind velocity-damping relation for inclined cable obtained by japanese researchers is compared to results obtained during the canadian tests, (Cheng et al., 2008a), these latter identified as *Current*.

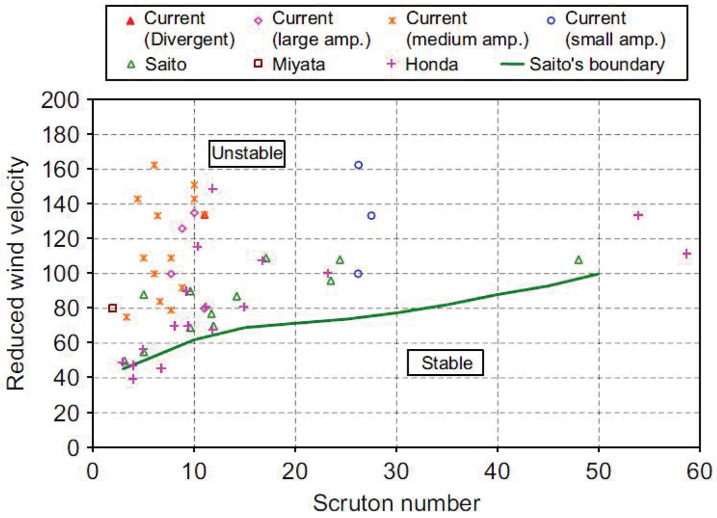

***Figure 2.18**: Comparison of wind-velocity damping relation for inclined cable, (Cheng et al., 2008a).*

The data presented in Fig. 2.18 implies that the onset conditions of divergent type of motion on a dry stay cable are not certain, i.e. it can happen in the subcritical (Saito et al., 1994), (Honda et al., 1995), at transition to the critical, (Miyata et al., 1994b), or in the the critical Reynolds number range (Cheng et al., 2008a). Recent results derived by Matteoni and Georgakis (2013a) confirmed that dry inclined instability can occur under a wide range of Reynolds number. This is due to non uniform distribution of surface roughness/shape of the cable. Thus depending on the wind angle-of-attack, the cable might exhibit unstable/stable response to the wind loading.

Properties of the cable models employed in several dynamic experimental test campaigns and the onset conditions for instability are summarised in Tables 2.9-2.12.

Vortex induced vibration at high reduced velocity was as well reproduced in experimental studies in Japan, (Matsumoto et al., 2001), in Canada (Cheng et al., 2003), (Cheng et al., 2008a), (Cheng et al., 2008b), and in Italy, (Diana et al., 2008).

Based on experimental evidence, Matsumoto et al. (2001) and Cheng et al. (2008a) suggested that there could be a strong interaction between dry

Table 2.9: *Critical geometrical attitude for dry inclined galloping for the cable models tested dynamically in wind tunnels.*

θ [°]	β [°]	Φ [°]	Reference
60	0	60	Saito et al. (1994)
45	0	45	Saito et al. (1994)
30	0	30	Saito et al. (1994)
0	45	45	Saito et al. (1994)
-	-	45	Honda et al. (1995)
45	45	60	Miyata et al. (1994b)
45	45	60	Cheng et al. (2008a)
25	60	63.05	Matteoni and Georgakis (2013a)

Table 2.10: *Critical geometrical characteristics for dry inclined galloping for the cable models tested dynamically in wind tunnels.*

D [m]	L [m]	Reference
0.16	9.5	Saito et al. (1994)
0.155	-	Honda et al. (1995)
0.1315	3	Miyata et al. (1994b)
0.16	6.7	Cheng et al. (2008a)
0.16	3.35	Matteoni and Georgakis (2013a)

Table 2.11: *Critical inertial and dynamic properties for dry inclined galloping for the cable models tested dynamically in wind tunnels.*

m [kg/m]	f [Hz]	Sc [-]	Reference
100	0.61	3.2	Saito et al. (1994)
-	0.26	10.5	Honda et al. (1995)
6.6	1.8	1.7-2.3	Miyata et al. (1994b)
60.8	1.4	11	Cheng et al. (2008a)
18.4	1.1	0.5	Matteoni and Georgakis (2013a)

inclined galloping and vortex induced vibration at high reduced wind velocity. In particular, Cheng et al. (2008a) stated that both excitation phenomena might initiate from vortex-induced vibration and as they develop and reach relatively large amplitudes of vibration, because of the differences in the physical conditions, such as cable orientation, wind velocity, wind turbulence, the motion would either decay with further increase in the wind velocity or continuously grow.

***Table 2.12**: Onset conditions of instability for dry inclined galloping for the cable models tested dynamically in wind tunnels.*

U_r [-]	Re [-]	A/D	Reference
72	7.23x10^4	0.75	Saito et al. (1994)
115	4.65x10^4	-	Honda et al. (1995)
79	1.81x10^5	-	Miyata et al. (1994b)
134	3.3x10^4	>0.49	Cheng et al. (2008a)
96-143	1.8-2.7x10^5	>2	Matteoni and Georgakis (2013a)

Cheng et al. (2008a) observed vortex induced vibrations at high reduced wind velocity to occur for a cable model whose longitudinal axis was oriented at 60°, 45° and 35° with respect to the wind direction, obtained by a combination of 60°, 45° and 35° vertical inclination and 0° yaw. Thus the wind was blowing along the cable axis. The cable model, in terms of length, diameter, mass was identical to the one where Cheng et al. (2008a) observed dry inclined galloping. Excitation developed for Reynolds number in the range of $2-4{\cdot}10^5$, i.e. in the critical. Maximum amplitudes of vibration were observed to be function of the cable orientation angle and became larger by increasing the vertical inclination angle. In particular, the recorded maximum amplitude amounted respectively to 67, 31 and 21 mm for cables charactersed by vertical inclination (and cable-wind angles) of 60°, 45° and 35°. A *lock-in* phenomenon of the vibration direction was observed to occur, i.e. as soon as the wind velocity increased to that of unstable motion a considerable change in the direction of motion occurs; within the range of instability the direction of motion thus remains constant, and it is characterised by a dominant cross-wind component; once the wind speed is above the unstable range, the component of cross-wind motion would considerably decrease. If the cable is both inclined and yawed to the wind, the predominant motion direction is not any longer perpendicular to the cable plane and the motion follows an elliptical path.

2.4.3 Static wind tunnel tests

In order to obtain a clearer insight into the instability of dry inclined cables, static wind tunnel tunnel have been performed in the past, mostly in association with vibration tests.

Reynolds number, cable-wind angle, and wind angle-of-attack effects are all important in relation to the cable instability, especially in the flow regimes where small increments of the mentioned parameters lead to significant changes to drag and lift forces, (Larose et al., 2003). In fact, depending on the attitude of the cable to the flow (i.e. cable wind angle and angle-of-attack), the behaviour of the separated shear layers that govern the aerodynamic forces may vary with the Reynolds number in a different manner from that of a circular cylinder in cross-flow.

Results of an extensive wind tunnel test investigation on the aerodynamic behaviour of bridge cables in static conditions, oriented perpendicular the wind and in an inclined/yawed configuration, for varying Reynolds numbers and wind angles-of-attack, is presented in Chapter 3. This is based on a study performed by Matteoni and Georgakis (2012). The investigation follows several studies performed in the past, i.e. Schewe (1983), Zdravkovich (1997) (in cross-flow), Bursnall and Loftin (1951), Larose et al. (2003), Larose et al. (2005), Cheng et al. (2008a), to the flow (in inclined/yawed configuration).

In order to give an overview of the static aerodynamic behavior of circular cylinders, brief conclusions of the previous studies are reported here below.

Schewe (1983) measured the steady and unsteady forces of a small-scale circular cylinder horizontally oriented and perpendicular to the wind. It was found that in the critical Reynolds-number range, two discontinuous transitions exist, which can be interpreted as bifurcations at two critical Reynolds numbers. The transitions are accompanied by critical fluctuations, symmetry breaking (the occurrence of a steady lift) and hysteresis of the flow. In addition, both transitions are coupled with a drop of the drag coefficient value and a jump of the Strouhal number. Similar phenomena were observed in the upper transitional region between the super- and the transcritical Reynolds-number ranges.

Larose et al. (2003) performed a series of static wind tunnel tests on a stay cable model made of a 89 mm diameter steel tube. Tests were undertaken in smooth flow, i.e. $I_u = 0.13\%$, for Reynolds number between $1 \cdot 10^5$ and $6 \cdot 10^5$, i.e. in the range where transition from laminar to turbulent boundary layer occurs. This is associated with the formation of the one-asymmetric bubble and two-symmetric bubble regimes, accompanied by a sudden drop of the drag coefficient, i.e TrBL0 to TrBL2 (Zdravkovich, 1997). Three model inclinations were tested, i.e. $\Theta = 90°$, $60°$, $54.7°$. In the reference case, i.e. $\Theta = 90°$, $\beta = 90°$ (cylinder perpendicular to the wind flow), the TrBL1 regime occurs at Reynolds numbers between 3.1×10^5 to 3.5×10^5; in this range of Reynolds number the static across-wind force reaches a mean coefficient of 0.8, while the drag coefficient at the same Reynolds was 0.55. Here, a single laminar separation bubble is suspected to occur causing asymmetry in the pressure distribution, while at Reynolds numbers above 3.5×10^5 two laminar separation bubbles are suspected to occur, one on each side of the cylinder, causing the drag to drop further and almost completely eliminating the lift.

Matteoni and Georgakis (2012) observed that for a cable model horizontally oriented and perpendicular to the wind (i.e. at $\Theta = 0°$, $\beta = 90°$, $\Phi = 90°$), the critical range generally spans from 2.5×10^5 to 3.0×10^5. On the other hand, small scale deviations in the cable surface roughness or shape, can lead to a variation in the critical range, which might span from 1.0×10^5 to 3.3×10^5. This behaviour might explain some of the observed aerodynamic instabilities, such as dry inclined galloping. In Table 2.13 are summarised the range of critical Reynolds number for cylinders in cross flow ($\Phi = 90°$).

***Table 2.13**: Range of critical Reynolds number for cross-flow cylinders ($\Phi = 90°$).*

Re_{cr} [-]	Reference
1.7×10^5-2.5×10^5	Schewe (1983)
3.1×10^5-3.5×10^5	Larose et al. (2003)
2.5×10^5-3.0×10^5	Matteoni and Georgakis (2012)

Bursnall and Loftin (1951) measured the pressure distributions on a smooth small-scale brass tube for a series of vertical inclination angles, i.e. $\Theta = 30°, 45°, 60°, 75°, 90°$, and zero yaw, $\beta = 0°$, for Reynolds numbers up to 5.0×10^5. Tests were performed in laminar flow, in a low turbulence wind tunnel (0.05%). It was mainly observed that in the subcritical range the cylinder's pressure distributions are quite insensitive to the inclination angle. On the other hand, a gradual change takes place in the pressure distribution through and beyond the critical range, as the inclination angle is increased. The laminar separation bubble, which is responsible for asymmetric pressure distributions and therefore across-wind forces, does not appear as well defined at $\Phi = 90°$; on the other hand, it is present at $\Phi = 75°$ and $\Phi = 60°$, and completely disappears at $\Phi = 45°$ and $\Phi = 30°$. Drag coefficients curves show that the lower is the cable inclination, the earlier is the transition from subcritical to critical regime, thus producing a similar effect as increased surface roughness or turbulence intensity. Similarily Larose et al. (2003) observed that for an inclined cylinder ($\Theta = 60°$), the variation of the lift coefficient shows that the TrBL1 still exists but it spans over a wider range of Reynolds number.

Larose et al. (2005) observed that the turbulence intensity of the natural wind on bridge sites is likey to be much larger in comparison to the smooth flow conditions tested in the past, i.e. corresponding to a wind tunnel turbulence intensity below 1%. Moreover, since in field conditions the critical mean wind speed can be reached either from lower or higher wind regime, a possible hysteresis of the single bubble regime might occur. For this reason, Larose et al. (2005) performed a series of wind tunnel tests on a 316 mm diameter HDPE tube, for Reynolds numbers spanning the subcritical to the supercritical range, i.e. 1×10^5 to 3.3×10^5. The cable was installed horizontally, leading to 0° inclination. By changing the yawing angle, cable-wind angles in the range of 20° to 85° were achieved. Tests were undertaken at turbulence intensities of 2.5% and 11%. As the cable-wind angle was increased, the drag coefficient in the subcritical range increased, while the drag crisis was anticipated. From the lift coefficient curves it was visible how the single bubble regime was present over a wider range of yaw angles, $(40° \leq \beta \leq 85°)$, in contrary to the range of $(55° \leq \beta \leq 65°)$ experienced by Larose et al. (2003). The effect of increasing the turbulence intensity up to 11% was to completely eliminate the single bubble regime, i.e. the lift curve becomes flat and close to 0, throughout the whole Re range.

2.5 Iced state

Ice accretion is a time-dependent modification of the shape of an object, occurring on a longer time scale compared with those of any possible dynamic response. Atmospheric icing occurs in different forms, i.e. hoar frost, caused by the condensation of vapour, in-cloud icing, involving the freezing of supercooled water droplets in clouds or fog, and precipiation icing, resulting from freezing rain, drizzle, wet snow or dry snow, Farzaneh (2008). The role of ice accretion on the aerodynamic instability of bridge cables has been recognised in the recent years. Nevertheless, a clear systematization of the knowledge on this form of instability doesn't exist, as neither field monitoring data nor dynamic wind tunnel test data have been collected. Static measurements of the aerodynamic drag, lift and moment coefficients of full-scale bridge cable sections have instead been performed recently in Denmark, (Koss and Matteoni, 2011), (Koss and Lund, 2013), (Demartino et al., 2013), (Demartino et al., 2013).

2.5.1 Field observations

As for the dry state, field monitoring data of bridge cable sections covered by ice accretions are scarce.

Records of cable vibrations in freezing conditions have been reported for bridges in the Northern Hemisphere, such as the Øresund bridge, located between Denmark and Sweden, (Svensson et al., 2004), the Great Belt East bridge in Denmark, (Gjelstrup et al., 2007), the Uddevalla Bridge in Sweden, (Vincentsen and Lundhus, 2006), the Severn Bridge in UK, (Vincentsen and Lundhus, 2006), the Zakim Bunker Hill Bridge, in USA, and the Hukaho Bridge, in Japan, (Gimsing and Georgakis, 2012). Besides vibration, episodes of cable icing might represent a safety problem for the bridge users, due to the phenomenon of ice shedding.

The Great East Belt Bridge was closed for several hours in March 2001, after the occurrence of large amplitude vibrations of the bridge hangers. The vibrations occurred for wind velocities in the range of 16-18 m/s and were characterised by amplitudes in the order of 2 m in the across-wind direction and in the order of 0.6 m in the along-wind direction, (Gjelstrup et al., 2007).

Several icing events were reported at the Toledo Skyway Bridge, in Ohio since its opening, (Nims, 2011). Figs. 2.19 show icing accumulations on the stays occurred on December 2007. It was reported that for this occurrence the wheather conditions causing the ice accumulation were characterised by freezing rain and fog. The bridge cable's sheat is made of stainless steel, with a brushed finish, and it lacks a helical spire. So far, no anti-icing systems have been installed at the bridge stays.

(a) (b)

(c)

Figure 2.19: *Ice hanging on the stay sheat (a); patter of ice release (b); ice fallen from the stays to the deck (c) at Toledo Skyway Bridge, in Ohio on December 2007, (Nims, 2011).*

Fig. 2.20 shows an overview of ice accretion occurred at the Toledo Skyway Bridge later in February 2011. The wheather conditions causing this event were again characterized by freezing rain.

In December 2012 the Portman Bridge in Vancouver, British Columbia, was closed for several hours after snow and ice falling from the supporting cables, causing injure to two people and dozen of vehicles. Fig. 2.21 shows a detail of the iced cable sections at the bridge.

In order to prevent snow and ice to fall on the bridge deck, sweepers were custom-designed to be fitted around the cables on the Port Mann Bridge. Fig. 2.22 shows a prototype of the sweepers.

2.5.2 Dynamic wind tunnel tests

Dynamic wind tunnel tests have not been performed so far on bridge cable sections. Thus the characteristics of the instability are still unclear.

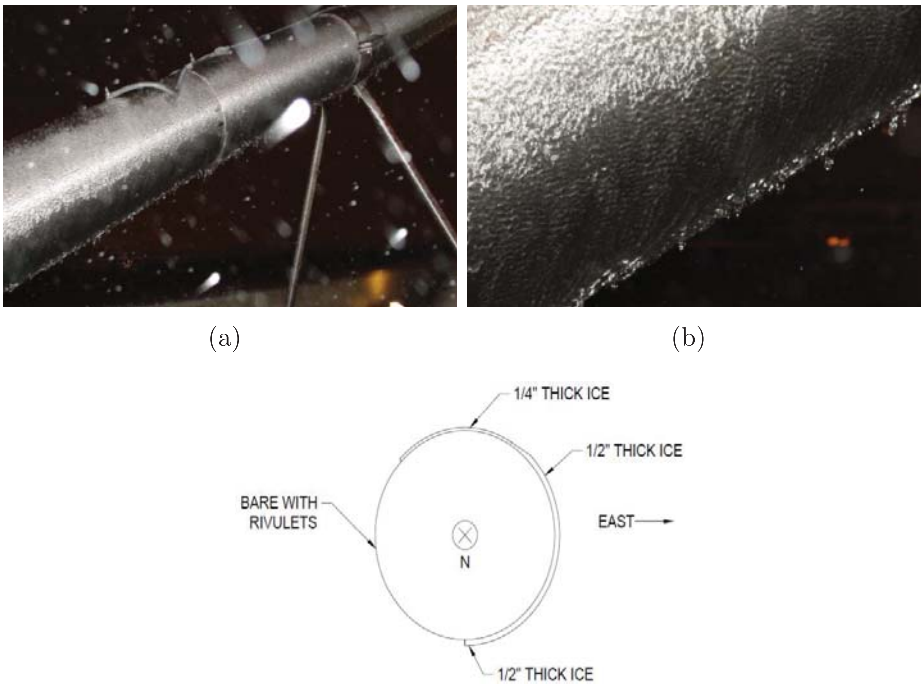
(a) (b)

(c)

Figure 2.20: *Overview (a) and close-up (b) of ice accumulation under freezing rain on the stays at Toledo Skyway Bridge, in Ohio on February 2011; diagramm of ice accumulation (c), (Nims, 2011).*


(a) (b)

Figure 2.21: *Ice formations on the cable sections at the Port Mann Bridge in Vancouver, British Columbia (a); damage on a passing car (b). (Pictures from* ***http://www.vancouversun.com/****).*

On the other hand, few experimental wind tunnel dynamic investigations have been undertaken for cable conductors covered by ice accretion, for example by Chabart and Lilien (1998). It is nevertheless unclear whether the

Figure 2.22: *Custom-designed ice/snow sweepers to be fitted to the stays at the Portmann Bridge in Vancouver, British Columbia. (Pictures from* ***http://www.news1130.com/****).*

results of such tests are directly applicable to bridge cable sections. In fact, the ratio between the size of the accretion and the conductor diameter is much higher than for a full-scale cable. The same applies for the associated mass ratios.

2.5.3 Static wind tunnel tests

Few wind tunnel tests have been performed in order to understand the instability of iced bridge cables. Koss et al. (2012) investigated, by performing a series of wind tunnel tests at NRC Canada, the characteristic shapes of ice accretions on circular cylinders under the specific climatic conditions where large amplitude vibrations of iced birdge cables have been observed in nature. In particular with reference to the episodes occurred at the Great East Belt (Gjelstrup et al., 2007). This study was followed by a long and still ongoing test campaign at the novel climatic wind tunnel recently constructed in Denmark,(Georgakis et al., 2009). The facility was specifically built for the purpose of testing bridge cable sections under variable flow and climatic conditions, in particular conditions related to low altitude atmospheric icing. Investigations have been performed on the aerodynamic coefficients of cross-flow horizontal, (Koss and Matteoni, 2011), (Koss and Lund, 2013) and vertical, (Demartino et al., 2013) bridge cables and inclined/yawed to the wind, (Demartino et al., 2013).

Koss and Lund (2013) studied in detail the features of ice accretion for a horizontally installed bridge cable. These are illustrated in Fig. 2.23. In an early stage of the accretion rime ice accumulates along the cable's stagnation line, which appears as a smoother core zone (a); curved jagged ice structures start later to grow towards the flow stagnation line resembling the appearence of feathers until they reach a limit near the stagnation line (b); depending on the temperature and on the liquid water content of the air some flow-out accumulations might develop, (c) and (d).

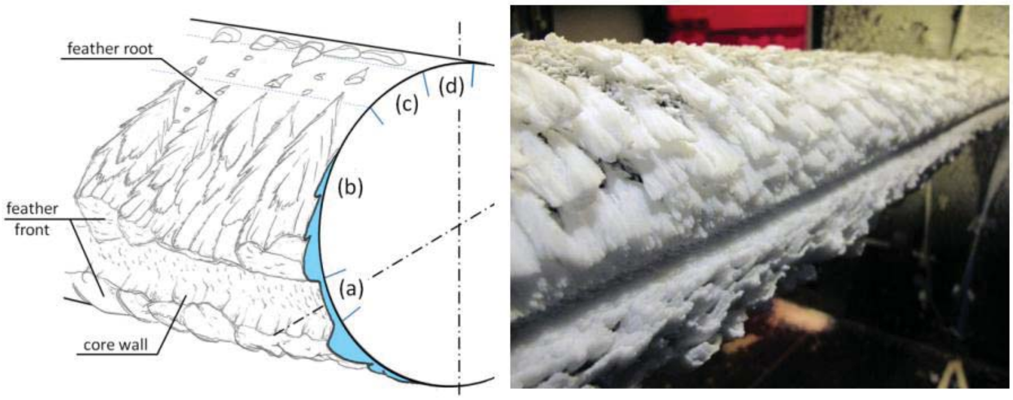

Figure 2.23: *Description of the ice accretion features, (Koss and Lund, 2013).*

Koss and Lund (2013) and Demartino et al. (2013) additionally determined the drag and lift coefficients for varying Reynolds number and angles-of-attack of horizontal and vertical iced cables respectively, under conditions of wet and dry ice accretion. The coefficients were employed in the classical Den Hartog 1 DOF critierion in order to predict the regions of galloping instability.

Force coefficients of inclined/yawed cable sections have been determined by Demartino et al. (2013). In this study the ice accretion was performed for selected orientations of the cable model with respect to the wind. After the accretion process was ultimated the force coefficients were evaluated for varying Reynolds numbers and for a series of cable-wind angles, obtained by changing the yaw angle of the cable and keeping the same inclination as the one adopted during the accretion process. Investigation of the dependency of the force coefficients on the wind-angle-of-attack for varying cable-wind angles and Reynolds numbers could instead be a topic of future research, as it was not investigated into details in this study.

2.6 Conclusion

Bridge cables are classified as bluff bodies and as such can only undergo instabilities of vortex shedding-, buffeting- and galloping-type. Depending on the climatic conditions they are subjected to, the characteristics of such instabilities differ significantly.

A literature review on the different excitation mechanisms of inclined cables under varying meteorological conditions, i.e. in the dry, rainy and iced state, was here given. The review was based on the most recent findings achieved from full scale monitoring, wind tunnel testing and theoretical modelling.

Systematization of the current knowledge leaded to conclude that:

- Rain-wind induced is a limited amplitude-type instability, occurring over a restricted range of wind velocities, under moderate rain conditions, for cables descending in the wind direction. The instability was mostly observed for plain surfaced cables, coated with polyethylene (PE), where the water rivulet could easily form, under the achievement of the right level of surface wettability. This form of instability has been observed both on full-scale and in wind tunnel tests, and a fair agreement in the characterization of the excitation mechanism, based on the two approaches, has been achieved.

- In dry conditions, two types of excitation have been recognised. Under a combination of parameters, such as cable attitude to the flow, wind velocity, stay cables may either undergo divergent motion (dry galloping) or limited amplitude motion under a limited interval of wind speed (vortex induced vibration at high reduced wind speed). Dry cable vibrations have been observed only in wind tunnel experimental studies, while they have never been fully verified on full-scale bridges.

- Instability of bridge cables in the iced state has been recognised as a form of galloping. The aerodynamic force coefficients of perpendicular and inclined/yawed full-scale bridge cables covered by ice accretions have been determined by performing static wind tunnel tests. On the other hand a complete characterization of the iced state instability, based on passive-dynamic wind tunnel tests and full-scale monitoring has never been performed.

Bibliography

Acampora, A., Georgakis, C.T., 2011. Recent monitoring of the Øresund Bridge: Observations of rain-wind induced cable vibrations. In: 13th International Wind Engineering Conference, Amsterdam.

Alam, MD., Zhou, Y., 2007. Turbulent wake of an inclined cylinder with water running. J. Fluid Mech. 589, 261-303.

Bearman, P.W., Trueman, D.M., 1972. An investigation of the flow around rectangular cylinders. The Aeronatical Quarterly, 23.

Benedir, A., Flamand, O., Gaillet, L., Dimitriadis, G., 1972. Dry galloping on bridge cables: Shape effects on an inclined circular cylinder in the wind tunnel. In: 6th European African Conference Wind Engineering, Cambridge.

Bosdogianni, A., Olivari, D., 1996. Wind-and rain-induced oscillations of cables of stayed bridges. J. Wind Eng. Ind. Aerodyn. 64, 171-185.

Boujard, O., 1996. Wind-and rain-induced oscillations of cables of stayed bridges. J. Wind Eng. Ind. Aerodyn. 64, 171-185.

Bursnall, W.J., Loftin, L.K., 1951. Experimental investigation of the pressure distribution about a yawed circular cylinder in the critical Reynolds number range. Technical report, Langley Aeronautical Laboratory, Langley Field, Va.

de Sá Caetano, E., 2007. Cable Vibrations in Cable-Stayed Bridges. International Association for Bridge and Structural Engineering.

Chabart, O., Lilien J.L., 1998. Galloping of electrical lines in wind tunnel facilities. J. Wind Eng. Ind. Aerodyn. 74-76, 967-976.

Cheng, S., Larose, G.L., Savage, M.G., 2003. Aerodynamic behaviour of an inclined circular cylinder. J. Wind and Structures 6 (3), 197-208.

Cheng, S., Larose G.L., Savage, M., Tanaka, H., Irwin, P.A., 2008a. Experimental study on the wind-induced vibration of a dry inclined cable - Part I: Phenomena. J. Wind Eng. Ind. Aerodyn. 96 (12), 2231-2253.

Cheng, S., Irwin P.A., Tanaka, H., 2008b. Experimental study on the wind-induced vibration of a dry inclined cable - Part II: Proposed mechanisms. J. Wind Eng. Ind. Aerodyn. 96 (12), 2254-2272.

Clobes, M., Steiln, O.., Peil, U., 2010. Aerodynamic force coefficients for rain-wind induced vibrations from full-scale measurements. In: 5th International Conference on Structural Engineering, Mechanics and Computation.

Collar, A., 1978. The first fifty years of aeroelasticity. Aeroespace, Royal Aeronautical Society, vol. 545.

Cosentino, N., Flamand, O., Ceccoli, C., 2003. Rain-wind-induced vibration of inclined stay cables. Part I: experimental investigation and physical explanation. Wind Struct. 6, 471-484.

Davenport, A.G., 1962. Buffeting of a suspension bridge by storm winds. J. Struct. Division ASCE, 88-3, 233-268.

Demartino, C., Koss, H.H., Ricciardelli, F., 2013. Experimental study of the effect of icing on the aerodynamics of circular cylinders - Part I: Cross flow. In: 6th European African Conference Wind Engineering, Cambridge.

Demartino, C., Georgakis, C.T., Ricciardelli, F., 2013. Experimental study of the effect of icing on the aerodynamics of circular cylinders - Part II: Inclined flow. In: 6th European African Conference Wind Engineering, Cambridge.

Den Hartog, J.P., 1958. Mechanical vibrations. Courier Dover Publications

Diana, G., Belloli, M., Giappino, S., Muggiasca, S., 2008. Vortex induced vibrations at high Reynolds numbers. In: 7th International Colloquium on Bluff Bodies Aerodynamics and Applications, Milano, Italy.

Ehsan, F., Scanlan, R.H., Bosch, H.R., 1990. Modeling spanwise correction effects in the vortex-induced response of flexible bridges. J. Wind Eng. Ind. Aerodyn. 36 (2), 1105-1114.

Farzaneh, M., 2008. Atmospheric icing of power networks. Springer.

Flamand, O., 1995. Rain-wind induced vibration of cables. J. Wind Eng. Ind. Aerodyn. 57, 353-362.

Flamand, O., Peube, J.-L., Papanikolas, P., 2001. An explanation of the rain-wind induced vibration of inclined stays. In: IV International Symposium on Cable Dynamics, Montreal, Canada, May 28-30, pp. 69-76.

Fujino, Y., Kimura, K., Tanaka, H., 2012. Wind Resistant Design of Bridges in Japan. Springer.

Georgakis, C.T., Koss, H.H., Ricciardelli, F., 2009. Design specifications for a novel climatic wind tunnel for testing of structural cables. In: 8th International Symposium on Cable Dynamics, Paris, pp. 333-340.

Gimsing, N.J., Georgakis, C.T., 2012. Cable Supported Bridges. Concep and Design. Third Edition. Wiley.

Gjelstrup, H., Georgakis, C.T., Larsen, A., 2007. A preliminary investigation of the hanger vibrations on the Great Belt East Bridge. In: VII International Symposium on Cable Dynamics, Vienna, pp. 469-476.

Gjelstrup, H., Georgakis, C.T., 2011. A quasi-steady 3 degree-of-freedom model for the determination of the onset of bluff body galloping instability. In: Journal of Fluids and Structures, 27 (7), 1021-1034.

Gu, M., Du, X., 2005. Experimental investigation of rain-wind-induced vibration of cables in cable-stayed bridges and its mitigation. J. Wind Eng. Ind. Aerodyn. 93, 79-95.

Gu, M., Huang, L., 2008. Theoretical and experimental studies on the aerodynamic instability of a two-dimensional circular cylinder with a moving attachment. J. Fluids and Structures 24, 200-211.

Hikami, Y., Shiraishi, N., 1988. Rain-wind induced vibrations of cables stayed bridges. J. Wind Eng. Ind. Aerodyn. 29, 409-418.

Hardy, C., Bourdon, P., 1979. The influence of spacer dynamic properties in the control of bundle conductor motion. IEEE PES Summer Meeting, Vancouver, British Columbia, Canada

Honda, A., Yamanaka, T., Fujiwaraa, T., Saito, T.,1995. Wind tunnel test on Rain-Induced Vibration of the Stay Cable. In: International Symposium on Cable Dynamics, Liege, Belgium, pp. 255-262.

Irwin, P.A., Nedim, A., Telang, N., 1999. Wind induced stay cable vibrations a case study. In: 3rd International Symposium on Cable Aerodynamics, Trondheim, Norway, pp. 171-176.

Jacobsen, J.B., Andersen, T.L., Macdonald, J.H.G., Nikitas, N., Larose, G.L., Savage, M.G., McAuliffe, B.R., 2012. Wind-induced response and excitation characteristics of an inclined cable model in the critical Reynolds number range. J. Wind Eng. Ind. Aerodyn. 110, 100-112.

Koss, H.H., Matteoni, G., 2011. Experimental investigation of aerodynamic loads on iced cylinders. In: 9th International Symposium on Cable Dynamics, Shanghai, 381-388.

Koss, H.H., Gjelstrup, H., Georgakis, C.T., 2012. Experimental study of ice accretion on circular cylinders at moderate low temperatures. J. Wind Eng. Ind. Aerodyn. 104-106, 540-546.

Koss, H.H., Lund Møller, M.S., 2013. Experimental Investigation of Aerodynamic Instability of Iced Bridge Cable Sections. In: 6th European African Conference Wind Engineering, Cambridge.

Langsoe, H.E., Larsen, O.D., 1987. Generating mechanisms for cable stay oscillations at the Faroe Bridge. In: Int. Conf. on Cable-stayed Bridges, Bangkok, pp. 18-20.

Larose, G.L., Smitt, L.W., 1999. Rain/wind induced vibrations of the parallel stay cables for the Oresund High Bridge. In: IABSE Conference, Malmo, June, pp. 1-12.

Larose, G.L., Savage, M.G., Jakobsen, J.B., 2003. Wind tunnel experiments on an inclined and yawed circular cylinder in the critical Reynolds number range. In: 11th International Conference on Wind Engineering, Lubbock.

Larose, G.L., Zasso, A., Giappino, S., 2005. Experiments on a yawed stay cable in turbulent flow in the critical Reynolds number range. In: 6th International Symposium Cable Dynamics, Charleston, pp. 279-286.

Liu, Q., Wang, Y., Zheng, Y.,Ma, W., 2012. Experimental study on the relation of water rivulet-Reynolds number effect-cable vibration. In: 7th International Colloquium on Bluff Body Aerodynamics and Applications, Shanghai, China.

Macdonald, J.HJ., Larose G.L., 2008a. A unified approach to aerodynamic damping and drag/lift instabilities, and its application to dry inclined cable galloping. J. Fluids Struct. 22, 229-252.

Main, J.A., Jones, N.P., Yamaguchi, H., 2001. Characterization of rain-wind induced stay-cable vibrations from full-scale measurements. In: Fourth International Symposium on Cable Dynamics, Montreal, Canada, pp. 235-242.

Matsumoto, M., Shiraishi, N., Kitazawa, M., Knisely, C., Shirato, H., Kim, S., Tsujii, M., 1990. Aerodynamic behaviour of inclined circular cylinders-Cable aerodynamics. J. Wind Eng. Ind. Aerodyn. (33), 63-72.

Matsumoto, M., Shiraishi, N., Shirato, H., 1992. Rain-wind induced vibration of cables of cable-stayed bridges. J. Wind Eng. Ind. Aerodyn. 43, 2011-2022.

Matsumoto, M., Saitoh, T., Kitazawa, M., Shirato, H., Nishizaki, T., 1995. Response characteristics of rain-wind induced vibration of stay cables of cable-stayed bridges. J. Wind Eng. Ind. Aerodyn. 57, 323-333.

Matsumoto, M., Yagi, T., Tsushima, D., 1999. Vortex-induced vibration of inclined cables at high wind velocity. In: 10th International Conference on Wind Engineering, Copenhagen, pp. 979-986.

Matsumoto, M., Yagi, T., Shigemura, Y., Tsushima, D., 2001. Vortex-induced cable vibration of cable-stayed bridges at high reduced wind velocity. J. Wind Eng. Ind. Aerodyn. 89 (7-8), 633-647.

Matsumoto, M., Shirato, H., Yagi, T., Goto, M., Sakai, S., Ohya, J., 2003. Field observation of the full-scale wind-induced cable vibration. J. Wind Eng. Ind. Aerodyn. 91, 13-26.

Matsumoto, M., 2005. The role of water rivulet on inclined cable aerodynamics. In: 6th Asia-Pacific Conference on Wind Engineering, Seoul, pp. 63-77.

Matsumoto, M., 2006. Review of Bridge Cable Vibrations in Japan. The practical Cases of Aerodynamic Vibration of Stayed Cables. Wind Induced Vibration Cable Workshop, April 25-27.

Matsumoto, M., Yagi, T., Hatsuda, H., Shima, T., Tanaka, M., Naito, H., 2010. Dry galloping characteristics and its mechanism of inclined/yawed cables. J. Wind Eng. Ind. Aerodyn. 98, 317-327.

Matteoni, G., Georgakis, C.T., 2013. Effects of bridge cable surface roughness and cross-sectional distortion on aerodynamic force coefficients. J. Wind Eng. Ind. Aerodyn., 104-106, 176-187.

Matteoni, G., Georgakis, C.T., 2013. Effects of surface roughness and cross-sectional distortion on the wind-induced response of bridge cables in dry conditions, submitted to the J. Wind Eng. Ind. Aerodyn.

Matteoni, G., Georgakis, C.T., 2013. Effects of surface and inertial properties of bridge cables on the rain-wind induced instability, submitted to the J. Wind Eng. Ind. Aerodyn.

Miyata, T., Yamada, H., Hojo, T.,1994b. Aerodynamic response of PE stay cables with pattern-indented surface. In: Proceedings of the International Conference A.I.P.C.-F.I.P. Deauville on Cable-stayed and Suspension Bridges, Vol. 2, pp. 515-522.

Miyata, T., 2003. Historical view of long-span bridge aerodynamics. J. Wind Eng. Ind. Aerodyn. 91, 1393-1410.

Nebres, J., Batill, S., 1993. Flow about a circular cylinder with a single large-scale surface perturbation. Exps. Fluids 15, 369-379.

Ni, Y.Q., Wang, X.Y., Chen, Z.Q., Ko, J.M., 2007. Field observations of rain-wind-induced cable vibration in cable-stayed Dongting Lake Bridge. J. Wind Eng. Ind. Aerodyn. 95, 303-328.

Nims, D., 2011. Ice Prevention or Removal on the Veteran's Glass City Skyway Cables. Interim Report.

Ohshima, K., Nanjo, M., 1987. Aerodynamic Stability of the Cables of a Cable-Stayed Bridge Subject to Rain (A Case History of the Ajigawa Bridge). In: 3rd US-Japan Bridge Workshop, Tsukuba, Japan.

Persoon, A.J., Noorlander, K., 1999a. Full-scale measurements on the Erasmus Bridge after rain/wind induced cable vibrations. In: Larsen, A., Larose, G.L., Livesey, F.M. (Eds.), Wind Engineering into the 21st Century.

Peil, U., Dreyer, O., 2007. Rain-wind induced vibrations of cables in laminar and turbulent flow. Wind and Structures 10, 83-97.

Robertson, A.C., Taylor, I.J., 2007. Effect of rivulets on a circular cylinder unsing a 2D discrete vortex method. In: 12th International Conference on Wind Engineering, Cairns, Australia, pp. 863-870.

Saito, T., Matsumoto, M., Kitazawa, M., 1994. Rain-wind excitation of cables on cable-stayed Higashi-Kobe Bridge and cable vibration control. In: International Conference on Cable-Stayed and Suspension Bridges (AFPC), vol. 2. Deauville, France, pp. 507-514.

Schewe, G., 1983. On the force fluctuations acting on a circular cylinder in crossflow from subcritical up to transcritical Reynolds number. J. Fluid Mech., 133, 265-285.

Scruton, C., 1963. Introductory review of wind effects on buildings and structures. In: 1st International Conference Wind Engineering, Teddington.

Solari, G., 1994. Gust-excited vibrations. In: Wind-excited vibrations of structures, Sockel, H., Ed. Springer Verlag, Wien, 195-291.

Strømmen, E., 2010. Theory of Bridge Aerodynamics. Third Edition, Springer.

Svensson, B., Emmanuelsson, L., Svensson, E., 2004. Oresund Bridge-Cable system. Vibration incidents, mechanisms and alleviating measures. In 4th International Cable Supported Bridge Operators Conference, Copenhagen, pp. 99-108.

Tubino, F., 2005. Relationships among aerodynamic admittance functions, flutter derivatives and static coefficients for long span bridges. J. Wind Eng. Ind. Aerodyn. 93, 929-950.

Van der Hoven, I., 1957. Power spectrum of wind velocity fluctuations in the frequency range from 0.0007 to 900 cycles per hour. J. Meteor, 14, 1254-1255.

Verwiebe, C., Ruscheweyh, H., 1998. Recent research results concerning the exciting mechanisms of rain-wind induced vibration. J. Wind Eng. Ind. Aerodyn., 74-76, 1005-1013.

Vincentsen, L.J., Lundhus, P., 2007. The Øresund and the Great Belt links Experience and Developments. In: IABSE Symposium Report, 93 (30), pp. 1-8.

Wang, Z.J., Zhou, Y., Huang, J.F., Xu, Y.L., 2005. Fluid dynamics around an inclined cylinder with running water rivulets. J. of Fluid and Structures 21, 49-64.

Virlogeux, M. Cable vibrations in cable-stayed bridges. In: Bridge Aerodynamics, Balkema, 213-233.

Wagner, P., Fuzier, J.P., 2003. Health monitoring of structures-which solutions. Dissemination of the results of the IMAC European Project. In: 5th Int. Symposium on Cable Dynamics, Santa Margherita Ligure, pp. 333-340.

Wianecki, J., 1979. Cables wind excited vibrations of cable-stayed bridges. In: 5th Int. Conf. of Wind Eng., Colorado, Oxford-New York, Pergamon Press, pp. 1381-1393.

Xu, L.S., Ge, Y.J., Zhao, L., 2009. Experimental investigation of rain-wind-induced vibration of stay cables based on high precision raining machine. In: The Seventh Asia-Pacific Conference on Wind Engineering, Taipei, Taiwan.

Yamaguchi, H., 1990. Analytical study on the growth mechanism of rain vibration of cables. J. Wind Eng. Ind. Aerodyn. 33, 78-80.

Yoshimura, K., Tanaka, C., Sasaki, N., Nakatani, S., Higa, S., 1988. Rain-Wind Induced vibration of the cables of the Aratsu Bridge. In: 10th National Symposium on Wind Engineering, pp. 127-132.

Zdravkovich, 1997. Flow around circular cylinders. Volume 1: Fundamentals. Oxford University Press.

Zhan, S., Xu, Y.L., Zhou, H.J., Shum, K.M., 2008. Experimental study of wind-rain-induced cable vibration using a new model setup scheme. J. Wind Eng. Ind. Aerodyn. 96, 2438-2451.

Zuo, D., Jones, N., Main, J., 2008. Field observation of vortex- and rain-wind-induced stay-cable vibrations in a three-dimensional environment. J. Wind Eng. Ind. Aerodyn. 96, 1124-1133.

Zuo, D., Jones, N., 2010. Interpretation of field observations of wind- and rain-wind-induced stay cable vibrations. J. Wind Eng. Ind. Aerodyn. 98, 73-87.

Chapter 3

Static wind tunnel tests

The results presented in this chapter are taken from the paper *Effects of bridge cable surface roughness and cross-sectional distortion on aerodynamic force coefficients*, G. Matteoni, C.T. Georgakis, published in the Journal of Wind Engineering and Industrial Aerodynamics 2012, (104-106) 176-187.

Abstract

Theoretical and experimental investigations to date have assumed that bridge cables can be modelled as ideal circular cylinders and the associated aerodynamic coefficients are invariant with the wind angle-of-attack. On the other hand, bridge cables are normally characterized by local alterations of their inherent surface roughness and shape, which might present a significant disturbance for the surrounding wind flow. The present study focuses on the experimental determination, based on static wind tunnel tests, of the aerodynamic coefficients of full-scale bridge cable section models both perpendicular and inclined to the flow, for varying wind angles-of-attack. The wind tunnel test results demonstrate that the aerodynamic coefficients of bridge cables can be significantly affected by the wind angle-of-attack.

3.1 Introduction

When modeling bridge cables for theoretical and experimental investigations, they are often assumed to be perfectly circular cylinders, belonging to a class of bodies which are termed *semi-aerodynamic*. In contrast to aerodynamic bodies, such as airfoils, which avoid flow separation, and non-aerodynamic bodies with sharp edges, such as squares, which have fixed flow separations at some of the corners, for semi-aerodynamic bodies the position of the separation point varies depending on the free-stream velocity, turbulence intensity and flow profile, and the geometry and roughness of the body's surface, (Niemann and Hölscher, 1990). For disturbance-free and ideal 2D flow conditions, the Reynolds number is the governing parameter of the transitions which occur in the disturbed regions of the flow around a circular cylinder, i.e. the wake, in the shear layer and the boundary layer. The lower and upper limits of the Reynolds numbers where such transitions occur show considerable hysteretic effects which depend on whether the flow velocity is increased or decreased, (Zdravkovich, 1997). On the other hand, real flows around actual cylindrical structures, such as bridge cables, are affected by a wide variety of surface disturbances and shape deviations, which are non-uniformly distributed along their surface. High density polyethylene (HDPE) tubing is commonly used to cover the steel strands or wires of bridge cables. The tubing might be expected to exhibit local alterations of its inherent surface roughness, resulting from mechanical damage and exposure to the elements, i.e. atmospheric pollution, the sun and water. Changes in the surface roughness may also augment a cable's wettability and lead to or enhance rain-wind induced vibrations, (Flamand, 1995). Furthermore, the cross-sectional shape of the HDPE tubing usually deviates from an ideal circular cylinder, as cross-sectional distortions are first introduced during the manufacturing process and later due to the rolling or stacking of the tubing for transportation and long-term creep. Flow disturbances can initiate transitions at lower Reynolds numbers and sometimes may significantly modify the resulting flow structures (Zdravkovich, 2003), i.e. microscopic changes on the body's surface can provoke macroscopic changes in the flow around it, (Schewe, 1983).

The critical state or transition-in-boundary layer state, as identified by Zdravkovich (1997), has attracted most research attention, since it is in this range of Reynolds numbers that significant changes in the aerodynamic coefficients, provoked by changes in the flow structure, are occurring and thus conditions for potential instability are set. In particular, two discontinuous flow transitions, accompanied by symmetry breaking of the flow field, and hysteresis, have been observed, which are interpreted as bifurcations at two critical Reynolds numbers (Schewe, 1983). In the first transition, a bi-stable asymmetric flow state occurs, characterized by a first drop in the drag coefficient and the simultaneous appearance of a steady lift. The state is called bi-stable, because - if the cylinder's surface is free from disturbances - there are two possible stable states corresponding to either a positive or a negative lift force. The asymmetric flow and the related steady lift are caused by rapid transition to turbulence in the separated boundary layer and subsequent reattachment to the cylinder's surface. Thus, a closed flow region between separation and re-attachment, called separation bubble, is formed. The span wise bubble formation may thus take place on either side of the cylinder, but once established it can not change side, due to the lengthening of the boundary layer on the bubble side, which stabilizes the bubble, and the shortening of the boundary layer on the opposite side, which precludes the formation of the second separation bubble. The concept of bi-stable flow is on the other end an idealization, since in practical cases, such as in bridge cables, the cylinder's surface as seen from the flow is never perfectly symmetric. Small perturbations or surface disturbances thus affect the location of the separation bubble and the sign of the lift force (Schewe, 1986). For example, a microscopic change in cylinder shape may result in acceleration of the fluid on the side where the boundary layer transition has occurred and deceleration on the other side of the cylinder. Furthermore, early studies performed on partially roughened cylinders, showed also that the presence of local disturbances on the body's surface has the smallest effect on the structure of the flow when distributed in the stagnation region, and in the rear surface region. In contrast, the flow is particularly sensitive to local surface roughness distributed on the remaining part of the cylinder, i.e. on the critical region, where boundary layer separation is expected to occur (Fage and Warsap, 1929). The second transition is associated with a second drop in the drag coefficient, to almost half its subcritical value, together with the abrupt disappearance of the steady lift. The transition occurs after reattachment of the boundary layer on the back of the cylinder and the appearance of a second separation bubble on the opposite side of the cylinder. Here, a symmetrical flow state is re-established. On the other hand, it's also been reported that fully symmetric flow can not be reached at once, after the establishment of the second separation bubble, but a residual lift exists which is eliminated as the Reynolds number undergoes further increase (Kamiya et al., 1979).

An added complexity of the flow must be factored-in when considering a cylinder that is yawed/inclined. Further changes in the flow structure with Reynolds number and the related drag and lift coefficients occur, which are strongly affected by the relative angle between the cable axis and the wind direction, i.e. the relative cable-wind angle. It has been demonstrated that the range of Reynolds numbers where the first critical flow transition appears, i.e. drag crisis accompanied by a steady lift force, becomes significantly wider for yawed circular cylinders if compared to the same non-yawed cylinders, (Matsumoto et al., 2010). Experimental work on the aerodynamic behaviour of inclined/yawed bridge cables for varying relative cable-wind angles in static conditions is unfortunately quite sparse, with only one know experimental study performed in full scale at a selected turbulence intensity of 2.5% (Larose et al., 2005).

Several researchers have attributed the role of the critical Reynolds number range and the related transitions in the boundary layer to the occurrence of self-excited flow-induced vibrations of bridge cables in dry conditions, such as galloping. In fact, whilst never fully verified in full scale, galloping vibrations have been observed in dynamic wind tunnel tests performed on dry inclined cable section models, i.e. characterized by a nominally circular in cross section, (Cheng et al., 2008a). Assuming quasi-steady forces, unfavorable changes in the aerodynamic force coefficients, as a function of Reynolds number, might lead, for certain relative cable-wind angles, to positive velocity-proportional wind loads or negative aerodynamic damping (Macdonald and Larose, 2008a). If these forces are greater than the cable's inherent mechanical damping, large amplitude cable oscillations might develop. As cables tend to be circular in shape, most theoretical and experimental work to date assumes that the force coefficients are invariant with wind angles-of-attack. Nevertheless, this has been shown to not always hold, (Flamand and Boujard, 2009), (Matteoni and Georgakis, 2011a,b). The current work investigates the effects of surface roughness and cross-sectional distortions on the aerodynamic force coefficients of cross flow and inclined/yawed bridge cables. In order to understand this dependency, static wind tunnel tests were performed on a section of a plain prototype HDPE tube perpendicular and inclined to the incoming flow, for varying wind angles-of-attack. The tubing roughness was measured at different positions in order to quantify its variability along the model. The model roughness was compared to levels measured on the HDPE casings from the Øresund Bridge. Finally, the 3-D geometry of the tested HDPE section model was measured using a specially devised test rig that employs a laser displacement transducer. Test results showed how a direct connection exists between the distorted tube shape with an inhomogeneous surface roughness, and the obtained aerodynamic force coefficients.

3.2 Materials and Methods

3.2.1 Surface roughness and shape distortion measurements

Roughness measurements were first performed on a plain 160 mm diameter HDPE tubing used for wind tunnel testing. To verify that the overall surface roughness of the section model was similar to that of an actual bridge cable, roughness measurements were performed on three sample cables at the

Øresund Bridge in October, 2010. The specific cables have a diameter of 250 mm and their surface is plain, similarly to the tested model. The first cable is located at the deck level, whilst the second and third are located at the top of the pylon. The cables do not have any structural function, and have been installed at the bridge for research and monitoring purposes (see Fig.3.4(a)). Roughness measurements of wind tunnel and full-scale cable section models were performed using a commercial fast curing two-part silicone rubber replicating system, which allowed for the transferral of the structure of the solid cable surface to a flexible, highly accurate and stable replica. A 3D optical measurement device was then used to perform roughness analysis on the 3D-replica of the cable surface. The measurements were performed at different positions along the cable sections, in order to understand the variability of the roughness average along their surface.

The shape of the section model used for wind tunnel testing was measured using a specially devised rigid frame in which the model could be placed and rotated. An analogue laser displacement transducer, produced by WayCon, (LAS-T-40), which can be moved along a longitudinal rail, was employed to measure the cable local diameters along the length and circumference. The laser distance measurement is performed based on the triangulation principle. The model circularity should not influence the measurements, as the sensor's receiver, made of a photo diode array, is equipped with an internal micro controller, which allows a minimum of undesiderable reflections. Therefore a precise distance measurement is possible, even on surfaces with a curvature. The resolution and the diameter of the laser spot depend linearly on the distance between the laser and the target surface. In the present case, the laser-surface distance was 54 mm, which corresponds to a laser spot diameter of 0.52 mm and a resolution of 0.014 mm.

3.2.2 Wind tunnel tests

Static wind tunnel tests were performed at the new DTU/Force Climatic Wind Tunnel in Lyngby, Denmark. The wind tunnel is a close circuit with a test section size of $L \times W \times H = 5\text{ m} \times 2\text{ m} \times 2\text{ m}$. The technical specifications of the wind tunnel are reported by Georgakis et al. (2009). The tested cable section model was made of a plain HDPE tube, provided by bridge cable suppliers, with a nominal diameter of 160 mm, placed on an inner aluminum tube. The HDPE and the aluminum tube were fixed by means of screws, one at each tube end, in order to avoid any relative movement. Circular end plates with a diameter of 800 mm, i.e. 5 times the cable diameter, were provided at the cable ends, at a distance of approximately 90 mm from the from the walls, in order to minimize end effects. Aerodynamic forces were measured at both ends of the cable using 6-DOF force transducers, installed in between the cable model and the supporting cardan joints fixed to the walls. The model drag and lift forces were obtained by averaging the respective force components measured at each cable end. The force transducers were covered by HDPE dummy pieces of the same cable and a gap of approximately 2 mm was allowed between the cable model and the dummy pieces.

In Fig. 3.1 the geometrical attitude of the cable section model in the wind tunnel test chamber is described. (X, Y, Z) is a global cartesian coordinate system, with Y parallel to the along-wind velocity U. (x, y, z) is the cable local coordinate system, z being parallel to the cable's longitudinal axis, and xy belonging to the cross-sectional plane perpendicular to the z axis. The cable's geometrical attitude to the wind is thus identified by the relative cable-wind angle Φ, i.e. the angle between the wind direction and the cable axis, obtained by combining the vertical cable inclination Θ and the horizontal yaw β. The wind angle-of-attack, α, identifies the degree of axial rotation of the cable model, i.e. is the angle formed by the projection of the along-wind velocity in the xy plane, U', and the y axis, so that

$$U' = U\sqrt{\sin^2\beta + \sin^2\Theta\cos^2\beta} \tag{3.1}$$

In cross-flow, ($\Theta = 0°$, $\beta = 90°$, or $\Theta = 90°$, $\beta = 0°$), $U' = U$.

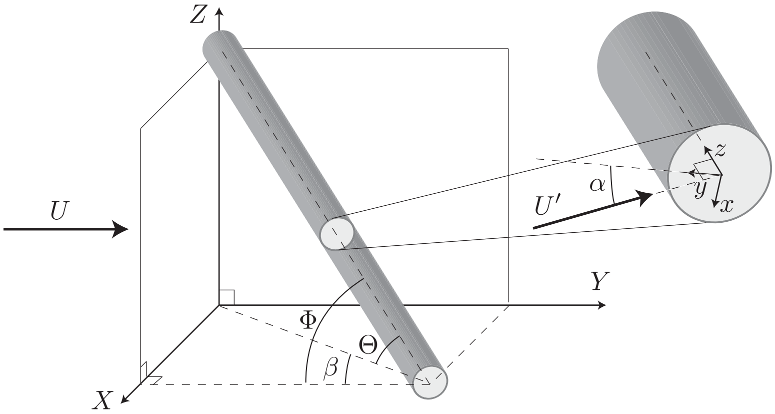

***Figure 3.1**: Cable geometry in the wind tunnel.*

The cable model was designed so to allow axial rotation of the HDPE tube leaving the remaining components, force transducers included, in their original geometrical configuration. For this purpose, the aluminum tube was provided with a set of 12 holes at each end, whose centers were placed at an angular distance of 30°, 25 mm from the tube edge. The HDPE tube was provided with only 1 hole at each end, 25 mm from the edge, in order to minimize disturbance to the wind flow. After releasing the bottom and top screws, the HDPE tube could be axially rotated and fixed to a new position at $30i°$, $i = 0, 2, ...12$, from the original position, thus leading to a change in the cable surface directly exposed to the wind, i.e. a change in the wind angle-of-attack α (see Fig. 3.1).

Test were performed in cross and inclined flow. In all tests the wind velocity was increased incrementally by approximately 1 m/s, spanning the interval of 2 to 31 m/s, corresponding to Reynolds numbers of 1.8×10^4 to 3.2×10^5. The turbulence intensity was measured by use of a TFI Cobra probe in the empty tunnel, at a cross-section located in the geometrical center of the test chamber. Measurements were undertaken at 50 cm intervals, horizontally and vertically, and for varying wind velocities. The turbulence intensity was found to be uniform across the test section, with values of $I_u = 0.4, 0.5, 0.6\%$ for $U = 10.33, 20.67, 31$ m/s. Hereforth, this flow condition, will be identified as $I_u = 0.5\%$ referring to the turbulence intensity measured at two-third of the maximum achievable wind velocity.

Cross flow tests were undertaken using a section model of length 1.528 m, placed in the geometrical center of the test section in a horizontal position, i.e. resulting in an inclination of $\Theta = 0°$ and yaw $\beta = 90°$, leading to a relative cable-wind angle of $\Phi = 90°$. The model aspect ratio was 9.55:1. Fig. 3.2(a) shows the test configuration in cross flow. In order to understand the effect of the model's non-uniform distribution of surface roughness and shape on the aerodynamic coefficients, cross-flow wind tunnel tests were undertaken for 12 selected cable-wind angles-of-attack, α, at intervals of 30°, in the range of 0°-330°. This was achieved by rotation of the HDPE tubing about its longitudinal axis. For each tested angle-of-attack, α, the drag CD and lift CL coefficients were calculated, based on the averaged along-wind and across-wind forces normalized by the along-wind flow velocity. Tests were performed in smooth flow, for a uniform turbulence intensity of $I_u = 0.5\%$. Tests were also performed at an increased level of turbulence intensity in cross flow. Cobra probe measurements performed at a cross-section located in the geometrical center of the test chamber revealed a uniform along-length turbulence intensity of $I_u = 1.0, 1.1, 1.13\%$ for $U = 10.33, 20.67, 31$. This latter flow condition, will be identified as $I_u = 1.1\%$ referring to the turbulence intensity measured at two thirds of the maximum achievable wind velocity. Note that this increased turbulence intensity was achieved through the presence of a partial grid.

Inclined tests were performed in order to understand the dependency of the aerodynamic coefficients on the relative cable-wind angle Φ. Two cable models with vertical inclination $\Theta = 40°$ and 55°, corresponding to a length

(a) (b)

***Figure 3.2**: Cross flow test configuration (a) and inclined test configuration (b).*

of 1.93 m and 2.45 m and aspect ratios of 12 and 15 respectively were adopted. By combining the cable's vertical inclination with the horizontal yaw, relative cable-wind angles Φ in the range of $40° - 75°$, at intervals of $\Delta\Phi = 5°$, were investigated. Fig. 3.2(b) shows the test setup for cable inclination 55° and yaw $\beta = 30°$, leading to a relative cable-wind angle of $\Phi = 60°$. The drag and lift coefficient components normal to cable axis were thus calculated, based on the averaged force components belonging and perpendicular to the cable-wind plane respectively, and normal to cable axis. The force components were thus normalized by the along-wind flow velocity component. All tests were performed with a uniform longitudinal turbulence intensity along the cable axis of $I_u = 0.5\%$.

For one selected relative cable-wind angle, i.e. $\Phi = 60°$, considered most prone to instability based on previous investigations (Cheng et al., 2008a) the dependency of the measured force coefficients on the wind angle-of-attack α was also tested.

3.3 Results and Discussion

3.3.1 Surface roughness and shape distortion measurements

Figs. 3.3(a) and 3.3(b) show digital versions of the 3-D replicas reproduced on two separate regions of the cable model surface. Note that, the replicas were acquired prior to wind tunnel tests on the cable model installed in cross flow. Thus, the horizontal direction of the replicas is shown to be parallel to the direction of extrusion of the material, whilst the vertical direction is parallel to the wind flow.

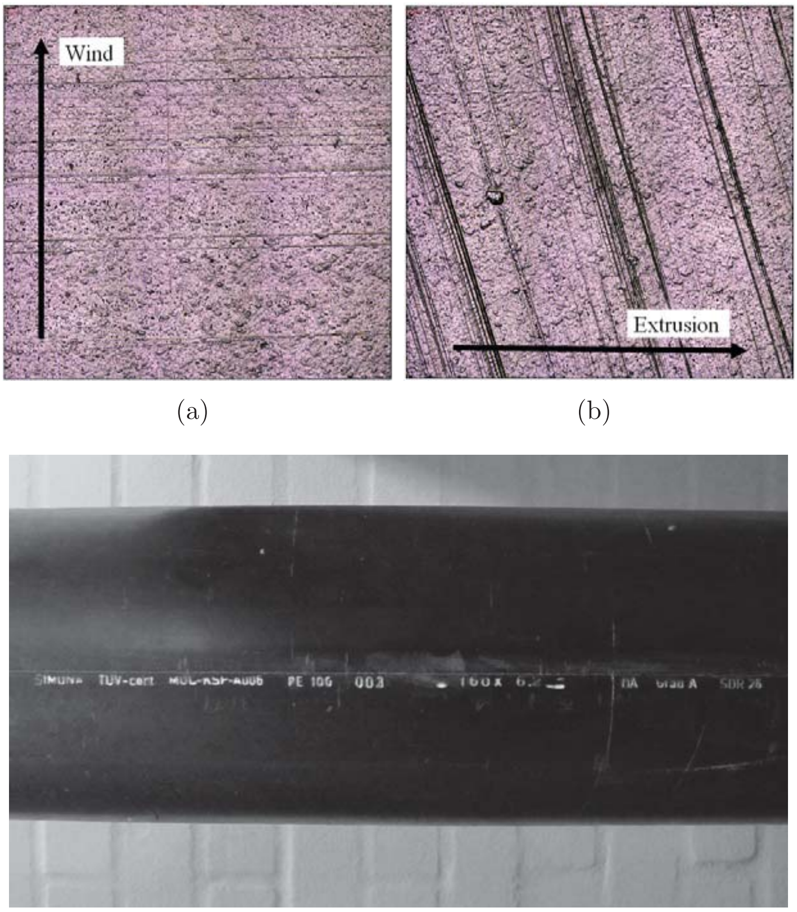

(a) (b)

(c)

Figure 3.3: *Cropped* $4{\times}4\ mm^2$ *surface replica of the 3D cable model installed in the wind tunnel test section in cross-flow (a and b), and roughness labeling (c).*

The HDPE tubing roughness is quantified in the along-wind direction by the roughness average Ra parameter:

$$R_a = \frac{1}{n}\sum_{i=1}^{n}|y_i^2| \tag{3.2}$$

where n is the number of equally spaced data points along the profile, and $|y_i^2|$ is the absolute value of the vertical distance from the mean line of the i^{th} data point. For each cable surface replica, the mean value of the measured


(a) (b)

***Figure 3.4**: Deck level cable section at the Øresund bridge (a) and evidence of local alterations of surface roughness (b).*

roughness average Ra along several profiles in the along wind direction is reported. The measured roughness average in the wind flow direction is Ra = 1.836 μm for the replica in Fig. 3.3(a) and Ra = 2.051 μm for the replica in Fig. 3.3(b). The roughness average measured on the two replicas is higher than in regions of the cable which appear almost undamaged and where the measured roughness average Ra ranges between 0.7 μm and 0.8 μm. A 4 mm wide indented commercial label was distributed along the length of the HDPE tubing, which further added to the tubing roughness locally, see Fig. 3.3(c). The height of indentation was not constant but ranged in the interval of 50 μm to 100 μm, thus the ratio of the indentation height to the cable surface height varied from a minimum of 50 to a maximum of 100.

Roughness measurements performed on cable sections at the Øresund bridge showed that the surface roughness was altered from its original state due to mechanical degradation. At the time the measurements were performed, no deposited pollutants were observed on the surface. The roughness average, Ra, measured along the length of the tubing and in regions of the cable that have not been mechanically damaged, was in the range of 0.7-1 μm. This is broadly in agreement with results of preliminary roughness measurements performed on the Second Severn Crossing Bridge (Macdonald, 2011). Where major mechanical degradation was observed, significant increases of surface roughness were measured, often leading to Ra values in the region of 4-5 μm. Fig. 3.4 shows the investigated cable at the deck level.

Shape measurements showed that the cable is nearly circular, with small-scale deviations in the local diameter along the length. A maximum diameter deviation of 1.25% (1 mm) from its nominal value was measured, see Fig. 3.5(b).

3.3.2 Wind tunnel tests

Cross flow

The model blockage ratio in cross flow was 8%. Drag coefficients were thus corrected for blockage following Maskell III Method, (Cooper et al., 1999). Measured drag and lift coefficients, CD and CL, for 12 selected angles-of-attack, α, at intervals of 30°, i.e. positions $30i°$, $i = 0, 1, 2, ..., 11$, and turbulence intensities of $I_u = 0.5\%$ and 1.1%, are presented in Figs. 3.6 and 3.7. Test results are grouped for symmetric axial rotations of the cable model about the position $\alpha = 0°$. Fig. 3.5(a) shows the wind rose, with the circle representing the perimeter of the cable model.

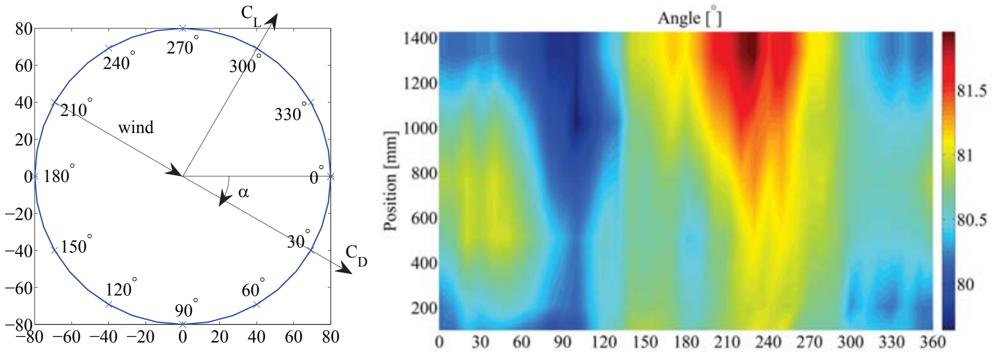

(a) (b)

***Figure 3.5**: Wind rose (a) and horizontal projection of the cable model radius (b).*

For the tested levels of turbulence intensity, and for the current cable diameter, the wind tunnel performance allows three flow regimes to be captured: subcritical, critical and the initiation of the supercritical regime. These three flow regimes can be identified from the drag and lift coefficient curves. Generally, it is observed that the same model exhibits variations in both the drag and lift coefficient with Reynolds number for varying wind angles-of-attack α and turbulence intensities I_u. In particular, for a fixed level of turbulence intensity, although drag coefficients are fairly consistent (with some exceptions), the same model exhibits large variations in the lift coefficient with Reynolds number for varying angle-of-attack. The perfect repeatability of the results for tests performed at the same angle-of-attack and the lack of repeatability when the cable is axially rotated, thus indicates that local roughness and shape distortion play a role in modifying the flow structure around the cable and in anticipating/delaying flow regimes. Moreover, for a given wind angle-of-attack, the role of turbulence intensity is to promote earlier flow transitions.

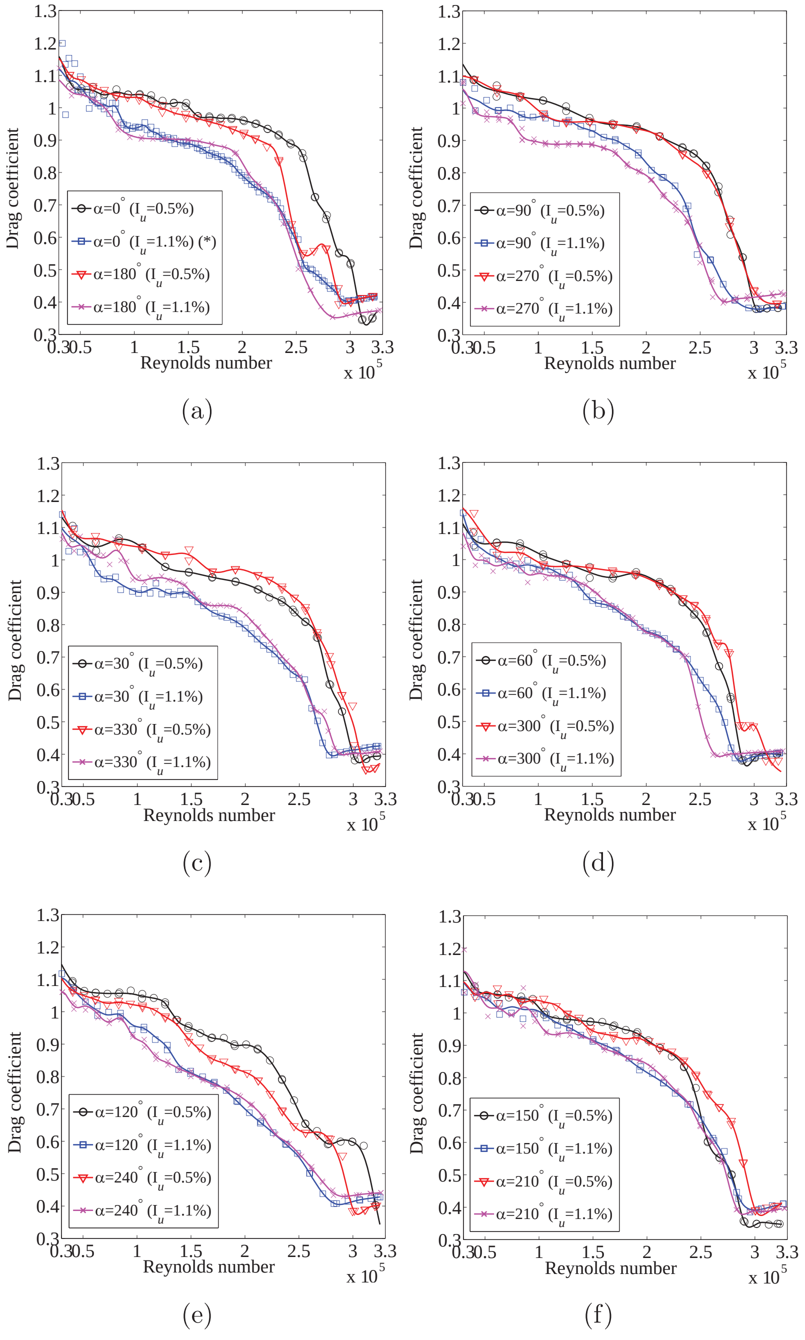

(a) (b)

(c) (d)

(e) (f)

Figure 3.6: *Drag coefficients over the tested wind angles-of-attack* α, $I_u = 0.5\%$ *and* 1.1%. *(*) from (Kleissl and Georgakis, 2011)*

For the lower turbulence intensity of $I_u = 0.5\%$, the duration of the

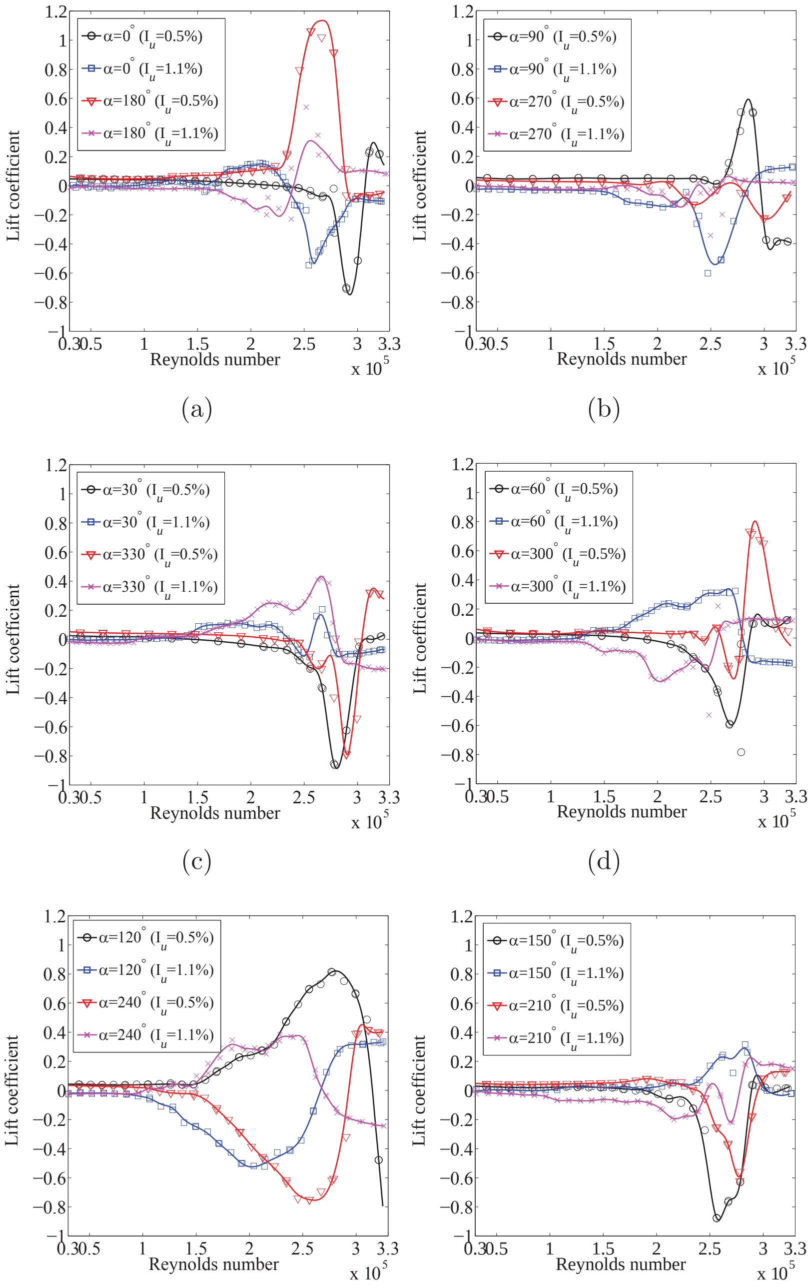

(a) (b)

(c) (d)

(e) (f)

Figure 3.7: *Lift coefficients over the tested wind angles-of-attack* α, $I_u = 0.5\%$ *and* 1.1%.

subcritical and critical regimes, is strongly dependent on the tested wind angle-of-attack. In particular, the upper limit of the subcritical regime, i.e.

the Reynolds number marking transition to critical, identified by the appearance of a steady lift, and the simultaneous drop in the drag coefficient, ranges in the interval of $Re = 1 - 2.7 \times 10^5$. In contrast, the upper limit of the critical regime, made evident by the recovery of the drag coefficient, after the crisis, and the occurrence of a constant lift equal or close to zero, ranges in the interval of $Re = 3 - 3.22 \times 10^5$. Larger consistency in the upper, rather than in the lower limit of the critical Reynolds number regime for varying angles-of-attack, implies that, for the test cases where the critical regime is initiated earlier, the regime lasts for a broader total range of Reynolds number. This effect is particularly evident for the test cases $\alpha = 120°$ and $\alpha = 240°$, (see Figs.3.6(e) and 3.7(e)), where a large lift develops over a range of $Re = 1.04 \times 10^5 - 3.21 \times 10^5$ ($\alpha = 120°$), and $Re = 1.06 \times 10^5 - 3.12 \times 10^5$ ($\alpha = 240°$), and is accompanied by a continuously dropping drag, significantly lower, through the whole critical Re range, than for other tested angles-of-attack. It should be noted that for these two test cases, an indented commercial label, distributed along the full length of the HDPE tubing, which increases the surface roughness of the tubing locally, is placed at 60° clockwise (for $\alpha = 120°$) and 60° counterclockwise (for $\alpha = 240°$) from the flow stagnation line. The role of the labeling roughness in triggering flow transitions is furthermore confirmed by the observed opposite sign of the lift coefficient for the two tested angles-of attack. Based on the development of the drag coefficient curves in Fig.3.6(e), it is assumed that the role of the indented labeling is similar to that of a tripping wire installed on the surface of a circular cylinder at a critical angular position from the stagnation line, (Igaraschi, 1986a). Igaraschi (1986a) in fact demonstrated that the boundary layer upstream of a tripping wire first decelerates, then separates, and finally forms an upstream separated region. A second separation takes place from the tripping wire itself, thus forming a downstream separated region. The downstream and upstream separated regions represent two consecutive separation bubbles occurring on the same side of the model which re-attach respectively at the tripping wire and at the cable surface position. This flow structure leads to a significant decrease of the drag coefficient when compared to the a smooth cable. Unfortunately, Igaraschi (1986a) did not present the lift coefficient. The smallest tripping wire size used by Igaraschi (1986a), which provoked this aerodynamic effect was 0.4 mm thick, thus 4 times thicker than the maximum height (Ra) of the commercial indentation. Although thinner than Igarashi's tripping wire, the commercial label must play a role in disturbing the flow around the cable, given the trend of the drag and the lift curves in Figs.3.6(e) and 3.7(e), i.e. a significant decrease of the drag coefficient though the whole critical Re range, similar to that described by Igaraschi (1986a), accompanied by a large lift, which doesn't return to zero, after the end of the critical *Re* range. Finally it should be noted that, since at low Reynolds numbers surface irregularities of a microscopic extent are normally completely embedded in the boundary layer, the localized roughness begins to play a role in triggering flow separation and reattachment only when its thickness overcomes the thickness of the boundary layer. The observed drag and lift tendencies in Figs. 3.6(e) and 3.7(e) seem to suggest that the thickness of the label and the accompanying flow structure produced by it overcome the thickness of the boundary layer at lower Reynolds number than for other tested wind angles-of-attack. For the other tested angles-of-attack, it is apparent that minor disturbances in the cable's shape and roughness trigger the generally observed narrow lift accompanied by a typical steep crisis of the drag coefficient in the critical range. Given the non-perfect circularity of the cable model, symmetric flow conditions may never be achieved in the supercritical range. This is clearly indicated by the non-zero lift, accompanied by a recovery of the drag coefficient after the crisis.

At the increased turbulence intensity of $I_u = 1.1\%$, a change is experienced in the magnitude of the drag and lift coefficients due to the general role of the turbulence intensity in triggering earlier transitions in the flow regimes. The angle-of-attack dependency of the aerodynamic coefficients is still significant. It is interesting to observe that for $\alpha = 120°$ and $\alpha = 240°$, (see Figs.3.6(e) and 3.7(e)), a large magnitude lift coefficient over a wider range of Reynolds number, accompanied by a continuously decreasing drag, still persists as found for the turbulence intensity of $I_u = 0.5\%$. Moreover, due to the increased turbulence intensity, the corresponding Reynolds number for the development of the lift coefficient is lower. After the end of the critical Re range, the lift doesn't stabilize to zero due to the non-establishment of symmetric flow.

The mean drag and lift coefficients for the tested angles-of attack range, $\alpha = 0° - 330°$, and for the two levels of turbulence intensity, $I_u = 0.5\%$ and 1.1%, are presented in Figs. 3.8.

The mean drag coefficient can more readily be used for design or theoretical analysis purposes. On the other hand, the actual lift coefficient of the cable model is not well represented by its average through the tested angle-of-attack range. The mean lift coefficient is instead representative of the distribution of surface disturbances over the cable model, and of how these surface disturbances are effective in changing the the aerodynamic behavior of the cable model for varying angles-of-attack. For the two tested levels of turbulence intensity, the mean lift coefficient is very close to zero for the full range of Reynolds numbers except in the critical region. It is unlikely that a mean zero lift could be expected throughout the full range of Reynolds

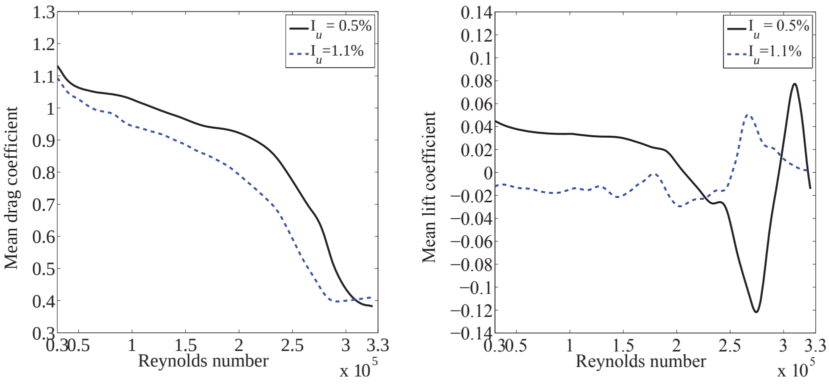

(a) (b)

Figure 3.8: *Mean drag coefficient (a) and mean lift coefficient (b) over the tested wind angles-of-attack* α*,* $I_u = 0.5\%$ *and* 1.1%*,* $\Phi = 90°$*.*

numbers. Even in the ideal case of a perfectly symmetrical cable model, free from disturbances on its surface, a zero averaged lift coefficient isn't likely to occur due to the establishment of the bi-stable flow, i.e. the random formation of the first separation bubble on either side of the cable and thus the lack of repeatability of the sign of the lift coefficient. On the other hand, if the cable model is characterized by a surface disturbance, like a microscopic protuberance, located on only one side of its surface and at a certain angular position from the stagnation line, the first separation bubble will occur on either side of the cable's surface, in such a way that the disturbance will lie in the critical area of the cable. The resulting lift coefficients will be of opposite signs and the resulting average will be zero, given the assumption that the positive and negative magnitude of the experienced lifts are equal in absolute value. On the other hand, when the axial rotation is such that the protuberance is located out of the critical area, random bi-stable flow will occur. Thus the total average lift will not be zero. Finally, for an actual cable with an non-uniform distribution of surface roughness the average behavior is more complicated, and no prediction can be made.

Inclined cable

The wind-tunnel blockage was lower than 2% in all of the inclined cable tests. Therefore, no correction was performed for blockage. The drag and lift coefficient components, normal to cable axis, for varying relative cable-wind angles Φ, are presented in Fig. 3.9.

The drag and lift coefficient components are determined based on the mean the free stream velocity component U. In the subcritical Reynolds

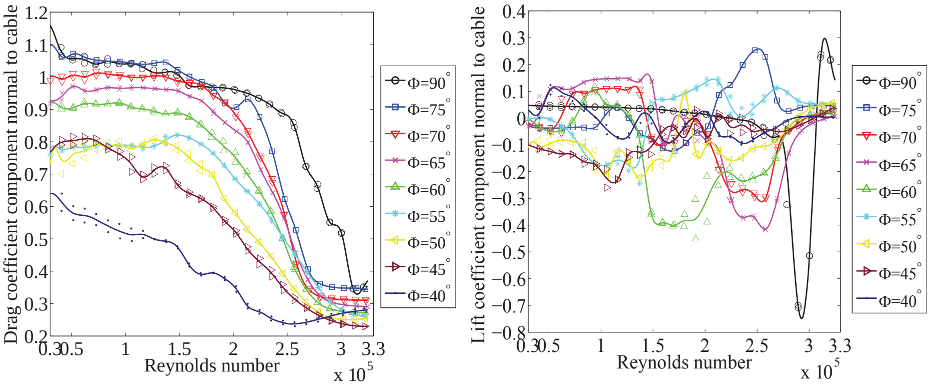

(a) (b)

Figure 3.9: *Drag coefficient component normal to cable axis (a) and lift coefficient component normal to cable axis (b) for varying relative cable-wind angles* Φ, $I_u = 0.5\%$.

number range, the drag coefficient components normal to cable axis are generally increasing, as the relative cable-wind angle Φ increases. Contrary to this, the lift coefficient components normal to cable axis are generally close to zero. The initiation of the critical Reynolds number range, made evident by a drop in the drag coefficient component accompanied by the appearance of a lift coefficient component, occurs as expected, as the relative cable-wind angle Φ decreases. For $\Phi = 40°$, $45°$, and $50°$, the slope of the drag coefficient component normal to cable-axis during the crisis is lower than for other test cases. Moreover, the lift coefficient component normal to cable axis is closer to zero in comparison to the other tested Φ angles throughout all the investigated Reynolds number ranges. When comparing the aerodynamic behavior of the remaining relative cable-wind angles, i.e. $\Phi = 55° - 75°$, it is apparent that the highest slope in the drag coefficient component is experienced for $\Phi = 65° - 75°$. Additionally for these angles, the critical Re range, from $Re \approx 2 - 3 \times 10^5$, is characterized by the appearance of a large lift coefficient component. Relative cable-wind angle $\Phi = 60°$ is characterized by a lift coefficient component normal to cable axis occurring over a much wider range of Reynolds numbers, accompanied by a slightly lower slope of for the drag coefficient component normal to cable axis in the critical Re region.

Larose et al. (2005) conducted wind-tunnel tests on a full scale yawed cable model, whose ends where fitted with half spheres. Tests were performed for the same total range of Reynolds number as the present tests, but at an increased turbulence intensity level, $I_u = 2.5\%$. Even if a direct comparison with the present results can not be established due to different test conditions, it is generally observed that the magnitude and the features of the drag and lift coefficient component curves are similar between the two test campaigns. In particular, the general tendency of drag component to increase with increasing relative cable-wind angle Φ and the non-zero lift through the full tested range of Reynolds number can be observed.

Based on dynamic and static tests undertaken on full-scale and scaled models respectively, Cheng et al. (2008a) predicted that a cable declining in the wind direction, and characterized by a relative cable-wind angle $\Theta = 60°$, may undergo divergent-type motion. It is for this reason that detailed wind angle-of-attack and Reynolds number sweeps have been performed for this angle. Figs. 3.10 and 3.11 show the measured drag and lift coefficient components normal to cable axis for $\Phi = 60°$ and varying wind angles-of-attack, for a turbulence intensity $I_u = 0.5\%$. As experienced for the cross-flow case, the drag coefficient component normal to cable axis remains fairly consistent, while the lift coefficient component normal to cable axis exhibits

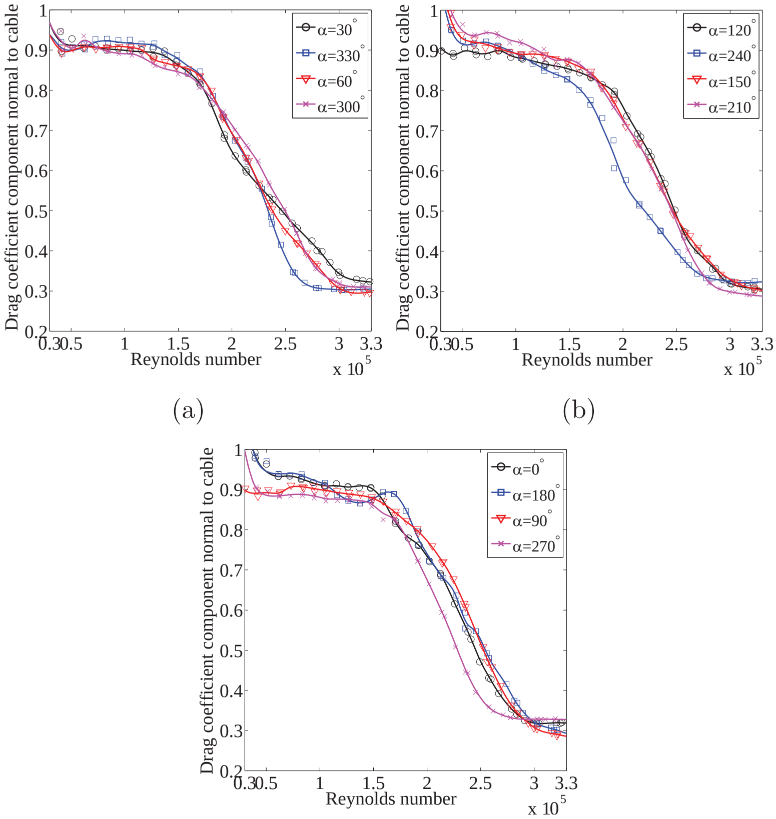

(a) (b)

(c)

***Figure 3.10**: Drag coefficient component normal to cable axis for varying wind angles-of-attack α, $\Phi = 60°$ and $I_u = 0.5\%$.*

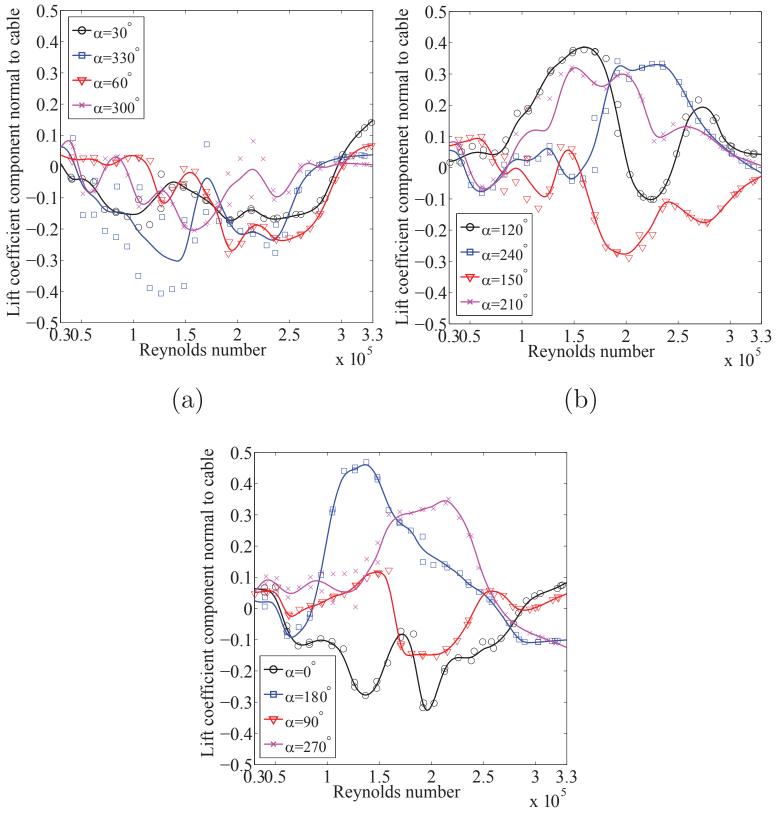

(a)

(b)

(c)

***Figure 3.11**: Lift coefficient component normal to cable axis for varying wind angles-of-attack α, $\Phi = 60°$ and $I_u = 0.5\%$.*

large variations as the wind angle-of attack is changed. For Reynolds number in the range of $Re \approx 1.5 - 2 \times 10^5$, the drag coefficient components are in the critical Reynolds range, for all tested angle-of-attack. The crisis here is quite abrupt, i.e. the negative slope of the drag component curve is quite large in absolute value. This implies that the significant decrease in the drag coefficient component from the subcritical value of approximately 0.9 to the end-of-critical-range value of approximately 0.3, could occur within a small region of Reynolds numbers. The decrease in the drag coefficient component was accompanied by a non-zero lift. In particular as the angle-of-attack changes, large variations of the measured lift coefficient component with the wind angle-of-attack occur, either in sign or in amplitude.

The mean drag and lift coefficient component normal to cable axis over the full tested range of angle-of-attack, $\alpha = 0° - 330°$, for a turbulence intensity $I_u = 0.5\%$, are shown in Fig. 3.12. Again, while the drag coefficient component could be used for design or theoretical analysis, the mean lift coefficient component is only a representation of the average effect of surface irregularities on the cable's aerodynamic response.

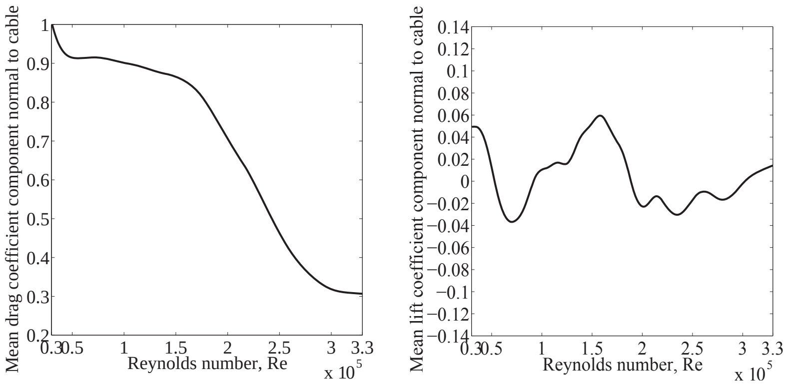

(a) (b)

Figure 3.12: *Mean drag coefficient component (a) and mean lift coefficient component (b) normal to cable axis over the tested wind angles-of-attack* α, $\Phi = 60°$ *and* $I_u = 0.5\%$.

Force correlation and repeatability

The averaged drag and lift forces measured at each cable end were used to determine the cable's drag and lift coefficients. In cross-flow and in the subcritical range, the measured drag and lift forces at either ends of the cable generally follow each other, with a maximum deviation of approximately 1% for the tested range of wind angles-of-attack α. More significant deviations are observed in the critical Reynolds number range where the cable end forces differ up to 10%. For the inclined/yawed test cases, the drag and lift force components again follow each other, with deviations though in the order of $10 - 15\%$ in the critical Reynolds number range. These deviations extend in certain cases into the subcritical range for the lift force. It is conjectured that variations in the measured aerodynamic forces along the model are due to the non-uniform distribution of surface disturbances, which trigger, in the critical Reynolds number range, a variation in the spacial structure of the flow along the cable. The three dimensional character of the flow structure around inclined cables, has also been reported by Larose et al. (2003) and has been considered responsible, together with critical Reynolds number effects, for potential aerodynamic instabilities.

Test repeatability has been checked by performing each test, i.e. Reynolds number sweeps for a selected relative cable-wind angle Φ and wind angle-of-attack α, at least twice in one day. In Figs. 3.6-3.7, 3.9, 3.10-3.11, data points from the first and second test repetition performed in the same day are reported for each test case. As can be observed, the degree of data repeatability is very high. A check on the repeatability was performed by repeating Reynolds number sweeps, for selected relative cable-wind angles and wind angles-of-attack, several days after the first tests. The same degree of data repeatability could be obtained.

3.4 Conclusion

Bridge cable force coefficients based on wind tunnel tests should not necessarily be regarded as invariant with wind angle-of-attack. Static wind tunnel tests conducted in cross and inclined flow for a short bridge cable model, characterized by a non-uniform distribution of surface roughness and shape, demonstrate that significant variations in the aerodynamic coefficients can be observed for varying wind angles-of-attack. These changes in the aerodynamic coefficients can be triggered by small geometrical imperfections of the cable model, such as surface roughness alterations or distortions of the shape. Assuming the validity of the quasi-steady theory, negative aerodynamic damping can be predicted in the critical Reynolds number range where the drag coefficient is reduced to its minimum and the lift coefficient experiences significant oscillations in sign and amplitude with angle-of-attack.

Note that, although important for theoretical modeling and section model testing, variations in the drag and lift coefficients with wind angle-of-attack may not ultimately be important when averaged over the full length of an inclined structural cable.

Bibliography

Cheng, S., Larose G.L., Savage, M., Tanaka, H., Irwin, P., 2008a. Experimental study on the wind-induced vibration of a dry inclined cable - Part I: Phenomena. J. Wind Eng. Ind. Aerodyn. 96 (12), 2231-2253.

Cooper, K., Mercker, E., Wiedemann, J., 1999. Improved blockage corrections for bluff-bodies in closed and open wind tunnels. In: 10th International Conference Wind Engineering, Copenhagen, pp. 1627-1634.

Fage, A., Warsap, G.H., 1929. The effects of turbulence and surface roughness on the drag of a circular cylinder. Brit. Aero. Res. Council, 1283.

Flamand, O., 1995. Rain-wind induced vibrations of cables. J. Wind Eng. Ind. Aerodyn. 57 (2/3), 353-362.

Flamand, O., Boujard, O., 2009. A comparison between dry cylinder galloping and rain-wind induced excitation. In: 5th European and African conference on wind engineering, Florence, pp. 485-488.

Georgakis, C.T., Koss, H.H., Ricciardelli, F., 2009. Design specifications for a novel climatic wind tunnel for testing of structural cables. In: 8th International Symposium on Cable Dynamics, Paris, pp. 333-340.

Igarashi, T., 1986a. Effect of tripping wires on the flow around a circular cylinder normal to an airstream. Bull. JSME 28, 2917-2924.

Kamiya, N., Suzuki, S., Nishi, T., 1979. On the aerodynamic force acting on a circular cylinder in the critical range of Reynolds number. In: AIAA meeting, paper79-1975.

Kleissl, K., Georgakis, C.T., 2011. Preliminary comparison of static wind tunnel tests of bridge cables with helical fillets and a pattern-indented surface. In: 13th International Wind Engineering Conference, Amsterdam.

Larose, G.L., Jakobsen, J.B., Savage, M.G., 2003. Wind-tunnel experiments on an inclined and yawed stay cable model in the critical Reynolds number range. In: 5th International Symposium Cable Dynamics, Santa Margherita Ligure, pp. 279-286.

Larose, G.L., Zasso, A., Giappino, S., 2005. Experiments on a yawed stay cable in turbulent flow in the critical Reynolds number range. In: 6th International Symposium Cable Dynamics, Charleston, pp. 279-286.

Macdonald, J.HJ., Larose G.L., 2008a. Two-degree-of-freedom inclined galloping - Part 1: general formulation and solution for perfectly tuned system. J. Wind Eng. Ind. Aerodyn. 96 (3), 291-307.

Macdonald, J.HJ., Private communication. University of Bristol, U.K.

Matsumoto, M., Yagi, T., Hatsuda, H., Shima, T., Tanaka, M., 2010. Dry galloping characteristics and its mechanism for yawed/inclined cylinders. J. Wind Eng. Ind. Aerodyn. 98 (6/7), 317-327.

Matteoni, G., Georgakis, C.T., 2011. Effects of bridge cable surface roughness and cross-sectional distortion on aerodynamic force coefficients. In: 13th International Wind Engineering Conference, Amsterdam.

Matteoni, G., Georgakis, C.T., 2011. Aerodynamic coefficients of dry inclined cables in smooth flow. In: 9th International Symposium on Cable Dynamics, Shanghai, pp. 365-372.

Niemann, H.-J., Hölscher, N., 1990. A review of recent experiments on the flow past circular cylinders. J. Wind Eng. Ind. Aerodyn. 33 (1/2), 197-209.

Schewe, G., 1983. On the force fluctuations acting on a circular cylinder in crossflow from subcritical up to transcritical Reynolds numbers. J. Fluid Mech. 133, 265-285.

Schewe, G., 1986. Sensitivity of transition phenomena to small perturbations in the flow field round a circular cylinder. J. Fluid Mech. 172, 33-46.

Zdravkovich, M.M., 1997. Flow around circular cylinders, vol.1: Fundamentals. Oxford University Press, New York.

Zdravkovich, M.M., 2003. Flow around circular cylinders, vol.2: Applications. Oxford University Press, New York.

Chapter 4

Passive-dynamic wind tunnel tests in dry state

The results presented in this chapter are taken from the paper *Effects of surface roughness and cross-sectional distortion on the wind-induced response of bridge cables in dry conditions*, G. Matteoni, C.T. Georgakis, submitted to the Journal of Wind Engineering and Industrial Aerodynamics.

Abstract

Theoretical and experimental investigations to date have assumed that bridge stay cables can be modelled as ideal circular cylinders and that their aerodynamic coefficients are invariant with wind angle-of-attack. On the other hand it has been demonstrated that bridge cables are characterised by local alterations of their inherent surface roughness and shape. Small deviations from ideal circularity result in significant changes in the static drag and lift coefficients with Reynolds number. The present study focuses on the wind-induced response of a full-scale yawed bridge cable section model, for varying Reynolds numbers and wind angles-of-attack. Based on passive-dynamic wind tunnel tests, it is shown that the in-plane aerodynamic damping of a bridge cable section, and the overall dynamic response, are strongly affected by changes in the wind angle-of-attack. Using the drag and and lift coefficients, determined in static conditions for an identical cable model as the one used for passive-dynamic tests, the in-plane aerodynamic damping is evaluated by employing a one-degree-of-freedom (1 DOF) quasi-steady analytical model. Similarly, it is shown that regions of instability associated with the occurrence of negative aerodynamic damping, are strongly dependent on the wind angle-of-attack.

4.1 Introduction

4.1.1 Overview of the dry inclined cable instability

The vibration of dry inclined cables, i.e. in the absence of rain or ice accretions, was first described by Japanese researchers. It is characterised by the presence of divergent-type vibrations, i.e. dry inclined galloping, or by limited amplitude vibrations, i.e. so called vortex shedding at high reduced velocities.

The cause of dry vibration is attributed by most authors to effects associated with the critical Reynolds number. In this range, small imperfections in the cable geometry, such as the ovalisation of the HDPE tube covering the cables, or added surface roughness are sufficient to introduce important flow transitions, which can lead to cable vibrations, particularly if the inherent structural damping of the cable is very low, (Larose and Zan, 2001). Moreover, for the specific case of dry inclined galloping, the secondary axial flow is considered to play a role. It is hypothesized that it acts as an *air curtain*, interrupting the fluid interaction between the cable's separated shear layers and generating an unsteady inner circulatory flow at either the lower leeward or upper leeward side of the cable circular surface. This determines a region of significantly lower surface pressure which results in higher oscillatory aerodynamic forces and consequently violent vibrations, (Matsumoto et al., 1990). On the other hand, the cause of high speed vortex shedding is attributed to the interaction between the conventional Karman vortex shedding and the axial vortex shedding, with the frequency of the latter being one third of the former. This implies that the cylinder's response is amplified when the axial vortexes shed once every three Karman vortices from either side of the cable's model, (Matsumoto et al., 1999).

Vibration of dry inclined cables has never been fully verified full-scale, and only a limited number of reports exist, for example (Virlogeux, 1998), (Irwin et al., 1999), (Boujard, 2007), (Zuo and Jones, 2010), (Matsumoto et al., 2010). On the other hand, it has been reproduced in wind tunnel experiments. By comparing results from different experimental campaigns, it is apparent that the characteristics of dry instability, are strongly affected by the test conditions.

The first experimental investigation on the instability of inclined/yawed full-scale bridge cables in dry conditions was undertaken by Saito et al. (1994). Based on dynamic wind tunnel tests performed on a cable model identical in mass as an actual bridge cable from the Higashi-Kobe Bridge in Japan, Saito et al. (1994) derived an instability criterion which suggests that dry inclined cable vibration can be excited at very low wind velocities corresponding to the subcritical Reynolds number range. The excitation can't be suppressed even if the cable's Scrouton number or structural damping is significantly increased. The former is defined herewith as

$$S_c = \frac{m\zeta}{\rho D^2} \tag{4.1}$$

where ζ is the cable's structural damping ratio, m is the cable's mass per unit length, ρ is the air density and D is the cable's diameter. This implied that the majority of bridge cables of exisiting bridges might be prone to dry inclined instability. A second instability criterion for dry cable vibration was later derived by Honda et al. (1995). The criterion suggests that for wind velocities corresponding to the transition from the subcritical to the critical Reynolds number regime divergent motion starts. Experimental tests undertaken by Miyata et al. (1994b) confirmed this finding. Honda et al. (1995) also observed that a significant increase in the structural damping (and thus in the Scrouton number) is not sufficient to suppress the instability.

Some years later, a series of wind tunnel tests were undertaken in collaboration between the University of Ottawa, Rowan Williams Davies and Irwin (RWDI), and the National Research Council Canada. The experimental campaign was part of a large study commissioned by the US Federal Highway Administration (FHWA). The main objective of the study was to verify the existence of dry inclined galloping and validate the severe instability criterion proposed by Saito et al. (1994). The test campaign consisted of three phases. In the first phase it was observed, based on passive-dynamic wind tunnel tests, that dry inclined cables can undergo two types of instability, i.e. a limited amplitude type, occurring over a narrow interval of wind velocities within the critical Reynolds number range, i.e. vortex shedding at high reduced velocity, and a divergent type, which is generated for all wind velocities above the critical one in the critical Reynolds number range, i.e. dry inclined galloping, (Cheng et al., 2008a). Contrary to previous tests, the dry inclined galloping instability could be restricted by increasing the structural damping (or Scrouton number). Static wind tunnel tests undertaken in the second phase of the campaign served to clarify the origins of the dry inclined galloping instability. This was explained in a similar way as the conventional galloping of ice coated cables, i.e. in terms of the Den Hartog criterion, (Cheng et al., 2008b). As a result of the experimental tests undertaken during phase 1 and 2, the FHWA proposed a new stability criterion for dry cable vibration, (FHWA/HNTB, 2005). The criterion established a value of 10 as the minimum desired Scrouton number for *regular cable arrangements*. The criterion is less conservative than the one established by Saito et al. (1994) and is currently used by bridge designers. In the third phase, displacement and pressure measurements were performed on a cable section with identical characteristics as the one used in phase 1, (Jacobsen et al., 2012). Divergent response was observed for a limited range of Reynolds numbers corresponding to the end of the critical region, where the drag coefficient drops to a minimum and a steady lift appears. This is in contrast with conventional galloping which occurs at any wind speed above the critical one. It was further observed that, due to the effect of minor imperfections of the cable surface or slight lack of roundness, the lift coefficient is a function of the cable orientation about its axis. Slight increases in the surface roughness of the model, due to the localised accumulation of insects on the cable section, significantly affected the response of the cable. In connection with these latter findings, a recent investigation undertaken by Matteoni and Georgakis (2012) showed that bridge cables are characterised by a non-uniform distribution of surface roughness and shape. Based on static wind tunnel tests undertaken on full-scale bridge cable section models, it was demonstrated that the drag and lift coefficient of both cross-flow and inclined/yawed bridge cable models are strongly dependent on the degree of axial rotation of the cable model, i.e. on the wind angle-of-attack. Some of the findings were also achieved by Flamand and Boujard (2009). Assuming quasi-steady theory, Matteoni and Georgakis (2012) hypothesized that negative aerodynamic damping can be predicted, especially in the critical Reynolds number range, where the drag coefficient is reduced to its minimum, while the lift coefficient experiences significant variations with wind angle-of-attack. Nevertheless, no experimental evidence of this occurrence, based on passive-dynamic tests, has been yet demonstrated.

4.1.2 Objectives and findings of the present investigation

Further to the work of Matteoni and Georgakis (2012), the current work investigates the effects of surface roughness and cross-sectional distortion on the wind-induced response of bridge cables in dry conditions. In order to understand this dependency, passive-dynamic wind tunnel tests were undertaken on a section of a bridge cable inclined/yawed to the incoming wind. The in-plane aerodynamic damping and the peak-to-peak amplitude of the cable response were identified for varying Reynolds numbers and varying degrees of axial rotation of the HDPE tubing, i.e. for varying wind angles-of-attack. Experimental observations of the investigation lead to the conclusion that dry instability of inclined/yawed bridge cables is very sensitive to microscopic geometrical imperfections of the cable model. It was found that the in-plane aerodynamic damping, as well as the peak to peak amplitude, changed significantly with Reynolds number for varying wind angles-of-attack. The unique alteration in the test setup when the cable is axially rotated, i.e. the surface roughness and shape of the model exposed to the oncoming wind, was sufficient enough to significantly alter the wind-induced response, and to trigger the cable instability over a broad range of Reynolds number.

The in-plane aerodynamic damping was additionally evaluated based on the static drag and lift coefficients obtained by Matteoni and Georgakis (2012) for a cable model oriented at the same cable-wind angle Φ as in the passive dynamic tests, for varying Reynolds numbers and wind angles-of-attack. This was done to compare the regions of dry instability based on the passive-dynamic and static tests. For this, a one-degree-of-freedom quasi-steady analytical model developed by Macdonald and Larose (2006) was implemented. It is not directly possible to compare the regions of instability based on the static and passive-dynamic tests. It should be noted that, due to a difference in the end conditions and in the relative roughness/shape distribution in the critical area of the cable, i.e. where flow separation is expected to occur, the flow regimes experienced by the static and passive-dynamic cable might not perfectly coincide. Nevertheless, both approaches demonstrate that the aerodynamic damping is strongly dependent on the wind angle-of-attack.

4.2 Materials and Methods

4.2.1 Passive-dynamic wind tunnel tests

Passive-dynamic tunnel tests were performed at the new DTU/Force Climatic Wind Tunnel in Lyngby. The wind tunnel is a close circuit with a test section size of $L \times W \times H = 5$ m $\times 2$ m $\times 2$ m. Technical spefications of the wind tunnel are reported by Georgakis et al. (2009).

The tested cable section model was made of a plain HDPE tube, provided by bridge cable suppliers, with a nominal diameter of 160 mm, placed on an inner aluminum tube, for increased rigidity. The tubing, of the same type as the one used for static wind tunnel tests undertaken by Matteoni and Georgakis (2012), was not characterised by a uniform roughness, due the presence of minor scratches and a 4 mm wide commercial indentation distributed all along its length, see Fig. 4.1. The roughness average, measured both in the direction of extrusion and of the wind flow, was found to be in the range of 0.7-2 μm. Increased roughness average was found along the commercial indentation, i.e. in the range of 50-100 μm. The measured roughness average of the tubing was comparable to values measured on the full-scale in-situ cables of the Øresund Bridge. Roundness measurements of the cable model, i.e. including the inner aluminum tube, showed that it is nearly circular, with a maximum deviation of the local diameter of 1.25 % (1mm) from its nominal value, (Matteoni and Georgakis, 2012).

Figure 4.1: *HDPE tubing used for passive-dynamic wind tunnel tests.*

The dynamic rig consisted of two hollow square steel sections positioned above and underneath the steel frame of the wind tunnel test chamber. The cable model was supported elastically on the outside of the wind tunnel test section, whilst protruding across lateral openings of 300 × 730 mm^2 area. Circular hollow pipes were mounted to the hollow square structural sections using special light weight steel fittings, and served to support the springs. Fig. 5.2.2 shows the cable model seen from the inside of the wind tunnel test section.

Figure 4.2: *Cable model seen from the inside of the wind tunnel test chamber.*

Extension coil springs, produced by Lesjoförs, were used as elastic supports. Their sizes were determined in terms of number of coils, outer diameter and wire diameter in order to achieve the desired frequency. Four extension coil springs, two per each cable end were used to allow vibration of the cable model in the in-plane direction. These were oriented perpendicularly to the cable axis, and belonged to the plane containing the cable axis and its projection in the horizontal plane. The size of the upper springs (i.e. in terms of outer diameter and wire diameters) was larger than the lower springs, as the upper springs are supposed to carry the weight of the cable model. The combined spring constant for the in-plane springs is c = 844.3 N/m. Fig. 4.3 shows a detail of the cable upper and lower end with in-plane springs. An axial spring wire was connected to the upper end of the cable model and served to carry the component of the gravitational force in the axial direction. The

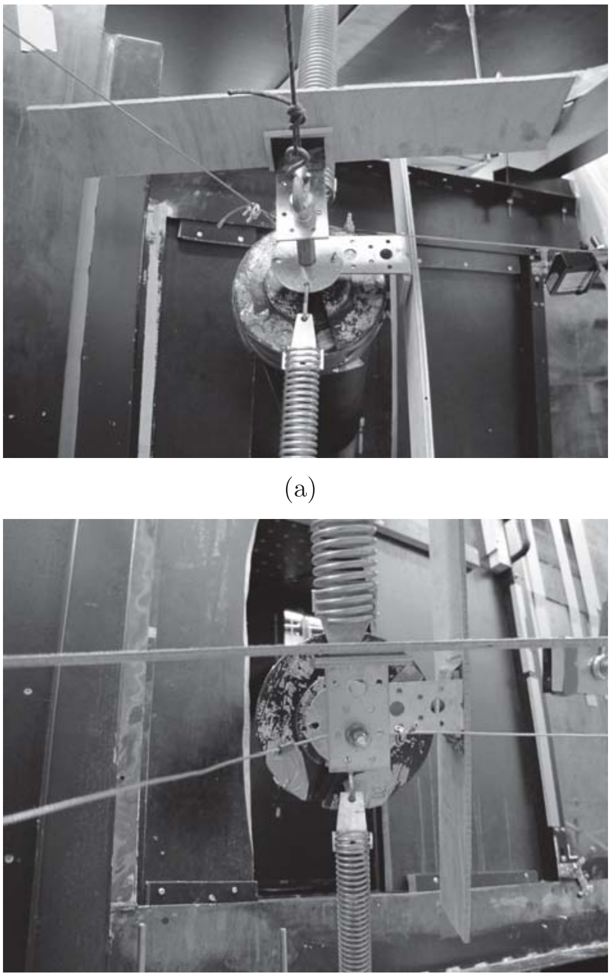

(a)

(b)

Figure 4.3: *Cable model upper end (a) and lower end (b).*

out-of-plane motion was prevented by use of four wires, two per each cable end, placed in the plane perdicular to the one which contains the in-plane springs (see Fig. 5.3). Additional technical specifications on the dynamic rig are reported by Eriksen (2012).

In Fig. 5.3 the cable's geometrical attitude in the wind tunnel tests chamber is identified. (X, Y, Z) is a global cartesian reference system, with Y parallel to the along-wind velocity U, and Z being vertical. (x, y, z) is the cable local reference system, with z being parallel to the cable's longitudinal axis, ad xy belonging to the cross-sectional plane perpendicular to the z axis. The cable's geometrical attitude is identified by the relative cable wind angle Φ, i.e. the angle between the wind direction and the cable axis, obtained by combining the vertical inclination, Θ, and the horizontal yaw, β. In the present tests, the cable was installed declining in the wind direction with a vertical inclination of $\Theta = 25°$, and a horizontal yaw of $\beta = 60°$. The resulting cable-wind angle, i.e. $\Phi = 63°$, is in the range where dry inclned galloping is predicted to occur (Raaesi et al., 2013). The wind angle-of-attack, α, identifies the degree of axial rotation of the cable, i.e. the angle formed by the projection of the free stream velocity U in the xy plane, U_N, (normal wind velocity) and the y axis, so that

$$U_N = U\sqrt{\sin^2\beta + \sin^2\Theta\cos^2\beta} \tag{4.2}$$

Tests were performed for ten selected wind angles-of-attack, namely $\alpha = 0°$, 30°, 60°, 90°, 105°, 120°, 150°, 180°, 195°, 210°, i.e. at intervals of $\Delta\alpha =$ 15°-30°. Effects of any flow disturbance on the cable surface could thus be investigated. This could be done by assuming that disturbances positioned above and below the flow stagnation line produce the same effect on the aerodynamic behaviour.

The total length of the cable model was $L_{tot} = 3.35$ m. The effective length, i.e. the length of the model inside of the wind tunnel test chamber, was $L_{eff} = 2.55$ m. The total mass of the cable model was $m_{tot} = 46.09$ kg, while the effective mass per unit length of the model, i.e. obtained considering its total length, was $m_{eff} = 18.07$ kg/m. Note that the mass per unit length of full-scale proto-type bridge cables can vary in the range $40 - 120$ kg/m. Thus the mass scaling factor between the current and prototype bridge cables ranges between 1:2.21 and 1:6.64. The cable's structural frequency was 1.10 Hz, while the measured structural damping, determined as the rig damping at zero wind velocity, was 0.1%. Based on this, the cable's Scrouton number was equal to 0.56.

All tests were conducted for a range of wind velocites of 0-30 m/s, in smooth flow conditions, i.e. for a uniform along cable axis turbulence inten-

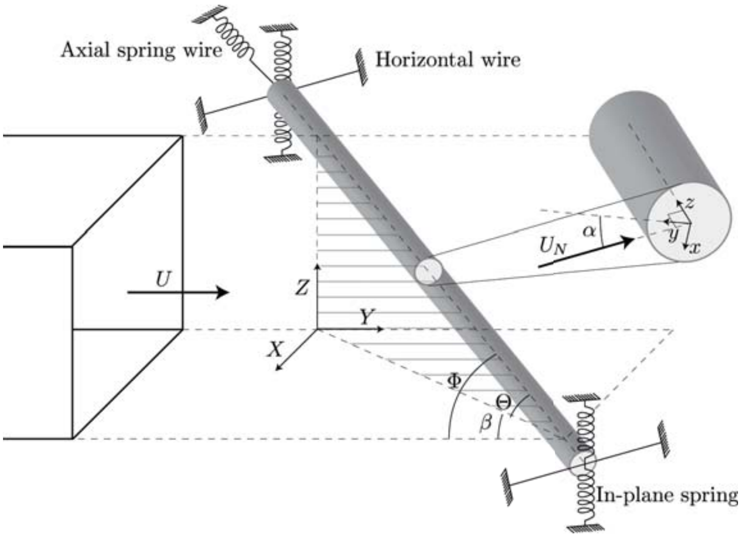

Figure 4.4*: Illustration of dynamic rig geometry.*

sity of $I_u = 0.53\%$, measured by use of a cobra probe at velocities of 9.6, 12.6 and 15.8 m/s.

Table 5.1 summarises the test parameters for the cable model.

Cable diameter, D [m]	0.16
Frequency of in-plane motion, f [Hz]	1.10
Vertical inclination, Θ [°]	25
Horizontal yaw, β [°]	30
Total length, L_{tot} [m]	3.35
Effective length, L_{eff} [m]	2.55
Total mass, m_{tot} [kg]	46.09
Effective mass per unit length, m_{eff} [kg/m]	18.07
Structural damping, ζ_s [%]	0.10
Scrouton number, S$_c$ [-]	0.56
Along-axis turbulence intensity, I_u [%]	0.53

Table 4.1*: Test parameters for the cable model.*

The model response in both in-plane and out-of-plane directions were measured by means of analogue laser displacement transducers produced by Waycon. The laser distance measurement is based on the triangulation principle. The laser transducers were fixed to the rig structure with the laser spot directed perpendicular to wooden plates mounted to the cable ends (see Figs. 4.3). The in-plane displacements were measured using a LAS-T-500 type laser, characterised by a range of 100-500 mm and a resolution of

0.03-0.6 mm, while the (restricted) out-of-plane displacements were measured using a LAS-T-250 type laser, characterised by a range of 50-300 mm and a resolution of 0.02-0.35 mm. The average signal at the two cable ends, giving the model displacement at mid length, was filtered in the time domain with a digital band-pass Butterworth filter in order to isolate the contribution of the in-plane vibration response.

In all tests the aerodynamic damping and the peak to peak amplitude of the response were evaluated, by either letting the cable freely vibrate under the wind or by manually exciting the cable. In particular, for wind velocities where the cable vibration grew spontaneously, the total damping was evaluated from the slope of the vibration growth. For the remaining wind velocities the total damping was evaluated by exciting the cable model manually, so as to reach an amplitude of vibration of approximately 1D-1.5D. The vibration decay indicated that the total damping was positive, thus the aerodynamic damping was either positive or negative but smaller in absolute value than the structural damping. The aerodynamic damping was evaluted as the difference between the total and the structural damping. For each tested wind velocity the mean and standard deviation aerodynamic damping was evaluated based on a number of test repetitions, i.e. vibration growth/decay events, comprising between 2 and 10. Finally, in order to evaluate the dependency of the aerodynamic damping on the vibration amplitude, the free decay/growth signals were divided into amplitude subintervals and the aerodynamic damping was evaluated for each of those. Fig. 4.5 shows an example of the evaluation of the total aerodynamic damping based on the slope of a free decay response at 9 m/s for $\alpha = 210°$. The total damping was evaluated for different ranges of vibration amplitude, i.e. 1D-0.1D, 1D-0.75D, 0.75D-0.50D, 0.50D-0.25D, 0.25D-0.10D.

4.2.2 Static wind tunnel tests

Drag and lift coefficients determined from static wind tunnel tests performed on a full-scale inclined/yawed cable model (Matteoni and Georgakis, 2012), were implemented in the 1 DOF quasi-steady instability model developed by Macdonald and Larose (2006) in order to compare the regions instability obtained with the passive-dynamic tests. The static wind tunnel tests were performed for a shorter cable section model, made of a plain HDPE tube fixed to an inner aluminum tube. The HDPE tube was of the same type and provided by the same suppliers as the tube used for passive dynamic tests. The static model, in contrast to the cable section used for passive-dynamic tests, was tested with circular end plates and was completely installed on the inside of the wind tunnel test chamber, see Fig. 4.6. The cable model

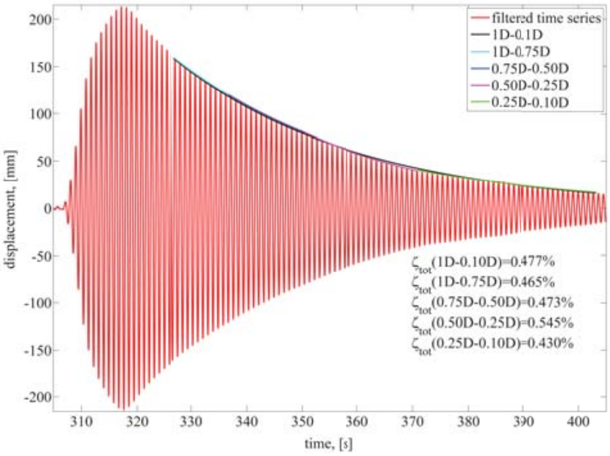

Figure 4.5: *Example of evaluation of the total aerodynamic damping* ζ_{tot} *for varying vibration amplitude intervals.*

was installed at a relative cable-wind angle $\Phi = 60°$ obtained by combining a vertical inclination of $\Theta = 55°$ and a horizontal yaw of $\beta = 30°$. Aerodynamic forces at the cable ends were measured by use of 6 DOF force transducers. A 3° descrepancy exists between the cable-wind angle used in the static and passive-dynamic tests. This is due to space constrictions in the dynamic test set-up which didn't allow for the same relative cable-wind angle as in the static tests. Technical details on the experimental setup for the static tests are reported by Matteoni and Georgakis (2012).

Figure 4.6: *Inclined test configuration in static conditions.*

4.3 Results and Discussion

4.3.1 Passive-dynamic wind tunnel tests

The cable model exhibited strong variations in the wind-induced dynamic response for varying Reynolds numbers and wind angles-of-attack. Fig. 4.7 shows a colour plot of the cable's in-plane aerodynamic damping as a function of Reynolds number and wind angle-of-attack. Black crosses represent the maximum tested Reynolds number for each wind angle-of-attack. White areas include the intervals of Reynolds number-wind angle of attack where the aerodynamic damping could not be evaluated due a lack of experimental data.

Figs. 4.9-4.18 show the aerodynamic damping, as well as the peak-to-peak amplitude of response, for varying Reynolds numbers and wind angles-of-attack, α. The mean aerodynamic damping is shown as a continuous line, while its standard deviation is shown as a grey shaded area about the mean line. The intervals of Reynolds number corresponding to the critical range, based on the averaged drag and lift coefficient (over wind angle-of-attack, α) obtained from static wind tunnel tests undertaken by Matteoni and Georgakis (2012) (see Fig. 4.8), are also shown in Figs. 4.9-4.18 as grey areas. The cable model used in the static tests is covered by an HDPE tube nearly identical to the one used for the present passive-dynamic tests and is oriented at the same cable-wind angle. Nevertheless, the flow regime boundaries might not perfectly correspond for the cable tested statically or passive-dynamically, due to a difference in the end conditions and in the relative roughness/shape distribution in the critical area of the cable, i.e. where flow separation is expected to occur.

In the passive-dynamic tests, in the interval of Reynolds numbers Re $= 0.5 \cdot 10^5 - 2 \cdot 10^5$, corresponding to the subcritical to the start of the critical Reynolds number range for the static cable, the aerodynamic damping as well as the peak-to-peak amplitudes were similar for all tested wind angles-of-attack, α. On the other hand, a lack of repeatability in the velocity dependent aerodynamic damping was obtained for higher Reynolds numbers. Here the cable model exhibited three different types of response. The first type of response was characterised by the occurrence of divergent type motion, accompanied by negative aerodynamic damping, for all wind velocities above the critical one, corresponding to the onset of instability, see Figs. 4.9-4.10. This type of response remsebled what is described in the literature as dry inclined galloping. The second type of response consisted of divergent type of motion, or large amplitude (but limited) motion, accompanied by negative aerodynamic damping, occurring for a limited range of Reynolds

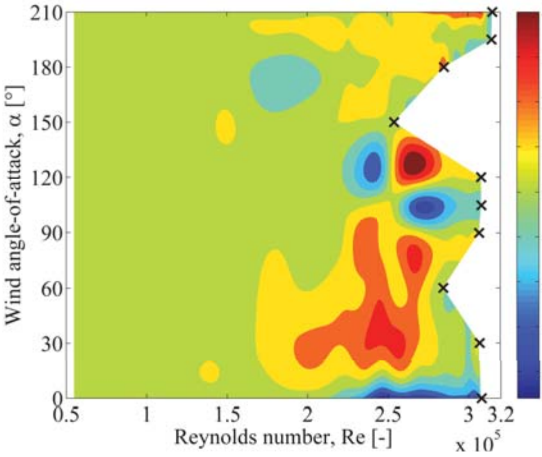

***Figure 4.7**: In-plane aerodynamic damping [%] as function of Reynolds number and wind angle-of-attack, α.*

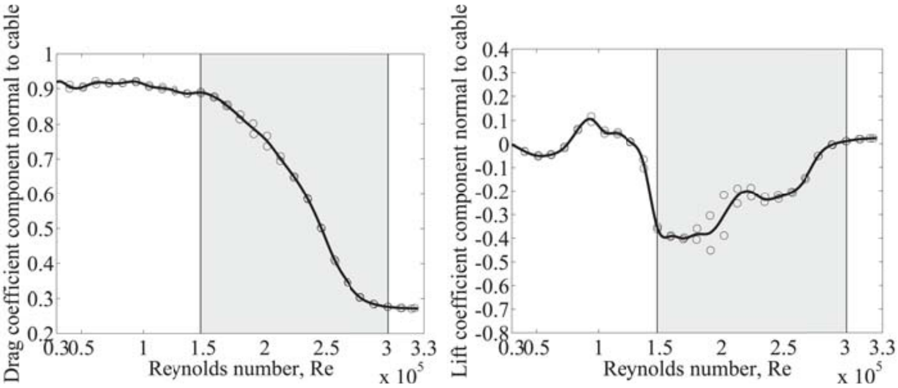

(a) (b)

***Figure 4.8**: Averaged drag (a) and lift (b) coefficients normal to cable axis for $\Phi = 60°$, based on static wind tunnel tests, (Matteoni and Georgakis, 2012).*

numbers within the critical, (see Figs. 4.11-4.12). This response resembled vortex induced vibration at high reduced velocity. The third type of response consisted of low amplitude vibrations, in the order of a fraction of one cable diameter, accompanied by positive aerodynamic damping throughout the whole tested range of Reynolds numbers, see Figs. 4.13-4.18.

Type 1 response

This type of response has been identified for two of the ten tested wind angles-of-attack, i.e. $\alpha = 0°$ and $\alpha = 105°$ (see Figs. 4.9-4.10). In the start of the subcritical Reynolds number range the aerodynamic damping undergoes a linear increase, accompanied by limited amplitude vibration (of a fraction of one cable diameter). Subsequently and still in the subcritical Reynolds number range, the aerodynamic damping stabilizes around nearly constant values and the amplitude of vibration remains limited. A change in sign in the aerodynamic damping (from positive to negative) occurs in the critical Reynolds number regime and the cable vibration amplitude builds up. At a specific Reynolds number the aerodynamic damping reaches an absolute minimum and the vibration becomes divergent. For higher Reynolds numbers, the aerodynamic damping increases, but still remains negative and the vibration remains divergent. Note that for $\alpha = 0°$, at Re $= 2.13 \cdot 10^5$, both positive and negative aerodynamic damping, i.e. $\zeta_a = 0.70\%$ and -0.81%, are measured. In fact, at this Reynolds number, after the cable is manually excited to the target amplitude of vibration it first undergoes a free decay (showing positive aerodynamic damping) until it reaches a certain level of vibration amplitude. From this level, it then starts to grow spontaneously, leading to negative aerodynamic damping. In particular, the slope of the decay is higher in absolute value than the slope of the growth. This behaviour is likely to be associated to specific flow transitions, for example the one bubble regime. Observe finally that the standard deviation of the aerodynamic damping reaches a maximum 0.10% in the subcritical Reynolds number range, while in the critical range it can reach values of up to 0.95%. This indicates that flow transitions occuring within the critical range make it more difficult to achieve repeability of the test results.

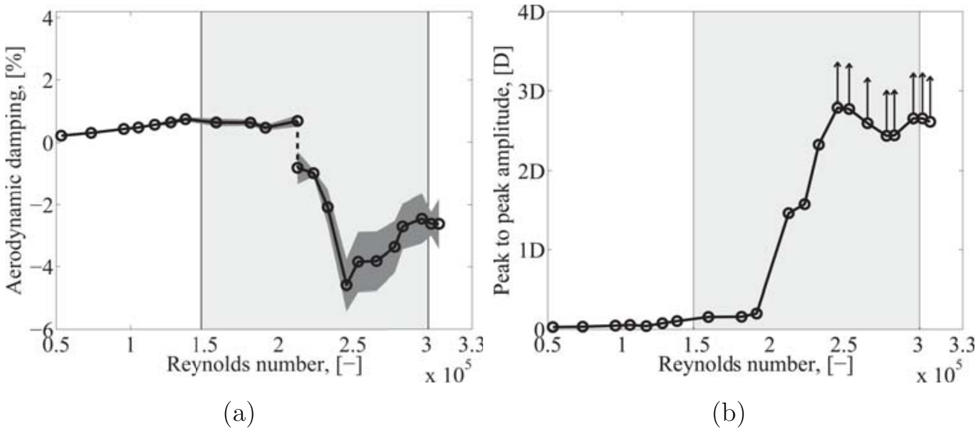

(a) (b)

Figure 4.9: *Aerodynamic damping (a) and peak to peak amplitude (b) for* $\alpha = 0°$.

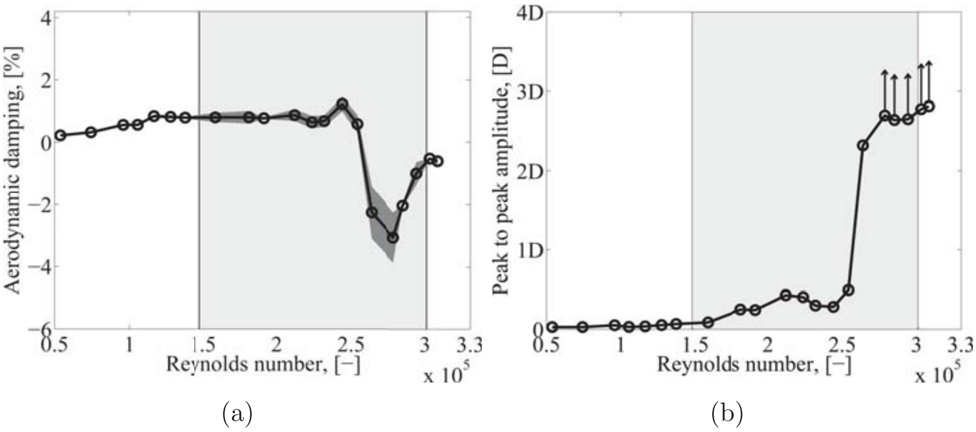

(a) (b)

Figure 4.10: *Aerodynamic damping (a) and peak to peak amplitude (b) for* $\alpha = 105°$.

Type 2 response

This response was identified for the wind angles-of-attack, i.e. $\alpha = 120°$ and $\alpha = 180°$ (see Figs. 4.11-4.12). As with response type 1, in the start of the subcritical Reynolds number range, the aerodynamic damping stays approximately constant after an initial linear increase, and the peak to peak amplitude is limited. A change in sign in the aerodynamic damping (from positive to negative) occurs in the critical range. Here, the damping remains negative, only for a limited Re range, and the amplitude of vibration is either of the divergent-type ($\alpha = 120°$) or large amplitude-type, but limited ($\alpha = 180°$). A second change in the sign of the aerodynamic damping, from negative to positive, accompanied by a consistent mitigation of the vibration amplitude, is experienced for both wind angles-of-attack for higher Reynolds numbers. This might be an indication of the transition from the end of critical to the supercritical regime.

Type 3 response

This response was identified for the majority of the tested wind angles-of-attack, i.e. $\alpha = 30°$, $\alpha = 60°$, $\alpha = 90°$, $\alpha = 150°$, $\alpha = 195°$, $\alpha = 210°$ (see Figs. 4.13-4.18). The aerodynamic damping undergoes an initial linear increase with Reynolds number in the start of the subcritical Reynolds number range (as with responses 1 and 2). It then remains positive and is accompanied by low amplitude vibration (of a fraction of one cable diameter) throughout the whole tested range of Reynolds numbers. Thus, the cable response is always stable. The critical Re range was thus not be characterised by negative aerodynamic damping. This leads to the conclusion

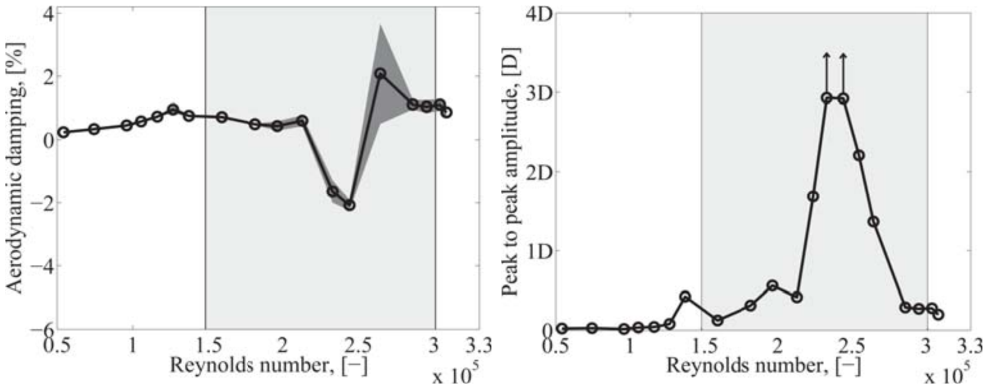

(a) (b)

Figure 4.11: *Aerodynamic damping (a) and peak to peak amplitude (b) for* $\alpha = 120°$.

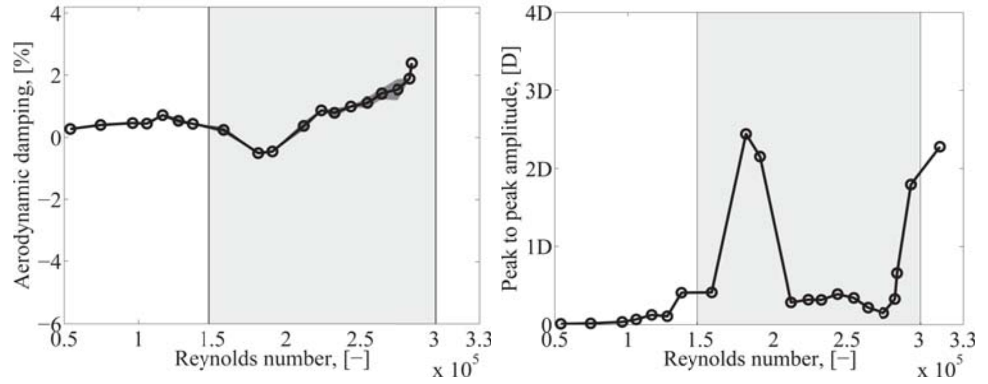

(a) (b)

Figure 4.12: *Aerodynamic damping (a) and peak to peak amplitude (b) for* $\alpha = 180°$.

that the critical Re range is a necessary precondition for the occurrence of large amplitude vibration, but it is not sufficient. Instability was triggered with the appropriate combination of roughness and or shape.

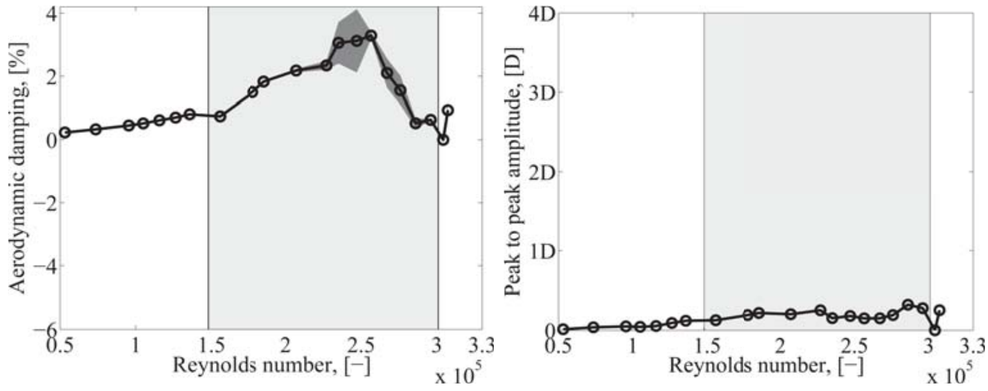

(a) (b)

Figure 4.13: *Aerodynamic damping (a) and peak to peak amplitude (b) for* $\alpha = 30°$.

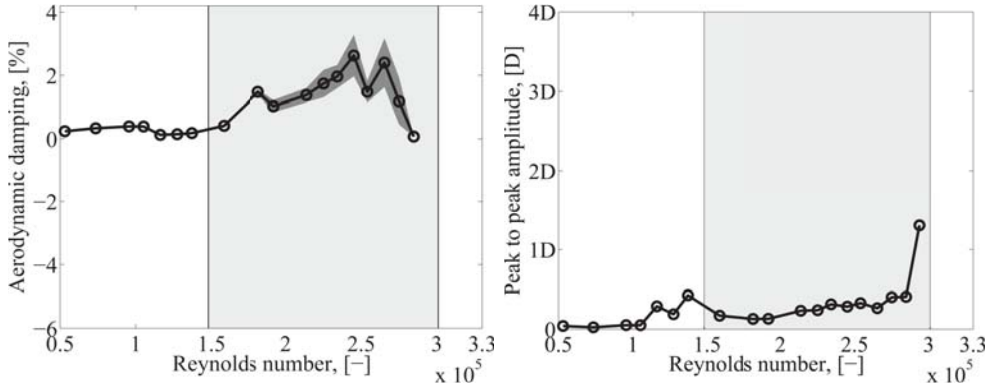

(a) (b)

Figure 4.14: *Aerodynamic damping (a) and peak to peak amplitude (b) for* $\alpha = 60°$.

4.3.2 Static wind tunnel tests

Static drag and lift coefficient components normal to cable axis obtained by Matteoni and Georgakis (2012) for a rigid cable model oriented at a relative cable-wind angle of $\Phi = 60°$, for varying Reynolds numbers and for twelve wind angles-of-attack, at intervals of $\alpha = 30 \cdot i$, i=0, 1, ..., 11, were employed. These are shown in Figs. 3.10-3.11 of Chapter 4.

For a given cable-wind angle Φ, the in-plane aerodynamic damping, based on the one-degree-of-freedom criterion developed by Macdonald and Larose (2006), reduces to

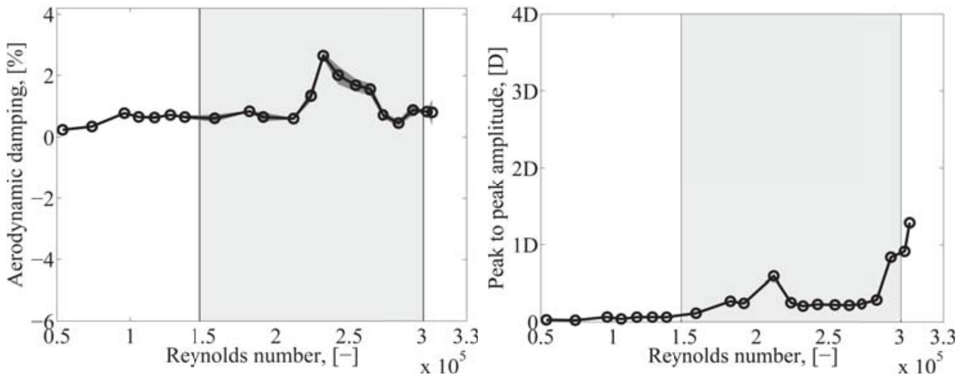

(a) (b)

Figure 4.15: *Aerodynamic damping (a) and peak to peak amplitude (b) for* $\alpha = 90°$.

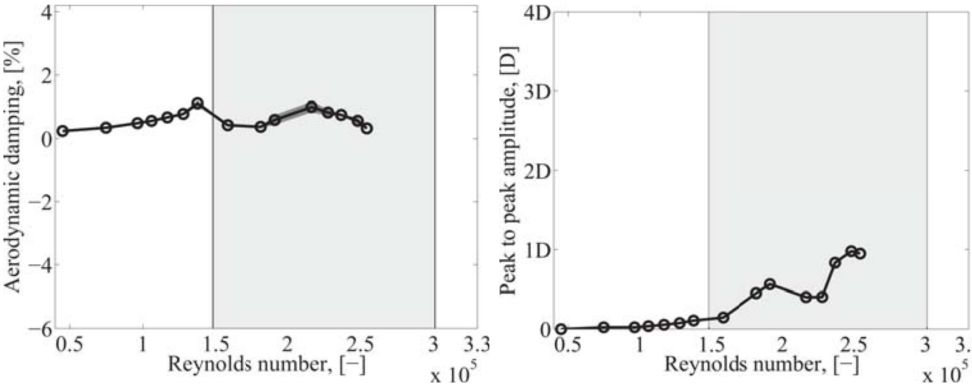

(a) (b)

Figure 4.16: *Aerodynamic damping (a) and peak to peak amplitude (b) for* $\alpha = 150°$.

$$\zeta_a = \frac{\mu Re}{4m\omega_n}\cos\alpha[\cos\alpha(C_D(2\sin\Phi + \frac{\tan^2\alpha}{\sin\Phi}) + \frac{\partial C_D}{\partial Re}Re\sin\Phi - \frac{\partial C_D}{\partial\alpha}\frac{\tan\alpha}{\sin\Phi}) \\ - \sin\alpha(C_L(2\sin\Phi - \frac{1}{\sin\Phi}) + \frac{\partial C_L}{\partial Re}Re\sin\Phi - \frac{\partial C_L}{\partial\alpha}\frac{\tan\alpha}{\sin\Phi})] \tag{4.3}$$

For in-plane vibrations, the angle α between the cable-wind plane and the plane of motion is described by Macdonald and Larose (2006)

$$\alpha = \alpha_{IP} = \arctan\frac{\tan\beta}{\sin\theta} \tag{4.4}$$

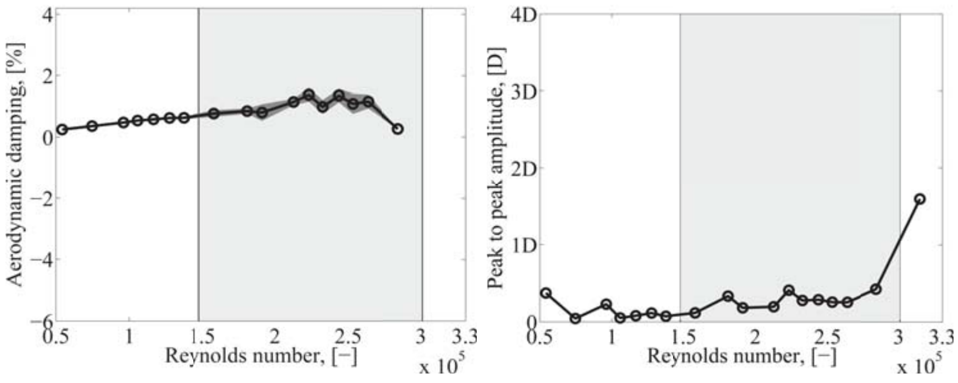

(a) (b)

***Figure 4.17**: Aerodynamic damping (a) and peak to peak amplitude (b) for* $\alpha = 195°$.

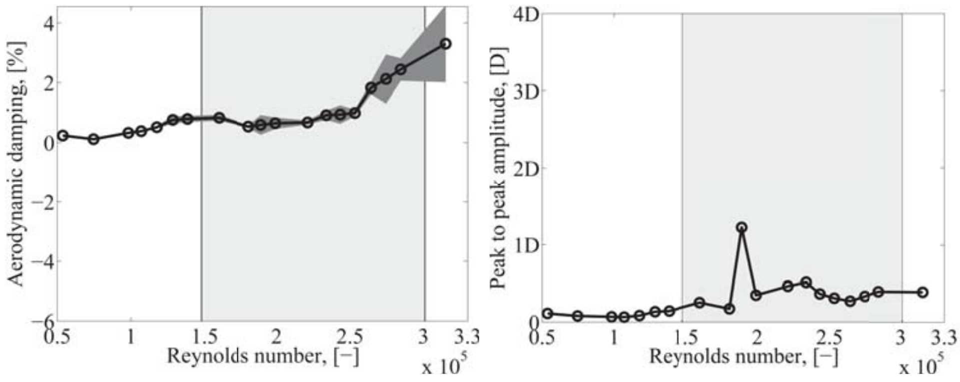

(a) (b)

***Figure 4.18**: Aerodynamic damping (a) and peak to peak amplitude (b) for* $\alpha = 210°$.

Here it is equal to 34.46°.

Fig. 4.19 shows the in-plane aerodynamic damping evaluated following equation 4.3.2 for varying Reynolds numbers and wind angles-of-attack, α.

Figs. 4.20(a) to 4.20(c) show the extrapolated in-plane aerodynamic damping - Reynolds number curves for $\alpha = 30i°$, i = 0, 1, ..., 11.

As observed experimentally from the passive-dynamic tests, the in-plane aerodynamic damping is strongly dependent on the Reynolds number and on the wind angle-of-attack, α. In the subcritical range the aerodynamic damping increases linearly with Reynolds number. Moreover, for selected wind angles-of-attack, i.e. $\alpha = 180°$, ζ_a is positive throughout the whole range of tested wind angles-of-attack. Negative aerodynamic damping occurs in the critical Reynolds number range for the remaining wind angles-of-attack.

It is not possible to directly compare the regions of instability based on the static and passive-dynamic tests, due to a variation in the boundary conditions and in the relative roughness/shape distribution in the critical area of the cable, i.e. where flow separation is expected to occur. Nevertheless, both approaches demonstrate that the aerodynamic damping is strongly dependent on the wind angle-of-attack.

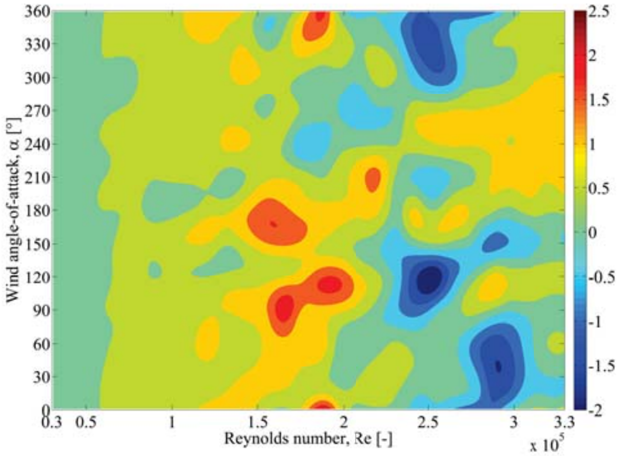

Figure 4.19: *Aerodynamic damping as function of Reynolds number and wind angle-of-attack.*

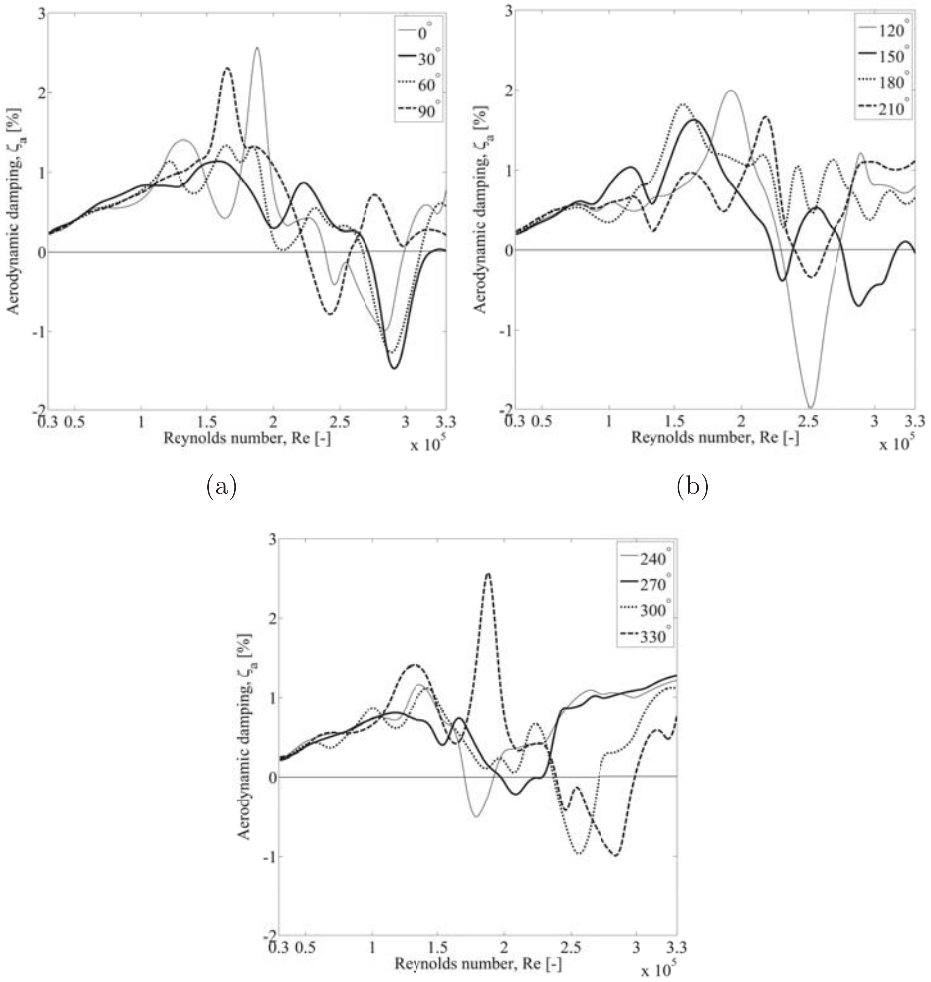

(a) (b)

(c)

***Figure 4.20**: In-plane aerodynamic damping for varying Reynolds number and wind angles-of-attack.*

4.4 Conclusion

Passive-dynamic wind tunnel tests undertaken in dry conditions for a bridge cable section characterised by a fixed mass and frequency, and oriented at a fixed relative cable-wind angle, showed that the aerodynamic damping as well as the peak to peak vibration amplitude change significantly with Reynolds number, for varying degrees of axial rotation of the cable model, i.e. wind angles-of-attack. Minor deviations in the cable response are observed in the subcritical Reynolds number range. Conversely, in the critical Reynolds number range the cable can either exhibit a stable response, characterised by positive aerodynamic damping and limited peak to peak amplitudes of vibration, or can undergo divergent vibration accompanied by negative aerodynamic damping. Thus, dry cable instability is very sensitive to microscopic geometrical imperfections of the cable model which trigger the instability over a broad range of Reynolds numbers.

This confirms experimental findings obtained from static tests which demonstrated that the drag and lift coefficients of an inclined/yawed cable model are significantly affected by wind angle-of-attack. The in-plane aerodynamic damping evaluated based on the statically determined drag and lift coefficient through use of a quasi-steady one degree-of-freedom analytical model is thus strongly dependent on the wind angle-of-attack. This is due to the occurrence of negative gradients of the lift coefficient with wind angle-of-attack, which are larger in absolute value than the drag coefficient.

Experimental and analytical observations of this invetigation lead to the conslusion that bridge cables should not be treated as ideal circular cylinders when modelled analytically or experimentally.

Bibliography

Boujard, O., 2007. Etude du phénomène de galop des câbles inclinés secs appliquée aux haubans de pont. Ph.D. Thesis.

Cheng, S., Larose G.L., Savage, M., Tanaka, H., Irwin, P.A., 2008a. Experimental study on the wind-induced vibration of a dry inclined cable - Part I: Phenomena. J. Wind Eng. Ind. Aerodyn. 96 (12), 2231-2253.

Cheng, S., Irwin P.A., Tanaka, H., 2008b. Experimental study on the wind-induced vibration of a dry inclined cable - Part II: Proposed mechanisms. J. Wind Eng. Ind. Aerodyn. 96 (12), 2254-2272.

Eriksen, M.B., 2012. Passive-Dynamic Wind Tunnel Tests of Rain-Wind Induced Vibrations. DTU Byg Internal Technical Report.

Flamand, O., Boujard, O., 2009. A comparison between dry cylinder galloping and rain-wind induced excitation. In: Fifth European and African Conference on Wind Engineering, Florence, pp. 485-488.

FHWA/HNTB, 2005. Wind induced vibration of stay cables. Interim final report, RDT 05-004.

Georgakis, C.T., Koss, H.H., Ricciardelli, F., 2009. Design specifications for a novel climatic wind tunnel for testing of structural cables. In: 8th International Symposium on Cable Dynamics, Paris, pp. 333-340.

Honda, A., Yamanaka, T., Fujiwaraa, T., Saito, T.,1995. Wind tunnel test on Rain-Induced Vibration of the Stay Cable. In: Proceedings of International Symposium on Cable Dynamics, Liege, Belgium, pp. 255-262.

Irwin, P.A., Nedim, A., Telang, N., 1999. Wind induced stay cable vibrations a case study. In: 3rd International Symposium on Cable Aerodynamics, Trondheim, Norway, pp. 171-176.

Jacobsen, J.B., Andersen, T.L., Macdonald, J.H.G., Nikitas, N., Larose, G.L., Savage, M.G., McAuliffe, B.R., 2012. Wind-induced response and excitation characteristics of an inclined cable model in the critical Reynolds number range. J. Wind Eng. Ind. Aerodyn. 110, 100-112.

Larose, G.L., Zan, S.J.,, 2001. The aerodynamic forces on the stay cables of cable-stayed bridges in the critical Reynolds number range. In: 4th International Symposium on Cable Dynamics, Montréal, pp. 77-84.

Macdonald, J.HJ., 2002. Separation of the contributions of aerodynamic and structural damping in vibrations of inclined cables. J. Wind Eng. Ind. Aerodyn. 90, 19-39.

Macdonald, J.HJ., Larose G.L., 2008a. A unified approach to aerodynamic damping and drag/lift instabilities, and its application to dry inclined cable galloping. J. Fluids Struct. 22, 229-252.

Matsumoto, M., Shiraishi, N., Kitazawa, M., Knisely, C., Shirato, H., Kim, Y., Tsujii, M., 1990. Aerodynamic behaviour of inclined circular cylinders-cable aerodynamics. J. Wind Eng. Ind. Aerodyn. 33, 63-72.

Matsumoto, M., Yagi, T., Tsushima, D., 1999. Vortex-induced vibration of inclined cables at high wind velocity. In: 10th International Conference on Wind Engineering, Copenhagen, pp. 979-986.

Matsumoto, M., Yagi, T., Hatsuda, H., Shima, T., Tanaka, M., 2010. Dry galloping characteristics and its mechanism for yawed/inclined cylinders. J. Wind Eng. Ind. Aerodyn. 98 (6/7), 317-327.

Matteoni, G., Georgakis, C.T., 2012. Effects of bridge cable surface roughness and cross-sectional distortion on aerodynamic force coefficients. J. Wind Eng. Ind. Aerodyn. 104-106, 176-187.

Miyata, T., Yamada, H., Hojo, T.,1994b. Aerodynamic response of PE stay cables with pattern-indented surface. In: Proceedings of the International Conference A.I.P.C.-F.I.P. Deauville on Cable-stayed and Suspension Bridges, Vol. 2, pp. 515-522.

Raaesi, A., Cheng, S., Ting, D.S-K., 2013. Aerodynamic damping of an inclined circular cylinder in unsteady flow and its application to the prediction of dry galloping. J. Wind Eng. Ind. Aerodyn. 113, 12-28.

Saito, T., Matsumoto, M., Kitazawa, M., 1994. Rain-wind excitation of cables on cable-stayed Higashi-Kobe Bridge and cable vibration control. In:

Proceedings of International Conference on Cable-Stayed and Suspension Bridges (AFPC), vol. 2. Deauville, France, pp. 507-514.

Virlogeux, M. Cable vibrations in cable-stayed bridges. In: Bridge Aerodynamics, Balkema, 213-233.

Zuo, D., Jones, N.P., 2010. Interpretation of field observations of wind- and rain-wind-induced stay cable vibrations. J. Wind Eng. Ind. Aerodyn. 98, 73-87.

Chapter 5

Passive-dynamic wind tunnel tests in wet state

A wind tunnel test series was carried out to investigate the rain-wind induced vibration (RWIV) instability of plain surfaced bridge cables. Focus of the investigation was the effect of the surface wettability of the cable and of the mass per unit length. Results of the wind tunnel tests are presented in this chapter.

Abstract

In the present study the response of inclined and yawed full-scale plain bridge cable sections was investigated, for varying surface conditions, i.e. in the dry and wet state, for varying levels of surface wettability, and cable mass per unit length. Test results helped to understand the driving mechanism of dry inclined instability and of rain-wind induced vibration. The first one being driven by effects of critical Reynolds number. The latter one by the achievement of the right level of cable surface wettability, which leads to the formation and oscillation of an upper and lower water rivulet, over a restricted range of Reynolds number, depending on the cable mass. The rivulet's oscillation, synchronizes with the cable vibration, thus leading to the instability.

5.1 Introduction

The instability mechanism of rain-wind induced vibration (RWIV) was introduced in the late 1980's in Japan, when, during the construction period of the Meiko-Nishi Bridge, several episodes of cable vibration occurring under the combined action of wind and rain were observed, (Hikami and Shairaishi, 1988). This followed previous reports where the instability of cables of cable-stayed bridges (Wianecki, 1979) or of overhead conductors (Hardy and Bourdon, 1979) under rain and wind conditions had been described in some details, leaving out an explanation of the origins of vibration. Twenty five years after its first observation, the RWIV instability remains an unsolved problem as the vibration mechanism has not been yet completely understood, and solutions for its suppression have not been fully developed. Several bridges in Europe, Asia and USA are continuously observed to undergo the RWIV instability. For example, the DongTing Bridge in China, (Ni et al., 2007), the Øresund Bridge, located between Denmark and Sweden, (Acampora and Georgakis, 2011), and the Fred Hartman Bridge in Texas, (Zuo and Jones, 2010), to name a few.

Until now it has been understood that RWIV is a form of instability which is self-limiting in amplitude and occurs under a restricted range of wind velocities and structural frequencies. In particular, vibration amplitudes increase with time following an exponential law until reaching an upper threshold, leading to negative aerodynamic damping. Wind velocities range approximately from 5 to 18 m/s, while cable frequencies range from 0.5 to 3 Hz. The instability normally occurs for cable sections declining in the wind direction. Critical vertical inclinations and horizontal yaw range from 25° to 45° and 45° to 70°, respectively. Angles are defined as in Fig. 5.3. Vibrations occur mostly in the in-plane direction, even if small out-of-plane components can be observed.

5.1.1 Interpretation of the excitation mechanism of RWIV

It has been cleared that the instability of RWIV is caused by the organization of the rainwater hitting the cable surface into an upper and lower rivulet, which are located at approximately the separation points of the aerodynamic flow field around a dry cable. The formation of the rivulets and their position is affected by the wind velocity and by the cable inclination and yaw angle, (Lemaitre et al., 2010). Nevertheless, controversy exists on the importance, for the excitation, of the mobility of the formed water rivulets.

Based on wind tunnel investigations, some authors concluded that the formation of steady water rivulets on the cable surface changes its cross section into a non-symmetrical one, leading to an anticipation of the critical Reynolds number regime, which is accompanied by large amplitude vibrations. Thus, RWIV was interpreted as a conventional galloping type instability. In this connection, Liu et al. (2012) demonstrated that the presence of fixed rivulets on the cable surface at a critical angular position from the stagnation line can induce a significant drop in the drag coefficient and the appearance of a lift at lower Reynolds number than it would occur for a plain circular cable. This is associated with the occurrence of galloping vibrations. Bosdogianni and Olivari (1996) claimed also that the rain changes the shape of the cable's body by forming two thin agglomerations of liquid (i.e. rivulets) on the upper and lower side of the cable surface, whose position is a function of the pressure distribution and of the gravity forces. The eventual motion of the water rivulets under the influence of increasing wind velocity has little or no influence on the instability. Previous conclusions were based on simulation of the water rivulets by means of fixed stripes or oil, this latter being characterised by a dynamic viscosity ninety times higher than water and thus less capable of motion.

On the contrary, still on the base of wind tunnel experiments, other authors stated that the water rivulets are composed of a liquid film, i.e. base carpet, and of an oscillating wave, this latter simply named rivulet. The angular oscillation of the upper and lower water rivulets is thus a fundamental requisite for the RWIV to get started. In fact, the instability is explained in terms of periodic change of the cable cross-section, seen from the flow, due to the circumferential oscillation of the water rivulets, (Hikami and Shairaishi, 1988), (Yoshimura et al., 1988). The synchronization between the rivulet and the cable motion produces regular flow regime fluctuations around the cable. These pressure fluctuations give rise to positive aerodynamic work and thus to the rain-wind induced excitation, (Cosentino et al., 2003a). A primary requisite for the formation of the upper and lower water rivulets, and of their angular oscillation in particular, is the achievement of a certain degree of surface wettability for the external sheath of actual bridge cables. In this connection, Flamand (1995) explained that the case material of bridge cables, i.e. HDPE (high density polyethylene) or HDPP (high density propylene), is normally coated with atmospheric pollutants, which provoke a significant increase in the surface material wettability, thus triggering, under a limited range of wind velocities, the formation and oscillation of water rivulets. In order to simulate the rise in surface energy due to the accumulation of pollution, Flamand (1995) coated the cable models used for passive-dynamic wind tunnel tests with sooth, resulting from fuel oil combustion. Similarly, Larose and Smitt (1999) stated that the wettability of the HDPE tube surface increases with time due to the combination of dust accumulation, saline deposit, acid rain or sunlight. Black HDPE tubes, containing a larger portion of carbon, which increases the cable wettability, are more prone to rain-wind induced vibration. In order to simulate the degree of wettability existing on the field, Larose and Smitt (1999) treated the cables with a wetting agent made of a coat of polyvinyl alcohol.

Instability identified as rain-wind induced has been finally reported for a drying cable section, covered by a plain tube, (Larose and Smitt, 1999). As water was not sprayed on the cable model at the moment the vibration started, the rivulets, initially steady, were likely to be disrupted as the time passed, so that the cable was only covered by water droplets. The tubing experienced a time varying surface roughness, decreasing with time as it became drier and drier. This type of instability was again likely to be induced by galloping.

5.1.2 Objectives and results

The different forms of instability observed by wind tunnel tests performed in the past were not originated by the same mechanism as the rivulets were modelled in different ways, i.e. steady, oscillating or simply as water droplets. On the other hand, a combination of the previously observed instabilities might occur on real bridges during rainy events, as, depending on the degree of surface wettability, bridge cables might be covered by oscillating or steady rivulets. After the rain has stopped, the cables are drying, and they are exposed to a time varying surface roughness, due to vanishing droplets. This surface condition differs from the dry state.

In this study the aerodynamic instability of bridge cable sections is investigated in terms of aerodynamic damping and peak to peak amplitude, for varying surface conditions of the cable model, i.e. in the dry state, and in the wet state. In the wet state two basic configurations of the cable surface are investigated: untreated and coated with a solution of 5% weight Gohsenol KP-08R commercialized by Nippon Gohsei (2012) dissolved in water. For the untreated case, two situations were investigated, i.e. water directly sprayed on the cable model and slowly drying cable.

As the surface wettability of bridge cables has never been measured on the field, its value could not be established a priori and the tested ones represent idealized situations. In fact when the cable was treated with Gohsenol its wettability was very high and even all along the cable length, leading to uniform lengthwise water rivulets. On the other hand, when the cable was not coated by the Gohsenol solution its wettability was very low, as the tubing was brand new, and clean.

All tests were performed for two different levels of the cable mass. The role of cable mass is of interest nowadays as in alternative to the classic steel solution, the strands of new generation bridge cables will be made of carbon fibre composites (CFRP) which combine with high tensile strength and stiffness, as well as excellent chemical resistance and high fatigue life, a low weight, (Noisternig, 2000).

In all tests, the geometrical attitude of the cable model was chosen so as to reproduce a configuration where the rain-wind induced instability had already been observed based on wind tunnel and full-scale measurements.

Test results showed that for the untreated surface, a steady upper and lower non-coherent water rivulets formed, when the spray system was turned on. These were not sufficient for the excitation to get started. The cable model was in fact manifestly stable and exhibited positive aerodynamic damping throughout the whole range of tested Reynolds number, being accompanied by limited peak-to-peak amplitude, for both levels of cable mass. Similar behaviour was experienced for the cable in the drying configuration. On the other hand, when the cable was coated with the Gohsenol solution an upper and lower oscillating water rivulets appeared which triggered large amplitude vibrations, accompanied by negative aerodynamic damping, under a limited range of Reynolds numbers. In the dry state the cable model was manifestly stable until it reached the critical Reynolds number regime, where it experienced galloping type vibrations for both mass levels.

5.2 Materials and Methods

5.2.1 Surface treatment

The cable's surface was first uniformly sanded in the along-axis direction using sand paper of grading P400. In this way effects of imperfections on the HDPE sheath which might affect the formation or shape of the water rivulet was eliminated.

The surface treatment used to increase the cable's wettability consisted of a 5% weight Gohsenol KP-08R non-toxic polyvinyl solution commercialized by Nippon Gohsei (2012) dissolved in water. The Gohsenol granulate was first poured into room temperature water. In order to completely dissolve the Gohsenol, it was slowly heated to $70-75°$C temperature (K type Gohsenol). After the target temperature was reached the solution was cooled down to 20°C temperature. The result was a clear solution with higher viscosity than water, which was applied on the cable surface with a soft brush. In order to eliminate effects of any contaminants which might have deposited on the cable surface, this was normally cleaned with terpentune and rinsed with water before applying the Gohsenol coating. The effect of the Gohsenol coating had a finite time duration, thus it was necessary to be re-applied after few hours of testing.

Fig. 5.2.1 shows the effect of polyvinyl coating on the cable surface when exposed to the water spray. On the left, the untreated cable is shown, which, after being exposed to the water spray, repelled water from the surface, so that only few water droplets were left; on the right, the newly treated cable, which, after being exposed to water spray, still exhibits the Gohsenol film as evenly distributed on the surface.

Figure 5.1: *Effect of polyvinyl coating: untreated cable to the left compared to newly treated cable to the right exposed to water spray.*

Note that preliminary tests were undertaken using the same surface treatment for the cable surface as the one adopted by Larose and Smitt (1999), i.e. Gohseonl dissolved into 95% ethanol. In this case not all Gohsenol granulates were dissolved into the ethanol solution leaving grains on the model surface after painting. Moreover no improvement in the surface wettability was observed in comparison to the water solution.

5.2.2 Passive-dynamic wind tunnel tests

Passive-dynamic tunnel tests were performed at the new DTU/Force Climatic Wind Tunnel in Lyngby. The wind tunnel is a close circuit with a test section size of $L \times W \times H = 5 \times 2 \times 2$ m^3. Technical specification of the wind tunnel are reported by Georgakis et al. (2009).

Technical specifications on the dynamic rig geometry/materials are reported by Eriksen (2012). The cable model was supported elastically on the outside of the wind tunnel test section, whilst protruding across lateral openings with rounded corners of 300×730 mm^2 area. Fig. 5.2.2 shows the cable model seen from the inside of the wind tunnel test section.

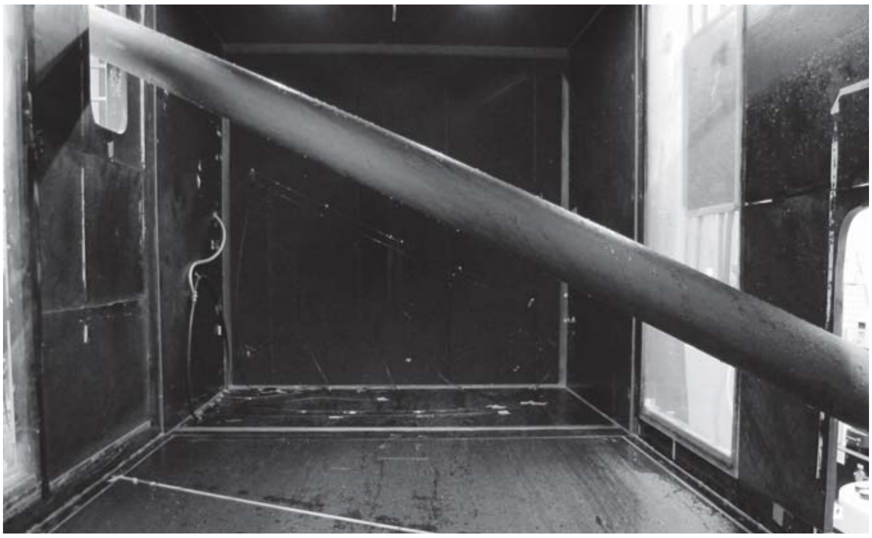

Figure 5.2: *Cable model seen from the inside of the wind tunnel test chamber.*

Four extension coil springs, two per each cable end were used to allow vibration of the cable model in the in-plane direction (or across-flow direction). These were oriented perpendicularly to the cable axis, and belonged to the plane containing the cable axis and its projection in the horizontal plane. In Fig. 5.3 they are identified as in-plane springs. An axial spring wire was connected to the upper end of the cable model and served to to carry the component of the gravitational force in the axial direction. As rain-wind induced vibration occurs mostly in the in-plane direction, the out-of-plane motion was prevented by use of four wires, two per each cable end, placed in the plane perdicular to the in-plane springs (see Fig. 5.3).

The tested cable section model was made of a plain HDPE tube, provided by bridge cable suppliers, with a nominal diameter of 160 mm, placed on an inner aluminium tube, for increased rigidity. The total length of the cable model was $L_{tot} = 3.35$ m. The effective length, i.e. the length of the model inside of the wind tunnel test chamber, was $L_{eff} = 2.55$ m. Tests were performed for two different levels of cable mass. The tested total mass of the cable model, including effective parts of the spring masses, were $m_{tot} = 46.09$ and 25.50 kg, while the effective mass per unit length of the model, i.e. obtained by dividing the total mass by the effective length, was m$_{eff}$=18.07 and 10 kg/m, respectively. The mass per unit length of full-scale proto-type bridge cables can vary in the range $40 - 120$ kg/m. Thus the scaling factor between the current and proto-type bridge cables ranges from 1:2.21 to 1:6.64 (for m_{eff}=18.07 kg/m) and 1:4 to 1:12 (for m_{eff}= 10 kg/m).

The stiffness of the in-plane springs was adjusted in order to achieve the same structural frequency for the two different effective mass levels of the cable model. For m_{eff}=18.07 kg/m, the combined spring constant for the in-plane springs is k = 844.3 N/m. For m_{eff}= 10 kg/m, the combined spring constant of the in-plane springs is k = 599.2 N/m.

The cable's structural frequency (for both effective mass levels) was 1.10 Hz, while the measured structural damping, determined as the rig damping at zero wind velocity, was 0.1%. The cable's Scrouton number defined as

$$S_c = \frac{m\zeta}{\rho D^2} \tag{5.1}$$

where ζ is the cable's structural damping ratio, m is the cable's mass per unit length, ρ is the air density and D is the cable's diameter, resulted equal to 0.56 and 0.31, for $m_{eff} = 12.75$ and 7.15 kg/m, respectively.

In Fig. 5.3 the cable's geometrical attitude in the wind tunnel tests chamber is fully described. (X, Y, Z) is a global cartesian reference system, with Y parallel to the free-stream velocity U, and Z being vertical. The relative cable-wind angle, Φ, i.e. the angle between the wind direction and the cable axis, is equal to 63°. This is obtained by combining a vertical inclination, $\Theta = 25°$, and a horizontal yaw, $\beta = 60°$. This is the geometry where rain-wind induced vibration is predicted to occur, based on wind tunnel experience, see for example (Flamand, 1995), (Cosentino et al., 2003a).

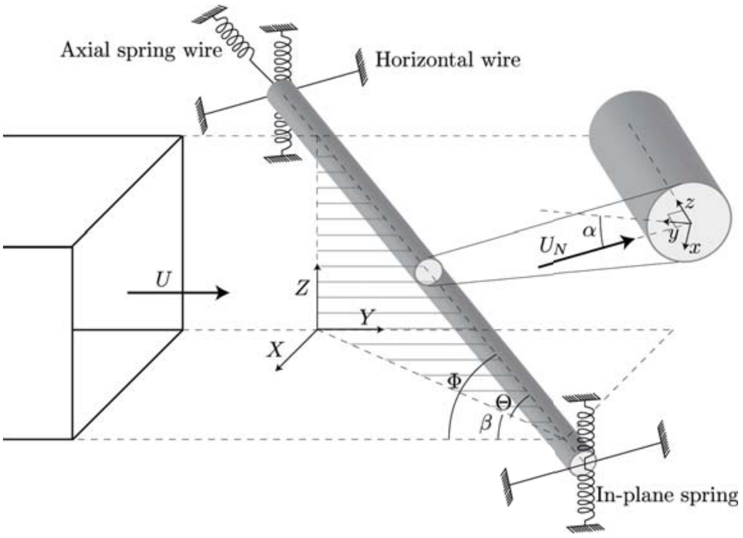

Figure 5.3: *Illustration of the dynamic rig geometry.*

The spray system (see Fig. 5.4) consisted of five nozzles connected to a piano wire, positioned upstream of the cable model. The piano wire position was determined as the projection of the cable axis along the vertical plane, which corresponded to an inclination of 28.3°. The distance of the spray nozzles to the model position varied in the interval between $1.6-2.5$ m. The water flow was adjusted in order to produce a *mist-type* rain and was kept constant at 1.6 litres/min. In this way, uniform water flow conditions were allowed along the cable model.

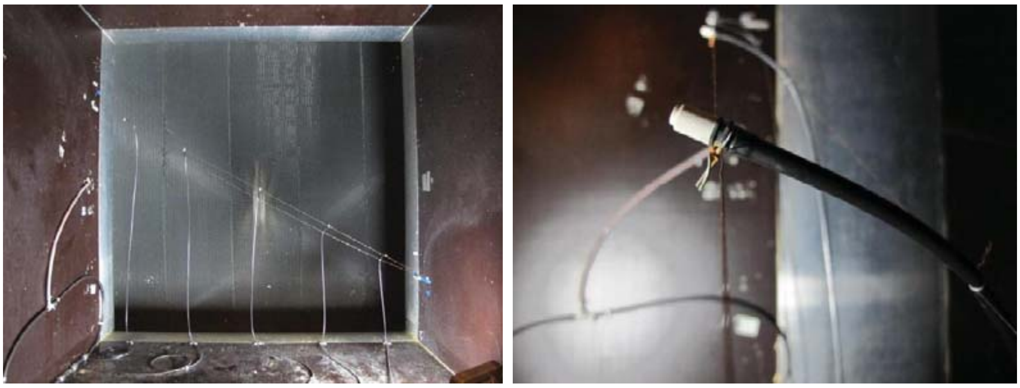
(a) (b)

Figure 5.4: *Spray system consisting of noozles positioned along the cable axis vertical projection.*

Flow measurements were performed in the wind tunnel to determine velocity profiles and turbulence intensities with an withouth the rain simulation systems installed. Measurements were performed by use of a TFI Cobra Probe along the model axis, i.e. along an inclined and yawed line. The cable model wasn't installed in the test section during the measurements. Measurements were performed for three wind velocities, i.e. corresponding to 9.6m/s, 12.6m/s and 15.8m/s. Test results showed that the presence of the piano wires and spray nozzles increased the turbulence intensity from 0.53% to 1.28%. Hence it was concluded that the presence of the rain simulation system did increase the turbulence level, but this was kept within the same order of magnitude.

Table 5.1 summarises the test parameters for the cable model.

Due to the mass scaling between the proto-type and the wind tunnel cable, the damping ratio and Scrouton number reported in Table 5.1 must be scaled accordingly.

The model vibration displacements in both in-plane and out-of-plane directions were measured by means of analogue laser displacement transducers

Cable diameter, D [m]	0.16
Frequency of in-plane motion, f [Hz]	1.10
Vertical inclination, Θ [°]	25
Horizontal yaw, β [°]	30
Total length, L_{tot} [m]	3.35
Effective length, L_{eff} [m]	2.55
Total mass, m_{tot} [kg]	42.70, 25.50
Effective mass per unit length, m_{eff} [kg/m]	18.07, 10
Structural damping, ζ_s [%]	0.10
Scrouton number, S_c [-]	0.56, 0.31
Along-axis turbulence intensity, I_u [%]	1.28

***Table 5.1**: Test parameters for the cable model.*

produced by Waycon. The laser distance measurement is based on the triangulation principle. The laser transducers were fixed to the rig structure with the laser spot directed perpendicular to wooden plates mounted to the cable ends. The in-plane displacement were measured using a LAS-T-500 type laser, characterised by a range of 100-500 mm and a resolution of 0.03-0.6 mm, while the out-of-plane displacements were measured using a LAS-T-250 type laser, characterised by a range of 50-300 mm and a resolution of 0.02-0.35 mm. The average signal at the two cable ends, giving the model displacement at mid length, was filtered in the time domain with a digital band-pass Butterworth filter in order to isolate the contribution of the in-plane vibration response.

Test programme

The test programme is illustrated in Figs. 5.5, 5.6.

Dry tests (Fig. 5.5) were first conducted (as reference) for the two levels of effective cable mass per unit length. In this configuration the cable surface was sanded but no additional surface treatment was applied.

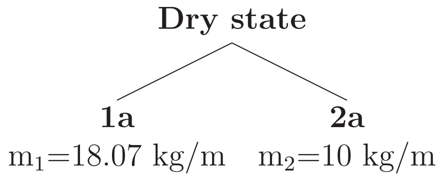

***Figure 5.5**: Three diagram, illustrating the dry state passive-dynamic tests.*

Wet tests (Fig. 5.6) were undertaken for two levels of effective cable mass per unit length and two surface conditions of the cable model, i.e. untreated and coated with a solution of 5% weight Gohsenol KP-08R commercialized by Nippon Gohsei (2012) dissolved in water. For the untreated case, the two situations of water directly sprayed on the cable model and slowly drying cable (i.e. with the spray system turned off) were investigated. In the first case steady water rivulets appeared on the cable surface, in the second case only water droplets.

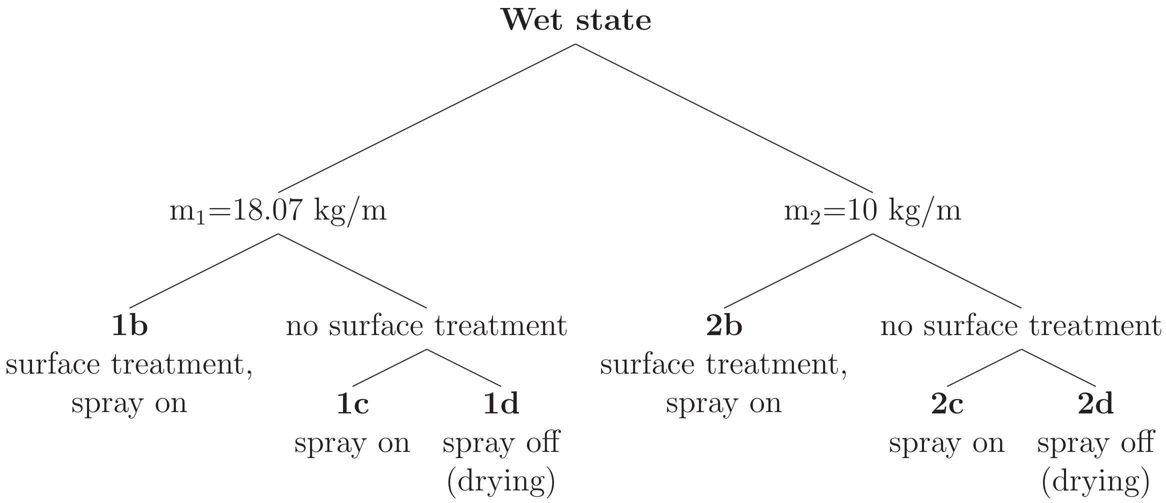

***Figure 5.6**: Tree diagram, illustrating the wet state passive-dynamic tests.*

All tests were conducted for a range of wind velocities from 5 to to 25 m/s, corresponding to Reynolds number, Re = $0.5{\cdot}10^5$ - $2.7\cdot10^5$. For each tested velocity the aerodynamic damping as well as the peak to peak amplitude of the response were evaluated. For wind velocities where the cable vibration grew spontaneously, the total damping was evaluated as the slope of the vibration growth. For the remaining wind velocities the total damping was evaluated from free vibration decays obtained after exciting the cable model manually, so as to reach an amplitude of vibration in the range of 1D-1.5D. Vibration growths indicated that the aerodynamic damping was negative and larger in absolute value than the structural damping. Vibration decays indicated that the total damping was positive, thus the aerodynamic damping was either positive or negative but smaller in absolute value than the structural damping. The aerodynamic damping was evaluated as the difference between the total and the structural damping. For both growth and decay events the total damping is evaluated for the range of vibration amplitude 1D-0.10D.

5.3 Results and Discussion

5.3.1 Dry state

Figs. 5.7 and 5.8 show the aerodynamic damping and peak to peak amplitude of cable vibration measured in dry conditions for the cases of $m_{eff} = 18.07$ kg/m (case 1a) and 10 kg/m (case 2a), respectively. Measured values of the aerodynamic damping and of the peak-to-peak amplitude of vibration are shown as single data points for each test performed. The continuous line represents the average of the measured data points.

For $m_{eff} = 18.07$ kg/m the average aerodynamic damping seems to follow an approximately linear trend and increases from 0.26% at Re $= 0.52 \cdot 10^5$ to 1.28% at Re $= 2.10 \cdot 10^5$. In this range of Reynolds number the peak to peak amplitude is always limited and lower than one cable diameter. At Re$=2.67 \cdot 10^5$, the aerodynamic damping becomes negative and its average value is equal to -6.14%. The peak to peak amplitude reaches a value of 2.18 cable diameters at the same Reynolds number. Note that the test repeatability, especially in terms of aerodynamic damping, decreases with increasing Reynolds number. Flow transitions occurring in the range of Re above $2 \cdot 10^5$, which is likely to be the critical, might in fact be responsible for dispersion of the tests results.

For $m_{eff} = 10$ kg/m the average aerodynamic damping increases from 0.48% to 1.68% in the range of Re $= 0.53{\cdot}10^5$ to $1.58{\cdot}10^5$. At Re $= 2.13{\cdot}10^5$ the average aerodynamic damping reaches a value of -2.86% and the peak to peak amplitude is equal to 2.18 cable diameters.

In Fig. 5.9(b) and 5.9(b) the average aerodynamic damping and peak to peak amplitude for the two effective mass per unit length cases are compared. As the cable mass decreases an increase in the mean aerodynamic damping is measured for the range of Reynolds number where ζ_a is positive. On the other hand the aerodynamic instability associated with the occurrence of negative aerodynamic damping is anticipated by lowering the mass level.

5.3.2 Wet state

Figs. 5.10(a) and 5.10(b) shows the aerodynamic damping and peak to peak amplitude of cable vibration measured in wet conditions for $m_{eff} = 18.07$ kg/m. The cable model was uniformly painted with Gohsenol solution. The tested case is 1b.

For Re$\leq 0.72 \cdot 10^5$ (corresponding to a wind velocity of 7 m/s) the aerodynamic damping is positive and near to zero (i.e. 0.05%). The associated peak to peak amplitude of vibration is limited. For $0.833 \cdot 10^5 \leq$ Re $\leq 1.53 \cdot 10^5$,

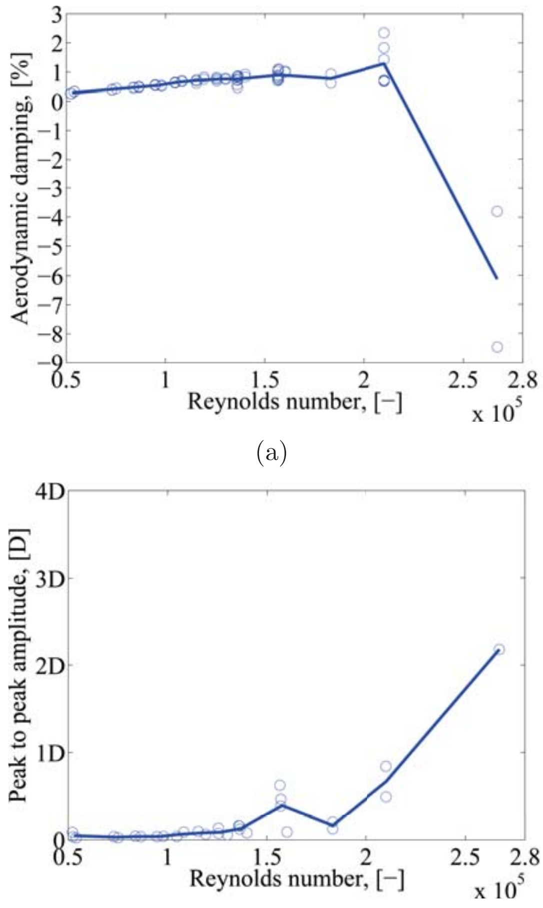

(a)

(b)

Figure 5.7*: Aerodynamic damping (a) and peak to peak amplitude (b) as function of Reynolds number in dry conditions, case 1a.*

which corresponds to wind velocities in the range of 8 to 15 m/s, the aerodynamic damping becomes negative and its average reaches a minimum of -0.45%. In this interval of Re the vibration amplitude is growing following an exponential trend until hitting the rig structure where it has to be stopped manually. An upper and lower water rivulets are formed on the cable surface and oscillate circumferentially (see Fig. 5.19(a)). This is thus identified as the interval of Reynolds number associated with the occurrence of rain-wind induced vibration.

For higher Reynolds number the aerodynamic damping becomes positive again and the peak to peak amplitude of vibration is limited.

Fig. 5.11 shows a time history of cable vibration for Re = $0.96 \cdot 10^5$ (U = 9 m/s). The cable vibration is growing spontaneously until reaching a

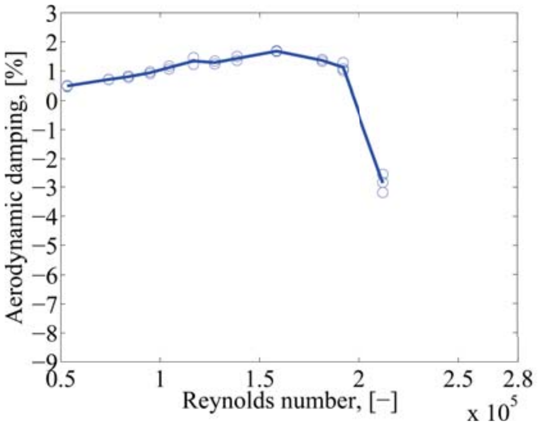

(a)

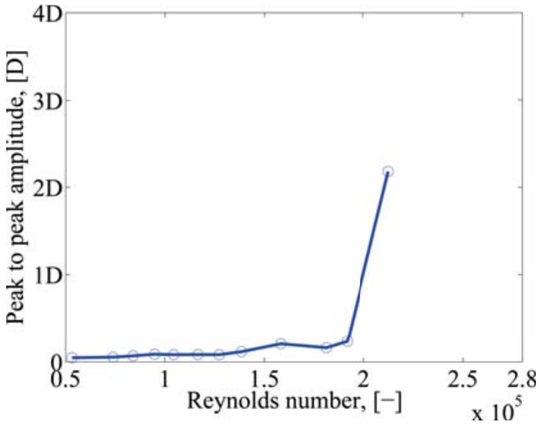

(b)

Figure 5.8: *Aerodynamic damping (a) and peak to peak amplitude (b) as function of Reynolds number in dry conditions, case 2a.*

peak to peak amplitude of vibration of 2.7D. As the peak to peak amplitude reaches the dynamic rig structure, the cable is stopped manually, so that the vibration amplitude is reduced to zero. After being released, the cable vibration starts to grow again. In Fig. 5.11 four consecutive growth events are shown.

Fig. 5.12(a) and 5.12(b) shows the aerodynamic damping and peak to peak amplitude of vibration for the cable model with m_{eff} = 18.07 kg/m, and untreated surface. The spray system was turned on and an upper and lower steady water rivulets formed on the cable surface (see Fig. 5.19(b)). The test case is 1c.

In this case the aerodynamic damping is positive throughout the whole tested range of Reynolds number and varies from 0.15% at Re=$0.55{\cdot}10^5$ to

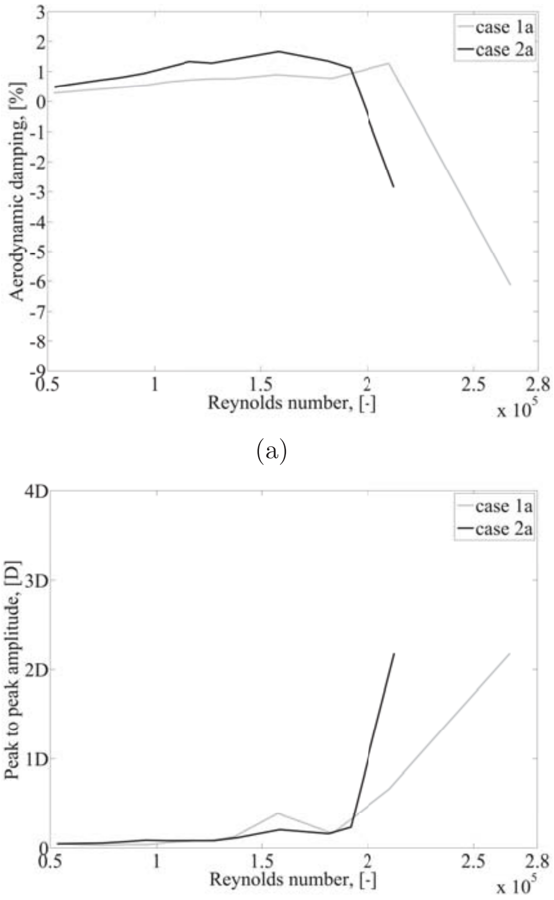

(a)

(b)

Figure 5.9: *Average aerodynamic damping (a) and peak to peak amplitude (b) as function of Reynolds number in dry conditions, case 2a and 2b.*

1.20% at Re=2.07·10^5. The peak to peak amplitude of vibration is near zero for the whole tested Re range. The cable is thus manifestly stable and the values of the aerodynamic damping are very similar to the ones measured in dry conditions. This indicates the the sole presence of the water rivulets (non-oscillating) is a necessary but not sufficient condition for the instability to develop. Their angular oscillation, which is achieved by the occurrence of the right level of wettability, is fundamental. Note finally, by comparing Figs. 5.19(a) and 5.19(b), that the geometry of the rivulets is completely different for the two cases. When the cable is more wettable the rivulets, become wider.

Figs. 5.13(a) and 5.13(b) show the aerodynamic damping and peak to peak amplitude of vibration for the cable model with m_{eff} = 18.07 kg/m, and

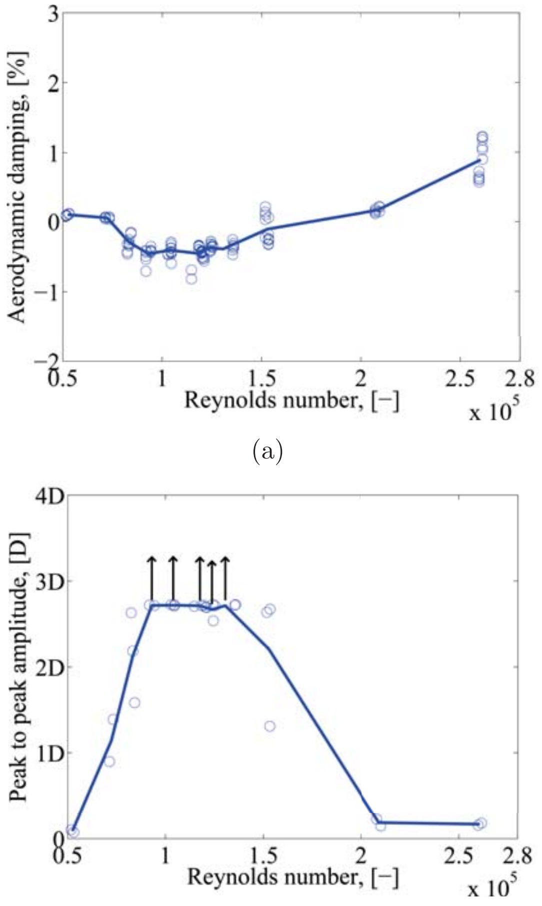

(a)

(b)

Figure 5.10*: Aerodynamic damping (a) and peak to peak amplitude (b) as function of Reynolds number in wet conditions, case 1b.*

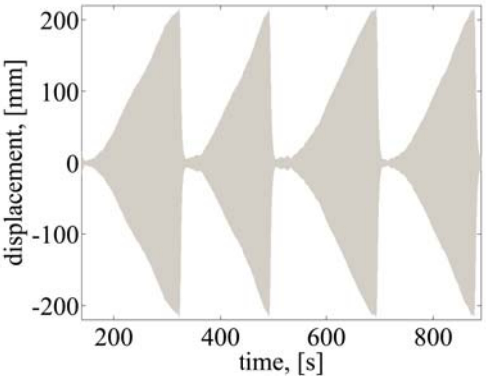

Figure 5.11*: Time history of cable vibration, at 9 m/s, case 1b.*

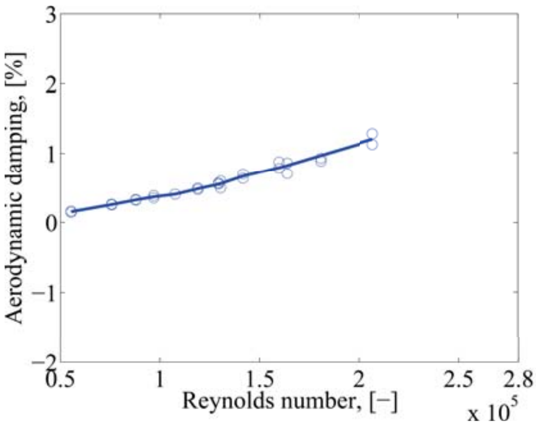

(a)

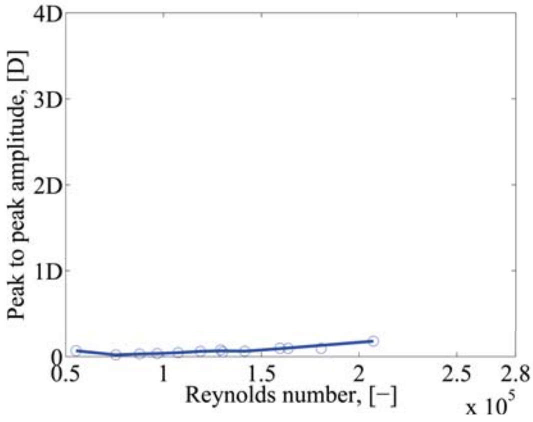

(b)

Figure 5.12: *Aerodynamic damping (a) and peak to peak amplitude (b) as function of Reynolds number in wet conditions, case 1c.*

untreated surface. The spray system was turned off and the cable surface was covered by water droplets (see Fig. 5.19(c)). The test case is 1d. Again, no aerodynamic instability was detected for the tested range of Reynolds number, being the aerodynamic damping positive and the peak to peak amplitude of vibration near zero. In particular, the aerodynamic damping ranges from 0.13% at Re=$0.55 \cdot 10^5$ to 0.94% at Re=$2.66 \cdot 10^5$ and doesn't follow a linear trend.

Figs. 5.14(a) and 5.14(b) show the aerodynamic damping and peak to peak amplitude of vibration measured in wet conditions for $m_{eff} = 10$ kg/m. The cable model is uniformly painted with Gohsenol solution. The tested case is 2b. The aerodynamic damping is positive for Re=$0.53 \cdot 10^5$ to $0.85 \cdot 10^5$ (corresponding to wind velocity of 5 to 8 m/s) and ranges from 0.24% to

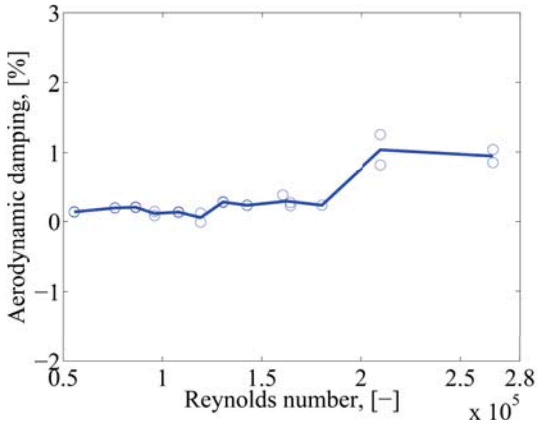

(a)

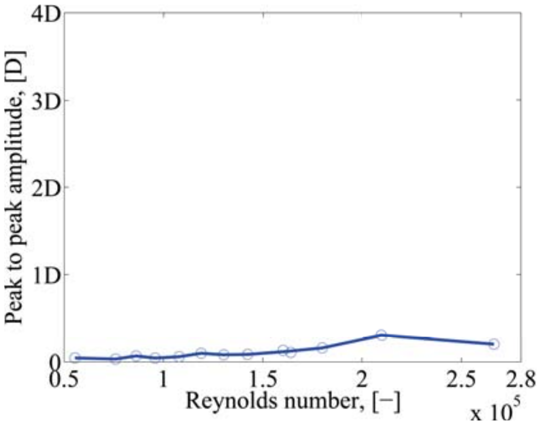

(b)

Figure 5.13: *Aerodynamic damping (a) and peak to peak amplitude (b) as function of Reynolds number in wet conditions, case 1d.*

0.74%. It becomes negative for Re=$0.97{\cdot}10^5$ to $1.44{\cdot}10^5$ (wind velocity equal to 9 to 13.5 m/s) and ranges from -1.28% to -0.44%.

Figs. 5.15(a) and 5.15(b) show the aerodynamic damping and peak to peak amplitude of vibration for the cable model with m_{eff} = 10 kg/m, and untreated surface. The spray system was turned on and an upper and lower steady water rivulets formed on the cable surface, as for case 1c. The test case is 2c.

As for the higher mass level the aerodynamic damping is positive throughout the whole tested Re range and varies from 0.31% to 2.64% for Re = $0.54{\cdot}10^5$ to $2.15{\cdot}10^5$. It is thus generally higher than for the respective case 1c. The peak to peak amplitude is near zero for the whole Re range.

Figs. 5.16(a) and 5.16(b) show the aerodynamic damping and peak to

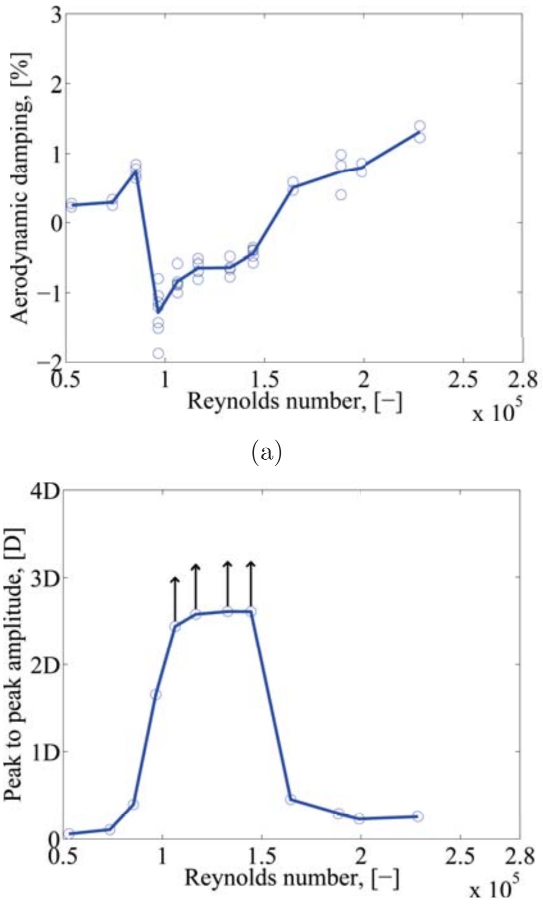

(a)

(b)

Figure 5.14: *Aerodynamic damping (a) and peak to peak amplitude (b) as function of Reynolds number in wet conditions, case 2b.*

peak amplitude of vibration for the cable model with m_{eff} = 10 kg/m, and untreated surface. The spray system was turned off and the cable surface was covered by water droplets, as for case 1d. The tested case is 2d. The aerodynamic damping is positive and ranges from 0.13% at Re=$0.55 \cdot 10^5$ to 1.49% at Re $= 2.14 \cdot 10^5$. It is thus generally higher than for the respective case 2d. The peak to peak amplitude of vibration is near zero for the whole Re range.

Fig. 5.17 shows the average aerodynamic damping (5.17(a)) and peak to peak amplitude vibration (5.17(b)) for cases 1b, 1c, 1d (m_eff = 18.07 kg/m) and 2b, 2c, 2d (m_eff = 10 kg/m).

Fig. 5.18 shows the average aerodynamic damping for m_{eff} = 18.07 kg/m (5.18(a)) and m_{eff} = 10 kg/m (5.18(b)) for cases 1a, 1c, 1d (m_eff

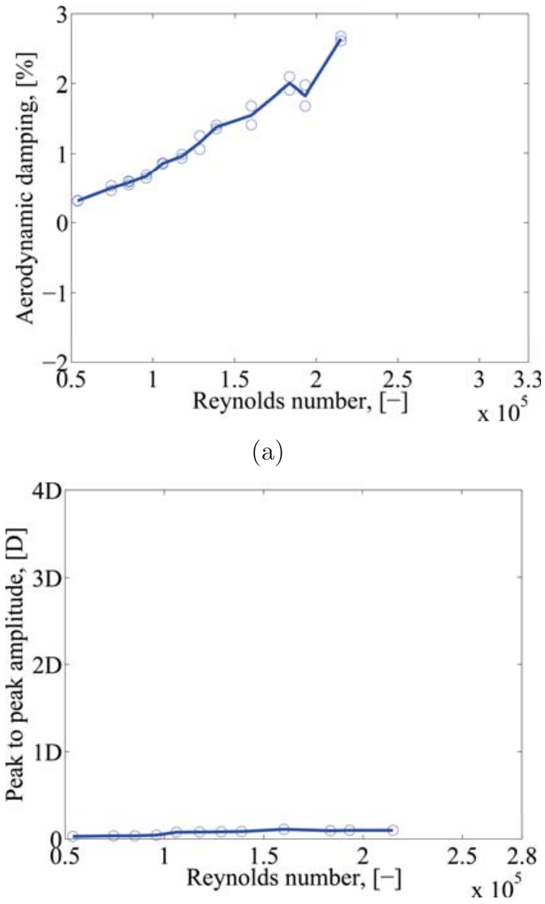

(a)

(b)

Figure 5.15: *Aerodynamic damping (a) and peak to peak amplitude (b) as function of Reynolds number in wet conditions, case 2c.*

= 18.07 kg/m) and 2a, 2c, 2d ($m_eff = 10$ kg/m). It is observed that the aerodynamic damping in dry conditions and in presence of steady upper and lower rivulet are very similar for both mass levels. Lower values of the aerodynamic damping occur for the cable covered by water droplets.

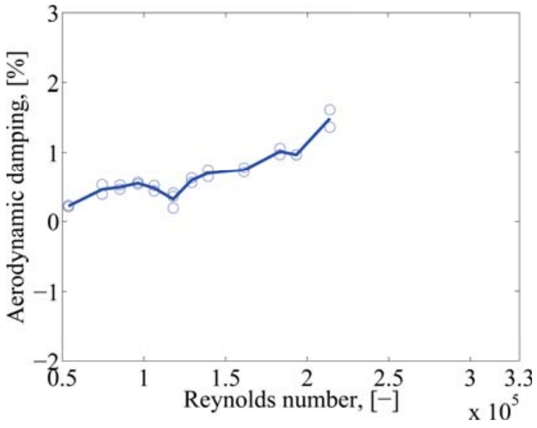

(a)

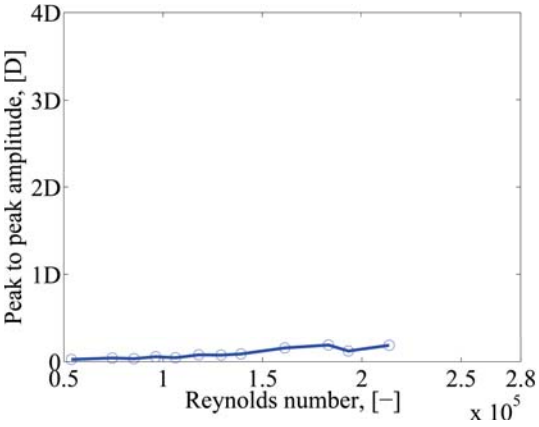

(b)

Figure 5.16: *Aerodynamic damping (a) and peak to peak amplitude (b) as function of Reynolds number in wet conditions, case 2d.*

5.4 Conclusion

Passive-dynamic wind tunnel tests were undertaken for a section of an inclined and yawed full-scale plain bridge cable model. Tests were performed for varying cable surface conditions, i.e. in the dry and wet state, for varying levels of surface wettability, and cable masses per unit length. Tests helped to better understand the instability mechanisms of bridge cable sections in dry and wet surface conditions.

In particular, galloping-type instability was detected in dry conditions in the critical Reynolds number range. Here the aerodynamic damping became negative and was accompanied by large amplitude vibrations. A decrease in the cable mass in dry conditions provoked an anticipation of the critical

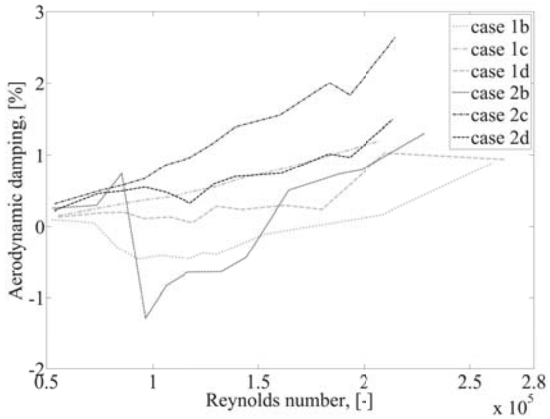

(a)

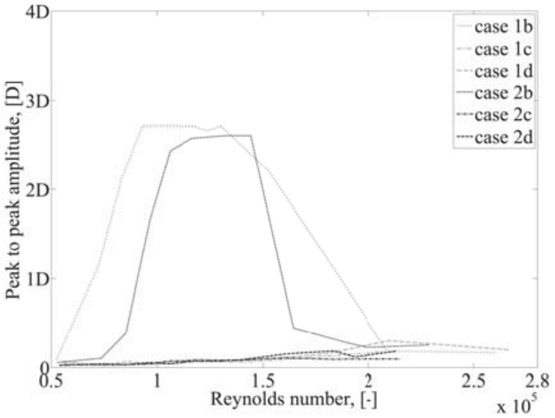

(b)

Figure 5.17: *Average aerodynamic damping (a) and peak to peak amplitude (b) as function of Reynolds number in wet conditions, cases 1b, 1c, 1d and 2b, 2c, 2d.*

Reynolds number and thus of the aerodynamic instability.

Under the effects of wind and rain, the cable model underwent different types of instability mechanisms, depending on the level of surface wettability and of mass. RWIV instability was observed only when the cable surface was characterised by an increased level of wettability, for all tested mass levels. The instability occurred only for a limited range of Reynolds number and was again characterized by the occurrence of large amplitude vibrations accompanied by negative aerodynamic damping. No RWIV instability was experienced for the cable model with very low wettability, either in presence of steady water rivulets, induced by a uniform water flow, or in presence of droplets, in the drying state. In particular, the aerodynamic damping of the

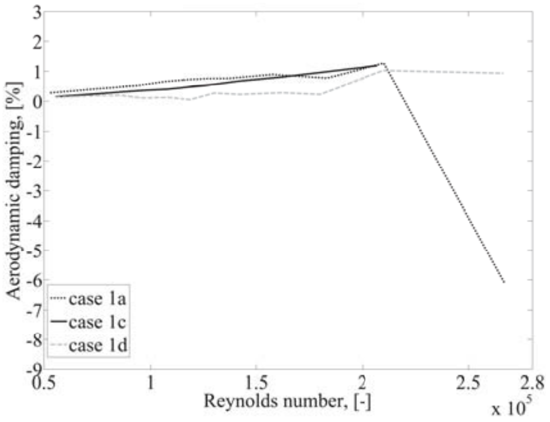

(a)

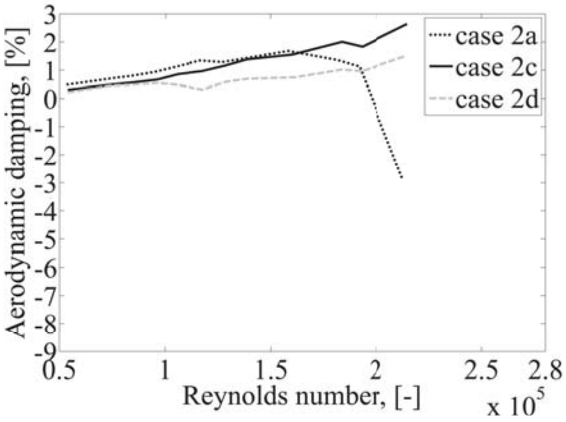

(b)

Figure 5.18: *Average aerodynamic damping as function of Reynolds number in wet conditions for cases 1a, 1c, 1d (a) and 2a, 2c, 2d (b)*

cable model in dry conditions and in wet conditions, in presence of steady water rivulets, were nearly equal for the range of Re up to $2{\cdot}10^5$ for both mass levels. For higher Re, the aerodynamic damping in dry conditions became negative and was accompanied by large amplitude vibrations, while in wet conditions it was still positive and the vibration was limited in amplitude. This implies that in the subcritical Re range the presence of steady rivulets doesn't lead to any kind of instability and the cable behaves as in dry conditions. The presence of the rivulets had instead a damping effect at high velocities; in fact, differently from the dry cable, the wet cable with steady rivulets was stable at high Reynolds numbers. In the drying state the cable model was characterized by a time dependent surface roughness, which leaded to a time dependency of the aerodynamic damping at a specific

Reynolds number. Finally in wet conditions, at the right level of surface wettability, the range of Re where the aerodynamic instability occurs is restricted by decreasing the cable mass. Thus at lower mass conditions, the oscillating water rivulets has a major damping effect than for higher mass. Note that for $m_{eff} = 18.07$ kg/m, occurs for a limited range of wind velocities which is narrower than for the $m_{eff} = 18.07$ kg/m. Decreasing the cable mass in wet conditions thus stabilizes the cable's aerodynamic behaviour for wind velocities of in the range of 8 to 9 m/s and 13.5 to 15 m/s.

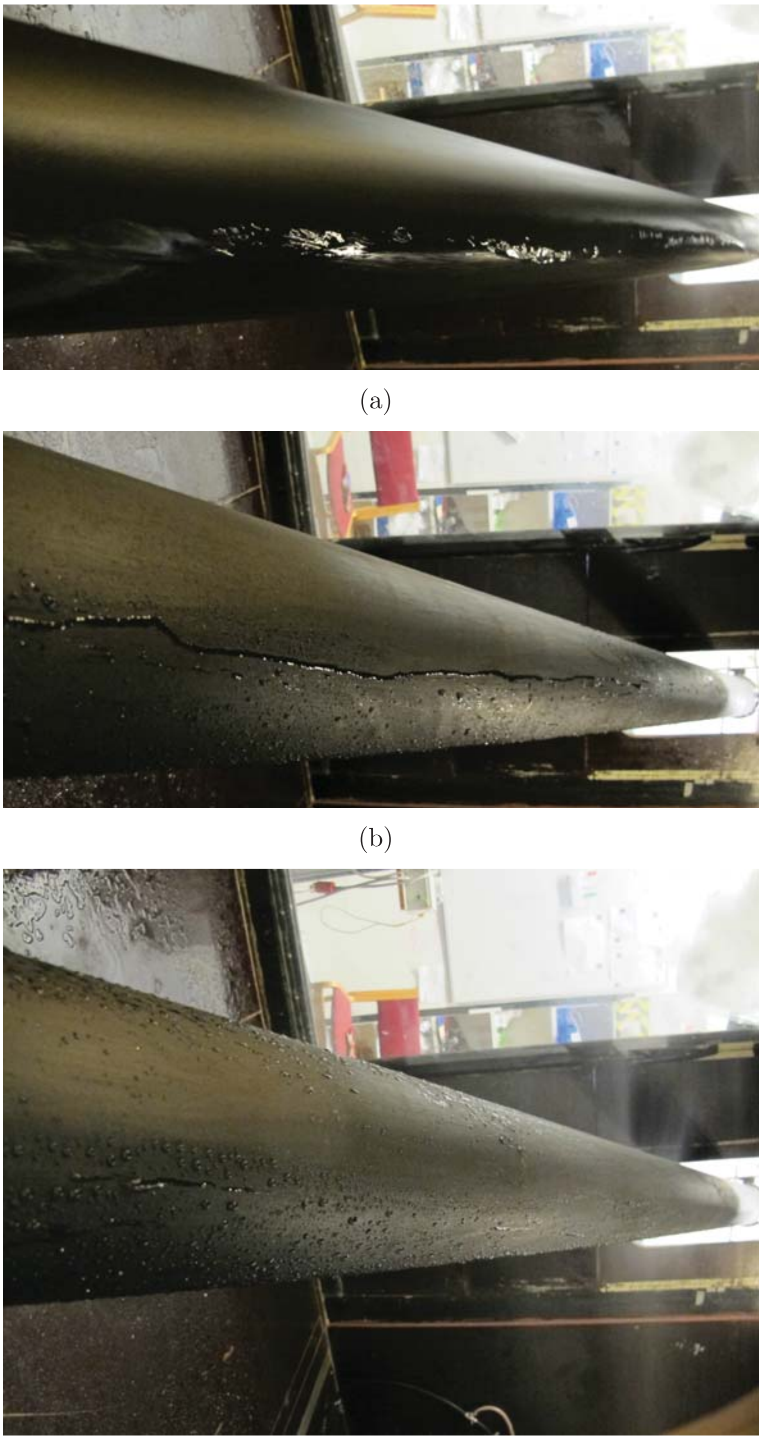
(a)

(b)

(c)

Figure 5.19*: View of the upper rivulet for the Gohsenol treated (a) and untreated (b) cable surface, and droplets formations for the untreated cable surface.*

Bibliography

Acampora, A., Georgakis, C.T., 2011. Recent monitoring of the Øresund Bridge: Observations of rain-wind induced cable vibrations. In: 13th International Wind Engineering Conference,Amsterdam.

Bosdogianni, A., Olivari, D., 1996. Wind- and rain-induced oscillations of cables of stayed bridges. J. Wind Eng. Ind. Aerodyn. 64, 171-185.

Cosentino, N., Flamand, O., Ceccoli, C., 2003a. Rain-wind induced vibration of inclined stay cables. Part I: Experimental investigation and physical explanation. J. Wind and Structures. 6, 471-484.

Eriksen, M.B., 2012. Passive-Dynamic Wind Tunnel Tests of Rain-Wind Induced Vibrations. Technical Report.

Flamand, O., 1995. Rain-wind induced vibrations of cables. J. Wind Eng. Ind. Aerodyn. 57, 353-362.

Georgakis, C.T., Koss, H.H., Ricciardelli, F., 2009. Design specifications for a novel climatic wind tunnel for testing of structural cables. In: 8th International Symposium on Cable Dynamics, Paris, pp. 333-340.

Hardy, C., Bourdon, P., 1979. The influence of spacer dynamic properties in the control of bundle conductor motion. IEEE PES Summer Meeting, Vancouver.

Hikami, Y., Shiraishi, N., 1988. Rain-wind induced vibrations of cables in cable stayed bridges. J. Wind Eng. Ind. Aerodyn. 29, 409-418.

Larose, G.L., Smitt, L.W., 1999. Rain/Wind induced vibration of parallel stay cables. In: IABSE Conference, Cable-Stayed Bridges - Past, Present and Future, Malmo, Sweden, pp - .

Lemaitre, C., de Langre, E., Hémon, 2010. Rainwater rivulets running on a stay cable subject to wind. European Journ. of Mechanics B/Fluids 29, 251-258.

Liu, Q., Wang, Y., Zheng, Y.,Ma, W., 2012. Experimental study on the relation of water rivulet-Reynolds number effect-cable vibration. In: 7th International Colloquium on Bluff Body Aerodynamics and Applications, Shanghai, China.

Ni, Y.Q., Wang, X.Y., Chen, Z.Q., Ko, J.M., 2007. Field observations of rain-wind-induced cable vibration in cable-stayed Dongting Lake Bridge. J. Wind Eng. Ind. Aerodyn. 95, 303-328.

Nippon Gohsei, How To Use GOHSENOL, October 2012.

Noisternig, J.F., 2000. Carbon Fibre Composites as Stay Cables for Bridges. Applied Composite Materials 7, 139-150.

Yoshimura, T., Tanaka, T., Sasaki, N., Nakatani, S., Higa, S., 1988. Rain-wind induced vibration of the cables of the Aratsu Bridge. In: 10th Nat. Conf. on Wind Engineering, Tokyo, pp. 127-132.

Wianecki, J., 1979. Cable wind excited vibrations of cable-stayed bridges. In: 5th Int. Conf. of Wind Eng., Colorado, Oxford-New York, Pergamon Press, pp. 1381-1393

Zuo, D., Jones, N.P., Main, J.A., 2008. Field observation of vortex- and rain-wind-induced stay-cable vibrations in a three-dimensional environment. J. Wind Eng. Ind. Aerodyn. 96, 1124-1133.

Zuo, D., Jones, N.P., 2010. Interpretation of field observations of wind-a nd rain-wind-induced stay cable vibrations. J. Wind Eng. Ind. Aerodyn. 98, 73-87.

Chapter 6

Analytical model

The results presented in this chapter are taken from the paper *Quasi-steady 3 DOF aerodynamic instability criterion for galloping and static divergence of an inclined/yawed prism*, to be submitted to the Journal of Fluids and Structures.

Abstract

A generalized quasi-steady three-degrees-of-freedom analytical model, capable of predicting the linear aerodynamic instability of a prism with generic cross-section, immersed in a turbulent wind flow is proposed. The three degrees-of-freedom refer to the two orthogonal displacements, perpendicular to the body's axis, plus the rotation about the longitudinal body axis. The model incorporates the inertial coupling, i.e. the non coincidence between the center of mass and the center of rotation between the degrees-of-freedom. It also allows for variation of the force coefficients, i.e. drag, lift, and moment, with Reynolds number based on the relative flow velocity, with relative angle-of-attack, and relative cable-wind angle. The aerodynamic forces acting on the structure are linearized about the static equilibrium configuration, i.e. about zero structural velocities along the three degrees-of-freedom, steady structural rotation about the body's longitudinal axis, and about the steady component of the total wind velocity. Based on the analytical solution of the eigenvalue problem, by applying the Routh-Hurwitz criterion, an expression of the galloping- and static divergence-type instability condition is derived. Additionally, a numerical solution of the minimum structural damping and structural stiffness required to prevent the same aerodynamic instabilities are given.

A practical application of the 3-DoFs instability model for the an iced

conductor section is finally proposed. The quasi-steady drag, lift and moment coefficients of the conductor were found in the existing literature, as well as the regions of aerodynamic instability, derived from passive-dynamic wind tunnel tests performed on the same conductor model. Maps of galloping and static divergence instability are presented for the test case and compared with predictions based on existing 1-DoF, 2-DoFs and 3-DoFs analytical models. It was found that the present model gives the best prediction of the regions of instability, when compared with dynamic test results.

6.1 Introduction

When a structure oscillates in steady flow, the flow field relative to the structure also oscillates, thus producing fluctuating aerodynamic force components, which can be coupled either linearly or non linearly, to the body's structural acceleration (a), velocity (b) or displacement/rotation (c), (Blevins and Iwan, 1975). In the first case, (a), a variation of the body's effective mass occurs. Nevertheless, as the mass of the surrounding air is normally negligible in comparison to the mass of the structural body, this variation is seldom sufficient to affect the system's stability. In the second case, (b), a variation of the body's effective damping occurs. This can eventually vanish when the flow field generates negative aerodynamic damping, equal in absolute value to the structural damping. This phenomenon can initiate instabilities of dynamic type, such as galloping, which are characterized by the occurrence of large amplitude vibrations, mostly in the cross-wind direction, at low frequencies. The galloping instability is of interest for a large class of bluff bodies, slender and with non-circular cross-section, typical examples being power line conductors or bridge cable sections covered by ice accretions, which experience flow separation and associated changes in the drag and lift coefficients at specific Reynolds numbers. In the third case, (c), a variation in the body's effective stiffness (frequency) is experienced. In particular, if the flow field generates negative aerodynamic stiffness, equal in absolute value to the structural stiffness, the body's effective stiffness becomes zero, causing a form of aerodynamic instability known as divergence. This instability is of static type and occurs for streamlined bodies, such as airfoil wings, when they experience an elastic rotation not counteracted by the body's torsional stiffness. All instabilities start suddenly, when a critical wind velocity is reached, and are characterized by a rapid increase in the structural displacements as the wind velocity increases, (Davenport and Novak, 2002).

Bluff-body aerodynamic instabilities of galloping-type have been modeled, based on the (QS) theory. According to the theory the aerodynamic forces on structures are expressed as nonlinear memoryless transformation of the flow-structure relative velocity and the angle-of-attack, which are variable in time due to the oscillation of the body and the presence of the turbulence of the oncoming flow (Kareem and Wu, 2013). The non linearities which arise in the aerodynamic force equations are normally approximated by means of polynomial expressions, i.e. for example by a Taylor series expansion, (Denoel and Degee, 2006), or by an optimization procedure aimed at minimizing some error measure, (Carassale and Kareem, 2010). The QS assumption is thus satisfied when the characteristic fluid-dynamic time scale of the velocity fluctuations in the wake of the body are much faster than the time scale of the body's oscillation. In fact, as galloping normally occurs at low reduced frequencies, the associated aerodynamic forces can be assumed as steady, and the susceptibility of a generic cross-section to galloping instability can be assessed by means of the aerodynamic force coefficients measured in static conditions.

First galloping instability models were based on the assumption that a structure responds to the aerodynamic excitation as a single DoF. Across-flow and along-flow instability criteria for a bluff body in cross-flow, known as 1-DoF galloping and drag crisis were derived by Den Hartog (1956) and Martin et al. (1981), respectively. In these models the aerodynamic force coefficients were assumed to only vary with angle-of-attack, (Den Hartog, 1956), and with Reynolds number, (Martin et al., 1981). Macdonald and Larose (2006) derived a generalized quasi-steady 1-DoF instability model, where the aerodynamic forces accounted for arbitrary orientation of the body's longitudinal axis with respect to the flow velocity (cable-wind angle), as well as orientation of the vibration axis with respect to the projection of the wind velocity in the body's cross-sectional plane (angle-of-attack). Moreover, the dependency of the force coefficients on the Reynolds number, was accounted for. The Reynolds number was evaluated based on the vectorial combination of the normal and axial flow velocities, as both affect the force coefficients in the critical range. The dependency of the force coefficients on the combination of the three latter parameters was neglected by previous galloping analyses, but it is fundamental for certain classes of bluff bodies, such as bridge stay cables. The model developed by Macdonald and Larose (2006) thus predicts different types of aerodynamic instabilities, and can be reduced, for specific combinations of the input parameters, to the Den Hartog galloping and drag crisis criteria.

Following analyses emphasized how real structures respond to aerodynamic excitation as multi-DoFs systems. Given the increased complexity of the analytical solution for a whole coupled 3-DoFs system, the instability models available in the literature mostly focus on reduced 2-DoFs systems.

These models are realistic only when the neglected mode has a frequency which is far away from the frequencies of the accounted DoFs. Jones (1992) analyzed the response of a bluff body in cross-flow, for coupled translational galloping, i.e. in vertical and horizontal motion. The force coefficients were modeled as function of the only angle-of-attack. By assuming that the vibration frequencies of the two selected modes were coincident (tuned case), a closed form solution to the fourth-order characteristic equation governing the instability problem was obtained. On the other hand, if this assumption is removed, numerical methods must be employed for the solution of the eigenvalue problem's characteristic equation; consequently only specific problems can be studied and an exhaustive description of all the possible critical conditions for varying system parameters is difficult to be obtained, (Luongo and Piccardo, 2005). By performing passive-dynamic wind tunnel tests, Cheng et al. (2008a) demonstrated that a 2-DoFs-type translatory galloping instability can also occur for bridge stay cables whose longitudinal axis is inclined/yawed with respect to the wind direction. The observed instability, known as dry inclined galloping, occurs in the critical Re range, and is characterized by major vibration components in the in-plane direction, with small vibration components in the out-of-plane direction, leading to elliptical trajectories. In this connection, Macdonald and Larose (2008a) and Macdonald and Larose (2008a) derived a 2-DoFs instability model able to predict the structural damping necessary to avoid galloping instability of an inclined/yawed cylinder moving in a 2D plane. As in the previous model, see (Macdonald and Larose, 2006), the force coefficients were modeled as function of the relative Reynolds number, cable-wind angle, and angle-of-attack. As Jones (1992), Macdonald and Larose (2008a) derived a closed form solution for the tuned case and Macdonald and Larose (2008b) derived a numerical solution for the detuned cases.

? pointed out that bluff bodies, whose center of mass doesn't coincide with the center of rotation, such as eccentrically iced conductors, can undergo instabilities associated with the torsional DoF, either of 1-DoF-type or multi-DoFs-type. The 1-DoF-type instability occurs when the torsional aerodynamic damping becomes negative and higher in absolute value than the inherent structural torsional damping; in this condition the torsional mode becomes self-exciting and the cylinder will oscillate at a frequency determined by the effective torsional stiffness and the polar moment of inertia. Multi-DoFs instability occurs when the torsional frequency approaches one of the resonant vertical or horizontal galloping frequencies; in this condition, the two lateral modes become excited through the coupled force terms. For ice-accreted cable conductors, it is apparent that the torsional stiffness and frequency are affected by the eccentric mass of the ice and by the slope of the moment coefficient against angle-of-attack. In particular, the torsional frequency is reduced when center of the eccentric ice mass is placed above the rotational center of the conductor and increased when this is placed below. Similarly, the torsional frequency is reduced when the slope of the aerodynamic moment is positive and increased when it is negative. The galloping response of a 2-DoFs system, vibrating in the across-flow and torsional direction, was investigated by Blevins and Iwan (1975) and Yu et al. (1992). Blevins and Iwan (1975) assumed that the mass-spring-damper system is uncoupled, i.e. the center of mass coincides with the elastic axis; this simplifying assumption was not made by Yu et al. (1992). Yu et al. (1993) extended the 2-DoFs model developed by Yu et al. (1993) to 3-DoFs, by additionally accounting of the along-flow vibration component. The models developed by Blevins and Iwan (1975), Yu et al. (1992) and Yu et al. (1993) are valid for cylinders in cross-flow. In all these models, the aerodynamic forces were linearized about angle-of-attack, while neglecting the Reynolds number dependency. A quasi-steady 2-DoF sectional model for galloping instability in the along- and across-flow direction was developed by Carassale et al. (2004). The model is valid for cylinders with generic orientation with respect to the wind flow, i.e. inclined/yawed. Similarly to Blevins and Iwan (1975) and Yu et al. (1992), Carassale et al. (2004) linearized the aerodynamic forces only about angle-of-attack.

Stoyanoff (2001) developed a 3-DoFs model valid for prisms with generic cross-section in cross-flow, such as bridge decks or towers. The total aerodynamic forces were modeled as the summation of the self-excited forces, i.e. aerodynamic damping and stiffness proportional terms, and the buffeting forces. The Reynolds number dependency of the force coefficients was neglected. Gjelstrup and Georgakis (2011) derived a 3-DoFs model for galloping instability of a bluff body with generic attitude to the wind flow. The model included the inertial coupling between the the 3-DoFs. The aerodynamic forces were represented following the same approach as adopted by Macdonald and Larose (2006) and Macdonald and Larose (2008a), Macdonald and Larose (2008b), i.e. by modeling the dependency of the force coefficients on the relative cable-wind angle, angle-of-attack and Reynolds number, and were later linearized only about zero structural velocities neglecting the expansion about the displacements. This leads to the elimination of all aerodynamic stiffness terms. Such simplification is valid only for compact sections (Gjelstrup and Georgakis, 2011).

The role of the wind turbulence on the aerodynamic instability of prismatic bodies has seldom been modeled analytically. Nevertheless, turbulent eddies are most effective in altering the flow structure around such bodies and thus affect their inherent aerodynamic stability. In particular, the main effect of the small-scale turbulence is to cause earlier reattachment of the flow through enhanced mixing in the shear layers. Turbulence in the range of the body's scale can enhance or weaken vortex shedding depending on the body's geometry, (Kareem and Wu, 2013). Effects of small-scale wind turbulence were considered by Symes and Macdonald (2006), who expanded 1-DoF analytical model developed by Macdonald and Larose (2006), by applying turbulence intensity corrections on both Reynolds number and associated force coefficients. Corrections were based on ESDU. Recently, Raeesi et al. (2013) proposed a 1-DoF instability model for inclined circular cylinders where the effect of small scale turbulence was included by means of an unsteady wind model. The model was developed by applying Discrete Wavelet Transform to a set of field wind data. The large scale turbulence, which changes more slowly, generates a variation in the wind velocity and in the associated aerodynamic loading. The load variation can produce random forced vibration which can generate a type of instability named as buffeting. The impact of large-scale turbulence was included by Symes and Macdonald (2007) in a 1-DoF analytical model valid for inclined prisms.

A generalized quasi-steady 3-DoFs analytical model, capable of predicting the aerodynamic instability of a prism with generic cross-section, immersed in turbulent wind flow, is here proposed. The model accounts for the inertial coupling between the 3-DoFs, and allows for variation of the force coefficients, i.e. drag, lift, and moment, with Reynolds number based on the relative flow velocity, with relative angle-of-attack, and relative cable-wind angle. The aerodynamic forces acting on the prism are modeled as non linear function of the prism's structural velocity along the 3 DoFs, of the structural rotation about the longitudinal axis, as well of the total wind velocity, which comprises a steady component and nil-mean fluctuating components. The aerodynamic forces are linearized about zero structural velocities, steady structural rotation and about the steady component of the total wind velocity. The equations of motion are written by following the Euler-Lagrange method. Later, they are expressed in the state space representation. Based on the analytical solution of the eigenvalue problem, by applying the Routh-Hurwitz criterion, an expression of the galloping- and static divergence-type instability condition is derived. Additionally, a numerical solution of the minimum structural damping and structural stiffness required to prevent the same aerodynamic instabilities are given.

An application of the 3-DoFs analytical model is proposed in order to study the galloping and static divergence stability conditions of two separate test cases, i.e. an ice-accreted model of a cable conductor in cross flow, (Chabart and Lilien, 1998). For the ice accreted cable in cross flow a comparison of the regions of galloping instability derived analytically, with results of passive-dynamic wind tunnel tests undertaken for the same conductor model, (Chabart and Lilien, 1998), revealed that the present model provides an improved prediction of the regions of galloping instability in comparison to existing models. Stability maps of galloping and static divergence were derived. It was found that for selected ranges of angle-of-attack and Reynolds number, the ice accreted cable in cross-flow can undergo both galloping and static divergence instability. An increase in the structural damping ratio along all DoFs helps to reduce the amplitude of the regions of galloping instability, while it doesn't produce any effect on the regions of static divergence instability. A reduction of the structural rotational stiffness reduces the amplitude of the regions of both galloping and static divergence instability. On the other hand a reduction of the along-wind structural stiffness reduces the regions of galloping instability but has no effect on the static divergence.

6.2 Linearization of the aerodynamic and mechanical model

6.2.1 Flow around fixed inclined prism

A prism of generic section is immersed in a conventional turbulent wind field. This is modeled by a mean wind velocity component, U, and fluctuating wind velocity components along three othrogonal directions, $\tilde{u}(t)$, $\tilde{v}(t)$, $\tilde{w}(t)$. A global reference system (X, Y, Z) is defined, where the X, Y axes lay on a horizontal plane and are parallel to U, $\tilde{u}(t)$ and $\tilde{v}(t)$, respectively, while Z is vertical, and parallel to $\tilde{w}(t)$, see Fig. 6.1. The total wind velocity $\mathbf{U}(t)$ is given by

$$\mathbf{U}(t) = \mathbf{U} + \tilde{\mathbf{U}}(t) = \begin{bmatrix} U & 0 & 0 \end{bmatrix}^T + \begin{bmatrix} \tilde{u}(t) & \tilde{v}(t) & \tilde{w}(t) \end{bmatrix}^T \tag{6.1}$$

The typical attitude in the flow of a prism is given by an inclination Θ, i.e. the angle between the body's longitudinal axis and its projection in the horizontal plane, and a yaw angle β, i.e. the angle between the free-stream velocity U and the projection of the body's axis in the horizontal plane. In general, for civil engineering applications, the inclination is a physical/geometrical characteristic, while the yaw depends on the wind direction. A local reference system for the prism (x, y, z) is introduced, where x, y belong to its cross-sectional plane and z is parallel to the prism's longitudinal axis, see Fig. 6.2. If the prism is considered to be initially oriented parallel to the global Z axis, so that the local and global reference systems are coincident, the inclined/yawed configuration is obtained after a sequence of two elemental rotations. The first one is a rotation about the Y axis of entity $(\pi/2-\Theta)$, while the second is a rotation about the Z axis of entity $-\beta$.

The total wind vector in the rotated local reference system for the prism is given by

$$\begin{aligned}\mathbf{U}_r(t) &= \mathbf{R}_Y(\pi/2-\Theta)\mathbf{R}_Z(-\beta)\mathbf{U}(t) = \\ &= \begin{bmatrix} \sin\Theta\cos\beta\,(U+\tilde{u}(t))+\sin\Theta\sin\beta\tilde{v}(t)+\cos\Theta\tilde{w}(t) \\ -\sin\beta\,(U+\tilde{u}(t))+\cos\beta\tilde{v}(t) \\ -\cos\Theta\cos\beta\,(U+\tilde{u}(t))-\cos\Theta\sin\beta\tilde{v}(t)+\sin\Theta\tilde{w}(t)\end{bmatrix}\end{aligned} \tag{6.2}$$

where $\mathbf{R}_Y(\pi/2-\Theta)$, $\mathbf{R}_Z(-\beta)$ are the rotation matrices around the axis Y and Z, respectively.

The total component of the wind velocity in the prism's section, named normal flow velocity, $U_N(t)$, is given by:

$$\begin{aligned}U_N(t) &= \sqrt{\left(U_{r,1}(t)\right)^2+\left(U_{r,2}(t)\right)^2} = \\ &= \sqrt{\begin{array}{l}\left(\sin\Theta\cos\beta\,(U+\tilde{u}(t))+\sin\Theta\sin\beta\tilde{v}(t)+\cos\Theta\tilde{w}(t)\right)^2+ \\ +\left(-\sin\beta\,(U+\tilde{u}(t))+\cos\beta\tilde{v}(t)\right)^2\end{array}}\end{aligned} \tag{6.3}$$

The component of the wind velocity along the prism's longitudinal axis, known as axial wind velocity, is:

$$U_A(t)=U_{r,3}(t)=-\cos\Theta\cos\beta\,(U+\tilde{u}(t))-\cos\Theta\sin\beta\tilde{v}(t)+\sin\Theta\tilde{w}(t) \tag{6.4}$$

The angle $\Phi(t)$ between the prism's axis and the free-stream velocity $\mathbf{U}$ is given by:

$$\begin{aligned}\Phi(t) &= \arccos\left(\frac{|U_A(t)|}{U+\tilde{u}(t)}\right) = \\ &= \arccos\left(\frac{|-\cos\Theta\cos\beta\,(U+\tilde{u}(t))-\cos\Theta\sin\beta\tilde{v}(t)+\sin\Theta\tilde{w}(t)|}{U+\tilde{u}(t)}\right)\end{aligned} \tag{6.5}$$

A second local reference system (x', y', z) is chosen for the prism, so that the local axis x' is parallel to the direction of the normal wind velocity $U_N(t)$, see Figs. 6.1, 6.2. The wind velocity vector in the (x', y', z) reference system is:

$$\mathbf{U}_{r'}(t)=\left[\begin{array}{ccc} U_N(t) & 0 & U_A(t)\end{array}\right]^T \tag{6.6}$$

The angle between $U_N(t)$ and the plane containing the prism's longitudinal axis and its horizontal projection, is:

$$\alpha_s(t)=\arccos\frac{U_{r,1}(t)}{U_N(t)} \tag{6.7}$$

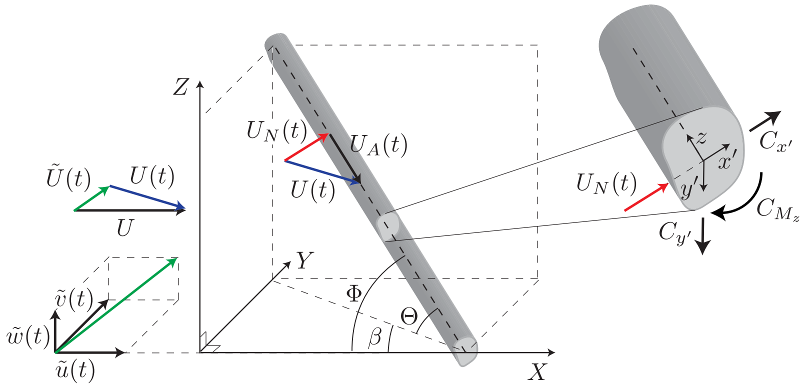

Figure 6.1: *3D geometry of the structural member.*

6.2.2 Flow around moving inclined prism

The model allows for the motion of the prism along three degrees of freedom (3 DOFs) represented by the vector

$$\mathbf{q}(t) = \begin{bmatrix} \xi(t) & \eta(t) & \theta(t) \end{bmatrix}^T \tag{6.8}$$

where $\xi(t)$, $\eta(t)$ are two orthogonal displacements belonging to a plane with generic spacial orientation with respect to the prism's cross section and $\theta(t)$ is the rotation about the prism's longitudinal axis. Most commonly, as in this analysis, the displacements $\xi(t)$ and $\eta(t)$, are assumed to be parallel to the vertical in-plane and out-of-plane directions, x and y, respectively. The structural velocity and acceleration, i.e. given by the first and second time derivatives of the displacement vector $\mathbf{q}(t)$, are indicated as $\dot{\mathbf{q}}(t)$ and $\ddot{\mathbf{q}}(t)$, respectively. The cross-radial tangential velocity varies in intensity and direction along the prism's cross-sectional boundary, due to the effect of $\dot{\theta}(t)$. In fact, its intensity is given by

$$\left| \mathbf{R} \wedge \dot{\theta}(t) \right| \tag{6.9}$$

where $\mathbf{R}$ is the distance of a generic point located on the prism's section boundary to the shear center (or center of rotation). The direction is tangent to the prism's cross-section at the specific point of evaluation. Following Blevins (1977), the velocity field on the cross section's boundary is thus approximated by choosing a reference point, which is representative of the net flow field. Normally this point is located at the leading edge, i.e. at distance R_δ from the shear center and at angular distance δ from the x' local axis. Alternative to this approach is to perform a full series of dynamic tests in order to characterize the forces on the rotating cross-section.

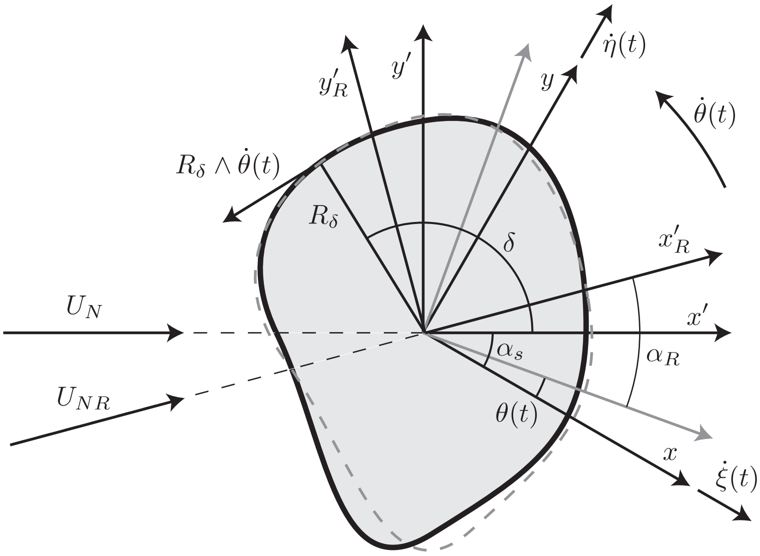

Figure 6.2: *Plane normal to the prism's axis.*

The angle $\varphi(t)$ is defined as

$$\begin{aligned}\varphi(t) &= \alpha_s(t) - \theta(t) = \\ &= \arctan\left(\frac{-\sin\beta\,(U+\tilde{u}(t)) + \cos\beta\tilde{v}(t)}{\sin\Theta\cos\beta\,(U+\tilde{u}(t)) + \sin\Theta\sin\beta\tilde{v}(t) + \cos\Theta\tilde{w}(t)}\right) - \theta(t)\end{aligned} \tag{6.10}$$

The vector $\dot{\mathbf{q}}_R(t)$, defined as

$$\begin{aligned}\dot{\mathbf{q}}_R(t) &= \mathbf{R}_z\,(-\varphi(t))\,\dot{\mathbf{q}}(t) + \dot{\boldsymbol{\omega}}(t) \wedge \mathbf{R}_\delta = \\ &= \begin{bmatrix}\cos\varphi(t) & \sin\varphi(t) & 0\\ -\sin\varphi(t) & \cos\varphi(t) & 0\\ 0 & 0 & 1\end{bmatrix}\begin{bmatrix}\dot{\xi}(t)\\ \dot{\eta}(t)\\ \dot{\theta}(t)\end{bmatrix} + \begin{bmatrix}0\\ 0\\ \dot{\theta}(t)\end{bmatrix} \wedge \begin{bmatrix}R_\delta\cos\delta\\ R_\delta\sin\delta\\ 0\end{bmatrix} \\ &= \begin{bmatrix}\dot{\xi}(t)\cos\varphi(t) + \dot{\eta}(t)\sin\varphi(t) - R_\delta\dot{\theta}(t)\cdot\sin\delta\\ -\dot{\xi}(t)\cdot\sin\varphi(t) + \dot{\eta}(t)\cos\varphi(t) - R_\delta\dot{\theta}(t)\cos\delta\\ \dot{\theta}(t)\end{bmatrix}\end{aligned} \tag{6.11}$$

represents the structural velocity in the (x', y', z) local reference system, where $\dot{q}_{R,1}$, $\dot{q}_{R,2}$ are the structural velocities in the prism's cross sectional plane, parallel to the x' and y' directions, while $\dot{q}_{R,3}$ represents the angular velocity.

The relative wind velocity $\mathbf{U}_R(t)$ in the (x', y', z) local reference system is the difference between the total wind velocity $\mathbf{U}_{r'}(t)$ and the components of $\dot{\mathbf{q}}_R(t)$ in the prism's cross-section.

$$\mathbf{U}_R(t) = \mathbf{U}_{r'}(t) - \dot{\mathbf{q}}_R(t) = \begin{bmatrix} U_N(t) & 0 & U_A(t) \end{bmatrix}^T - \begin{bmatrix} \dot{q}_{R,1} & \dot{q}_{R,2} & 0 \end{bmatrix}^T \\ = \begin{bmatrix} U_N(t) - \dot{\xi}(t)\cos\varphi(t) - \dot{\eta}(t)\sin\varphi(t) + R_\delta\dot{\theta}(t)\cdot\sin\delta \\ \dot{\xi}(t)\cdot\sin\varphi(t) - \dot{\eta}(t)\cos\varphi(t) + R_\delta\dot{\theta}(t)\cos\delta \\ U_A(t) \end{bmatrix} \tag{6.12}$$

The intensity $U_{NR}(t)$ of relative normal wind velocity is

$$U_{NR}(t) = \sqrt{(U_{R,1})^2 + (U_{R,2})^2} \\ = \sqrt{\begin{matrix}\Big(U_N(t) - \dot{\xi}(t)\cos\varphi(t) - \dot{\eta}(t)\sin\varphi(t) + R_\delta\dot{\theta}(t)\cdot\sin\delta\Big)^2 + \\ \Big(\dot{\xi}(t)\sin\varphi(t) - \dot{\eta}(t)\cos\varphi(t) + R_\delta\dot{\theta}(t)\cdot\cos\delta\Big)^2\end{matrix}} \tag{6.13}$$

The angle between $\mathbf{U}_{NR}(t)$ and the local x axis is

$$\alpha_R(t) = \varphi(t) + \arctan\left(\frac{U_{R,2}}{U_{R,1}}\right) \\ = \arctan\left(\frac{-\sin\beta\,(U + \tilde{u}(t)) + \cos\beta\tilde{v}(t)}{\sin\Theta\cos\beta\,(U + \tilde{u}(t)) + \sin\Theta\sin\beta\tilde{v}(t) + \cos\Theta\tilde{w}(t)}\right) - \theta(t) + \\ + \arctan\left(\frac{\dot{\xi}(t)\sin\varphi(t) - \dot{\eta}(t)\cos\varphi(t) + R_\delta\dot{\theta}(t)\cos\delta}{U\cdot\sin\phi - \dot{\xi}(t)\cos\varphi(t) - \dot{\eta}(t)\sin\varphi(t) + R_\delta\dot{\theta}(t)\sin\delta}\right) \tag{6.14}$$

Following eq. 6.5, the relative cable-wind angle $\Phi_R(t)$ is:

$$\Phi_R(t) = \arccos\left(\frac{|U_A(t)|}{|\mathbf{U}_R(t)|}\right) = \\ = \arccos\left(\frac{|-\cos\Theta\cos\beta\,(U + \tilde{u}(t)) - \cos\Theta\sin\beta\tilde{v}(t) + \sin\Theta\tilde{w}(t)|}{|\mathbf{U}_R(t)|}\right) \tag{6.15}$$

The linearized expression of $U_R(t)$, $\Phi_R(t)$, $\alpha_R(t)$ is:

$$\mathbf{b}(\dot{\mathbf{q}}(t), \theta(t), \mathbf{U}(t)) = \begin{bmatrix} U_R(\dot{\mathbf{q}}, \theta(t), \mathbf{U}(t)) & \alpha_R(\dot{\mathbf{q}}, \theta(t), \mathbf{U}(t)) & \Phi_R(\dot{\mathbf{q}}, \theta(t), \mathbf{U}(t)) \end{bmatrix}^T \tag{6.16}$$

where

$$\begin{aligned}
U_R(\dot{\mathbf{q}},\theta(t),\mathbf{U}(t)) &= U + \tilde{u}(t) - \sin\Phi\left(\cos\bar{\varphi}\dot{\xi}(t) + \sin\bar{\varphi}\dot{\eta}(t) - R_\delta \sin\delta\dot{\theta}(t)\right)\\
\alpha_R(\dot{\mathbf{q}},\theta(t),\mathbf{U}(t)) &= \bar{\varphi} + \frac{1}{U(\sin^2\Theta + \tan^2\beta)}\left(\sin\Theta(1+\tan^2\beta)\widetilde{v}(t) + \frac{\cos\Theta\sin\beta}{\cos^2\beta}\widetilde{w}(t)\right)\\
&\quad + \frac{1}{U\sin\Phi}\left(\sin\bar{\varphi}\dot{\xi}(t) - \cos\bar{\varphi}\dot{\eta}(t) - R_\delta\cos\delta\dot{\theta}(t)\right) - \theta(t)\\
\Phi_R(\dot{\mathbf{q}},\theta(t),\mathbf{U}(t)) &= -\frac{1}{U\sin\Phi}\left(\cos\Theta\sin\beta\tilde{v}(t) - \sin\Theta\tilde{w}(t)\right)\\
&\quad + \frac{\sin\Theta}{U}\Phi - \frac{\cos\Phi}{U}\left(\cos\bar{\varphi}\dot{\xi}(t) + \sin\bar{\varphi}\dot{\eta}(t) - R_\delta\sin\delta\dot{\theta}(t)\right)
\end{aligned} \tag{6.17}$$

Detailed derivation of eq. 6.17 is reported in Appendix A.2.

6.2.3 Aerodynamic forces

The aerodynamic force coefficients, $\mathbf{C}$ depend on the Reynolds number, Re, wind angle-of-attack, α, and cable-wind angle, Φ. This dependency can be expressed as

$$\mathbf{C}(\mathbf{d}) = \begin{bmatrix} C_{x'}(\mathbf{d}) & C_{y'}(\mathbf{d}) & DC_{Mz}(\mathbf{d}) \end{bmatrix}^T \tag{6.18}$$

where the vector $\mathbf{d}$ is obtained by applying the transformation

$$\begin{aligned}
\mathbf{d}(\dot{\mathbf{q}}(t),\theta(t),\mathbf{U}(t)) &= \mathbf{T}\mathbf{b}(\dot{\mathbf{q}}(t),\theta(t),\mathbf{U}(t))\\
&= \begin{bmatrix} Re_R(\dot{\mathbf{q}}(t),\theta(t),\mathbf{U}(t))\\ \alpha_R(\dot{\mathbf{q}}(t),\theta(t),\mathbf{U}(t))\\ \Phi_R(\dot{\mathbf{q}}(t),\theta(t),\mathbf{U}(t)) \end{bmatrix}
\end{aligned} \tag{6.19}$$

$\mathbf{T}$ is the transformation matrix

$$\mathbf{T} = \begin{bmatrix} \frac{D}{\nu} & 0 & 0\\ 0 & 1 & 0\\ 0 & 0 & 1 \end{bmatrix} \tag{6.20}$$

and Re_R is the Reynolds number based on U_R. Detailed derivation of eq. 6.19 is reported in Appendix A.2.

The aerodynamic forces $\mathbf{F}_a$ per unit length along the x'_R, y'_R axes, and the moment about the z axes are

$$\begin{aligned}\mathbf{F}_a(\dot{\mathbf{q}}(t), \theta(t), \mathbf{U}(t)) &= \begin{bmatrix} F_x(\dot{\mathbf{q}}(t), \theta(t), \mathbf{U}(t)) \\ F_y(\dot{\mathbf{q}}(t), \theta(t), \mathbf{U}(t)) \\ M_z(\dot{\mathbf{q}}(t), \theta(t), \mathbf{U}(t)) \end{bmatrix} = \\ &= \frac{1}{2}\rho D U_R^2(\dot{\mathbf{q}}(t), \mathbf{U}(t)) \mathbf{R}_z(d_2)\mathbf{C}(\mathbf{d}) = \\ &= \frac{\rho \nu^2}{2D} Re_R^2(\dot{\mathbf{q}}(t), \mathbf{U}(t)) \mathbf{R}_z(d_2)\mathbf{C}(\mathbf{d})\end{aligned} \tag{6.21}$$

where $\mathbf{R}_z(d_2)$ is the rotation matrix about the z axis.

The aerodynamic forces are non linear functions of $\dot{\mathbf{q}}(t)$, $\theta(t)$, $\mathbf{U}(t)$. A first order Taylor expansion of the aerodynamic forces about $\dot{\mathbf{q}}(t) = \mathbf{0}$, $\mathbf{q}(t) = \mathbf{0}$, $\mathbf{U}(t) = \mathbf{U}$ is performed:

$$\begin{aligned}\mathbf{F}_a(\dot{\mathbf{q}}(t), \mathbf{q}(t), \mathbf{U}(t)) = \mathbf{F}_a\big|_{(\mathbf{0},\mathbf{0},\mathbf{U})} + \nabla_{\dot{\mathbf{q}}(t)}\mathbf{F}_a\big|_{(\mathbf{0},\mathbf{0},\mathbf{U})} \dot{\mathbf{q}}(t) + \\ + \nabla_{\mathbf{q}(t)}\mathbf{F}_\mathbf{a}\big|_{(\mathbf{0},\mathbf{0},\mathbf{U})} \mathbf{q}(t) + \nabla_{\mathbf{U}(t)}\mathbf{F}_\mathbf{a}\big|_{(\mathbf{0},\mathbf{0},\mathbf{U})} (\mathbf{U}(t) - \mathbf{U})\end{aligned} \tag{6.22}$$

The first term of equation 6.22, i.e.

$$\mathbf{F}_{\mathbf{a}(\mathbf{0},\mathbf{0},\mathbf{U})} = \frac{\rho Re^2 \nu^2}{2D} \begin{bmatrix} C_{x'} \cos\bar{\varphi} - C_{y'} \sin\bar{\varphi} \\ C_{x'} \sin\bar{\varphi} + C_{y'} \cos\bar{\varphi} \\ DC_M \end{bmatrix} \tag{6.23}$$

contains the steady components of the aerodynamic forces per unit length.

The second and third terms of equation 6.22 can be rearranged as

$$\nabla_{\dot{\mathbf{q}}(t)}\mathbf{F}_a\big|_{(\mathbf{0},\mathbf{0},\mathbf{U})} \dot{\mathbf{q}}(t) = \mathbf{C}_a\dot{\mathbf{q}}(t) = \begin{bmatrix} 2m\omega_x & 2m\omega_x & 2m\omega_x \\ 2m\omega_y & 2m\omega_y & 2m\omega_y \\ 2J\omega_\theta & 2J\omega_\theta & 2J\omega_\theta \end{bmatrix} \cdot \boldsymbol{\xi}_a \dot{\mathbf{q}}(t) \tag{6.24}$$

and

$$\nabla_{\mathbf{q}(t)}\mathbf{F}_\mathbf{a}\big|_{(\mathbf{0},\mathbf{0},\mathbf{U})} \mathbf{q}(t) = \mathbf{K}_a\mathbf{q}(t) = \begin{bmatrix} m & m & m \\ m & m & m \\ J & J & J \end{bmatrix} \cdot \boldsymbol{\omega}_a^2 \mathbf{q}(t) \tag{6.25}$$

where m is the prism's mass per unit length, J is the rotational inertia, ω_i are the angular frequencies along the i DOF. $\mathbf{C}_a\dot{\mathbf{q}}(t)$ and $\mathbf{K}_a\mathbf{q}(t)$ represent the aerodynamic damping and stiffness forces per unit length.

In order to represent the aerodynamic damping and stiffness matrices in eqs. 6.24-6.25 in terms of aerodynamic damping ratio, $\boldsymbol{\xi}_a$, and angular frequency, $\boldsymbol{\omega}_a^2$, the following transformation is applied:

$$\boldsymbol{\xi}_a = \mathbf{T}_{\xi C} \cdot \mathbf{C}_a \quad \boldsymbol{\omega}_a^2 = \mathbf{T}_{\omega K} \cdot \mathbf{K}_a \tag{6.26}$$

where $\mathbf{T}_{\xi C}$ is the tensor transforming $\mathbf{C}$ in $\boldsymbol{\xi}$ and $\mathbf{T}_{\omega K}$ is the tensor transforming $\mathbf{K}$ in $\boldsymbol{\omega}^2$. The two tensors are:

$$\mathbf{T}_{\xi C} = \begin{bmatrix} \dfrac{1}{2m\omega_x} & \dfrac{1}{2m\omega_x} & \dfrac{1}{2m\omega_x} \\ \dfrac{1}{2m\omega_y} & \dfrac{1}{2m\omega_y} & \dfrac{1}{2m\omega_y} \\ \dfrac{1}{2J\omega_\theta} & \dfrac{1}{2J\omega_\theta} & \dfrac{1}{2J\omega_\theta} \end{bmatrix} \quad \mathbf{T}_{\omega K} = \begin{bmatrix} \dfrac{1}{m} & \dfrac{1}{m} & \dfrac{1}{m} \\ \dfrac{1}{m} & \dfrac{1}{m} & \dfrac{1}{m} \\ \dfrac{1}{J} & \dfrac{1}{J} & \dfrac{1}{J} \end{bmatrix} \tag{6.27}$$

The transformation matrices are valid for both structural and aerodynamic parameters. The inverse transformation from the damping ratio and the frequency to the damping and stiffness respectively can be obtained by applying the transformation matrices $\mathbf{T}_{C\xi}$ and $\mathbf{T}_{\mathrm{K}\omega}$. These latter are obtained by inverting each element of the matrix representing the inverse transformation, i.e. $T_{\xi Ci,j} = T^{-1}_{C\xi i,j}$.

The fourth term of equation 6.22, i.e.

$$\nabla_{\mathbf{U}(t)}\mathbf{F_a}\big|_{(\mathbf{0},\mathbf{0},\mathbf{U})}\left(\mathbf{U}(t)-\mathbf{U}\right) = \mathbf{B}\left(\mathbf{U}(t)-\mathbf{U}\right) \tag{6.28}$$

represents the buffeting forces, i.e. given by the product of the buffeting matrix $\mathbf{B}$ to the fluctuating velocity vector $(\mathbf{U}(t)-\mathbf{U})$.

Detailed derivation of equation 6.22 is reported in the Appendix A.1, A.3.

6.2.4 Structural properties and EOM

The prism is modeled as a spring-damped rigid body of indefinite length, i.e. a sectional model, see Fig. 6.3. The mechanical properties are assumed to be linear and time invariant. A more sophisticated model can consider the mechanics as non-linear. In this case the equation of motion should be linearized about the stationary steady state, i.e. the equilibrium point of the steady forces.

The equations of motion for the prism are written by following the Euler-Lagrange approach, as in Gjelstrup and Georgakis (2011). Their detailed derivation is reported in Appendix A.4. The final EOM is

$$\mathbf{M}_s\ddot{\mathbf{q}}(t) + \mathbf{C}_s\dot{\mathbf{q}}(t) + \mathbf{K}_s\mathbf{q}(t) = \mathbf{F}_m + \mathbf{F}_a(\dot{\mathbf{q}}(t), \mathbf{q}(t), \mathbf{U}(t)) \tag{6.29}$$

where $\mathbf{M}_s$, $\mathbf{C}_s$, $\mathbf{K}_s$ are the structural mass, damping and stiffness matrices, respectively, $\mathbf{F}_m$ represents the gravitational force vector and $\mathbf{F}_a$ represents the aerodynamic force vector (eq. 6.21). In the following, it will be assumed that $\mathbf{M}_s$, $\mathbf{C}_s$, $\mathbf{K}_s$ are symmetric. Additionally, $\mathbf{M}_s$ is positive definite, and

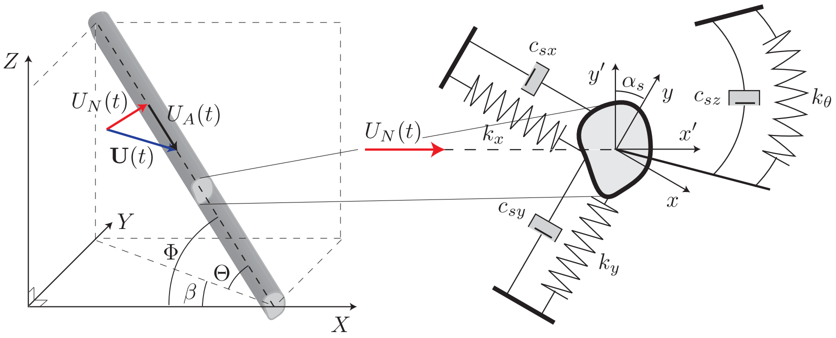

Figure 6.3: *Mechanical model.*

$\mathbf{C}_s$ and $\mathbf{K}_s$ are non negative definite. The gravitational forces are taken into account in the equation of motion, as, when the section's shear section is not coincident with the center of mass, a sectional rotation can be induced by $\mathbf{F}_m$. For instance, this phenomenon can take place on iced conductors. In this case the rotation of the section can change the parameter $\bar{\theta}$, which represents the steady rotation of the section.

6.3 State space representation

The system's representation in the state space form before and after linearization (see 6.2) is presented here below.

The state space representation is widely used in control engineering, where the methods of solution and stability analysis of linear and non-linear systems are well established. The state space representation is a mathematical model of a physical system as a set of input, output and state variables related by first order differential equations. To abstract from the number of inputs, outputs and states, the variables are expressed as vectors. In order to obtain first order differential equations, the system is transformed from a system of 3 differential equations of order 2, to a system of 6 first order differential equations, i.e. the state space representation.

Fig. 6.4(a) describes the system before its linearization. The state of the system is be fully described by the state vector $\mathbf{x}(t)$, given by

$$\mathbf{x}(t) = \left[\begin{array}{cc} \mathbf{q}(t) & \dot{\mathbf{q}}(t) \end{array}\right] \tag{6.30}$$

The inputs are the total wind velocity described by the vector $\mathbf{U}(t)$ and the gravity vector $\mathbf{g}'_s$. The inputs are transformed into the aerodynamics and the mass accelerations by applying the input matrix, which in this case is decomposed in $\mathbf{B}_a(\mathbf{x}(t),\mathbf{U}(t))$ and $\mathbf{B}_g$. $\mathbf{B}_a(\mathbf{x}(t), \mathbf{U}(t))$ is a nonlinear vector which depends on the state parameters $\mathbf{x}(t)$ and on the instantaneous wind speed vector $\mathbf{U}(t)$:

$$\mathbf{B_a}(\mathbf{x}(t), \mathbf{U}(t)) = \mathbf{M}_s^{-1} \left[\begin{array}{c} \mathbf{0} \\ \mathbf{F}_a(\dot{\mathbf{q}}(t), \theta(t), \mathbf{U}(t)) \end{array} \right] \tag{6.31}$$

where $\mathbf{F}_a(\dot{\mathbf{q}}(t), \theta(t), \mathbf{U}(t))$ is derived from eq. 6.21 . $\mathbf{B}_g$ is equal to the identity matrix $\mathbf{I}$. The mechanical properties of the structure are assumed to be linear and time invariant.

If the dynamical system is linear and time invariant, the differential and algebraic equations may be written in matrix form. The study of the motion of the system about the equilibrium points and the study of the stability for small amplitude vibrations is undertaken by a linearization of the system about its equilibrium the equilibrium points which are described by

$$\dot{\mathbf{x}}(t) = \mathbf{0} \tag{6.32}$$

The equilibrium points are evaluated considering the non linear system. Fig. 6.4(b) describes the system after linearization. The linearization is described in paragraph 6.2.3. In this case, the system's input is represented by the gravity vector $\mathbf{g}'_s$, the mean wind vector $\mathbf{U}$, and by the turbulence vector $\tilde{\mathbf{U}}(t)$. The two latter can be summed in one vector which represents the instantaneous wind speed $\mathbf{U}(t)$, see eq. 6.1. After linearization $\mathbf{F}_a(\dot{\mathbf{q}}(t), \theta(t), \mathbf{U}(t))$ is decomposed into four components (eq. 6.22). The first one is a constant term which depends on $\mathbf{U}$. This term is given by the product of the input matrix The second and third terms depend on the structural velocities and displacements, $\mathbf{x}(t)$, respectively and are referred to as self-excited or aeroelastic terms. These terms are given by the product of the matrix $\mathbf{A}_a$ times the state vector $\mathbf{x}(t)$. From a state space description the aeroelastic term $\mathbf{A}_a$ can be considered as a feedback state term that can be summed to the state structural matrix $\mathbf{A}_s$. The state matrix, $\mathbf{A}_s + \mathbf{A}_a$ is time invariant for a given mean wind velocity. The so obtained system is LTI, i.e. linear time invariant.

The state space representation consists of two systems of equations, i.e.

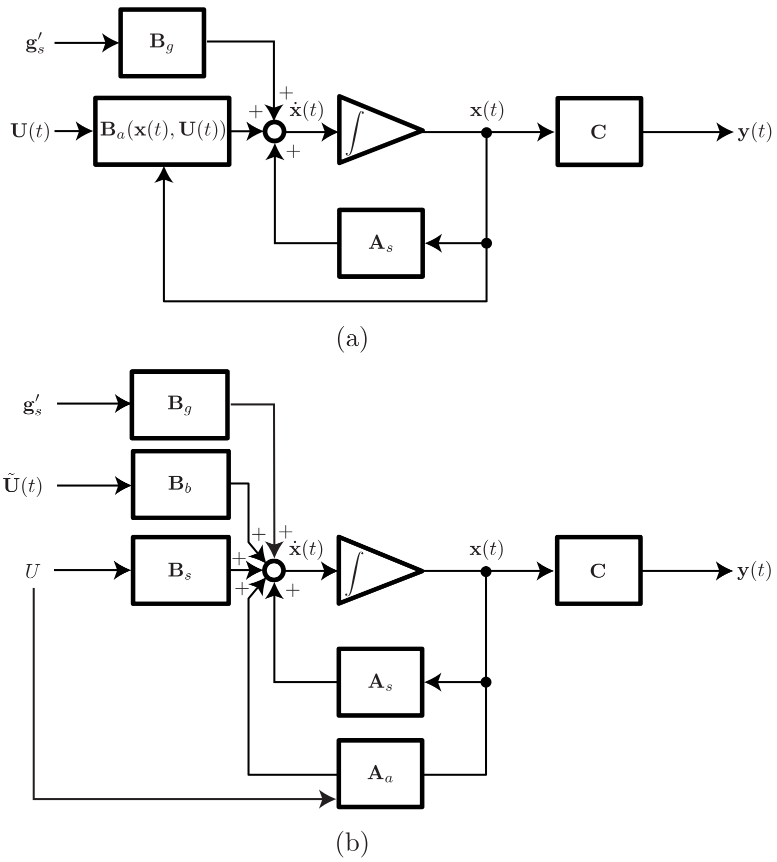

Figure 6.4: *System description pre (a) and after linearization (b)*

the state and output system. The state equation is:

$$
\begin{aligned}
\dot{\mathbf{x}}(t) &= (\mathbf{A}_s + \mathbf{A}_a)\,\mathbf{x}(t) + \mathbf{B}_s U + \mathbf{B}_b \tilde{\mathbf{U}}(t) + \mathbf{B}_g \mathbf{g}'_s \\
\left[\begin{array}{c} \dot{\mathbf{q}}(t) \\ \ddot{\mathbf{q}}(t) \end{array}\right] &= \left[\begin{array}{cc} \mathbf{0} & \mathbf{I} \\ -\mathbf{M}_s^{-1}\mathbf{K_s} & -\mathbf{M}_s^{-1}\mathbf{C}_s \end{array}\right] \left[\begin{array}{c} \mathbf{q}(t) \\ \dot{\mathbf{q}}(t) \end{array}\right] + \\
&\quad + \left[\begin{array}{cc} \mathbf{0} & \mathbf{0} \\ \mathbf{M}_s^{-1}\, \nabla_{\mathbf{q}(t)} \mathbf{F}_a\big|_{(\mathbf{0},\mathbf{0},\mathbf{U})} & \mathbf{M}_s^{-1}\, \nabla_{\dot{\mathbf{q}}(t)} \mathbf{F_a}\big|_{(\mathbf{0},\mathbf{0},\mathbf{U})} \end{array}\right] \left[\begin{array}{c} \mathbf{q}(t) \\ \dot{\mathbf{q}}(t) \end{array}\right] + \\
&\quad + \left[\begin{array}{c} \mathbf{0} \\ \mathbf{M}_s^{-1}\mathbf{F}_a\big|_{(\mathbf{0},\mathbf{0},\mathbf{U})} U^{-1} \end{array}\right] U + \left[\begin{array}{c} \mathbf{0} \\ \mathbf{M}_s^{-1}\, \nabla_{\mathbf{U}(t)} \mathbf{F_a}\big|_{(\mathbf{0},\mathbf{0},\mathbf{U})} \end{array}\right] \tilde{\mathbf{U}}(t) \\
&\quad + \left[\begin{array}{c} \mathbf{0} \\ \mathbf{I} \end{array}\right] \mathbf{g}'_s
\end{aligned}
\tag{6.33}
$$

The output equation, giving the displacement, is:

$$\mathbf{y}(t) = \mathbf{cx}(t) + \mathbf{dU} = \begin{bmatrix} I & 0 \end{bmatrix} \begin{bmatrix} \mathbf{q}(t) \\ \dot{\mathbf{q}}(t) \end{bmatrix} \tag{6.34}$$

The general solution of the problem is:

$$\begin{aligned} \mathbf{y}(t) &= \mathbf{c}e^{(\boldsymbol{A}_s+\boldsymbol{A}_a)t}\mathbf{x}(0) + \int_0^t \mathbf{c}e^{(\boldsymbol{A}_s+\boldsymbol{A}_a)(t-\tau)} \left[\mathbf{B}_s U + \mathbf{B}_b \tilde{\mathbf{U}}(\tau) + \mathbf{B}_g \mathbf{g}_s'\right] d\tau \\ &= \mathbf{\Phi}(t)\mathbf{x}(0) + \int_0^t \mathbf{c}e^{(\boldsymbol{A}_s+\boldsymbol{A}_a)(t-\tau)} \left[\mathbf{B}_s U + \mathbf{B}_b \tilde{\mathbf{U}}(\tau) + \mathbf{B}_g \mathbf{g}_s'\right] d\tau \end{aligned} \tag{6.35}$$

As in the classical solution method for ordinary differential equations with constant coefficients, the total system state response $\mathbf{x}(t)$ is considered as summation of two parts, a homogeneous solution, $\mathbf{\Phi}(t)\mathbf{x}(0)$, which describes the response of the system to an arbitrary set of initial conditions $\mathbf{x}(0)$, and a particular solution which satisfies the state equations for the given input. The two components are then combined to form the total response. $\mathbf{\Phi}(t) = e^{(\boldsymbol{A}_s+\boldsymbol{A}_a)t}$ is defined to be the state transition matrix.

In state-space terminology, a system is said to be asymptotically stable if the homogeneous response of the state vector $\mathbf{x}(t)$ returns to the origin of the state-space from any arbitrary set of initial conditions $\mathbf{x}(0)$ as time $t \to \infty$. This definition of stability is equivalent to stating that the homogeneous response of all state variables must decay to zero in the absence of any input to the system, or:

$$\lim_{t\to\infty} \mathbf{\Phi}(t)\mathbf{x}(0) = \mathbf{0} \tag{6.36}$$

A linear system, described by state equations $\dot{\mathbf{x}}(t) = \mathbf{Ax}(t) + \mathbf{B}\boldsymbol{U}$, is asymptotically stable if and only if all eigenvalues of the matrix $\boldsymbol{A}$ have negative real parts. In the next paragraph the solution of the eigenvalue problem and the determination of the condition of the linear instability will be analyzed.

6.4 Eigenvalue problem and instability analysis

In order to find the find the eigenvalues, the characteristic equation is solved:

$$\det([\mathbf{A}_s + \mathbf{A}_a] - \lambda\,[\mathbf{I}]) = 0 \tag{6.37}$$

where $[\mathbf{A}_s + \mathbf{A}_a]$ is the state-space matrix and $[\mathbf{I}]$ is the identity matrix. Equation 6.37 can be reduced to a monic polinomial of order 6, of the form

$$p(\lambda) = p_0\lambda^6 + p_1\lambda^5 + p_2\lambda^4 + p_3\lambda^3 + p_4\lambda^2 + p_5\lambda + p_6 = 0 \tag{6.38}$$

where $p_0 = 1$, and p_1-p_6 are reported in the Appendix A.5. The problem's eigenvalues are either real values or complex conjugate pairs. The system is stable if the real parts of all eigenvalues are negative. The characteristic equation governing this specific eigenvalue problem is of 6^{th} degree. The Abel-Ruffini theorem states that there is no general algebraic solution to polynomial equations of 5^{th} degree or higher degree. In these cases, the eigenvalue problem is normally solved numerically. This in order to find the value of the structural damping/stiffness at the boundary of instability. On the other hand, the Routh-Hurwitz criterion (Hurwitz, 1895) allows to check the stability of the system without solving the characteristic equation. The criterion establishes that the system is stable, i.e. all roots of the characteristic polinomium have negative real parts, if and only if all the leading principal minors of the Hurwitz matrix H, i.e. the so called Hurwitz determinants, are positive. The Hurwitz matrix is given by

$$H = \begin{bmatrix} p_1 & 1 & 0 & 0 & 0 & 0 \\ p_3 & p_2 & p_1 & 1 & 0 & 0 \\ p_5 & p_4 & p_3 & p_2 & p_1 & 1 \\ 0 & p_6 & p_5 & p_4 & p_3 & p_2 \\ 0 & 0 & 0 & p_6 & p_5 & p_4 \\ 0 & 0 & 0 & 0 & 0 & p_6 \end{bmatrix} \tag{6.39}$$

The principal diagonal minors of the Hurwitz matrix are

$$\Delta_1 = p_1 \tag{6.40}$$

$$\Delta_2 = p_1p_2 - p_3 \tag{6.41}$$

$$\Delta_3 = -p_4p_1^2 + p_2p_3p_1 + p_5p_1 - p_3^2 \tag{6.42}$$

$$\Delta_4 = -p_4^2p_1^2 + p_2p_6p_1^2 + p_2p_3p_4p_1 - p_2^2p_5p_1 + 2p_4p_5p_1 - p_3p_6p_1 - p_5^2 - p_3^2p_4 + p_2p_3p_5 \tag{6.43}$$

$$\begin{aligned}\Delta_5 = {} & -p_6^2p_1^3 - p_4^2p_5p_1^2 + p_3p_4p_6p_1^2 + 2p_2p_5p_6p_1^2 - p_2^2p_5^2p_1 + 2p_4p_5^2p_1 + p_2p_3p_4p_5p_1 + \\ & - p_2p_3^2p_6p_1 - 3p_3p_5p_6p_1 - p_5^3 + p_2p_3p_5^2 - p_3^2p_4p_5 + p_3^3p_6\end{aligned} \tag{6.44}$$

$$\Delta_6 = p_6\Delta_5 \tag{6.45}$$

As $\Delta_6 = p_6\Delta_5$, the stability condition on $\Delta_6 = p_6\Delta_5$ reduces to imposing $p_6 > 0$

If the 5 principal minors of the Hurwitz matrix, i.e. $\Delta_1 - \Delta_5$ are positive and the 6^{th} order minor is zero, i.e. $\Delta_6 = 0$, the system is at the boundary of stability. Since $\Delta_6 = p_6\Delta_5$, then there are two options:

- the coefficient $p_6 = 0$; this corresponds to the case when one of the roots of the characteristic equation is zero; the system is on the boundary of the aperiodic stability;
- the determinant $\Delta_5 = 0$; in this case, there two complex conjugate roots and the system is on the boundary of the oscillatory stability.

In order to simplify the computational problem of the stability analysis, the Lienard-Chipart criterion is here used (Liénard and Chipart, 1914). The criterion has the advange of providing a test for the system instability by means of a lower number of determinants to be computed. According to the criterion the system is stable if:

$$p_2,\, p_4,\, p_6 > 0 \text{ and } \Delta_1 = p_1,\, \Delta_3,\, \Delta_5 > 0 \tag{6.46}$$

Note that as

$$p_6 = \omega_x^2 \omega_y^2 \left(-\omega_{a\theta\theta}^2 + \omega_\theta^2\right) \tag{6.47}$$

its sign is associated with the occurrence of static divergence-type instability, which occurs when $\omega_{a\theta\theta}$ becomes larger than ω_θ. The sign of the remaining terms in eq. 6.46 is instead associated with the occurrence of galloping-type instabilities.

6.5 Application of the 3 DOF model

The 3-DOF instability model allows to verify the stability of a system against galloping and static divergence, to design the minimum structural damping and stiffness in order to avoid the occurrence of such instabilities, and to derive the trajectories of the motion.

The stability of the system can be verified once its geometrical and structural properties are assigned, i.e. the cable diameter, D, the mass per unit length, m, the rotational inertia in relation to the mass centre of the cable, J, the angle offset and distance of the mass center to the shear center of the cable section, ς_0 and L_e, as well as the vibration frequencies $f_{x'}$, $f_{y'}$, f_θ, and the damping ratios $\xi_{x'}$, $\xi_{y'}$, $\xi_{\theta'}$ in the x', y', and θ directions. The aerodynamic properties of the prism, i.e. in terms of drag, lift and moment coefficients for varying Re, α, Φ, as well as the angle between the wind direction and the prism's axis, Φ, must also be specified. The stability is verified by applying the Lienard-Chipart criterion as illustrated in paragraph 6.4.

In the following, an example of application of the 3-DOF instability model is proposed. The aerodynamic data, i.e. the quasi-steady drag, lift and moment, refer to a a series of wind tunnel tests undertaken by Chabart and Lilien (1998) for an iced cable conductor. These are reported in Figs. 6.6-6.8. The conductor (see Fig. 6.5) was oriented perpendicular to the wind flow, so that $\Phi = 90°$. The coefficients were found as independent of the Reynolds number for the tested angles-of-attack. Chabart and Lilien (1998) later suspended the same conductor in a wind tunnel with a system of springs, in order to obtain a system as close as possible to an overhead line, where the vertical, horizontal and rotational movements are allowed. In table 6.1 are summarised the structural and aerodynamic parameters for the iced cable tested by Chabart and Lilien (1998). As the quasi-steady force coefficients were obtained in smooth flow conditions, all unsteady terms affecting the stability were set equal to zero in the present model. Same data were employed by Gjelstrup and Georgakis (2011) as an example of application of the 3 DOF model.

Parameter	Value
$m\ [kg]$	2.99
$D\ [m]$	0.0325
$J\ [kg/m^2]$	4.9689e-4
$L_e\ [m]$	0.0025
$\varsigma_0\ [°]$	0
$\Phi\ [°]$	90
$f_x\ [Hz]$	0.995
$f_y\ [Hz]$	0.845
$f_\theta\ [Hz]$	0.865
$\xi_x\ [\%]$	0.08
$\xi_y\ [\%]$	0.08
$\xi_\theta\ [\%]$	0.3

Table 6.1*: Parameters of the iced conductor employed in the passive-dynamic tests performed by Chabart and Lilien (1998).*

In Fig. 6.10(a)-6.10(b) the maps of galloping and static divergence instability obtained by implementing the Lienard-Chiepard criterion are shown. In Fig. 6.10(a) the red colored areas represent the regions where the condition

$$p_2,\, p_4 \text{ and } \Delta_1 = p_1,\, \Delta_3,\, \Delta_5 > 0 \tag{6.48}$$

is satisfied, thus they system in stable against galloping. The blue areas represent the regions where at least one of the terms in eq. 6.48 becomes

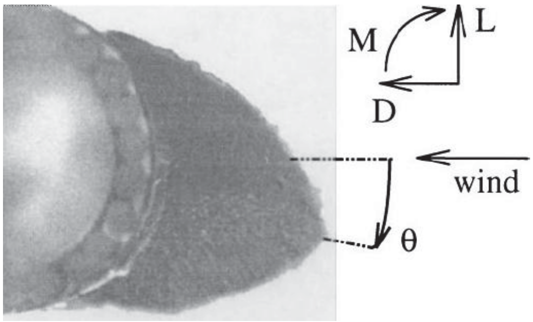

Figure 6.5: *Ice shape and aerodynamic forces convention, (Chabart and Lilien, 1998).*

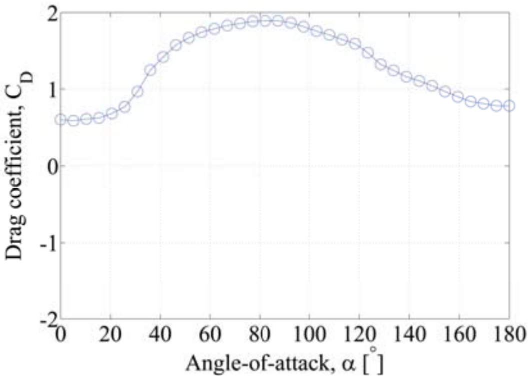

Figure 6.6: *Drag coefficient for varying angles-of-attack, (Chabart and Lilien, 1998).*

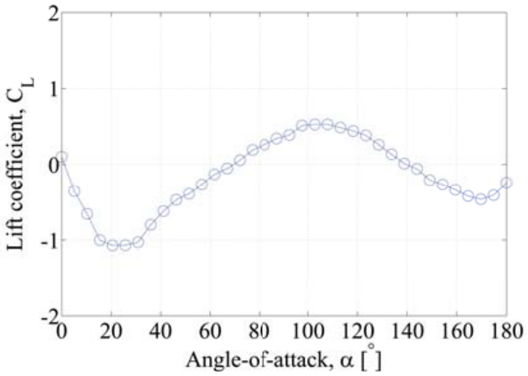

Figure 6.7: *Lift coefficient for varying angles-of-attack, (Chabart and Lilien, 1998).*

negative, thus the system becomes unstable against galloping. In Fig. 6.10(b)

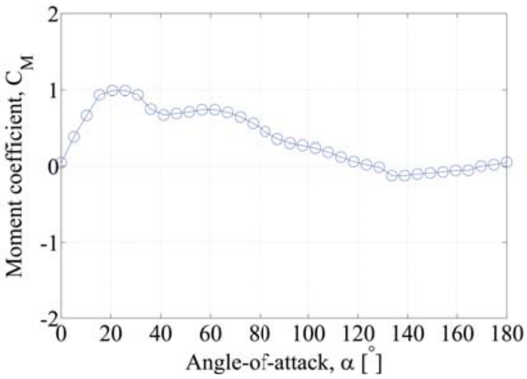

Figure 6.8: *Moment coefficient for varying angles-of-attack, (Chabart and Lilien, 1998).*

the red areas represent the regions where the condition

$$p_6 > 0 \tag{6.49}$$

is satisfied, thus the system is stable against static divergence instability. The blue areas are instead associated with negative sign of p_6 and thus to static divergence-type instability. It is observed that the angle-of-attack region of galloping instability ranges from 12°-150°. On the other hand, static divergence instability occurs for angles-of-attack in the range of 25°-40° and 60°-130°.

Fig. 6.9 shows the regions of instability, i.e. in terms of angle-of-attack, obtained by comparing results of the dynamic tests performed by Chabart and Lilien (1998) (see *Test*), with the 1 DOF Den Hartog criterion (Den Hartog, 1956) (see *1 DOF*), the 2 DOF and 3 DOF instability models derived by Macdonald and Larose (2008a), and Gjelstrup and Georgakis (2011), (see *2 DOF* and *3 DOF*). The figure was reported by Gjelstrup and Georgakis (2011). The region of instability obtained from the dynamic tests performed by Chabart and Lilien (1998) spans in the range of 20°-180° angle-of-attack. It is observed that the 3 DOF criterion developed by Gjelstrup and Georgakis (2011) gives a better prediction in comparison to the 1 DOF and 2 DOF criteria. On the other hand, the present 3 DOF criterion gives an improved prediction in comparison to Gjelstrup and Georgakis (2011) of the regions of instability.

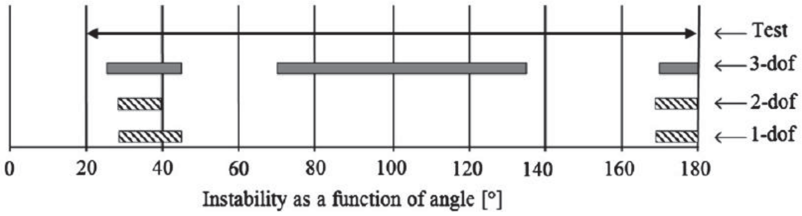

Figure 6.9: *Regions of instability obtained by comparing experimental results of dynamic tests performed by Chabart and Lilien (1998), with the 1 DOF Den Hartog criterion (Den Hartog, 1956), the 2 DOF and 3 DOF instability models derived by Macdonald and Larose (2008a), and Gjelstrup and Georgakis (2011).*

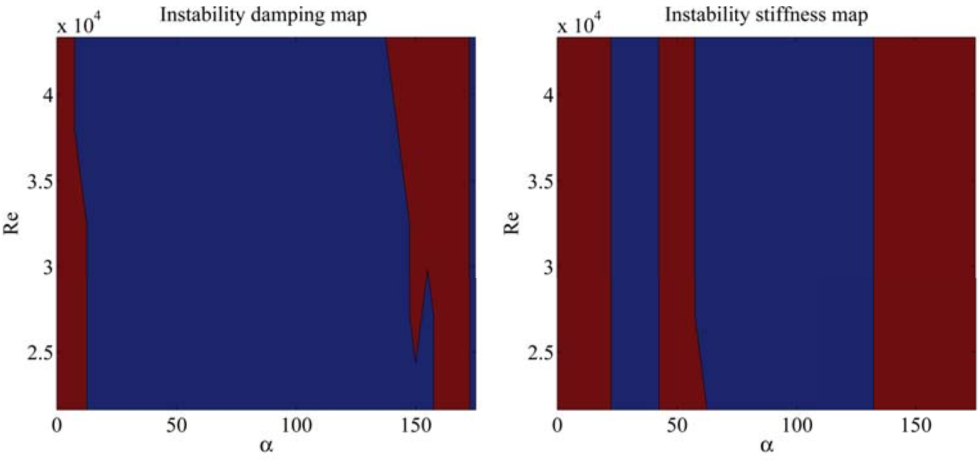

(a) (b)

Figure 6.10: *Maps of galloping (a) and static divergence (b) instability; blue areas represent the regions of predicted galloping (a) and static divergence (b) instability.*

6.6 Conclusion

A new generalized quasi-steady three-degrees-of-freedom analytical model, capable of predicting the aerodynamic instability of a prismatic body with generic cross section, and arbitrary orientation with respect to the flow, was here developed. The novelty of the model is the ability to predic two different types of instabilities which can potentially affect the prism, i.e. galloping-type instability associated with the occurrence of negative aerodynamic damping and static divergence type associated with negative aerodynamic stiffness. The model includes finally effects of unsteadiness of the wind field.

An practical implementation to a set of existing wind tunnel data obtained for an iced conductor, reveals that the current model gives the best prediction of the regions of aerodynamic instability, when compared to existing models.

Bibliography

Blevins, R.D., Iwan, W.D., 1975. The galloping response of a two-degree-of-freedom system. Page 1975 of: American Society of Mechanical Engineers, Applied Mechanics Western Conference, University of Hawaii, Honolulu, Hawaii.

Blevins, R.D., 1977. Flow-induced vibration. New York, Van Nostrand Reinhold Co., 377,1.

Carassale, L., Freda, A., Piccardo, G., 2004. Quasi-static model for aerodynamic instability of yawed circular cylinder. In: 5th International Colloquium Bluff Body Aerodynamics and Applications, pp. 401-404.

Carassale, L., Kareem, A., 2010. Modeling nonlinear systems by Volterra series. Journal of Engineering Mechanics, 136 (6), 801-818.

Chabart, O., Lilien J.L., 1998. Galloping of electrical lines in wind tunnel facilities. J. Wind Eng. Ind. Aerodyn. 74-76, 967-976.

Cheng, S., Larose G.L., Savage, M., Tanaka, H., Irwin, P.A., 2008a. Experimental study on the wind-induced vibration of a dry inclined cable - Part I: Phenomena. J. Wind Eng. Ind. Aerodyn. 96 (12), 2231-2253.

Cheng, S., Irwin P.A., Tanaka, H., 2008b. Experimental study on the wind-induced vibration of a dry inclined cable - Part II: Proposed mechanisms. J. Wind Eng. Ind. Aerodyn. 96 (12), 2254-2272.

Davenport, A.G., Novak, M., 2002. Vibrations of structures induced by fuid flow. In: Chap. 29-II of Harris' shock and vibration handbook. McGraw-Hill.

Den Hartog, J.P., 1956. Mechanical vibrations. Courier Dover Publications.

Denoel, V., Degee, H. 2006., 1956. Influence of the non-linearity of the aerodynamic coefficients on the skewness of the buffeting drag force. Wind and Structures, 9, 457-471.

Gjelstrup, H., Georgakis, C.T., 2011. A quasi-steady 3 degree-of-freedom model for the determination of the onset of bluff body galloping instability. In: Journal of Fluids and Structures, 27 (7), 1021-1034.

Gjelstrup, H., Georgakis, C.T., 2011. A quasi-steady 3 degree-of-freedom model for the determination of the onset of bluff body galloping instability. In: Journal of Fluids and Structures, 27 (7), 1021-1034.

Hurwitz, A., 1895. Ueber die Bedingungen, unter welchen eien Gleichung nur Wurzeln mit negativen reellen Theilen besitzt. Mathematische Annalen, 46, 273-284.

Jones, K., 1992. Coupled vertical and horizontal galloping. Journal of Engineering Mechanics, 118 (1), 92-107.

Kareem, A., Wu, T., 2013. Wind-induced effects on bluff bodies in turbulent flows: Nonstationary, non-Gaussian and nonlinear features. Journal of Wind Engineering and Industrial Aerodynamics, 122, 21-37.

Liénard, A., Chipart, M.H., 1914. Sur le signe de la partie réelle des racines dune équation algébrique. J. Math. Pure Appl, 10 (4), 291-346.

Luongo, A., Piccardo, G., 2005. Linear instability mechanisms for coupled translational galloping. J. of Sound and Vibration, 288, 1027-1047.

Macdonald, J.HJ., Larose G.L., 2008a. A unified approach to aerodynamic damping and drag/lift instabilities, and its application to dry inclined cable galloping. J. Fluids Struct. 22, 229-252.

Macdonald, J.HJ., Larose G.L., 2008a. Two-degree-of-freedom inclined galloping - Part 1: general formulation and solution for perfectly tuned system. J. Wind Eng. Ind. Aerodyn., 96 (3), 291-307.

Macdonald, J.HJ., Larose G.L., 2008a. Two-degree-of-freedom inclined galloping - Part 2: analysis and prevention for an arbitrary frequency ratio. J. Wind Eng. Ind. Aerodyn., 96 (3), 308-326.

Martin, W.W., Currie, I.G., Naudascher, E., 1981. Streamwise oscillations of cylinders. Journal of the Engineering Mechanics Division-ASCE 107 (3), 589-607.

Nakamura, Y., Mizota, T., 1975. Torsional flutter of rectangular prisms. Journal of the Engineering Mechanics Division-ASCE. (NEM2), 125-142.

Nigol, O., Buchan, P.G., 1981b. Conductor galloping-part II Torsional Mechanism. Power Apparatus and Systems, IEEE Transactions on, 708-720.

Raeesi, A., Cheng, S., Ting, D. S-K. 2013. Aerodynamic damping of an inclined circular cylinder in unsteady flow and its application to the prediction of dry inclined galloping. Journal of Wind Engineering and Industrial Aerodynamics, 113, 12-28.

Symes, J.A., Macdonald, J.H.G., 2006. Quasi-steady dry-galloping analysis of inclined cables in turbulent flow. Pages 121-124 of: Proceedings of 7th UK Conference on Wind Engineering, Glasgow.

Symes, J.A., Macdonald, J.H.G., 2007. Combined buffeting and dry galloping analysis of inclined stay-cables. Pages 201-208 of: 7th International Symposium on Cable Dynamics, Vienna.

Stoyanoff, S., 2001. A unified approach for 3D stability and time domain response analysis with application of quasi-steady theory. J. Wind Eng. Ind. Aerodyn., 89 (14), 1591-1606.

Yu, P., Shah, A.H., Popplewell, N., 1992. Inertially coupled galloping of iced conductors. J. of Applied Mechanics, 59, 140.

Yu, P., Desai, Y.M., Shah, A.H., Popplewell, N., 1993. Three-degree-of-freedom model for galloping. Part I: Formulation. J. of Engineering Mechanics, 119 (12), 2404-2425.

Chapter 7

Conclusions

In the present thesis the mechanisms of vibration of bridge cables under varying meteorological conditions have been investigated by following a twin research approach, i.e. climatic wind tunnel testing of full-scale bridge cable sections and theoretical modelling.

Bridge cables are classified as bluff bodies and as such can only undergo instabilities of vortex shedding-, buffeting- and galloping-type. A literature review on the possible excitation mechanisms of inclined bridge cables under different climatic conditions, i.e. dry, wet and iced, was first undertaken. The study helped to systematize the current knowledge of the associated excitation mechanisms, based on results of full-scale monitoring, wind tunnel testing and theoretical modelling. Several aspects of the instability needing more clarification were identified, so to inspire the wind tunnel test campaign programme and the theoretical modelling.

Static wind tunnel tests were first undertaken on full-scale plain surfaced bridge cable section models, oriented perpendicular or inclined/yawed to the flow, in dry conditions. Tests were undertaken for varying Reynolds numbers, cable-wind angles, angles-of-attack and turbulence intensities. It was observed that the cable's drag coefficient is fairly consistent with angle-of-attack, while the lift coefficient changes significantly, given all other parameters fixed. These changes can be triggered by small geometrical imperfections of the cable model, such as surface roughness alterations or distortions of the shape. Assuming the validity of the quasi-steady theory, negative aerodynamic damping can be predicted in the critical Reynolds number range where the drag coefficient is reduced to its minimum and the lift coefficient experiences significant variations in sign and amplitude with angle-of-attack. Although important for theoretical modeling and section model testing, variations in the drag and lift coefficients with angle-of-attack may not ultimately be important when averaged over the full length of an inclined structural cable.

Passive-dynamic wind tunnel tests were later undertaken for a dry plain surfaced cable section model of the same type as the one tested in static conditions. Tests were undertaken at a critical cable-wind angle for the occurrence of dry inclined galloping, which had equally been been tested using the static setup. The cable's mass and frequency were fixed. Results showed that the aerodynamic damping as well as the peak to peak amplitude change significantly with Reynolds number, for varying degrees of axial rotation of the cable model, i.e. angles-of-attack. In particular, minor deviations in the cable response are observed in the subcritical Reynolds number range. On the other hand, in the critical Reynolds number range the cable can either exhibit a stable response, characterised by positive aerodynamic damping and limited peak to peak amplitudes of vibration, or can undergo divergent vibration accompanied by negative aerodynamic damping. Thus, dry instability is very sensitive to microscopic geometrical imperfections of the cable model and can occur over a large range of Reynolds numbers. This confirms experimental findings of the static tests.

Passive-dynamic wind tunnel tests were later undertaken for an inclined and yawed plain surfaced full-scale plain bridge cable model in rainy condtions. Tests were performed for varying levels of the mass and wettability of the cable and helped to better understand the rain-wind induced and dry instabilities. In particular, galloping-type instability was detected in dry conditions in the critical Reynolds number range. Under the effects of wind and rain, the cable model underwent different types of instability mechanisms, depending on the level of surface wettability and of mass. RWIV instability was observed only when the cable surface was characterised by an increased level of wettability, for all tested mass levels. The instability occurred only for a limited range of Reynolds number and as in the dry state was again characterized by the occurrence of large amplitude vibrations accompanied by negative aerodynamic damping. No RWIV instability was experienced for the cable model with very low wettability, either in presence of steady water rivulets, induced by a uniform water flow, or in presence of droplets, in the drying state.

In order to complement the understanding achieved by wind tunnel experiments, a new generalized quasi-steady three-degrees-of-freedom analytical model, capable of predicting the aerodynamic instability of a prismatic body with generic cross section, and arbitrary orientation with respect to the flow, was finally developed. The novelty of the model is the ability to predic two different types of instabilities which can potentially affect the prism, i.e. galloping instability associated with the occurrence of negative aerodynamic damping and torsional divergence, associated with negative aerodynamic stiffness. Effects of unsteadiness of the wind field were included in the model. Note also that the time dependency of the prism's cross section was neglected. Thus, the current model applies only to the dry and iced state, but not to the wet state. In fact, even though the ice accretion provokes a temporal change of cable's cross section, the time scale of such variation is much slower than other aerodynamic phenomena which might be responsible for the instantaneous instability. On the other hand, in rainy conditions, the time fluctuations of the cross-sectional shape are much faster and need to be accounted for in the mathematical modelling of the associated excitation. A practical implementation of the present model to a set of existing wind tunnel data obtained for an iced conductor, revealed that it gives the best prediction of the regions of aerodynamic instability, when compared to existing criteria.

7.0.1 Future work

Understanding of bridge vibrations under varying meteorological conditions is a very wide and complex topic of research. It is fair to state that after many years of experimental and theoretical research bridge cable instabilities are still not completely predictable. Investigations performed within this dissertation have attempted to understand and explain part of the vibration issues. Nevertheless numerous topics of potential investigation exist. A selection of these is here suggested.

Effects of roughness/shape deviations of the HPDE sheat on the force coefficients at varying levels of turbulence intensity

In the present study the dependency of the force coefficients of inclined cables on Reynolds number and angle-of-attack has been presented only for smooth flow conditions, i.e. at turbulence intensity below 1%. It was demonstrated that the lift coefficients is significantly affected by changes in the angle-of-attack, due to the non uniform shape/roughness of the cable model. It is interesting to understand whether this effect is evident at larger turbulence intensities, which are likely to occur on bridges. Additional tests should be carried out, at increased levels of wind tunnel along-cable axis turbulence intensity. Tests should be performed for varying orientations of the cable axis with respect to the wind direction and angles-of-attack. The so obtained aerodynamic data might as well be useful for design purposes. The drag, lift and moment coefficients should then be implemented in the quasi-steady analytical model developed within this dissertation, in order to predict regions of aerodynamic instability. For verification, passive-dynamic studies should also be performed at the same level of turbulence intenstity and for the same geometrical attitudes of the cable model.

Investigation of vortex induced vibration at high reduced velocity and dry inclined galloping by means of static and passive-dynamic wind tunnel tests

Passive-dynamic wind tunnel tests have shown that stay cables may either undergo divergent motion, i.e. dry galloping, or limited amplitude motion under a limited interval of wind speed, i.e. vortex induced vibration at high reduced wind velocities. It is still not yet clear whether the two forms of instability can only occur under a specific combination of parameters such as geometrical orientation of the cable model to the wind flow, wind velocity, surface roughness, mass and frequency, or they are interconnected, so that one form of instability could evolve into the other. Additional passive-dynamic wind tunnel tests should be performed in order to better understand and characterise these two forms of instability. Static wind tunnel tests should also be undertaken, for cable models charactersed by the same surface properties, orientations to the wind flow, and end conditions. For completeness smoke visualization tests could be performed in order to understand the features of the flow in the cable's wake, for example the axial flow, which is believed to play a crucial role in the dry inclined excitation.

Angle-of-attack dependency of the force coefficients of inclined/yawed cable models in the iced state

Numerous experimental and theoretical studies have demonstrated that for inclined cables, especially when characterised by a generic cross-sectional shape, as in the iced state, the combination of three parameters affects the trend of the force coefficients and the associated aerodynamic instabilities, i.e the Reynolds number, the angle between the cable axis and the wind direction, and the angle-of-attack.

Static tests have been performed at the DTU/Force climatic wind tunnel in iced conditions for horizontal and vertical cable models for varying Reynolds number and angles-of-attack. Aerodynamic force coefficients have been implemented in the 1 DOF Den Hartog instability criterion in order to predict the regions where galloping vibrations could potentially occur. Static wind tunnel tests have been performed additionally for inclined/yawed cable models in the iced state. In this case the focus of the investigation was the dependency of the force coefficients on the angle between the cable axis and the wind direction, leaving out the dependency on the angle-of-attack.

Additional wind tunnel tests should be performed where the combination of all three parameters (i.e Reynolds number, cable-wind angle, and angle-of-attack) on the aerodynamic force coefficients is investigated. The aerodynamic data should be implemented in the quasi-steady analytical model developed within this dissertation in order to predict the regions of instability.

Passive-dynamic wind tunnel testing of cable sections in iced state

Passive-dynamic wind tunnel tests should be performed for horizontal/vertical and inclined/yawed bridge cables, in iced conditions. It is recognised that at present moment the characteristics of this iced cable instability are unknow, as no wind tunnel dynamic or full scale monitoring investigation have been performed. This implies that a very large parametric study should be undertaken, where the combination of numerous parameters should be investigated such as range of critical cable-wind angles, Reynolds number, angle-of-attack. Moreover, attention should be payed the role on the instability of cable mass, frequency and structural damping. Data from passive-dynamic tests could be useful for validating predictions of aerodynamic instability based on application of quasi-steady aerodynamic criteria.

Investigation of the aerodynamic instability of a streamlined body

The analytical model derived within this dissertation applies for a prism with generic cross-section, i.e. either bluff or streamlined. It could be of interest to attempt an application of the model to a streamlined body, which is expected to exhibit a completely different aerodynamic behaviour from a bridge cable. Static and passive-dynamic tests should be performed, so implement the quasi-steady aerodynamic coefficients in the model, and to compare the regions of aerodynamic instability determined analytically with experimental (dynamic) predictions.

Elimination of the quasi-steady steady assumption in the 3 DOF analytical model

The analytical model derived within this dissertation could be extended in order to predict unsteady aerodynamic phenomena such as flutter. This requires a reformulation of the aerodynamic damping and stiffness matrices, i.e. as in terms of flutter derivatives.

Appendix A

Analytical model

A.1 Derivation of the aerodynamic forces

In the following, detailed derivation of the linearized expression of the aerodynamic forces, based on equation 6.22, is reported. Generally, the gradient of the aerodynamic force per unit length $F_a(\dot{\mathbf{q}}(t), \theta(t), \mathbf{U}(t))$ with respect to a generic vector time function $\mathbf{f}(t)$ can be written as

$$\begin{aligned}\nabla_{\mathbf{f}(t)} \mathbf{F}_a \big|_{(\mathbf{0},\mathbf{0},\mathbf{U})} = \frac{\rho \nu^2}{2D} \big\{ \left[(\mathbf{R}_z(\alpha_R)\mathbf{C}) \otimes \left(\nabla_{\mathbf{f}(t)} Re_R^2 \right) \right] + Re_R^2 \left[\left(\nabla_{\mathbf{f}(t)} \mathbf{R}_z(\alpha_R)\mathbf{C} \right) + \right. \\ \left. + \mathbf{R}_z(\alpha_R) \left(\nabla_{\mathbf{f}(t)} \mathbf{C} \right) \right] \big\} \big|_{(\mathbf{0},\mathbf{0},\mathbf{U})}\end{aligned} \tag{A.1}$$

Equation A.1 is made of three main terms which can be further simplified. In particular:

$$\nabla_{\mathbf{f}(t)} Re_R^2 = 2Re_R \nabla_{\mathbf{f}(t)} Re_R = 2Re_R \nabla_{\mathbf{f}(t)} T_{11} b_1 = 2Re_R \frac{D}{\nu} \nabla_{\mathbf{f}(t)} U_R \tag{A.2}$$

The second term is a third order tensor obtained from the derivation of the rotation matrix with respect to the structural velocity vector. This tensor can be reduced in the tensorial product of two vectors considering the properties:

$$\frac{\partial \cos f(x)}{\partial x} = -\frac{\partial f(x)}{\partial x} \sin x \quad \frac{\partial \sin f(x)}{\partial x} = \frac{\partial f(x)}{\partial x} \cos x \tag{A.3}$$

that are the term contained in the rotation matrix. After simple manipulation it is obtained:

$$\nabla_{\mathbf{f}(t)} \mathbf{R}_z(\alpha_R)\mathbf{C} = \mathbf{F}\mathbf{C} \otimes \nabla_{\mathbf{f}(t)} \alpha_R \tag{A.4}$$

where

$$\mathbf{F} = \nabla_x \mathbf{R}_z(x)\big|_{x=\bar{\varphi}} = \begin{bmatrix} -\sin(\bar{\varphi}) & -\cos(\bar{\varphi}) & 0 \\ \cos(\bar{\varphi}) & -\sin(\bar{\varphi}) & 0 \\ 0 & 0 & 0 \end{bmatrix} \tag{A.5}$$

As the vector of the aerodynamic coefficients $\mathbf{C}$ depends on $\mathbf{f}(\mathbf{t})$, where $\mathbf{f}(t) = \dot{\mathbf{q}}(t)$, $\mathbf{q}(t)$ or $\mathbf{U}(t)$, towards $\mathbf{d}$, the chain rule need to be implemented. This is given by:

$$\nabla_{\dot{\mathbf{q}}(t)}\mathbf{C}\big|_{(\mathbf{0},\mathbf{0},\mathbf{U})} = \left[(\nabla_{\mathbf{d}}\mathbf{C})\left(\nabla_{\mathbf{f(t)}}\mathbf{d}\right)\right]\big|_{(\mathbf{0},\mathbf{0},\mathbf{U})} \tag{A.6}$$

Eq. A.1 may thus be re-written as

$$\begin{aligned}\nabla_{\mathbf{f}(t)}\mathbf{F}_a\big|_{(\mathbf{0},\mathbf{0},\mathbf{U})} = \frac{\rho\nu^2}{2D}\Bigg\{\Bigg[(\mathbf{R}_z(\alpha_R)\mathbf{C}) \otimes \left(\left(2Re\frac{D}{\nu}\right)\nabla_{f(t)}U_R\right)\Bigg] + Re_R^2\Big[\big(\mathbf{FC}\otimes\nabla_{\mathbf{f}(t)}\alpha_R\big) + \\ +\mathbf{R}_z(\alpha_R)\left[(\nabla_{\mathbf{d}}\mathbf{C})\left(\nabla_{\mathbf{f(t)}}\mathbf{d}\right)\right]\Big]\Bigg\}\Big|_{(\mathbf{0},\mathbf{0},\mathbf{U})}\end{aligned} \tag{A.7}$$

The structural velocity and displacement proportional terms of equation 6.22 are obtained by setting $\mathbf{f}(t) = \dot{\mathbf{q}}(t)$ and $\mathbf{f}(t) = \mathbf{q}(t)$ in equation A.1.

The nil-mean fluctuating wind velocity proportional terms, i.e. buffeting terms, are similarly obtained upon substitution of $\mathbf{f}(t) = \mathbf{U}(t)$ in equation A.1.

A.2 Flow variables linearization

The vector $b(\dot{q}(t), \theta(t), \mathbf{U}(t))$

$$\mathbf{b}(\dot{\mathbf{q}}(t), q_3(t), \mathbf{U}(t)) = \begin{bmatrix} U_R(\dot{\mathbf{q}}, \theta(t), \mathbf{U}(t))) \\ \alpha_R(\dot{\mathbf{q}}, \theta(t), \mathbf{U}(t))) \\ \Phi_R(\dot{\mathbf{q}}, \theta(t), \mathbf{U}(t))) \end{bmatrix} \tag{A.8}$$

is equally Taylor expanded as

$$\begin{aligned}
\mathbf{b}(\dot{\mathbf{q}}(t), \theta(t), \mathbf{U}(t)) &= \mathbf{b}\big|_{(\mathbf{0},\mathbf{0},\mathbf{U})} + \nabla_{\mathbf{U}(t)}\mathbf{b}\big|_{(\mathbf{0},\mathbf{0},\mathbf{U})} (\mathbf{U}(t) - \mathbf{U}) + \\
&+ \nabla_{\dot{\mathbf{q}}(t)}\mathbf{b}\big|_{(\mathbf{0},\mathbf{0},\mathbf{U})} \dot{\mathbf{q}}(t) + \nabla_{\mathbf{q}(t)}\mathbf{b}\big|_{(\mathbf{0},\mathbf{0},\mathbf{U})} \mathbf{q}(t) = \\
&= \begin{bmatrix} U \\ \bar{\varphi} \\ \Phi \end{bmatrix} + \\
&+ \begin{bmatrix} 1 & 0 & 0 \\ 0 & \dfrac{\sin\Theta(1+\tan^2\beta)}{U(\sin^2\Theta + \tan^2\beta)} & \dfrac{\sin\beta\cos\Theta}{U\cos^2\beta(\sin^2\Theta + \tan^2\beta)} \\ 0 & -\dfrac{\cos\Theta\sin\beta}{U\sin\Phi} & \dfrac{\sin\Theta}{U\sin\Phi} \end{bmatrix} \begin{bmatrix} \tilde{u}(t) \\ \tilde{v}(t) \\ \tilde{w}(t) \end{bmatrix} + \\
&+ \begin{bmatrix} -\cos\bar{\varphi}\sin\Phi & -\sin\bar{\varphi}\sin\Phi & R_\delta\sin\delta\sin\Phi \\ \dfrac{\sin\bar{\varphi}}{U\sin\Phi} & -\dfrac{\cos\bar{\varphi}}{U\sin\Phi} & \dfrac{-R_\delta\cos\delta}{U\sin\Phi} \\ -\dfrac{\cos\bar{\varphi}\cos\Phi}{U} & -\dfrac{\sin\bar{\varphi}\cos\Phi}{U} & \dfrac{R_\delta\sin\delta\cos\Phi}{U} \end{bmatrix} \begin{bmatrix} \dot{\xi}(t) \\ \dot{\eta}(t) \\ \dot{\theta}(t) \end{bmatrix} \\
&+ \begin{bmatrix} 0 & 0 & 0 \\ 0 & 0 & -1 \\ 0 & 0 & 0 \end{bmatrix} \begin{bmatrix} \xi(t) \\ \eta(t) \\ \theta(t) \end{bmatrix}
\end{aligned} \tag{A.9}$$

The linearized version of $\mathbf{d}(\dot{\mathbf{q}}(t), \mathbf{q}(t))$ is obtained:

$$
\begin{aligned}
\mathbf{d}(\dot{\mathbf{q}}(t), \theta(t), \mathbf{U}(t)) &= \mathbf{Tb}(\dot{\mathbf{q}}(t), \theta(t)) = \\
&= \begin{bmatrix} Re_R(\dot{\mathbf{q}}, \theta(t), \mathbf{U}(t)) & \alpha_R(\dot{\mathbf{q}}, \theta(t), \mathbf{U}(t)) & \Phi_R(\dot{\mathbf{q}}, \theta(t), \mathbf{U}(t)) \end{bmatrix}^T = \\
&= \begin{bmatrix} Re \\ \bar{\varphi} \\ \Phi \end{bmatrix} + \\
&+ \begin{bmatrix} \frac{D}{\nu} & 0 & 0 \\ 0 & \frac{D \sin\Theta (1 + \tan^2\beta)}{\nu Re (\sin^2\Theta + \tan^2\beta)} & \frac{D \sin\beta \cos\Theta}{\nu Re \cos^2\beta (\sin^2\Theta + \tan^2\beta)} \\ 0 & -\frac{D \cos\Theta \sin\beta}{\nu Re \sin\Phi} & \frac{D \sin\Theta}{\nu Re \sin\Phi} \end{bmatrix} \begin{bmatrix} \widetilde{u}(t) \\ \tilde{v}(t) \\ \tilde{w}(t) \end{bmatrix} + \\
&+ \begin{bmatrix} -\frac{D \cos\bar{\varphi} \sin\Phi}{\nu} & -\frac{D \sin\bar{\varphi} \sin\Phi}{\nu} & \frac{D R_\delta \sin\delta \sin\Phi}{\nu} \\ \frac{D \sin\bar{\varphi}}{\nu Re \sin\Phi} & -\frac{D \cos\bar{\varphi}}{\nu Re \sin\Phi} & \frac{-D R_\delta \cos\delta}{\nu Re \sin\Phi} \\ -\frac{D \cos\bar{\varphi} \cos\Phi}{\nu Re} & -\frac{D \sin\bar{\varphi} \cos\Phi}{\nu Re} & \frac{D R_\delta \sin\delta \cos\Phi}{\nu Re} \end{bmatrix} \begin{bmatrix} \dot{\xi}(t) \\ \dot{\eta}(t) \\ \dot{\theta}(t) \end{bmatrix} + \\
&+ \begin{bmatrix} 0 & 0 & 0 \\ 0 & 0 & -1 \\ 0 & 0 & 0 \end{bmatrix} \begin{bmatrix} \xi(t) \\ \eta(t) \\ \theta(t) \end{bmatrix}
\end{aligned}
\tag{A.10}
$$

In eq. A.10, U is set equal to $Re\,\nu/D$.

A.3 Aerodynamic forces linearization

The linearization of the aerodynamic damping matrix is

$$\begin{aligned}\nabla_{\dot{\mathbf{q}}(t)}\mathbf{F}_a\big|_{(\mathbf{0},\mathbf{0},\mathbf{U})} = \frac{\rho\nu^2}{2D}\Big\{\Big[(\mathbf{R}_z(\alpha_R)\mathbf{C})\otimes\Big(\Big(2Re\frac{D}{\nu}\Big)\nabla_{\dot{\mathbf{q}}(t)}U_R\Big)\Big] + Re_R^2\big[\big(\mathbf{FC}\otimes\nabla_{\dot{\mathbf{q}}(t)}\alpha_R\big) + \\ +\mathbf{R}_z(\alpha_R)\big[(\nabla_{\mathbf{d}}\mathbf{C})\big(\nabla_{\dot{\mathbf{q}}(\mathbf{t})}\mathbf{d}\big)\big]\big]\Big\}\big|_{(\mathbf{0},\mathbf{0},\mathbf{U})}\end{aligned} \tag{A.11}$$

$$\frac{\rho\nu^2}{2D}(\mathbf{R}_z(\alpha_R)\mathbf{C})\otimes(2Re\frac{D}{\nu}\nabla_{\dot{\mathbf{q}}(t)}U_R)\Big|_{(\mathbf{0},\mathbf{0},\mathbf{U})} = \rho\nu Re\sin\Phi\begin{bmatrix} f_1 & f_2 & f_3\\ f_4 & f_5 & f_6\\ f_7 & f_8 & f_9\end{bmatrix} \tag{A.12}$$

$$f_1 = -\cos\bar{\varphi}\,(C_{x'}\cos\bar{\varphi} - C_{y'}\sin\bar{\varphi}) \tag{A.13}$$

$$f_2 = -\sin\bar{\varphi}\,(C_{x'}\cos\bar{\varphi} - C_{y'}\sin\bar{\varphi}) \tag{A.14}$$

$$f_3 = R_\delta\sin\delta\,[C_{x'}\cos\bar{\varphi} - C_{y'}\sin\bar{\varphi}] \tag{A.15}$$

$$f_4 = -\cos\bar{\varphi}\,(C_{x'}\sin\bar{\varphi} + C_{y'}\cos\bar{\varphi}) \tag{A.16}$$

$$f_5 = -\sin\bar{\varphi}\,(C_{x'}\sin\bar{\varphi} + C_{y'}\cos\bar{\varphi}) \tag{A.17}$$

$$f_6 = R_\delta\sin\delta\,(C_{x'}\sin\bar{\varphi} + C_{y'}\cos\bar{\varphi}) \tag{A.18}$$

$$f_7 = -DC_M\cos\bar{\varphi} \tag{A.19}$$

$$f_8 = -DC_M\sin\bar{\varphi} \tag{A.20}$$

$$f_9 = DC_MR_\delta\sin\delta \tag{A.21}$$

$$\frac{\rho\nu^2}{2D}Re_R^2(\mathbf{FC}\otimes\nabla_{\dot{\mathbf{q}}(t)}\alpha_R)\Big|_{(\mathbf{0},\mathbf{0},\mathbf{U})} = \frac{\rho\nu Re}{2\sin\Phi}\begin{bmatrix} g_1 & g_2 & g_3\\ g_4 & g_5 & g_6\\ 0 & 0 & 0\end{bmatrix} \tag{A.22}$$

$$g_1 = -\sin\bar{\varphi}\,(C_{x'}\sin\bar{\varphi} + C_{y'}\cos\bar{\varphi}) \tag{A.23}$$

$$g_2 = \cos\bar{\varphi}\left(C_{x'}\sin\bar{\varphi} + C_{y'}\cos\bar{\varphi}\right) \tag{A.24}$$

$$g_3 = R_\delta\cos\delta(C_{x'}\sin\bar{\varphi} + C_{y'}\cos\bar{\varphi}) \tag{A.25}$$

$$g_4 = \sin\bar{\varphi}\left(C_{x'}\cos\bar{\varphi} - C_{y'}\sin\bar{\varphi}\right) \tag{A.26}$$

$$g_5 = -\cos\bar{\varphi}\left(C_{x'}\cos\bar{\varphi} - C_{y'}\sin\bar{\varphi}\right) \tag{A.27}$$

$$g_6 = -R_\delta\cos\delta\left(C_{x'}\cos\bar{\varphi} - C_{y'}\sin\bar{\varphi}\right) \tag{A.28}$$

$$\frac{\rho\nu^2}{2D}Re_R^2R_z(\alpha_R)\left[\left(\nabla_{\mathbf{d}}\mathbf{C}\right)\left(\nabla_{\dot{\mathbf{q}}(\mathbf{t})}\mathbf{d}\right)\right]\bigg|_{(\mathbf{0},\mathbf{0},\mathbf{U})} = \frac{\rho\nu Re}{2}\begin{bmatrix} h_1 & h_2 & h_3 \\ h_4 & h_5 & h_6 \\ h_7 & h_8 & h_9 \end{bmatrix} \tag{A.29}$$

$$\begin{aligned} h_1 = \Bigg[&\cos\bar{\varphi}\left(\frac{\sin\bar{\varphi}}{\sin\Phi}\frac{\partial C_{x'}}{\partial\alpha_R} - \cos\bar{\varphi}\left(\cos\Phi\frac{\partial C_{x'}}{\partial\Phi} + \sin\Phi\frac{\partial C_{x'}}{\partial Re}Re\right)\right) \\ &+\sin\bar{\varphi}\left(-\frac{\sin\bar{\varphi}}{\sin\Phi}\frac{\partial C_{y'}}{\partial\alpha_R} + \cos\bar{\varphi}\left(\cos\Phi\frac{\partial C_{y'}}{\partial\Phi} + \sin\Phi\frac{\partial C_{y'}}{\partial Re}Re\right)\right)\Bigg] \end{aligned} \tag{A.30}$$

$$\begin{aligned} h_2 = \Bigg[&\cos\bar{\varphi}\left(-\frac{\cos\bar{\varphi}}{\sin\Phi}\frac{\partial C_{x'}}{\partial\alpha_R} - \sin\bar{\varphi}\left(\cos\Phi\frac{\partial C_{x'}}{\partial\Phi} + \sin\Phi\frac{\partial C_{x'}}{\partial Re}Re\right)\right) \\ &+\sin\bar{\varphi}\left(\frac{\cos\bar{\varphi}}{\sin\Phi}\frac{\partial C_{y'}}{\partial\alpha_R} + \sin\bar{\varphi}\left(\cos\Phi\frac{\partial C_{y'}}{\partial\Phi} + \sin\Phi\frac{\partial C_{y'}}{\partial Re}Re\right)\right)\Bigg] \end{aligned} \tag{A.31}$$

$$\begin{aligned} h_3 = R_\delta\Bigg[&\cos\bar{\varphi}\left(-\frac{\cos\delta}{\sin\Phi}\frac{\partial C_{x'}}{\partial\alpha_R} + \sin\delta\left(\cos\Phi\frac{\partial C_{x'}}{\partial\Phi} + \sin\Phi D\frac{\partial C_{x'}}{\partial Re}Re\right)\right) \\ &+\sin\bar{\varphi}\left(\frac{\cos\delta}{\sin\Phi}\frac{\partial C_{y'}}{\partial\alpha_R} - \sin(\delta)\left(\cos\Phi\frac{\partial C_{y'}}{\partial\Phi} + \sin\Phi D\frac{\partial C_{y'}}{\partial Re}Re\right)\right)\Bigg] \end{aligned} \tag{A.32}$$

$$\begin{aligned} h_4 = \sin\bar{\varphi}&\left[\frac{\sin\bar{\varphi}}{\sin\Phi}\frac{\partial C_{x'}}{\partial\alpha_R} - \cos\bar{\varphi}\left(\cos\Phi\frac{\partial C_{x'}}{\partial\Phi} + \sin\Phi\frac{\partial C_{x'}}{\partial Re}Re\right)\right] \\ +\cos\bar{\varphi}&\left[\frac{\sin\bar{\varphi}}{\sin\Phi}\frac{\partial C_{y'}}{\partial\alpha_R} - \cos\bar{\varphi}\left(\cos\Phi\frac{\partial C_{y'}}{\partial\Phi} + \sin\Phi\frac{\partial C_{y'}}{\partial Re}Re\right)\right] \end{aligned} \tag{A.33}$$

$$\begin{aligned} h_5 = \sin\bar{\varphi}&\left[-\frac{\cos\bar{\varphi}}{\sin\Phi}\frac{\partial C_{x'}}{\partial\alpha_R} - \sin\bar{\varphi}\left(\cos\Phi\frac{\partial C_{x'}}{\partial\Phi} + \sin\Phi\frac{\partial C_{x'}}{\partial Re}Re\right)\right] \\ +\cos\bar{\varphi}&\left[-\frac{\cos\bar{\varphi}}{\sin\Phi}\frac{\partial C_{y'}}{\partial\alpha_R} - \sin\bar{\varphi}\left(\cos\Phi\frac{\partial C_{y'}}{\partial\Phi} + \sin\Phi\frac{\partial C_{y'}}{\partial Re}Re\right)\right] \end{aligned} \tag{A.34}$$

$$\begin{aligned} h_6 = R_\delta\Bigg[&\sin\bar{\varphi}\left(-\frac{\cos\delta}{\sin\Phi}\frac{\partial C_{x'}}{\partial\alpha_R} + \sin\delta\left(\cos\Phi\frac{\partial C_{x'}}{\partial\Phi} + \sin\Phi\frac{\partial C_{x'}}{\partial Re}Re\right)\right) \\ &+\cos\bar{\varphi}\left(-\frac{\cos\delta}{\sin\Phi}\frac{\partial C_{y'}}{\partial\alpha_R} + \sin\delta\left(\cos\Phi\frac{\partial C_{y'}}{\partial\Phi} + \sin\Phi\frac{\partial C_{y'}}{\partial Re}Re\right)\right)\Bigg] \end{aligned} \tag{A.35}$$

$$h_7 = D\left[\frac{\sin\bar{\varphi}}{\sin\Phi}\frac{\partial C_M}{\partial \alpha_R} - \cos\bar{\varphi}\left(\cos\Phi\frac{\partial C_M}{\partial \Phi} + \sin\Phi\frac{\partial C_M}{\partial Re}Re\right)\right] \tag{A.36}$$

$$h_8 = D\left[-\frac{\cos\bar{\varphi}}{\sin\Phi}\frac{\partial C_M}{\partial \alpha_R} - \sin\bar{\varphi}\left(\cos\Phi\frac{\partial C_M}{\partial \Phi} + \sin\Phi\frac{\partial C_M}{\partial Re}Re\right)\right] \tag{A.37}$$

$$h_9 = DR_\delta\left[-\frac{\cos\delta}{\sin\Phi}\frac{\partial C_M}{\partial \alpha_R} + \sin\delta\left(\cos\Phi\frac{\partial C_M}{\partial \Phi} + \sin\Phi\frac{\partial C_M}{\partial Re}Re\right)\right] \tag{A.38}$$

The linearization of the aerodynamic stiffness matrix is

$$\begin{aligned}\nabla_{\mathbf{q}(t)}\mathbf{F}_a\Big|_{(\mathbf{0},\mathbf{0},\mathbf{U})} = \frac{\rho\nu^2}{2D}\Bigg\{&\left[(\mathbf{R}_z(\alpha_R)\mathbf{C})\otimes\left(\left(2Re\frac{D}{\nu}\right)\nabla_{\mathbf{q}(t)}U_R\right)\right] + Re_R^2\left[\left(\mathbf{FC}\otimes\nabla_{\mathbf{q}(t)}\alpha_R\right) + \right.\\ &\left.+\mathbf{R}_z(\alpha_R)\left[(\nabla_{\mathbf{d}}\mathbf{C})\left(\nabla_{\mathbf{q(t)}}\mathbf{d}\right)\right]\right]\Bigg\}\Big|_{(\mathbf{0},\mathbf{0},\mathbf{U})}\end{aligned} \tag{A.39}$$

$$\frac{\rho\nu^2}{2D}(\mathbf{R}_z(\alpha_R)\mathbf{C})\otimes(2Re\frac{D}{\nu}\nabla_{\mathbf{q}(t)}U_R)\Bigg|_{(\mathbf{0},\mathbf{0},\mathbf{U})} = \mathbf{0} \tag{A.40}$$

$$\frac{\rho\nu^2}{2D}Re_R^2(\mathbf{FC}\otimes\nabla_{\mathbf{q}(t)}\alpha_R)\Bigg|_{(\mathbf{0},\mathbf{0},\mathbf{U})} = \frac{\rho\nu^2}{2D}Re^2\begin{bmatrix}0 & 0 & C_{x'}\sin\bar{\varphi} + C_{y'}\cos\bar{\varphi}\\ 0 & 0 & -C_{x'}\cos\bar{\varphi} + C_{y'}\sin\bar{\varphi}\\ 0 & 0 & 0\end{bmatrix} \tag{A.41}$$

$$\frac{\rho\nu^2}{2D}Re_R^2\mathbf{R}_z(\alpha_R)\left[(\nabla_{\mathbf{d}}\mathbf{C})\left(\nabla_{\mathbf{q(t)}}\mathbf{d}\right)\right]\Bigg|_{(\mathbf{0},\mathbf{0},\mathbf{U})} = \frac{\rho\nu^2}{2D}Re^2\begin{bmatrix}0 & 0 & -\frac{\partial C_{x'}}{\partial\alpha}\cos\bar{\varphi} + \frac{\partial C_{y'}}{\partial\alpha}\sin\bar{\varphi}\\ 0 & 0 & -\frac{\partial C_{x'}}{\partial\alpha}\sin\bar{\varphi} - \frac{\partial C_{y'}}{\partial\alpha}\cos\bar{\varphi}\\ 0 & 0 & -D\frac{\partial C_M}{\partial\alpha}\end{bmatrix} \tag{A.42}$$

The linearization of the buffeting matrix is

$$\begin{aligned}\nabla_{\mathbf{U}(t)}\mathbf{F_a}\Big|_{(\mathbf{0},\mathbf{0},\mathbf{U})} = \frac{\rho\nu^2}{2D}\Bigg\{&\left[(\mathbf{R}_z(\alpha_R)\mathbf{C})\otimes\left(\left(2Re\frac{D}{\nu}\right)\nabla_{\mathbf{U}(t)}U_R\right)\right] + Re_R^2\left[\left(\mathbf{FC}\otimes\nabla_{\mathbf{U}(t)}\alpha_R\right) + \right.\\ &\left.+\mathbf{R}_z(\alpha_R)\left[(\nabla_{\mathbf{d}}\mathbf{C})\left(\nabla_{\mathbf{U(t)}}\mathbf{d}\right)\right]\right]\Bigg\}\Big|_{(\mathbf{0},\mathbf{0},\mathbf{U})}\end{aligned} \tag{A.43}$$

$$\frac{\rho\nu^2}{2D}(\mathbf{R}_z(\alpha_R)\mathbf{C})\otimes(2Re\frac{D}{\nu}\nabla_{\mathbf{U}(t)}U_R)\Bigg|_{(\mathbf{0},\mathbf{0},\mathbf{U})} = \rho\nu Re\begin{bmatrix}\cos\bar{\varphi}C_{x'} - \sin\bar{\varphi}C_{y'} & 0 & 0\\ \sin\bar{\varphi}C_{x'} + \cos\bar{\varphi}C_{y'} & 0 & 0\\ DC_M & 0 & 0\end{bmatrix} \tag{A.44}$$

$$\frac{\rho\nu^2}{2D}Re_R^2(\mathbf{FC}\otimes\nabla_{\mathbf{U}(t)}\alpha_R)\Bigg|_{(\mathbf{0},\mathbf{0},\mathbf{U})} = \frac{\rho\nu Re}{2}\begin{bmatrix}0 & l_1 & l_2\\ 0 & l_3 & l_4\\ 0 & 0 & 0\end{bmatrix} \tag{A.45}$$

$$l_1 = -(\sin\bar{\varphi} C_{x'} + \cos\bar{\varphi} C_{y'}) \frac{\sin\Theta\,(1+\tan^2\beta)}{\left(\sin^2\Theta + \tan^2\beta\right)} \tag{A.46}$$

$$l_2 = -(\sin\bar{\varphi} C_{x'} + \cos\bar{\varphi} C_{y'}) \frac{\sin\beta\cos\Theta}{\cos^2\beta\left(\sin^2\Theta + \tan^2\beta\right)} \tag{A.47}$$

$$l_3 = (\cos\bar{\varphi} C_{x'} - \sin\bar{\varphi} C_{y'}) \frac{\sin\Theta\,(1+\tan^2\beta)}{\left(\sin^2\Theta + \tan^2\beta\right)} \tag{A.48}$$

$$l_4 = (\cos\bar{\varphi} C_{x'} - \sin\bar{\varphi} C_{y'}) \frac{\sin\beta\cos\Theta}{\cos^2\beta\left(\sin^2\Theta + \tan^2\beta\right)} \tag{A.49}$$

$$\frac{\rho\nu^2}{2D} Re_R^2 \mathbf{R}_z(\alpha_R)\left[(\nabla_{\mathbf{d}}\mathbf{C})\left(\nabla_{\mathbf{U(t)}}\mathbf{d}\right)\right]\Big|_{(\mathbf{0},\mathbf{0},\mathbf{U})} = \frac{\rho\nu Re}{2}\begin{bmatrix} m_1 & m_2 & m_3 \\ m_4 & m_5 & m_6 \\ m_7 & m_8 & m_9 \end{bmatrix} \tag{A.50}$$

$$m_1 = \frac{\partial C_{x'}}{\partial Re} Re\cos\bar{\varphi} - \frac{\partial C_{y'}}{\partial Re} Re\sin\bar{\varphi} \tag{A.51}$$

$$\begin{aligned} m_2 = {} & \cos\bar{\varphi}\left(-\frac{\partial C_{x'}}{\partial\Phi}\frac{\cos\Theta\sin\beta}{\sin\Phi} + \frac{\partial C_{x'}}{\partial\alpha}\frac{\sin\Theta\,(1+\tan^2\beta)}{\left(\sin^2\Theta+\tan^2\beta\right)}\right) \\ & -\sin\bar{\varphi}\left(-\frac{\partial C_{y'}}{\partial\Phi}\frac{\cos\Theta\sin\beta}{\sin\Phi} + \frac{\partial C_{y'}}{\partial\alpha}\frac{\sin\Theta\,(1+\tan^2\beta)}{\left(\sin^2\Theta+\tan^2\beta\right)}\right) \end{aligned} \tag{A.52}$$

$$\begin{aligned} m_3 = {} & \cos\bar{\varphi}\left(\frac{\partial C_{x'}}{\partial\Phi}\frac{\sin\Theta}{\sin\Phi} + \frac{\partial C_{x'}}{\partial\alpha}\frac{\cos\Theta\sin\beta}{\cos^2\beta\left(\sin^2\Theta+\tan^2\beta\right)}\right) \\ & -\sin\bar{\varphi}\left(\frac{\partial C_{y'}}{\partial\Phi}\frac{\sin\Theta}{\sin\Phi} + \frac{\partial C_{y'}}{\partial\alpha}\frac{\cos\Theta\sin\beta}{\cos^2\beta\left(\sin^2\Theta+\tan^2\beta\right)}\right) \end{aligned} \tag{A.53}$$

$$m_4 = \frac{\partial C_{y'}}{\partial Re} Re\cos\bar{\varphi} + \frac{\partial C_{x'}}{\partial Re} Re\sin\bar{\varphi} \tag{A.54}$$

$$\begin{aligned} m_5 = {} & \sin\bar{\varphi}\left(-\frac{\partial C_{x'}}{\partial\Phi}\frac{\cos\Theta\sin\beta}{\sin\Phi} + \frac{\partial C_{x'}}{\partial\alpha}\frac{\sin\Theta\,(1+\tan^2\beta)}{\left(\sin^2\Theta+\tan^2\beta\right)}\right) + \\ & +\cos\bar{\varphi}\left(-\frac{\partial C_{y'}}{\partial\Phi}\frac{\cos\Theta\sin\beta}{\sin\Phi} + \frac{\partial C_{y'}}{\partial\alpha}\frac{\sin\Theta\,(1+\tan^2\beta)}{\left(\sin^2\Theta+\tan^2\beta\right)}\right) \end{aligned} \tag{A.55}$$

$$\begin{aligned} m_6 = {} & \sin\bar{\varphi}\left(\frac{\partial C_{x'}}{\partial\Phi}\frac{\sin\Theta}{\sin\Phi} + \frac{\partial C_{x'}}{\partial\alpha}\frac{\cos\Theta\sin\beta}{\cos^2\beta\left(\sin^2\Theta+\tan^2\beta\right)}\right) + \\ & +\cos\bar{\varphi}\left(\frac{\partial C_{y'}}{\partial\Phi}\frac{\sin\Theta}{\sin\Phi} + \frac{\partial C_{y'}}{\partial\alpha}\frac{\cos\Theta\sin\beta}{\cos^2\beta\left(\sin^2\Theta+\tan^2\beta\right)}\right) \end{aligned} \tag{A.56}$$

$$m_7 = \frac{D\partial C_M}{\partial Re} Re \tag{A.57}$$

$$m_8 = -\frac{D\partial C_M}{\partial \Phi} \frac{\cos\Theta \sin\beta}{\sin\Phi} + \frac{D\partial C_M}{\partial \alpha} \frac{\sin\Theta \left(1 + \tan^2\beta\right)}{\left(\sin^2\Theta + \tan^2\beta\right)} \tag{A.58}$$

$$m_9 = \frac{D\partial C_M}{\partial \Phi} \frac{\sin\Theta}{\sin\Phi} + \frac{D\partial C_M}{\partial \alpha} \frac{\cos\Theta \sin\beta}{\cos^2\beta \left(\sin^2\Theta + \tan^2\beta\right)} \tag{A.59}$$

A.4 Equations of motion

Fig. A.1 shows the definition of the mass center coordinates. The center of mass CM is located at distance L_e from the origo of the local body's reference system (x, y) and at angular distance γ_0 from the x axis. Due to movement of the body along both x and y directions, the the center of mass is displaced to CM'. Due to torsional rotation θ the final position of the center of mass is CM''.

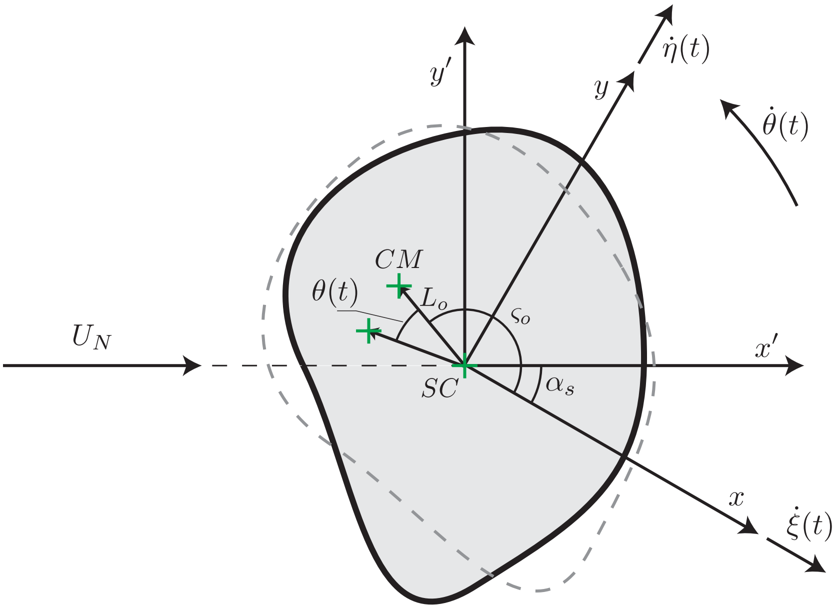

***Figure A.1**: Definition of the mass center coordinates.*

The rigid rotation and translation of the section about the Shear Center (SC) is evaluated for the Center of Mass (CM) as A.1:

$$\mathbf{r}_g(t) = \mathbf{q}(t) + \boldsymbol{\omega}(t) \wedge \mathbf{L}_0 \tag{A.60}$$

The kinetic energy is evaluated as:

$$T = \frac{1}{2}\left(\left|\mathbf{I}\mathbf{r}_g^2(t)\right|\right) \tag{A.61}$$

The potential energy is evaluated as:

$$V = \frac{1}{2}\left(\left|\mathbf{K}_s\dot{\mathbf{r}}_g^2(t)\right|\right) \tag{A.62}$$

The dissipative terms are:

$$\mathbf{F}_D = \mathbf{C}_s\dot{\mathbf{q}}(t) \tag{A.63}$$

where:

$$\mathbf{I} = \begin{bmatrix} m & 0 & 0 \\ 0 & m & 0 \\ 0 & 0 & J \end{bmatrix} \tag{A.64}$$

$$\mathbf{C}_s = \begin{bmatrix} c_{sx} & 0 & 0 \\ 0 & c_{sy} & 0 \\ 0 & 0 & c_{sz} \end{bmatrix} = 2 \begin{bmatrix} m\xi_x\omega_x & 0 & 0 \\ 0 & m\xi_y\omega_y & 0 \\ 0 & 0 & J\xi_\theta\omega_\theta \end{bmatrix} \tag{A.65}$$

$$\mathbf{K}_s = \begin{bmatrix} k_{sx} & 0 & 0 \\ 0 & k_{sy} & 0 \\ 0 & 0 & k_{s\theta} \end{bmatrix} = \begin{bmatrix} m\omega_x^2 & 0 & 0 \\ 0 & m\omega_y^2 & 00 \\ 0 & 0 & J\omega_\theta^2 \end{bmatrix} \tag{A.66}$$

The equation of motion:

$$\nabla_t \left(\nabla_{\dot{\mathbf{q}}(t)} (T - V) \right) - \nabla_{\mathbf{q}(t)} (T - V) + \mathbf{F}_D = \mathbf{F}_m + \mathbf{F}_a \tag{A.67}$$

The final result of the EOM is:

$$\mathbf{M}_s \ddot{\mathbf{q}}(t) + \mathbf{C}_s \dot{\mathbf{q}}(t) + \mathbf{K}_s \mathbf{q}(t) = \mathbf{F}_m + \mathbf{F}_a \tag{A.68}$$

where:

$$\mathbf{M}_s = \begin{bmatrix} m & 0 & -mL_0 \sin\varsigma_0 \\ 0 & m & mL_0 \cos\varsigma_0 \\ -mL_0 \sin\varsigma_0 & mL_0 \cos\varsigma_0 & J + mL_0^2 \end{bmatrix} \tag{A.69}$$

A.5 Terms of the characteristic polynomium

$$p_0 = 1 \tag{A.70}$$

$$\begin{aligned}
p_1 = {} & \xi_x\omega_x\left(2+\frac{2m\sin\varsigma_0^2\omega_x L_e^2}{J}\right)+\xi_y\omega_y\left(2+\frac{2m\cos\varsigma_0^2 L_e^2}{J}\right)+2\xi_\theta\omega_\theta+ \\
& +\omega_x\left(-2\xi_{\mathrm{axx}}+\frac{2mL_e}{J}\left(-L_e\sin\varsigma_0^2\xi_{\mathrm{axx}}+\sin(2\varsigma_0)L_e\xi_{\mathrm{axy}}-\sin\varsigma_0\xi_{\mathrm{ax}\theta}\right)\right)+ \\
& +\omega_y\left(-2\xi_{\mathrm{ayy}}+\frac{2mL_e}{J}\left(\cos\varsigma_0\sin\varsigma_0 L_e\xi_{\mathrm{ayx}}-\cos\varsigma_0^2 L_e\xi_{\mathrm{ayy}}+\cos\varsigma_0\xi_{\mathrm{ay}\theta}\right)\right)+ \\
& +\omega_\theta\left(-2\xi_{\mathrm{a}\theta\theta}+2L_e\left(-\sin\varsigma_0\xi_{\mathrm{a}\theta\mathrm{x}}+\cos\varsigma_0\xi_{\mathrm{a}\theta\mathrm{y}}\right)\right)
\end{aligned} \tag{A.71}$$

$$\begin{aligned}
p_2 = {} & \xi_x\omega_x\left(\left(-4\xi_{\mathrm{ayy}}+\frac{4mL_e}{J}\left(-L_e\xi_{\mathrm{ayy}}+\cos\varsigma_0\xi_{\mathrm{ay}\theta}\right)\right)\omega_y\right)+ \\
& +\xi_x\omega_x\left(4\cos\varsigma_0 L_e\xi_{\mathrm{a}\theta\mathrm{y}}-4\xi_{\mathrm{a}\theta\theta}\right)\omega_\theta+ \\
& +\xi_y\left(\left(-4\xi_{\mathrm{axx}}-\frac{4mL_e}{J}\left(L_e\xi_{\mathrm{axx}}+\sin\varsigma_0\xi_{\mathrm{ax}\theta}\right)\right)\omega_x\omega_y\right)+ \\
& -\xi_y\left(4\sin\varsigma_0 L_e\xi_{\mathrm{a}\theta\mathrm{x}}+4\xi_{\mathrm{a}\theta\theta}\right)\omega_y\omega_\theta+ \\
& -\xi_\theta\left(4\xi_{\mathrm{axx}}\omega_x+4\xi_{\mathrm{ayy}}\omega_y\right)\omega_\theta+\xi_x\xi_y\left(4+\frac{4mL_e^2}{J}\right)\omega_x\omega_y+4\xi_x\xi_\theta\omega_x\omega_\theta+ \\
& +4\xi_y\xi_\theta\omega_y\omega_\theta+\left(1+\frac{m\sin\varsigma_0^2 L_e^2}{J}\right)\omega_x^2+\left(1+\frac{m\cos\varsigma_0^2 L_e^2}{J}\right)\omega_y^2+\omega_\theta^2+ \\
& +\left(\xi_{\mathrm{ayy}}\left(4\sin\varsigma_0 L_e\xi_{\mathrm{a}\theta\mathrm{x}}+4\xi_{\mathrm{a}\theta\theta}\right)-\xi_{\mathrm{a}\theta\mathrm{y}}\left(4\sin\varsigma_0 L_e\xi_{\mathrm{ayx}}+\xi_{\mathrm{ay}\theta}\right)\right)\omega_y\omega_\theta+ \\
& +\omega_x\left(\left(4\left(\xi_{\mathrm{axx}}\xi_{\mathrm{ayy}}-\xi_{\mathrm{axy}}\xi_{\mathrm{ayx}}\right)+\frac{4mL_e}{J}\left(\xi_{\mathrm{axx}}\left(L_e\xi_{\mathrm{ayy}}-\cos\varsigma_0\xi_{\mathrm{ay}\theta}\right)+\right.\right.\right. \\
& \left.\left.-\xi_{\mathrm{axy}}\left(L_e\xi_{\mathrm{ayx}}+\sin\varsigma_0\xi_{\mathrm{ay}\theta}\right)+\xi_{\mathrm{ax}\theta}\left(\cos\varsigma_0\xi_{\mathrm{ayx}}+\sin\varsigma_0\xi_{\mathrm{ayy}}\right)\right)\right)\omega_y+ \\
& \left.+\left(4\xi_{\mathrm{a}\theta\mathrm{x}}\left(\cos\varsigma_0 L_e\xi_{\mathrm{axy}}-\xi_{\mathrm{ax}\theta}\right)+4\xi_{\mathrm{axx}}\left(-\cos\varsigma_0 L_e\xi_{\mathrm{a}\theta\mathrm{y}}+\xi_{\mathrm{a}\theta\theta}\right)\right)\omega_\theta\right)+ \\
& +\frac{mL_e}{J}\left(-\sin\varsigma_0\omega_{\mathrm{ax}\theta}^2+\cos\varsigma_0\omega_{\mathrm{ay}\theta}^2\right)-\omega_{\mathrm{a}\theta\theta}^2
\end{aligned} \tag{A.72}$$

$$
\begin{aligned}
p_3 = {}& \xi_x \omega_x \left(\frac{2m \cos \varsigma_0 L_e \omega^2_{\mathrm{ay}\theta}}{J} - 2\omega^2_{\mathrm{a}\theta\theta} + \left(2 + \frac{2mL_e^2}{J} \right) \omega_y^2 + 2\omega_\theta^2 \right) + \\
& + \xi_x \omega_x \left(-8\xi_{\mathrm{ay}\theta}\xi_{\mathrm{a}\theta\mathrm{y}} + 8\xi_{\mathrm{ayy}}\xi_{\mathrm{a}\theta\theta} \right) \omega_y \omega_\theta + \\
& + \xi_y \left(\left(2 + \frac{2mL_e^2}{J} \right) \omega_x^2 \omega_y + \left(-8\xi_{\mathrm{ax}\theta}\xi_{\mathrm{a}\theta\mathrm{x}} + 8\xi_{\mathrm{axx}}\xi_{\mathrm{a}\theta\theta} \right) \omega_x \omega_y \omega_\theta \right) + \\
& + \xi_y \omega_y \left(-\frac{2m \sin \varsigma_0 L_e \omega^2_{\mathrm{ax}\theta}}{J} - 2\omega^2_{\mathrm{a}\theta\theta} + 2\omega_\theta^2 \right) + \\
& \xi_\theta \left(2\omega_x^2 \omega_\theta + \left(-8\xi_{\mathrm{axy}}\xi_{\mathrm{ayx}} + 8\xi_{\mathrm{axx}}\xi_{\mathrm{ayy}} + 8\xi_x\xi_y \right) \omega_x \omega_y \omega_\theta + 2\omega_y^2 \omega_\theta \right) + \\
& - 8\xi_x\xi_y\xi_{\mathrm{a}\theta\theta}\omega_x\omega_y\omega_\theta - 8\xi_x\xi_\theta\xi_{\mathrm{ayy}}\omega_x\omega_y\omega_\theta - 8\xi_y\xi_\theta\xi_{\mathrm{axx}}\omega_x\omega_y\omega_\theta + \\
& + \omega_x^2 \left(\left(-2\xi_{\mathrm{ayy}} + \frac{2mL_e}{J} \left(-L_e\xi_{\mathrm{ayy}} + \cos \varsigma_0 \xi_{\mathrm{ay}\theta} \right) \right) \omega_y + 2 \left(\cos \varsigma_0 L_e \xi_{\mathrm{a}\theta\mathrm{y}} - \xi_{\mathrm{a}\theta\theta} \right) \omega_\theta \right) + \\
& + \omega_x \Bigg(-\frac{2mL_e}{J} \left(\cos \varsigma_0 \xi_{\mathrm{axx}} + \sin \varsigma_0 \xi_{\mathrm{axy}} \right) \omega^2_{\mathrm{ay}\theta} + 2\xi_{\mathrm{axx}}\omega^2_{\mathrm{a}\theta\theta} + \\
& - 2 \left(\xi_{\mathrm{axx}} + \frac{mL_e}{J} \left(L_e \xi_{\mathrm{axx}} + \sin \varsigma_0 \xi_{\mathrm{ax}\theta} \right) \right) \omega_y^2 + \\
& + 8\xi_{\mathrm{axx}} \left(\xi_{\mathrm{ay}\theta}\xi_{\mathrm{a}\theta\mathrm{y}} - \xi_{\mathrm{ayy}}\xi_{\mathrm{a}\theta\theta} \right) + 8\xi_{\mathrm{axy}} \left(\xi_{\mathrm{ayx}}\xi_{\mathrm{a}\theta\theta} - \xi_{\mathrm{ay}\theta}\xi_{\mathrm{a}\theta\mathrm{x}} \right) + \\
& + 8\xi_{\mathrm{ax}\theta} \left(\xi_{\mathrm{ayy}}\xi_{\mathrm{a}\theta\mathrm{x}} - \xi_{\mathrm{ayx}}\xi_{\mathrm{a}\theta\mathrm{y}} \right) \omega_y \omega_\theta - 2\xi_{\mathrm{axx}}\omega_\theta^2 + \\
& + \omega_y \left(\frac{2mL_e}{J} \left(\cos \varsigma_0 \xi_{\mathrm{ayx}} \omega^2_{\mathrm{ax}\theta} + \sin \varsigma_0 \xi_{\mathrm{ayy}} \omega^2_{\mathrm{ax}\theta} \right) + 2\xi_{\mathrm{ayy}} \left(\omega^2_{\mathrm{a}\theta\theta} - \omega_\theta^2 \right) \right) + \\
& - 2\omega_\theta \left(\xi_{\mathrm{a}\theta\mathrm{x}} \omega^2_{\mathrm{ax}\theta} + \xi_{\mathrm{a}\theta\mathrm{y}} \omega^2_{\mathrm{ay}\theta} \right) + \\
& - \left(2 \sin \varsigma_0 L_e \xi_{\mathrm{a}\theta\mathrm{x}} + 2\xi_{\mathrm{a}\theta\theta} \right) \omega_y^2 \omega_\theta
\end{aligned}
\tag{A.73}
$$

$$
\begin{aligned}
p_4 = {} & \xi_x\omega_x\left(-4\xi_{\mathrm{a}\theta\mathrm{y}}\omega^2_{\mathrm{ay}\theta}\omega_\theta - 4\xi_{\mathrm{a}\theta\theta}\omega_y^2\omega_\theta + \omega_y\left(4\xi_{\mathrm{ayy}}\omega^2_{\mathrm{a}\theta\theta} - 4\xi_{\mathrm{ayy}}\omega^2_\theta\right)\right) + \\
& + \xi_y\left(-4\omega_y\omega_\theta\left(\xi_{\mathrm{a}\theta\mathrm{x}}\omega^2_{\mathrm{ax}\theta} + \xi_{\mathrm{a}\theta\theta}\omega^2_x\right) + 4\omega_x\omega_y\left(\xi_{\mathrm{axx}}\omega^2_{\mathrm{a}\theta\theta} - \xi_{\mathrm{axx}}\omega^2_\theta\right)\right) \\
& + \xi_\theta\left(-4\omega_x^2\omega_y\omega_\theta\left(\xi_{\mathrm{ayy}} + \xi_{\mathrm{axx}}\right)\right) + \xi_x\xi_y\omega_x\omega_y\left(-4\omega^2_{\mathrm{a}\theta\theta} + 4\omega^2_\theta\right) + \\
& + 4\xi_y\xi_\theta\omega_x^2\omega_y\omega_\theta + 4\xi_x\xi_\theta\omega_x\omega_y^2\omega_\theta + \\
& + \omega_x^2\left(\frac{m\cos\varsigma_0 L_e\omega^2_{\mathrm{ay}\theta}}{J} - \omega^2_{\mathrm{a}\theta\theta} + \left(1 + \frac{mL_e^2}{J}\right)\omega_y^2 + +\omega_\theta^2\right) + \\
& + \omega_x^2\left(-4\xi_{\mathrm{ay}\theta}\xi_{\mathrm{a}\theta\mathrm{y}} + 4\xi_{\mathrm{ayy}}\xi_{\mathrm{a}\theta\theta}\right)\omega_y\omega_\theta + \\
& + \omega_y^2\left(-\frac{m\sin\varsigma_0 L_e\omega^2_{\mathrm{ax}\theta}}{J} - \omega^2_{\mathrm{a}\theta\theta} + \omega^2_\theta\right) + \left(-4\xi_{\mathrm{axy}}\xi_{\mathrm{ayx}} + 4\xi_{\mathrm{axx}}\xi_{\mathrm{ayy}}\right)\omega_\theta^2 + \\
& + \omega_x\left(4\omega^2_{\mathrm{ay}\theta}\omega_\theta\left(-\xi_{\mathrm{axy}}\xi_{\mathrm{a}\theta\mathrm{x}} + \xi_{\mathrm{axx}}\xi_{\mathrm{a}\theta\mathrm{y}}\right) + \omega_y\left(4\omega^2_{\mathrm{a}\theta\theta}\left(\xi_{\mathrm{axy}}\xi_{\mathrm{ayx}} - \xi_{\mathrm{axx}}\xi_{\mathrm{ayy}}\right)\right)\right) + \\
& + 4\omega_y^2\omega_\theta\left(-\xi_{\mathrm{ax}\theta}\xi_{\mathrm{a}\theta\mathrm{x}} + \xi_{\mathrm{axx}}\xi_{\mathrm{a}\theta\theta}\right) + \omega_y\omega_\theta\omega^2_{\mathrm{ax}\theta}\left(4\xi_{\mathrm{ayy}}\xi_{\mathrm{a}\theta\mathrm{x}} - 4\xi_{\mathrm{ayx}}\xi_{\mathrm{a}\theta\mathrm{y}}\right)
\end{aligned}
\tag{A.74}
$$

$$
\begin{aligned}
p_5 = {} & \xi_x\omega_x\omega_y^2\left(-2\omega^2_{\mathrm{a}\theta\theta} + 2\omega^2_\theta\right) + \xi_y\omega_x^2\omega_y\left(-2\omega^2_{\mathrm{a}\theta\theta} + 2\omega^2_\theta\right) + 2\xi_\theta\omega_x^2\omega_y^2\omega_\theta + \\
& \omega_x^2\left(-2\xi_{\mathrm{a}\theta\mathrm{y}}\omega^2_{\mathrm{ay}\theta}\omega_\theta - 2\xi_{\mathrm{a}\theta\theta}\omega_y^2\omega_\theta + \omega_y\left(2\xi_{\mathrm{ayy}}\omega^2_{\mathrm{a}\theta\theta} - 2\xi_{\mathrm{ayy}}\omega^2_\theta\right)\right) + \\
& + \omega_x\omega_y^2\left(2\xi_{\mathrm{axx}}\omega^2_{\mathrm{a}\theta\theta} - 2\xi_{\mathrm{axx}}\omega^2_\theta\right) - 2\xi_{\mathrm{a}\theta\mathrm{x}}\omega^2_{\mathrm{ax}\theta}\omega_y^2\omega_\theta
\end{aligned}
\tag{A.75}
$$

$$
p_6 = \omega_x^2\omega_y^2\left(-\omega^2_{a\theta\theta} + \omega^2_\theta\right) \tag{A.76}
$$